Development of a fast and reliable solver based on simplified formulae for ship grounding analyses

Jean-Philippe Pineau

To cite this version:

Jean-Philippe Pineau. Development of a fast and reliable solver based on simplified formulae for ship grounding analyses. Modeling and Simulation. École centrale de Nantes, 2022. English. NNT : 2022ECDN0028 . tel-03868392

HAL Id: tel-03868392
https://theses.hal.science/tel-03868392

Submitted on 23 Nov 2022

HAL is a multi-disciplinary open access archive for the deposit and dissemination of scientific research documents, whether they are published or not. The documents may come from teaching and research institutions in France or abroad, or from public or private research centers.

L'archive ouverte pluridisciplinaire **HAL**, est destinée au dépôt et à la diffusion de documents scientifiques de niveau recherche, publiés ou non, émanant des établissements d'enseignement et de recherche français ou étrangers, des laboratoires publics ou privés.

THESE DE DOCTORAT DE

L'ÉCOLE CENTRALE DE NANTES

ECOLE DOCTORALE N° 602
Sciences pour l'Ingénieur
Spécialité : Mécanique des solides, des matériaux des structures et des surfaces

Par
Jean-Philippe PINEAU

Development of a fast and reliable solver based on simplified formulae for ship grounding analyses

Thèse présentée et soutenue à Icam Nantes, le 23/06/2022
Unité de recherche : UMR 6183, Institut de recherche en Génie Civil et Mécanique (GeM)

Rapporteurs avant soutenance :

Jorgen AMDHAL	Professeur, Norwegian University of Science and Technology, Trondheim
Jean-Baptiste CASIMIR	Professeur des universités, ISAE-SUPMECA, Saint-Ouen

Composition du Jury :

Président :	Patrice CARTRAUD	Professeur des universités, Ecole Centrale Nantes
Examinateurs :	Sara ECHEVERRY JARAMILLO	Chargée de recherche, Université de Liège, Belgique
	Spyros HIRDARIS	Associate Professor, Aalto University, Finland
	Philippe RIGO	Professeur, Université de Liège, Belgique
Dir. de thèse :	Hervé LE SOURNE	Chargé de recherche HDR, ICAM Ouest, Carquefou

Invité
Fabien CONTI : Ingénieur de recherche, Bureau Veritas Marine & Offshore, Saint-Herblain

Remerciements

La réalisation de cette thèse a été rendue possible grâce aux financements octroyés par les programmes de recherches H2020 de l'Union Européenne ainsi que la région Pays de la Loire.

Je souhaite avant tout exprimer toute ma gratitude à Hervé Le Sourne pour la confiance qu'il m'a accordée en me proposant de réaliser cette thèse sous sa direction. Je le remercie de m'avoir fait découvrir le formidable domaine des approches analytiques appliquées aux calculs de collisions. Son expertise, sa rigueur, son implication et sa bienveillance tout au long de ces trois années ont sans aucun doute, grandement contribuées au bon déroulement de ces travaux. J'ai éprouvé beaucoup de plaisir à travailler avec lui, non seulement en raison de sa compétence scientifique, mais également pour ses nombreuses qualités humaines. J'ai beaucoup appris à ses côtés au cours de ces années et j'espère que cette collaboration pourra se poursuivre d'une quelconque façon.

Je remercie également Thibaut Looten de m'avoir initié aux arcanes de la programmation objet. Je le remercie pour le temps passé à mes côtés dans le développement (et surtout le débogage. . .) du solveur, et pour les précieux conseils qu'il m'a partagé tant en programmation qu'en choix de bières.

Ce travail n'aurait pu être mené à bien sans les moments de décompressions partagés avec l'ensemble des collègues. Je les remercie pour leur bonne humeur et tous les bons moments passés ensemble. Je remercie particulièrement Christelle, pour sa confiance et son soutien qu'elle m'a accordée dans la gestion des différents projets durant ces trois dernières années.

J'ai également une pensée pour mes compagnons d'infortunes Rémy, Antoine, Rémy et Luce. Je les remercie pour toutes ces conversations plus ou moins scientifiques (plutôt moins que plus d'ailleurs !), ces raclettes/tartiflettes party. Bien plus que des compagnons, j'y ai trouvé des amis.

Merci également à mes parents, sans qui tout cela n'aurait été possible. Je leur suis reconnaissant de m'avoir permis de réaliser ces études d'ingénieur à l'Icam, de leur soutient, mais également pour le temps passé à lire, relire, modifier et remodifier les différents rapports tout au long de ces années.

Enfin, à ma compagne, Julie, qui a toujours su me soutenir, m'encourager même dans les moments de doutes, sans qui cette thèse aurait été infiniment plus difficile et pour qui mon amour grandit de jour en jour.

"Tempora mori, tempora mundis recorda
Ça ne veut absolument rien dire, mais l'effet reste le même"
Kaamelott, Livre III, tome 1, épisode 27

Contents

List of Figures

List of Tables

Part I

Context, physics and numerical analysis of ship grounding

Chapter 1

General introduction

1.1 Context of the research

The present thesis concerns the mechanics of ship grounding, and is part of **FLARE** [1] research project granted by Europe.

Recent accidents of the *MV Wakashio* and *Costa Concordia* (Figure 1.1) have shown that although the maritime sector is continually investing in increasing and maintaining safety on board ships, further efforts are needed to limit the number and consequences of ship accidents. Currently, to minimise damage extents and hence the probability of capsize during and after a ship collision, the maritime sector refers to SOLAS2009 and 2020 regulatory instruments. SOLAS2020 regulation are based on probabilistic damage distributions derived from statistic analyses of ship accidents, mainly cargo ships. In addition, SOLAS requirement do not consider ship scantlings (presence of a double hull for instance) or energy absorption capacity (material, thickness...) since the damage distribution is only driven by ship length, width and draft. Therefore, when a new ship is designed, it can be very difficult, not to say impossible to quantified the effect of the new design on grounding damage reduction.

Figure 1.1: Capsize of Costa Concordia - 2012

The European **FLARE** project started in June 2019 with the objective to develop a risk-based methodology for the assessment and control of “real” flooding risks. This collaborative project is still on-going and involves the cooperation of cruise ship owners, European shipyards, classification societies, research centres and universities. **FLARE** research project also aims to develop innovative technical solutions for passenger ship design and proposals to the IMO (International Maritime Organisation) regulation to

---

[1] **FL**ooding **A**ccident **RE**sponse: `https://www.flare-project.eu/`

contain and control risk in passenger ships from flooding incidents.

According to the European Maritime Safety Agency (EMSA) [1], collision and grounding accidents contribute significantly to ship structural damage and represent more than 44% of the causality events. Therefore, FLARE project focuses on the response of cruise ships in accidental scenarios involving ship-ship collisions and ship grounding.

In order to evaluate the probability of sinking of a vessel, two different approaches may be employed, namely the *direct* approach and the *indirect* approach.

Direct approach
Given a geographical area and a ship, the first step of the direct approach focuses on collecting data such as ship velocity, draft, ground topology, ship routes from AIS system and traffic databases. Since the previous parameters are uncertain, they should be given in terms of density or probability functions for a large variety of ship accidents. Once the scenario parameters are known, the consequences in terms of oil outflow, damage extent, stability or residual strength may be quantified. Given the probability and the consequences of the accident, the risk (probability * consequences) is evaluated and compared to acceptance criteria. An example of the direct approach using the AIS database may be found in *Zhang et al.* [2]. The major drawback of this method concerns the numerous approximations on the input parameters influencing the collision and grounding preconditions.

Indirect approach
In the indirect or comparative approach, the objective is to focus on the structural improvements of a given structure. Without any consideration of the probability of the accident, numerous scenarios involving a reference ship design and an improved one regarding the crashworthiness are simulated. The influence of alternative scantlings on the damage extent is then evaluated. An example of application of this methodology may be found in *Conti et al.* [3] for ship-ship collision. It is worth noting that since the comparative method is a statistical approach (Monte Carlo type), hundreds or thousands of simulations have to be performed. Figure 1.2 illustrates the direct and indirect approaches.

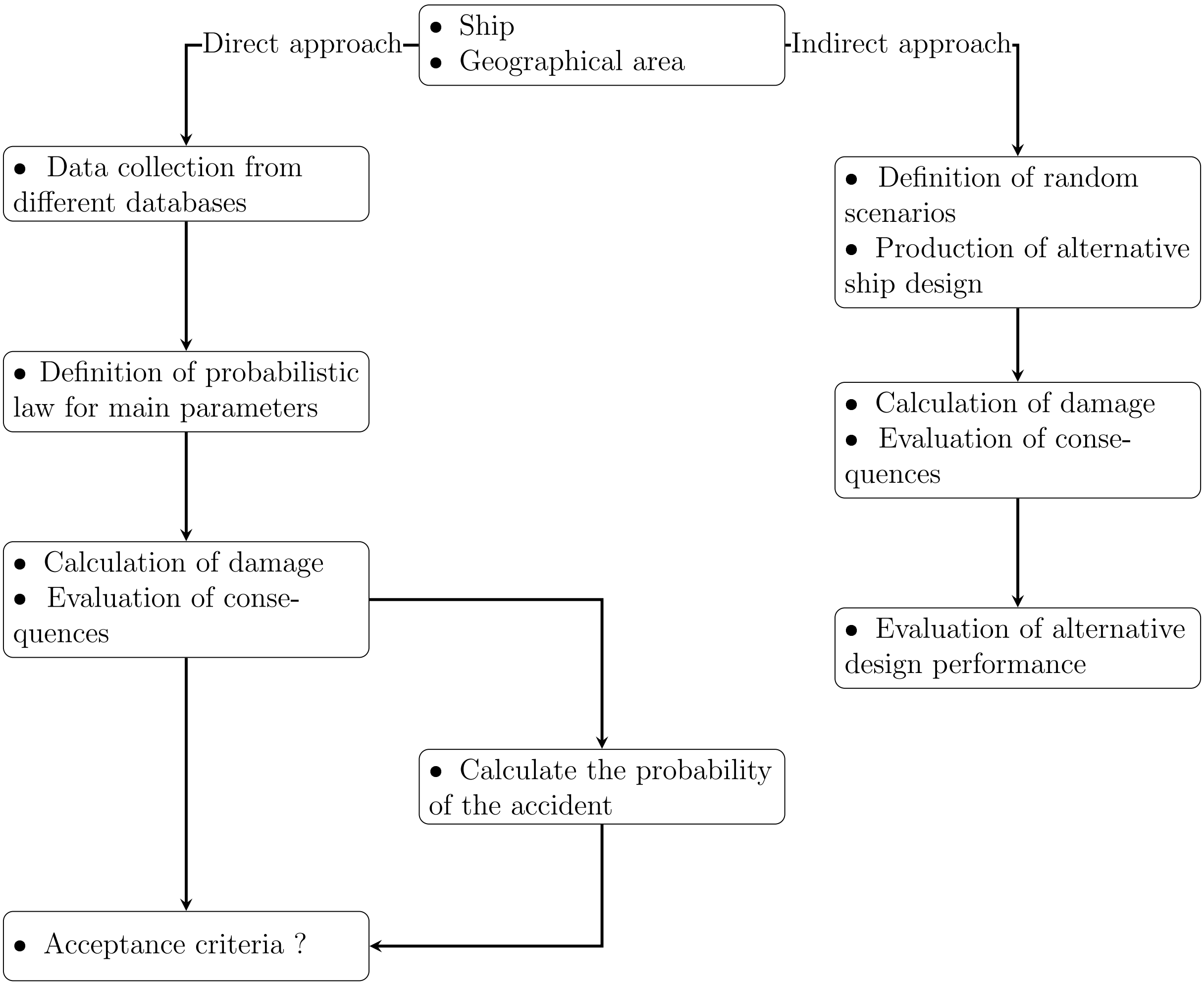

Figure 1.2: Direct and indirect approaches in risk analysis

In summary, both direct and indirect approaches are of interest. On one hand, the direct approach based on real accident database analysis is helpful in the definition of realistic scenario parameters such as impact velocity, collision angle, rock shapes for grounding analyses, etc. However, its major drawback is that for each ship category and each parameter, a probabilistic distribution law must be established, given that such law is obviously linked to both the type of the ship and the area of navigation. With regards to the simulation of ship grounding accidents, various statistical distributions of parameters like ship velocity, rock dimensions, impact transverse location, etc. have been recently proposed by *Youssef* & *Paik* [4]. On the other side, the indirect approach allows to evaluate the performance of an alternative (improved) design. In other words, the aim of this approach is to demonstrate that an alternative scantling allows for a better ship crashworthiness than the initial one.

Whatever the approach considered, it is necessary to accurately evaluate the consequences of the accident in terms of ship damage. Used for a long time in the automotive industry, full or scaled experimental tests can be carried out to quantify the efficiency of an alternative design. However, due to high cost, experimental methods are rarely used for ship collision or grounding analysis. Non linear finite element analysis is nowadays a credible alternative but, as it will be shown later, such approach still remains very time consuming and consequently not well suited when hundreds or thousands of collision/-grounding scenarios have to be simulated. In this context, Icam Engineering school as partner of **FLARE** work package 3 was in charge of developing simplified but reliable tools to rapidly assess the damage of a collided or grounded ship, taking into account its structural arrangement.

The work presented in this PhD thesis is concerned with the mechanical response of a passenger ship in grounding accident with the aim of developing a fast and reliable semi-analytical tool.

1.2 Scope and objectives of the work

Formal risk assessment requires to quantify the consequences of such accidents considering numerous scenarios. Nonlinear finite element analysis (NLFEA) appears nowadays to be the most accurate and multipurpose approach for simulating a ship grounding event. Nevertheless, despite the increasing computing capacity of computers, the use of numerical tools is not always possible as both the model set-up and numerical solution may be very time consuming. To have an idea, the numerical simulation of a 130m-long ship bottom raking over a sharp rock may last more than 10 days using a parallel 12 CPUs Intel core i7 computer. As a consequence, NLFEA is not well suited at pre-design stage or when a full grounding risk analysis involving many ship velocities, rock shapes and impact locations is needed.

Due to their rapidity, alternative tools based on simplified analytical formulations are more appropriate for analysis involving many scenarios. Such tools have already been developed and successively validated by various authors such as *Zhang et al.* [5] and *Le Sourne et al.* [6] for ship collision analysis and *Friis-Hansen & Simonsen* [7] for ship grounding.

It is obvious that the shape of the seabed has a substantial influence on the structural damage of a grounded ship. Therefore, the first step in ship hard grounding analysis consists in choosing the geometry of a rock representing the sea floor. Until today, three principal types of seabed have been defined, namely "rock", "reef" and "shoal" see *Alsos & Amdahl* [8]. In the earliest analytical developments, the seabed was idealised by a sharp wedge and such simplification allowed to calculate approximate solutions for the problem of plate tearing - see *Wang & Ohtsubo* [9] or *Simonsen & Wierzbicki* [10]. In the 1990s, the sea floor was represented by a blunt conical shape. This idealisation has been used for a long time (more than 20 years) by different authors like *Simonsen* [11], *Zeng et al.* [12] or *Sun et al.* [13]. It is worth mentioning that the conical shape is mainly used to study the problem of ships raking on sharp rocks. As for the response of a ship bottom sliding without rupture on a shallow rock, a truncated pyramidal shape like the one proposed by *Hong & Amdahl* [14] is generally preferred.

Based on the previous research, it appears that the response of the ship hull is mainly governed by the choice of the rock shape. A wedge or a cone will generally lead to premature rupture of the outer shell so the expected response is of raking type. On contrary, shallow rocks are modelled with the shape proposed by Hong & Amdahl for sliding scenarios in which the outer shell is not supposed to rupture. A unique rock idealisation suitable for both sliding and raking problems was proposed by *Nguyen et al.* [15] and *Heinvee et al.* [16] who modelled the rock as an elliptic paraboloid. Such a shape allows to represent both sharp and shallow rocks by varying only the two parameters C and E of the following parabolic equation:

$$z = Cx^2 + Ey^2 \tag{1.1}$$

The four aforementioned seabed idealisations are depicted on Figure 1.3.

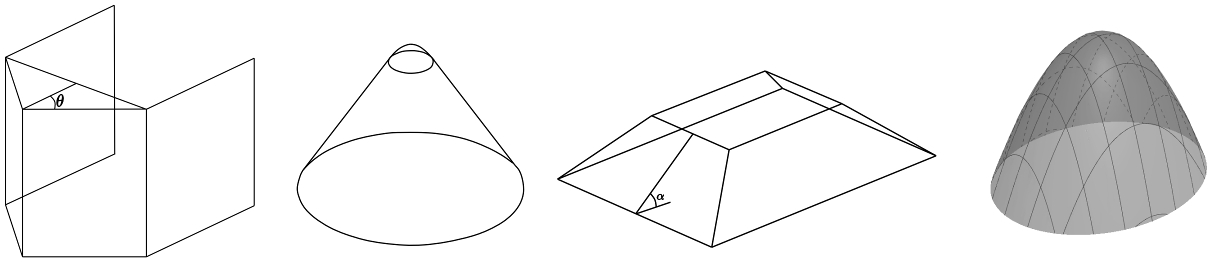

Wedge Blunt cone Trapezium Paraboloide

Figure 1.3: Different rock representations

At the beginning of this thesis, the lack of closed-form solutions for such general rock shape was identified and the necessity of developing simplified models to quickly assess the ship bottom damage resulting from hard grounding events was underlined.

The following objectives for the present PhD thesis work were thus defined:

- Derive analytical formulations allowing for a quick estimation of the damage of a ship hull grounding over a paraboloid shaped rock.
- Develop a fast and reliable tool based on analytical formulations to be used at pre-design stage or for probabilistic damage stability analyses.
- Validate all the different features of the tool i.e., sliding, raking, sliding to raking transition and coupling with an external dynamics solver, by comparison with numerical simulations.
- Perform some structural sensitivity analyses with the tool once validated.

1.3 Outlines of the chapters

Chapter 1 - General introduction

This chapter introduces the context of the research. The objectives of the thesis are defined and the structure of the work is described.

Chapter 2 - Ship grounding physics and damage analysis

In this chapter the theoretical basis of ship grounding accidents are presented as well as a literature review.

Chapter 3 - Finite element analysis - Calibration of parameters

This chapter aims to calibrate some finite element parameters such as the mesh size or the failure strain criterion by comparison with collision and grounding experiments extracted from the literature.

Chapter 4 - Ship sliding

The analytical developments performed to assess the resisting force and the dissipated energy of the different structural members involved in sliding grounding accidents are detailed and validated by comparison with FE simulations.

Chapter 5 - Ship raking

The analytical developments performed to assess the resisting force and the dissipated energy of the different structural members involved in raking grounding accidents are detailed and validated by comparison with FE simulations.

Chapter 6 - Heave and surge combined motions

In this chapter, the response of a grounded ship having both initial surge and heave velocities at moment of impact is investigated. Specific analytical solutions are also derived and validated by comparison with FE calculations.

Chapter 7 - Simplified tool FLAGS

In this chapter, the simplified formulations are implemented into a new analytical solver named *FLAGS* and this later is coupled with the existing external dynamics solver *MCOL*. The resulting tool is then validated by confrontation to FE simulations and the influence of various parameters on the response of the ship are discussed.

Chapter 8 - General conclusion and Perspectives

This chapter summarises the work done in the scope of thesis as well as the personal contributions of the author. Recommendation for further research work are finally provided.

In addition to these main chapters, six appendices are given in order to increase the readability of the PhD thesis manuscript.

Chapter 2

Ship grounding physics and damage analysis

2.1 Introduction

Ship grounding is a complex process involving large contact forces, crushing, tearing and bending of the hull structure. When dealing with such accidents, it is usual to distinguish between *bottom* grounding and *side* grounding - see Figure 2.1.

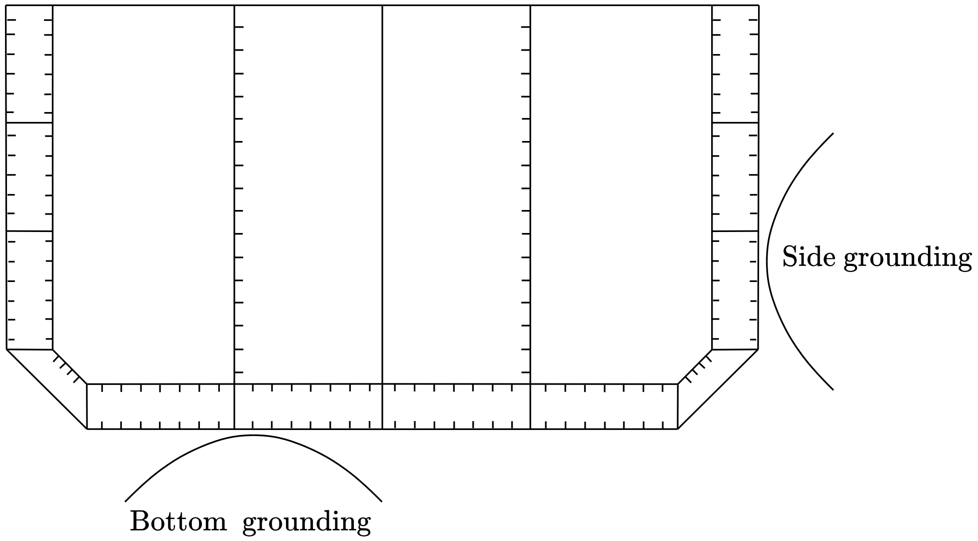

Figure 2.1: Bottom and side grounding situations

In **bottom** grounding events, the seabed is impacted by the ship bottom structure. Such accidents have been historically investigated by numerous authors, see for instance [11, 17–20]. Damages concentrate on the ship bottom, as illustrated in Figure 2.2. Ship bottom components involved in the deformation process are the outer/ inner bottom plating, transverse floors, longitudinal girders and secondary stiffeners.

On the other hand, **side** grounding refers to accidents where a rock is impacted by the ship side. The damaged area is thus located in the side shell as shown for example in Figure 2.3. Ship components involved in the deformation are the side / inner side shells, webs and transverse bulkheads, decks and stringers and secondary stiffeners.

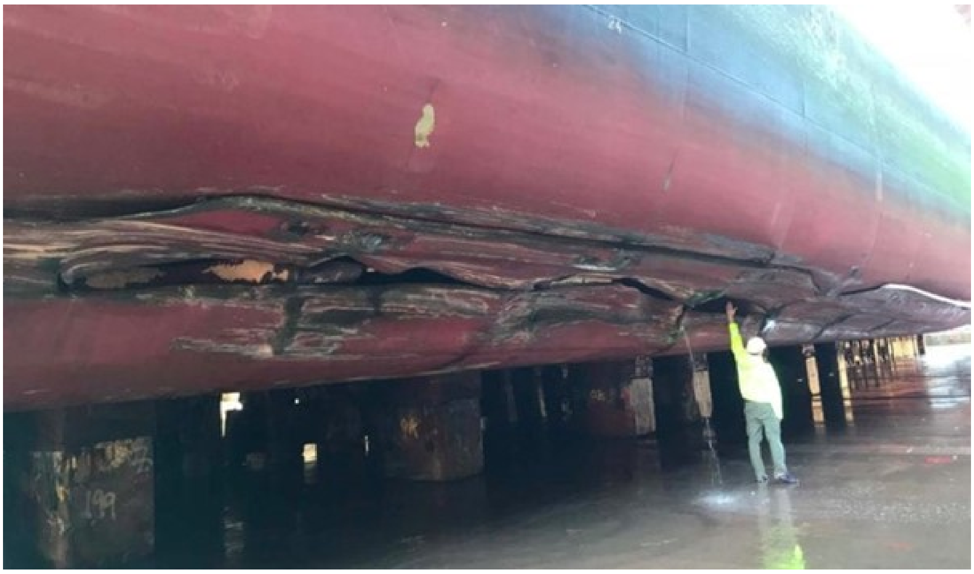

Figure 2.2: Seatruck performance grounding damage - From [21]

Figure 2.3: Costa concordia grounding damage - From [22]

The consequences of such accident on the ship hull are severe and may be either local (Figures 2.2, 2.3) or global depending on the seabed, see for example Figure 2.4 for large damaged area.

Figure 2.4: SKS Satilla grounding - From [23]

Depending on the state of the outer plating (bottom or side shell), the deformation mechanisms of the ship components may be completely different. When the bottom plating is indented without fracturing, transverse floors are vertically crushed, longitudinal girder are sheared and the damage area is generally not restrained to the vicinity of the rock but rather extends along both transverse and longitudinal directions. In contrast, once the outer shell plating has fractured, the damage mainly concentrates in the vicinity of the rock. Figure 2.2 illustrates local tearing damage of the outer bottom.

If the outer plating fractures below waterline, water ingress occurs in different ship compartments. Depending on the damage location, damage extent and subdivision of the vessel, the flooding phase may lead to capsize and even to the loss of the ship. Simulations of water ingress may be found in [24–28] for instance. From various analyses of ship grounding accidents, it transpires that the damage extent greatly depends on various parameters such as ship structural arrangement, impact position, rock shape, friction coefficient, initial kinetic energy and ship heave motion. It is therefore difficult not to say impossible to give an accurate general expression for the estimation of the damage extent in ship grounding. Moreover, analysis of actual ship grounding damage indicates that the damage is not necessarily composed of one long continuous breach but may spread over multiple breaches [29].

This chapter is concerned with the description of the physics involved during a ship grounding event. A review of the different methods used to predict the response of collided and grounded ships is also provided.

2.2 Ship grounding physics

Starting from the energy conservation principle, one can write for ship grounding applications:

$$K_0 = K_{ship} + U_{ship} + P_{ship} + E_{hydro} + U_{soil} + U_{sliding} \tag{2.1}$$

Where K_0 denotes the initial kinetic energy of the ship while K_{ship} corresponds to kinetic energy of the ship at the end of the impact, U_{ship} is the energy absorbed by structural deformations, P_{ship} is the potential energy related to the ship vertical motion, E_{hydro} corresponds to the energy dissipated inside the surrounding water (wave radiation and viscous damping), U_{soil} is for the energy absorbed by the deformation of the soil, and finally $U_{sliding}$ denotes the energy dissipated through friction between the rock and the ship hull. Eq. 2.1 may be adapted to the type of grounding event. For soft grounding, deformation of the soil may be accounted for or not - see *Simonsen* [11], *Pedersen* [30] or *Quéméner et al.* [31]. In hard grounding events, the seabed is mostly assumed as rigid so $U_{soil} = 0$. In the remaining part of the present thesis, only hard grounding will be considered.

In classical ship collision theory, striking and struck ships dynamics may be divided in two distinct processes:

- External dynamics
- Internal mechanics

The analysis of *external dynamics* target the global rigid movements of the striking and struck ships. External dynamics are governed not only by the impact force, but also by the hydrodynamic forces acting on the immersed part of the ship hull. The *internal mechanics*, on the other hand, focuse on the modes of deformation and failure of the crushed components like hull plating, decks, bulkheads and secondary stiffeners for the struck ship and generally stiffened bow and bulb for the striking ship. These deformation and rupture modes (bending, membrane straining, tearing, crushing, buckling, etc.) essentially occur near the impact area.

Splitting the physics into external dynamics and internal mechanics is also a convenient way to tackle the problem of ship grounding. Nonetheless, it should be mentioned that deformation mechanisms and ship overall motions may be strongly coupled. Indeed, the force exerted by the rock pushes vertically the ship and, depending on the position of the rock with respect to the ship centre of gravity, modifies its roll and pitch angles. Moreover, a ship running aground over a sharp rock may result in flooding of some compartments. The water ingress will modify the mass of the ship and consequently influence her stability as both the draft and roll and/or pitch angles will change. In return, these changes will affect the deformation modes and damaged areas.

As for ship collision, different approaches to consider or not the coupling between external dynamics and internal mechanics exist in ship grounding analysis. The so-called *uncoupled*, *semi-coupled* and *fully coupled* methods will be presented in next section as well as their advantages and limitations.

2.3 External dynamics

Ship external dynamics are concerned with the rigid body motion of the ship during and after the collision or grounding event. Using the fundamental principle of dynamics (Newton's 2^{nd} law), the kinematic of the collided or grounded ship may be found. According to *Le Sourne et al.* [32], Newton's 2^{nd} law may be written as:

$$\underline{\underline{M}}[\dot{y}] + \underline{\underline{G}}[y] = [F_C(x)] + [F_W(y,x)] + [F_H(y,x)] + [F_V(y,x)] \tag{2.2}$$

In Eq. 2.2, vector x denotes the position of the ship centre of gravity (CoG) with respect to the earth-fixed reference while vector y denotes its absolute body-fixed velocity. $\dot{x}$ and y are related by:

$$\dot{x} = \begin{bmatrix} R & 0 \\ 0 & Q \end{bmatrix} y \tag{2.3}$$

Where R is the rotation matrix that transforms the vector components from the body-fixed frame to the earth-fixed frame. Q is the matrix relating the angular velocities from body-fixed to earth-fixed frame. More details may be found in *Le Sourne et al.* [6].

The mass matrix of the ship $\underline{\underline{M}}$ is defined as the sum of the rigid body matrix $\underline{\underline{M_{ship}}}$ and the water added mass matrix $\underline{\underline{M_{added}}}$:

$$\underline{\underline{M}} = \underline{\underline{M_{ship}}} + \underline{\underline{M_{added}}} \tag{2.4}$$

Where $\underline{\underline{M_{ship}}}$ and $\underline{\underline{M_{added}}}$ include both mass and rotational inertia terms.

$\underline{\underline{G}}$ is the gyroscopic matrix, defined as the sum of rigid-body $\underline{\underline{G_{ship}}}$ and water added $\underline{\underline{G_{added}}}$ gyroscopic matrices:

$$\underline{\underline{G}} = \underline{\underline{G_{ship}}} + \underline{\underline{G_{added}}} \tag{2.5}$$

The right hand side of Eq. 2.2 includes external forces and moments that apply on the ship's hull:

- $[F_C(x)]$ is the vector of contact force/moment exerted by the rock on the ship and expressed at the ship's CoG,
- $[F_W(y,x)]$ and $[F_V(y,x)]$ are the wave radiation and drag damping force/moment vectors respectively,
- $[F_H(y,x)]$ is the hydrostatic restoring force/moment vector.

Since the contact force and hydrodynamic loads depend on the ship motion, solving Eq. 2.2 for y is not trivial. Depending on the grounding scenarios (bottom grounding, side grounding, combined vertical and horizontal ship movements), further simplifications might be done regarding Eq. 2.2.

A common simplification when dealing with ship bottom grounding is (i) to resume the fluid structure interaction (FSI) to the water inertial effect and, (ii) to neglect both the transverse and vertical movements of the vessel - see for instance [33, 34]. By doing so, the equation of motion can be simplified as:

$$(m_{ship} + m_x)\frac{\partial V_x}{\partial t} = F_C \tag{2.6}$$

Where m_{ship} and m_x are respectively the ship mass and the added mass in surge direction while V_x is the ship surge velocity. In Eq. 2.6, the ship is supposed to move along a prescribed path in surge direction and does not deviate from it. Although practical, this approximation should be taken with caution because in long or/and non-centred grounding events, yaw, heave and sometimes roll motions might be significant and lead to a different damage extent.

As side grounding is concerned, the effect of surrounding water is often limited to water inertial terms, although wave radiation and drag damping forces dissipate part of the energy. The external dynamics may be approximated using an in-plane 3-DOF model (surge, sway and yaw). The rigid-body motion problem comes to solve Eq. 2.7 for V_x, V_y and ω, given the contact forces F_x, F_y and moment M_z calculated at the ship's CoG.

$$\left(\begin{bmatrix} m_{ship} & 0 & 0 \\ 0 & m_{ship} & 0 \\ 0 & 0 & J_{ship} \end{bmatrix} + \begin{bmatrix} m_x & 0 & 0 \\ 0 & m_y & 0 \\ 0 & 0 & J_z \end{bmatrix}\right) \begin{bmatrix} \dot{V}_x \\ \dot{V}_y \\ \dot{\omega} \end{bmatrix} = \begin{bmatrix} F_x \\ F_y \\ M_z \end{bmatrix} \tag{2.7}$$

Here, m_x and m_y are the water added masses in surge and sway directions respectively while J_z is the added moment of inertia related to the ship's yaw motion.

Finally, when the ship grounds over a rock with both surge and heave velocities, hydrodynamics forces can not be omitted anymore as the ship vertical motion is mainly governed by the buoyancy forces - see for instance *Le Sourne et al.* [35].

To solve problems of ship collision or grounding, different levels of interaction between internal mechanics and external dynamics may be considered. It is common to refer to the so-called *uncoupled*, *semi-coupled* and *fully-coupled* methods.

2.3.1 Uncoupled methods

As previously discussed, especially in ship collision analysis, external dynamics and internal mechanics are sometimes assumed to be entirely uncoupled. In the early work on vessel collisions, *Minorsky* [36] assumed that ship movements during the contact phase were sufficiently small to neglect buoyancy and damping forces. Constant water added masses equal to 40% and 5% of the ship mass for sway and surge motions respectively were taken into account. Since this pioneer work, several authors suggested improved solutions to model the effect of hydrodynamic forces. *Zhang* [37] proposed a simplified method to estimate the available energy dissipated by plastic deformation during ship-ship collision. The ship movements considered were surge, sway, and yaw. Plastic deformations were supposed to concentrate near the impact point, and the collision was assumed as instantaneous, each vessel exerting a punctual force one on each other. Frictional contact between both ships was included and sliding between striking and struck ships was considered.

For collision scenarios, where hydrodynamic effects are strongly coupled to rigid-body motions the assumption of a constant equivalent added mass coefficient might lead to inaccurate results. This is the case, for example, with long duration impacts. As the equivalent added mass depends on the collision duration and transient collision forces (*Motora et al.* [38]), it varies with time and the assumption of a constant coefficient becomes unrealistic. Besides, *Brown* [39], *Tabri et al.* [40] and *Yu & Amdahl* [41] demonstrated that although decoupled approaches generally give reasonable estimation of the dissipated energy, the predicted damage extent might not be as accurate, especially in case of oblique collisions. Moreover, encompassing different hydrodynamic components (added mass, wave and viscous damping, and hydrostatic restoring forces) into a single term is not realistic in many collision scenarios as these might have some influence on the motion of the colliding structures and the resulting damage. Investigations on this problematic can be found in *Kim et al.* [42] for ship grounding and collisions, in *Le Sourne et al.* [32] for ship-submarine collisions and in *Echeverry et al.* [43] for ship-FOWT[1] collisions.

Alternative approaches to solve external dynamics and internal mechanics simultaneously can be grouped into two categories: *semi-coupled* and *fully-coupled* methods.

2.3.2 Semi-coupled methods

While fully-coupled methods are particularly time expensive, semi-coupled methods offer an interesting compromise between computation time and accuracy.

Petersen & Pedersen [44] and *Petersen* [45] were among the first to develop a time domain method capable of treating ship-offshore and ship-ship oblique collisions in two dimensions. The force - penetration curve was assumed to be a known parameter and only surge, sway, and yaw motions were considered. In 2010, *Tabri* [46] presented a 3D simulation model that couples the motion of ship to the contact and hydrodynamic forces. Sloshing and dynamic bending of the hull girder were also considered. The model highlighted the importance of sloshing for the dynamics of collisions. Indeed, when considering a partially filled tank, the energy dissipated by strain deformation is reduced by 30% as compared to dry condition.
A general solution for 3D problem was proposed by *Liu & Amdahl* [47] for ship-ship collision the problem of ship-iceberg accidents. The results highlighted the dependency of the energy dissipated by deformation on the vertical position of impact. Moreover, an in-plane 2D approach was shown to overestimate the energy dissipated by ship plastic deformation.
Finally, *Brown* [48] presented a semi-coupled method for probabilistic ship collision assessment. The ship movements were limited to surge, sway and yaw and the internal mechanics were solved by the use of semi-empirical formulations. The fluid structure interaction was modelled through constant added mass coefficients.

The first 3D model including the 6 rigid-body ship's movements (heave, sway, surge, yaw, roll, pitch) was developed at the end of the 90's by Mitsubishi Heavy Industry and included in *Ls-Dyna* finite element solver as a "subroutine" called *MCOL*. In the initial version of *MCOL* solver, only small rotational movements of the floating structure were considered. In order to correctly assess the roll motion of a submarine collided on its superstructure, *Le Sourne et al.* [32] developed and implemented into *Ls-Dyna* a new

---

[1] Floating Offshore Wind Turbine

version of *MCOL* able to simulate large rotational movements as well as Coriolis and drag damping effects. The principle of interaction between *Ls-Dyna* core solver and *MCOL* subroutine is illustrated on Figure 2.5.

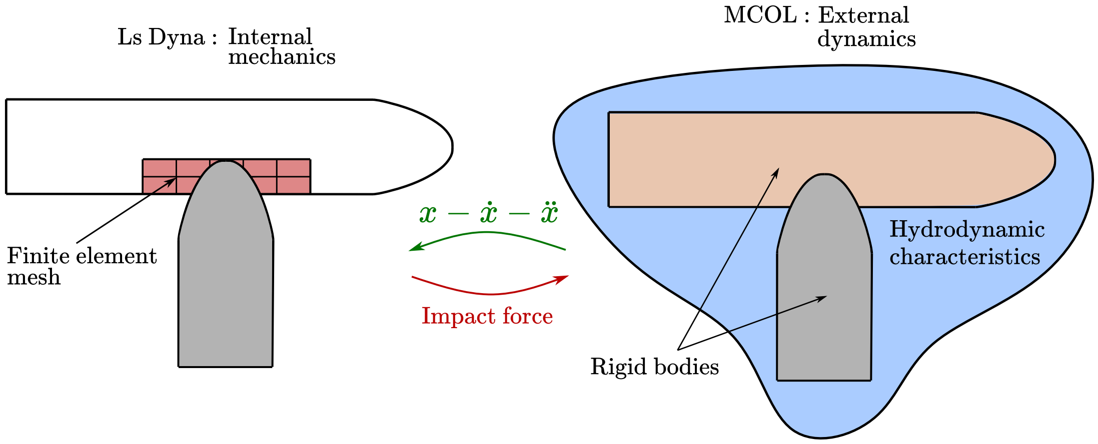

Figure 2.5: *Ls-Dyna* - *MCOL* interaction

At each time step, *Ls-Dyna* mechanical solver transfers the contact force vector F_C (expressed at the ship centre of gravity) to *MCOL* subroutine. Then, starting from hydrodynamic characteristics (water added mass, restoring stiffness, wave and drag damping) calculated by a seakeeping code and provided in a matrix form, *MCOL* solver calculates the hydrodynamic loads F_H, F_V, and F_W and solves Eq. 2.2 for y and its derivative. New acceleration, velocity and position of the ship centre of gravity are then transmitted back to *Ls-Dyna*. More details on *MCOL* theory and functionalities might be found in [49, 50] and some *Ls-Dyna/MCOL* applications are presented for instance in [35, 43, 51–53].

Comparisons between semi-coupled and uncoupled approaches were made by *Brown* [48], *Tabri* [54] or *Liu et al.* [55] for the case of ship-ship impacts. According to *Tabri* [54] and *Liu et al.* [55], the two methods generally lead to different penetrations for a given scenario. For the special case of right angle collision, the decoupled method appears to be able to predict with good accuracy the energy dissipated by plastic deformations. On contrary, when the collision angle moves away from 90°, the decoupled approach is no longer capable of predicting the damage extent with such accuracy.

2.3.3 Fully-coupled methods

Taking advantage of the increasing computing power, other numerical methods have been developed to tackle the fluid-structure interaction by explicitly model the water surrounding the ship. Among them, Arbitrary Lagrangian Eulerian (ALE), Coupled Eulerian Lagrangian (CEL) and Computational Fluid Dynamics (CFD) methods are increasingly popular. A comparison of dissipated energy calculated using ALE and simplified method based on momentum conservation was performed by *Song et al.* [56]. More recently, *Rudan et al.* [57] compared for different models the results between ALE and *Ls-Dyna/MCOL* simulations of ship-ship collisions. From the study it results that, first, for long collision time the ALE model appears to loose its numerical stability, second, the effects of ship motions on the surrounding water and vice-versa can be treated quite accurately by the ALE approach, while *MCOL* is not capable of modelling the full hydrodynamic interaction between the two ships involved in the collision. Although ALE methods can accurately model hydrodynamic phenomena, calibrating the fluid mesh size as well as ALE parameters is not that easy. Moreover, according to the authors, *MCOL* was shown to be stable and considerably faster (about 450 times), even tough it requires a preliminary hydrodynamic analysis using an external seakeeping code.

In this thesis, *MCOL* program will be used as it provides results with a good accuracy in an efficient computation time.

2.4 Internal mechanics

Internal mechanics deal with the energy dissipated by grounded body deformation (U_{ship} and U_{soil} in Eq. 2.1) and friction ($U_{sliding}$). As already mentioned, when dealing with hard grounding accident, the rock is assumed to be infinitely rigid, hence $U_{soil} = 0$. Internal mechanics thus resume to estimate the energy dissipated through both the deformation of the structure and the friction between the hull and the rock. A typical double hull arrangement is depicted in Figure 2.6. Methods dealing with internal mechanics may be classified into four groups:

- Statistical method
- Experimental method
- Non-linear finite elements method
- Simplified analytical method

A non-exhaustive list of the use of the different methods over time is given in Table 2.1 at the end of the chapter.

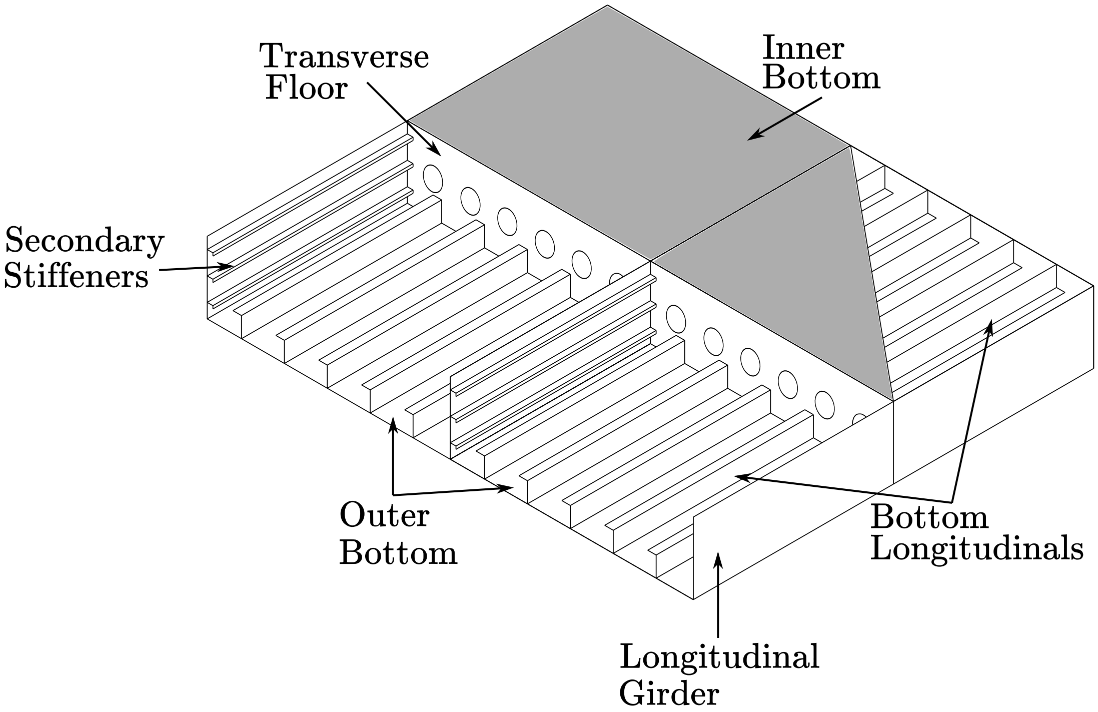

Figure 2.6: Ship bottom components

2.4.1 Statistical method

From the analysis of 27 ship collision events, *Minorsky* [36] was the first to establish an empirical relation between the absorbed energy and the damaged volume of the involved ships:

$$E = 47.2 \cdot R + 32.7 \tag{2.8}$$

Where R is the overall damaged volume of both striking and struck ships and E is the absorbed energy. Minorsky's empirical relation, plotted in Figure 2.7, was based on following assumptions:

- Only the component of the striking ship speed normal to the course of the struck ship contributes to the kinetic energy available to cause damage.
- The collision in fully plastic.
- The mass of water pulled along the sway direction of the struck ship equals 40% of its mass.

Used by engineers for many years to estimate the indentation of a struck ship given an initial kinetic energy, this relation is known to be valid only for high-energy impacts ($\geq$ 80 MJ).

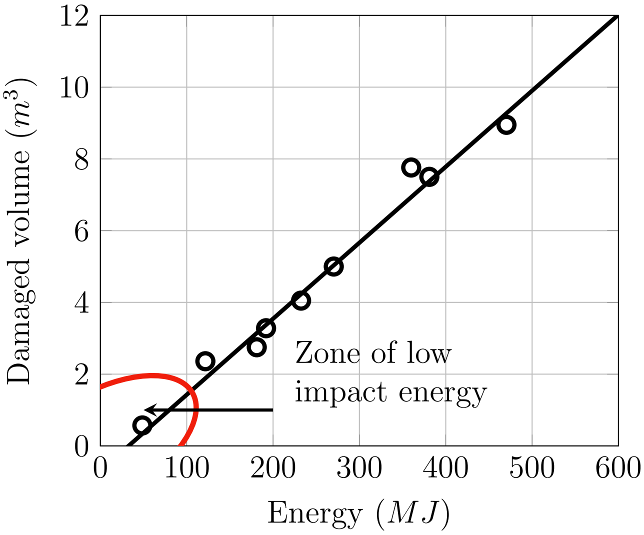

Figure 2.7: Minorsky's correlation

Ship grounding statistical analyses remain scarce. Using Luukkomen's data (18 ship accidents), *Sormunen* [58] proposed a simple formula to estimate the damage extent of a grounded ship. The damage length l was shown to be related to the ship initial kinetic energy E_k by:

$$l = 13.88 + 0.25E_k \tag{2.9}$$

Although useful, statistical methods suffer from two major drawbacks:

1. Using a relation based on statistical analysis is only relevant when the studied vessel is similar to the vessels considered in the statistical analysis.
2. The data available to derive empirical relations were limited (only 27 cases for Minorsky's relation and 18 cases for Sormunen's one) so the reliability of the proposed relations may be questionable.

In order to extend the range of application of Minorsky's formulae, *Zhang* [37] and *Pedersen et al.* [59] introduced geometrical and material considerations into the energy/volume relation. The improved semi-empirical model was successfully confronted to experimental results by *Zhang* & *Pedersen* [60] and to finite element simulations by *Zhang et al.* [5].

2.4.2 Experimental method

Full scale or even reduced scale collision and grounding experiments are very expensive and therefore limited. Moreover, with the development of numerical methods, few experimental tests were carried out in the last ten years [61–64].

Over the time, various experimental studies have been conducted in order to better understand the dissipation mechanisms during ship grounding and collision accidents. Ship collision experiments were performed in Italy, Germany and Japan. Between 1962 and 1976, trials were mainly carried out on reduced scale ship sections in order to optimise anti-collision barriers on nuclear-powered vessels. Several authors such as *Amdahl* [65], *Pedersen et al.* [66], *Jones* [67] or *Ellinas* & *Valsgard* [68] presented detailed reviews of these experiments.

Regarding ship grounding, most of experiments were historically concerned with wedge cutting of bare plates - see Figure 2.8. Such tests were useful to understand the deformation mechanisms involved and the contribution of friction to the energy dissipation. Larger experimental tests were also performed using conical shape impactors against bare plates [63, 69] and scaled double bottom structures [61, 70].

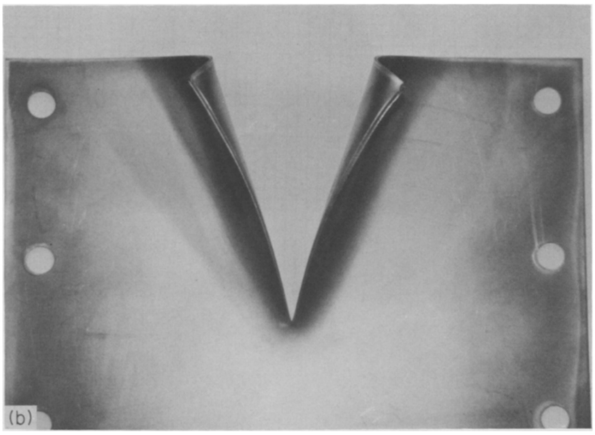

Figure 2.8: Bare plate cutting from *Lu* & *Calladine* [71]

For instance, a 1:5 scaled double bottom was attached to a vehicle mounted onto railroad cars and placed on an inclined plane [70]. At the instant of impact with the rock, the speed of the system was 6.17m/s giving an initial kinetic energy of 4.32 MJ. After crushing of the double bottom, the final velocity of the moving structure was 3.66 m/s so only 35 % of the initial kinetic energy was dissipated through plastic deformation, friction and rupture.
Several observations were made from this experiment:

- Outer and inner hulls conformed to the rock's shape and large shear bands were observed.
- Transverse webs can act as initiators of the inner shell fracture.

Regarding the grounding response of intact ship hulls, the only experimental works that have been published are the studies of *Turgeon* [18] and *Muscat-Fenech* [69].

2.4.3 Non-linear finite element method

Non linear finite element analysis (NLFEA) is considered as the most powerful tool for analysing structural problems and is often regarded as "a numerical experiment". Commercial explicit solvers like *Ls-Dyna* or *ABAQUS/explicit* are often used for simulating ship collision or grounding events.

Examples of NLFEA of large-scale ship collision and grounding accidents may be found in *Kuroiwa* [72], *Kitamura et al.* [73], *Gu et al.* [74], *Hong & Amdahl* [75], *Zheng et al.* [76] and *Aga* [77]. Quite recently, *Heinvee et al.* [16] and *Heinvee & Tabri* [78] simulated grounding scenarios involving three different tankers (120/190/260 meters) and four different sizes of rock. From these numerical experiments, they derived a set of simple formulas to estimate the resistance force according to the impact location, the vessel size and the rock penetration.

Since the finite element method is based on the discretization of the structure into small elements, a fine meshing is always required to correctly grasp all the deformation modes occurring in a grounding event such as the creation of flaps in raking as illustrated in Figure 2.9. In the grounding analysis benchmark recently documented by *Brubak et al.* [79], the average mesh size considered by the participants was about 10 to 30mm. Such element size combined with the large extent of the ship bottom model often leads to prohibitive calculation times.

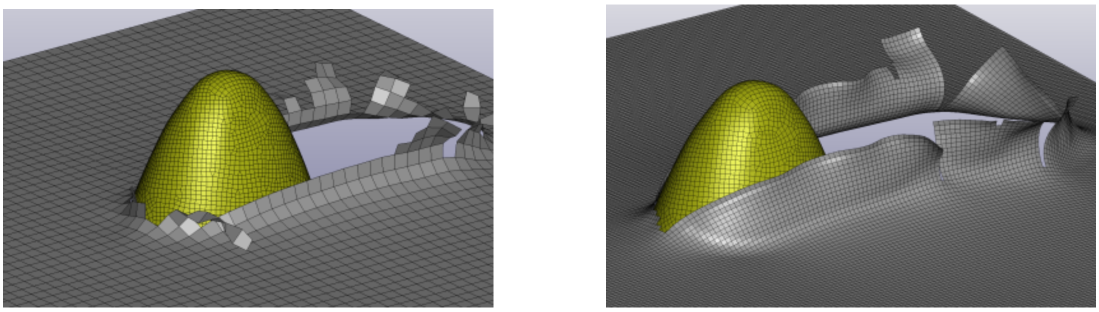

(a) 100mm mesh size (b) 30mm mesh size

Figure 2.9: Observed deformation of bottom plating depending on mesh size

Even though NLFEA is the prefered method for the analysis of most structural problems, modelling the structural failure remains a challenge. Indeed, the main difficulty concerns the choice of the failure criterion. In the erosive laws commonly proposed in commercial codes like *Ls-Dyna*, a unique failure strain threshold value is considered and often taken as the one measured in a uni-axial tensile test. However, as the crushing mechanism often involves tension, bending, shear, buckling and tearing, the stress state of the crushed area is anything but uni-axial. Multi-axial failure criteria have been proposed by different authors like *Zhu* [80] and *Ehlers & Varsta* [81] for instance. The latter proposed a new method using optical measurements in order to obtain strain and stress until fracture. A good agreement was found with the experimental results. However, due to the amount of measurements necessary for input data, the proposed criterion is still not integrated into commercial codes like *Ls-Dyna*.

The influence of strain rate and element size on steel plate fracture was recently investigated by *Calle et al.* [82]. Using three different experimental tests (tensile, tearing and perforation tests) at different velocities, the failure strain was demonstrated to highly depend on the strain rate. Moreover, from comparisons between NLFEA and scaled experiments, the authors were able to claim that tensile tests are insufficient to properly characterise the material failure in a complex stress state.

Another difficulty arises from the so-called stress localisation. Large stresses develop at the vicinity of a perforated area. Therefore, the smaller the element size in the neighbouring of a hole, the higher the strain calculated at element integration points, and the faster the deletion of the over-strained elements. As clearly shown by *Yu* [83], *Lehmann* & *Yu* [84], *Simonsen* & *Lauridsen* [85] and *Simonsen* & *Törnqvist* [86], a fine mesh will thus tend to degrade much faster than a coarse one. One solution consists in choosing the failure strain threshold value according to the finite element size l_e and the structure thickness t. One of the most used approach to estimate a threshold value for a mild steel thin-walled structure was proposed by *Lehmann* & *Peschmann* [87].

$$\epsilon_{rup} = 0.056 + 0.54 \cdot \frac{t}{l_e} \tag{2.10}$$

It is however worth noting that using Eq. 2.10 is theoretically only relevant when the main deformation mode of the failing structure is membrane tension. As a consequence, the erosive law combined with a failure strain calculated from Eq. 2.10 should be used with caution, as recently demonstrated by *Le Sourne et al.* [35] for ship grounding numerical analysis. Resulting shell openings should systematically be validated by confrontation to experimental results.

Another criterion is the *RTCL* criterion proposed by *Tørnqvist* [88]. It consists of the combination of two continuum damage models, the *Rice* & *Tracey* [89] and *Cockroft* & *Latham* [90] damage models. The RCTL criterion is represented by a damage variable D expressed as:

$$D = \begin{cases} 0 \quad for \ T \leq -1/3 \\ \\ 2\frac{1+T\sqrt{12-27T^2}}{3T+\sqrt{12-27T^2}} \ for \quad -1/3 < T < 1/3 \\ \\ \frac{1}{1.65}exp(3T) \ \ for \ T \geq 1/3 \end{cases} \tag{2.11}$$

Where T is the ratio between the hydrostatic stress σ_H and the effective stress σ_e. When the damage variable D reaches a certain level, the element is deleted from the mesh. According to *Ehlers et al.* [91], the RCTL model seems to correctly capture the initiation of the fracture. However, as soon as the tearing process starts, the criterion is not able to predict with accuracy the resisting forces. In addition, the critical damage variable must be calibrated from experiments involving the material which actually constitutes the structure to be analysed.

To conclude, although the finite element approach may give reliable results and is able to accurately reproduce experimental tests, it remains very time consuming in practical applications, especially in ship grounding analysis. As a consequence, this approach is uneasy, or impossible to use at pre-design stage or when a complete ship damage stability analysis involving a lot of scenarios has to be carried out.

2.4.4 Plastic limit analysis

As previously presented, one of the main drawbacks of NLFEA is the modelling and computational cost. As an alternative, plastic limit analysis has been used since several decades to quickly estimate the resisting force of simple structures like beams or rectangular plates when they are crushed by a rigid impactor. Plastic limit analysis is based on the principle of virtual work according to which :

$$\int_A F_i \dot{u}_i \, dA + \int_V T_i \dot{u}_i \, dV = \dot{E}_{int} \tag{2.12}$$

Where F_i and T_i are the external and body forces respectively and $\dot{u}_i$ is the velocity field. A and V are respectively the surface and volume of the considered structure.

For a general solid body, the internal energy rate is given by:

$$\dot{E}_{int} = \int_V \sigma_{ij} \dot{\varepsilon}_{ij} \, dV \tag{2.13}$$

Where V is the solid body volume, σ_{ij} and $\dot{\varepsilon}_{ij}$ are respectively the stress and the strain rate components. According to *Jones* [92], from the virtual work principle, two theorems may be constructed, the “Lower-bound theorem” and the “Upper-bound theorem”.

Lower-bound theorem
The Lower-bound methods search for any system of generalised stresses (σ_{ij}) in the structure which is in equilibrium with the applied loads (F) and nowhere violates the yield condition. The solutions are called statically admissible, and the loads will not cause the collapse of the structure.

Upper-bound theorem
If the work rate of a system of applied loads during any kinematically admissible collapse of the structure is equated to the corresponding internal energy rate, then the system of loads (F) will cause the collapse of the structure.

If a calculated load F verifies both the Upper and Lower bound theorems, then F is the force that causes the collapse of the structure. Exact analytical solutions for the problem of deformable body must satisfy simultaneously equilibrium, compatibility and constitutive equations - see Figure 2.10.

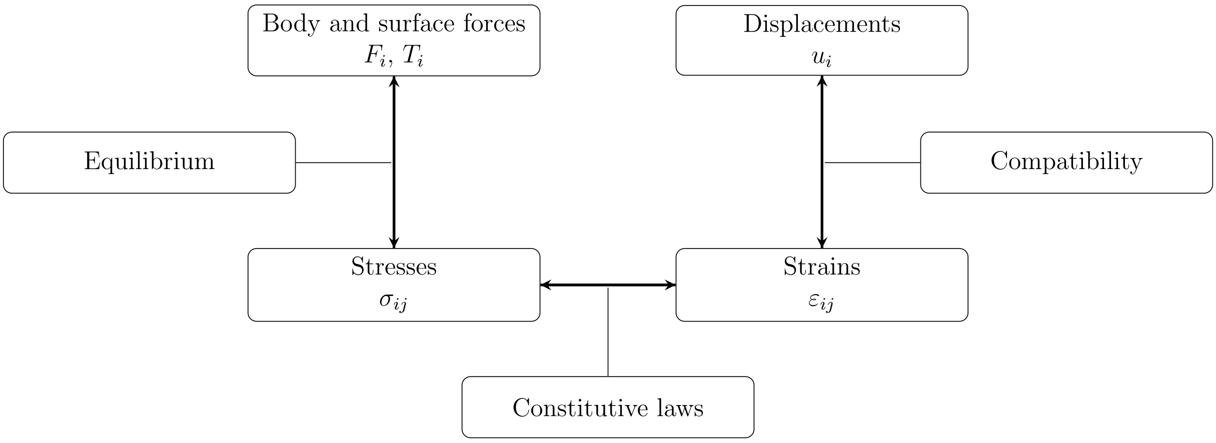

Figure 2.10: Relations of variables in solving a deformable mechanics problem

Nevertheless, regarding the complexity of the structure considered in this work, it is difficult, not to say impossible to find an exact solution. With the purpose to derive simplified solutions, the Upper-bound theorem has been intensively used by numerous authors such as *Amdahl* [65], *Wierzbicki* [93], *Zhang* [37]; *Buldgen* [94] or *Pire* [95] for ship collision and *Simonsen* [11], *Wierzbicki* & *Thomas* [96], *Hong* [97], *Zeng et al.* [12] or *Turgeon* [18] for ship grounding application. The approach adopted in the framework of this PhD to derive analytical solutions in ship grounding is based on the Upper-bound theorem.

According to previous authors, the work rate of external forces $\dot{W}$ must be equal to the overall dissipated energy rate, which may be expressed as the sum of elastic ($\dot{E}_e$), plastic ($\dot{E}_p$) and friction ($\dot{E}_f$) energy rates:

$$\dot{W} = \dot{E}_e + \dot{E}_p + \dot{E}_f \tag{2.14}$$

It has been demonstrated that the elastic energy can be most of the time neglected in ship collision or grounding analyses as it does not exceed 6% of the overall energy - see for instance *Pedersen* & *Li* [98]. Eq. 2.14 thus becomes:

$$F_L V_x + F_T V_y + F_V V_z = \dot{E}_p + \int_S \mu p V_{rel} \, dS \tag{2.15}$$

Where :
F_L is the longitudinal resisting force
F_T is the transverse resisting force
F_V is the vertical resisting force
V_x is the surge velocity of the ship
V_y is the sway velocity of the ship
V_z is the heave velocity of the ship
$\dot{E}_p$ is the rate of plastic energy dissipation
μ is the friction coefficient between the ship and the rock
p is the normal pressure of the rock from element dS
V_{rel} is the relative velocity between the ship and the rock
S is the contact area between the rock and the plate

The basis idea behind Eq. 2.15 is to postulate a displacement field on a given ship component in order to calculate its resisting forces F_L, F_T and F_V. The approach may be divided as follows:

1. Identify the deformation mechanisms using experiments or NLFEA.
2. Postulate a displacement field that matches the observed deformation modes.
3. Add the effect of friction.
4. Derive the internal plastic energy rate from the displacement field and deformation mechanisms.
5. Calculate the resisting forces F_L, F_T and F_V from Eq. 2.15.

The main difficulties lies in choosing a realistic displacement field and finding the major dissipation mechanisms. To deal with hand-tractable formulations, some further assumptions are necessary:

- Firstly, structural dynamic effects are neglected so the problem is assumed as quasi-static. In fact, as shown by *Jones* [92], dynamic effects may be significant when the impact speed exceeds 23 m/s. With a ship service speed of around 10 m/s (around 20 *knots*), structural dynamic effects are thus often neglected. Strain rate effect is usually not considered as well. Indeed, a recent study by *Çerik* & *Choung* [99] highlighted that this effect may usually be disregarded in ship collision analysis.
- A second hypothesis concerns the plastic behaviour of the material. Once the yield stress has been reached, steel material starts to harden with the increase of the plastic strain. Except for limited cases (*Simonsen* & *Lauridsen* [85], *Calder* & *Goldsmith* [100]), the hardening effect is often neglected so the material is supposed to be rigid-perfectly plastic (see Figure 2.11) and to obey to the Von Mises' yield locus.

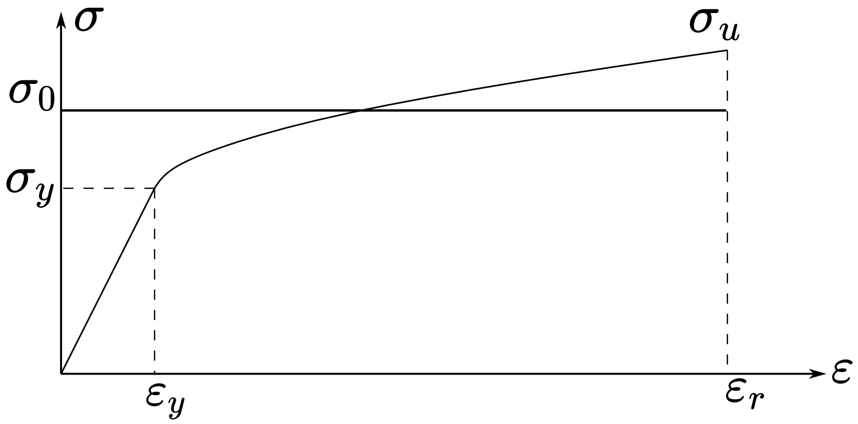

Figure 2.11: Rigid plastic assumption

For a deforming plate, it is convenient to divide the internal energy rate from Eq. 2.13 into the sum of bending ($\dot{E}_b$) and membrane ($\dot{E}_m$) energy dissipation rates, these two quantities being expressed as:

$$\dot{E}_m = \int_S N_{\alpha\beta}\dot{\varepsilon}_{\alpha\beta}\, dS \tag{2.16}$$

$$\dot{E}_b = \int_S M_{\alpha\beta}\dot{k}_{\alpha\beta}\, dS + \sum_{i=1}^{n} M_{0i}\dot{\theta}_i l_i \tag{2.17}$$

Where $N_{\alpha\beta}$ and $M_{\alpha\beta}$ are the membrane forces and bending moments. $\dot{\varepsilon}_{\alpha\beta}$ and $\dot{k}_{\alpha\beta}$ are the generalised strain and curvature rates, $\dot{\theta}_i$ and l_i are the rotation rate and length of *ith* plastic hinge line. Eq. 2.17 contains two distinct terms. The first one corresponds to the continuous bending and the other one corresponds to the plastic hinge lines. For most of practical applications, the continuous bending is neglected [37, 94, 101]. However for ship grounding application, continuous bending may have an important contribution and will therefore be considered in the analysis.

According to the theory of plasticity, $N_{\alpha\beta}$ and $M_{\alpha\beta}$ are interrelated via a yield function. However taking into account this interaction leads to cumbersome expressions and it is therefore neglected in the present analysis.

For plane stress condition, the Von Mises yield locus can be written as:

$$\sigma_{xx}^2 + \sigma_{yy}^2 + 3\sigma_{xy}^2 - \sigma_{xx}\sigma_{yy} = \sigma_0^2 \tag{2.18}$$

Where σ_0 is the flow stress of the material. Using Eq. 2.18 and the associated flow rule, the membrane energy rate may be expressed as:

$$\dot{E}_m = \frac{2}{\sqrt{3}}\sigma_0 t_h \int_S \sqrt{\dot{\varepsilon}_x^2 + \dot{\varepsilon}_y^2 + \dot{\varepsilon}_{xy}^2 + \dot{\varepsilon}_x\dot{\varepsilon}_y} dS \tag{2.19}$$

Here, $\dot{}$ corresponds to the time derivative operator. For grounding applications, since the problem is assumed to be in a steady-state and the material flows through the deformation zone, the problem appears to be similar to the problem of a fluid flowing around a rock. Then, using an Eulerian description, the total time derivative of strain are rewritten as:

$$\begin{cases} \dot{\varepsilon}_x = \frac{\partial \varepsilon_x}{\partial t} + \overrightarrow{grad}\left(\varepsilon_x\right).\overrightarrow{V} = V\frac{\partial \varepsilon_x}{\partial x} \\ \\ \dot{\varepsilon}_y = \frac{\partial \varepsilon_y}{\partial t} + \overrightarrow{grad}\left(\varepsilon_y\right).\overrightarrow{V} = V\frac{\partial \varepsilon_y}{\partial x} \\ \\ \dot{\varepsilon}_{xy} = \frac{\partial \varepsilon_{xy}}{\partial t} + \overrightarrow{grad}\left(\varepsilon_{xy}\right).\overrightarrow{V} = V\frac{\partial \varepsilon_{xy}}{\partial x} \end{cases} \tag{2.20}$$

Finally, with the steady state condition, the equivalent strain rate $\dot{\varepsilon}_{eq}$ becomes:

$$\dot{\varepsilon}_{eq} = \frac{2}{\sqrt{3}}V\sqrt{\frac{\partial \varepsilon_x}{\partial x}^2 + \frac{\partial \varepsilon_y}{\partial x}^2 + \frac{\partial \varepsilon_{xy}}{\partial x}^2 + \frac{\partial \varepsilon_x}{\partial x}\frac{\partial \varepsilon_y}{\partial x}} \tag{2.21}$$

The last simplification is to suppose that strain is linearly varying with the x variable and doing so leads to:

$$\dot{E}_m = \sigma_0 t_h \frac{2}{\sqrt{3}}V \int_y \sqrt{\varepsilon_x^2 + \varepsilon_y^2 + \varepsilon_{xy}^2 + \varepsilon_x\varepsilon_y} dy \tag{2.22}$$

Using the same procedure, the continuous bending energy rate may be written as:

$$\dot{E}_b = \frac{2}{\sqrt{3}}\frac{\sigma_0 t_h^2}{4}\int_y \frac{1}{R(y)}dy \tag{2.23}$$

Where R is the radius of curvature. In the previous equation, strains and stresses are related to the initial volume of material.

From Eqs. 2.22 and 2.23, two terms may be defined: $N_0 = 2/\sqrt{3}\sigma_0 t_h$ and $M_0 = \sigma_0 t_h^2/(2\sqrt{3})$. N_0 is called the plastic normal force while M_0 is the fully plastic bending moment capacity.

In the simplified method, the material is solely represented by the flow stress σ_0. Even if the hardening is neglected, some authors such as *Zhang* [37] or *Simonsen* [11] recommended to select the flow stress as the mean value $(\sigma_y + \sigma_u)/2$ while *Wierzbicki et al.* [102] suggested a value of $0.92\sigma_u$. However, the Upper-bound theorem already provides an overestimation of the resisting forces. That is why in the present work and following the studies of *Buldgen* [94] and *Pire* [95], the flow stress will be taken equal to the yield stress, i.e., $\sigma_0 = \sigma_y$.

2.4.5 The Super element method

The brief literature review illustrates that several analytical formulae already exist for the problem of ship collision and grounding. At a pre-design stage, such simplified approaches can be a time and cost effective alternative to NLFEA.

Initially introduced by *Ueda et al.* [103], the idealised structural unit method (ISUM) consists in reducing the number of DoFs by considering very large sized unit structures. In the current version of ISUM, eigen functions are adopted to represent the lateral deflection of the elements depending on the unit element average strain, see [104, 105] for instance. Obviously, the accuracy of the ISUM depends on how correctly the selected shape functions correspond to the observed deformations. Although effective and accurate, this simplified method is mostly used for the determination of ship ultimate strength in hogging and sagging conditions.

The super element (S.E.) method was firstly introduced by *Lützen* [106] and looks like the ISUM method. The ship is divided into large structures and closed-form solutions derived from plastic analysis allow to rapidly assess the resistance of each impacted S.E. It is worth noting this method differs from ISUM in that each S.E. is assumed to behave independently from the others. The total resistant force of the ship is thus obtained by summing the contributions of all the impacted S.E. First S.E. were developed by *Lützen* [106] for ship collision analysis assuming 90° collision angle. Later, various authors such as *Buldgen et al.* [107] or *Wang et al.* [101] extended the formulations to oblique collision cases. Based on this approach, several fast calculation codes were developed such as SHARP (*Le Sourne et al.* [6]) for ship-ship collision and GRACAT (*Friis-Hansen & Simonsen* [7]) for ship grounding analysis. An outline schematic of a S.E. program is depicted on Figure 2.12.

The main advantage of this approach compared to the F.E. method is its rapidity. A large number of scenarios can be simulated in a short time. Very recently, *Conti et al.* [3] used SHARP S.E. code to simulate almost 2 000 ship collision scenarios with the objective to analyse the influence of ship structural design on damage extent. Each calculation typically lasts 1 or 2 minutes while one F.E. simulation may take from several hours up to several days. Although based on simplified expressions, collision breaches obtained by the S.E. method were recently shown by *Kim et al.* [108] or *Taimuri et al.* [109] to be in good accordance with F.E. results.

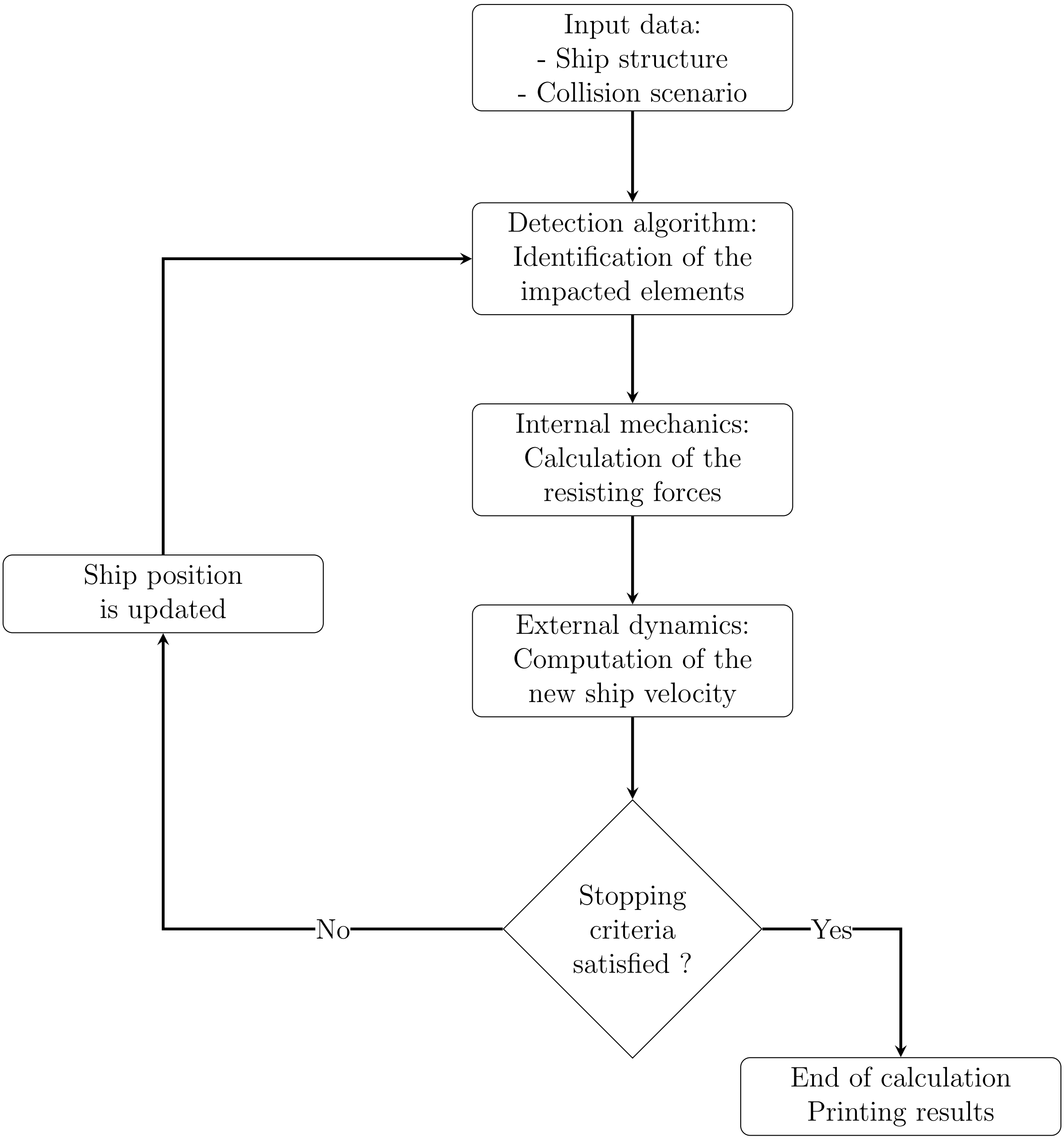

Figure 2.12: Flowchart of a Super-Element program

2.5 Ship grounding simplified analysis

As presented in Chapter 1, four main simplified forms are used to describe the seabed in hard grounding analysis namely wedges, cones, truncated pyramids and paraboloids. In the earliest analytical developments, the seabed was idealised by a sharp wedge and such simplification allowed to calculate approximate solutions for the problem of plate tearing - see [10, 17, 71, 110, 111]. Later on, the sea floor was represented by a blunt conical shape and the response of bottom structures was studied by *Simonsen* [11] and *Zeng et al.* [12], while transverse floors were investigated by *Simonsen* [11] and *Sun et al.* [13]. It is worth mentioning that the conical shape is mainly used to study the problem of ships raking on sharp rocks, assuming that the outer shell rupture is triggered almost instantaneously.

To deal with ship bottom grounding without rupture (sliding grounding), a truncated pyramidal shape was proposed by *Hong & Amdahl* [112] as this form is generally preferred when dealing with shallow rocks. Analytical formulations describing the response of mains components (bottom/double bottom plating, floors and girders) were derived from plastic limit analysis by *Hong & Amdahl* [19], while the response of small longitudinal stiffeners attached to bottom plating was investigated by *Yu et al.* [113].

From all previous considerations, it appears that the response of the ship hull is mainly governed by the choice of the rock shape. A wedge or a cone will generally lead to premature rupture of the outer shell so the expected response is of raking type. On contrary, shallow rocks are modelled with the shape proposed by Hong & Amdahl for sliding scenarios in which no rupture is supposed to occur. A unique rock idealisation suitable for both sliding and raking problems was proposed quite recently by *Nguyen et al.* [15] and *Heinvee et al.* [16] who modelled the rock as an elliptic paraboloid. Such a shape allows to represent both sharp and shallow rocks by varying only the two parameters C and E. Nevertheless, to the author's knowledge, no analytical formulations were developed for this last rock shape.

In the existing simplified analytical tools, the external dynamics often reduces to its minimum, when it is not totally omitted. For instance, in *GRACAT* (**GR**ounding **A**nd **C**ollision **A**nalysis **T**oolbox) only surge, heave, roll and pitch motions of the ship are considered. The action of buoyancy forces is totally ignored and the surrounding water is embedded in a unique parameter, the added mass - see [7]. On the other side, in the simplified program proposed by *Song & Hu* [114], the ship is assumed to be clamped on its edges so the action of the hydrodynamic forces is ignored. Nevertheless, as demonstrated by *Le Sourne et al.* [35], the effect of hydrodynamic forces may be of great importance for ship grounding analysis, especially when the initial heave velocity of the ship is non zero. In addition to the previous study, recent research performed by *Kim et al.* [115] showed that the solely added mass is insufficient when dealing with bottom grounding. Restoring forces must be considered since they affect both structural damages and absorbed energy. Finally, although the sway velocity is generally much smaller than the surge velocity, it may significantly affect the damage extent in lateral direction.

At the end of this general bibliographical analysis, it appeared that we had to focus our work on:

- Deriving analytical models to assess the resistance of the principal components of a ship that grounds over a paraboloid shaped rock. The proposed models should cover both bottom and side grounding scenarios.
- Extending the models in order to tackle situations where the ship is given both initial surge and heave velocities.
- Implementing the derived formula in a unique S.E. solver and coupling this latter with a 6-DOF external dynamics program.

Article	Method	Grounding Type	Rock shape	Structure Type	FSI	Considered motion
Little [116]	Analytical Experimental	Bottom Raking	Wedge	Bottom plating, Floor	No	-
Turgeon [18]	Analytical Experimental	Bottom Sliding	Ogive	Bottom plating, Floor	No	-
Bracco [110]	Analytical Experimental	Bottom Raking	Wedge	Bottom plating longitudinal stiffener	No	-
Pippenger [117]	Analytical Experimental	Bottom Raking	Wedge	Bottom plating, longitudinal stiffener	No	-
Zheng [111]	Analytical Experimental	Bottom Raking	Wedge	Bottom plating	No	-
Wierzbicki et al. [118]	Analytical	Bottom Raking	Wedge	Bottom plating	No	-
Lu & Calladine [71]	Experimental	Bottom Raking	Wedge	Bottom plating	No	-
Puente [119]	Analytical	Bottom Raking	Conical	Bottom, Floor, Girder	No	-
Rodd & Sikora [70] *Rood* [120]	Experimental	Bottom Raking	Conical	Bottom, Floor, Girder longitudinal stiffener	No	-
Muscat-Fenech [69] *Muscat-Fenech & Atkins* [121]	Experimental	Bottom Raking	Conical	Bottom plating	No	-
Simonsen [11]	Analytical	Bottom Raking	Conical	Bottom, Floor, Girder longitudinal stiffener	Yes	Surge, Heave, Roll, Pitch
Simonsen & Lauridsen [85]	Analytical Experimental	Bottom Stranding	Conical	Bottom plating	No	-
Samuelides et al. [122]	Numerical	Bottom Raking	Conical	Bottom, Floor, Girder	No	-
Hong & Amdahl [19, 112]	Numerical/Analytical	Bottom Sliding	Pyramid	Girder	No	-
Nguyen et al. [15]	Analytical	Bottom Sliding	Paraboloide	Bottom, Floor, Girder	No	-
Yu et al. [123] and *Yu et al.* [124]	Analytical	Bottom Sliding	Pyramid	Longitudinal stiffener	No	-
Abubakar & Dow [125]	Numerical	Bottom Raking	Conical	Bottom, Floor, Girder	No	-
Heinvee [20]	Numerical	Sliding/Raking Bottom	Paraboloide	Bottom, Floor, Girder	No	-
Sun et al. [13]	Analytical	Bottom Raking	Conical	Floor	No	-
Hu et al. [126]	Simplfieid	Bottom Sliding	Pyramid	Bottom, Floor, Girder	No	-
Song & Hu [114]	Simplified tool	Sliding/Raking Bottom	Conical / Pyramid	Bottom, Floor, Girder	No	-
Zhou et al. [63]	Analytical	Bottom Raking	Conical	Bottom plating	No	-
Lee et al. [127]	Numerical	Bottom Raking	Conical	Bottom, Floor, Girder	Yes	6-DOF
Calle et al. [61, 62]	Numerical Experimental	Bottom Raking	Wedge	Bottom, Floor, Girder	No	-
Le Sourne et al. [35]	Numerical	Bottom Combined	Conical	Bottom, Floor, Girder	Yes	6-DOF
Kim et al. [51]	Numerical	Sliding/Raking Bottom	Cylinder	Bottom, Floor, Girder	Yes	6-DOF
Le Sourne et al. [53]	Numerical Super Element	Bottom Raking	Conical / Paraboloide	Bottom, Floor, Girder	Yes	6-DOF

Table 2.1: Summary of methods for ship grounding calculation

Chapter 3

Finite element analysis - Calibration of parameters

3.1 Introduction

Maritime engineering covers a wide range of technical topics, from structural arrangement, ship stability, powering, survivability after accident, to ecological and economic performance. By its nature, ship design is an iterative process as initially introduced by *Evans* [128] and may be illustrated with the spiral representation depicted in Figure 3.1.

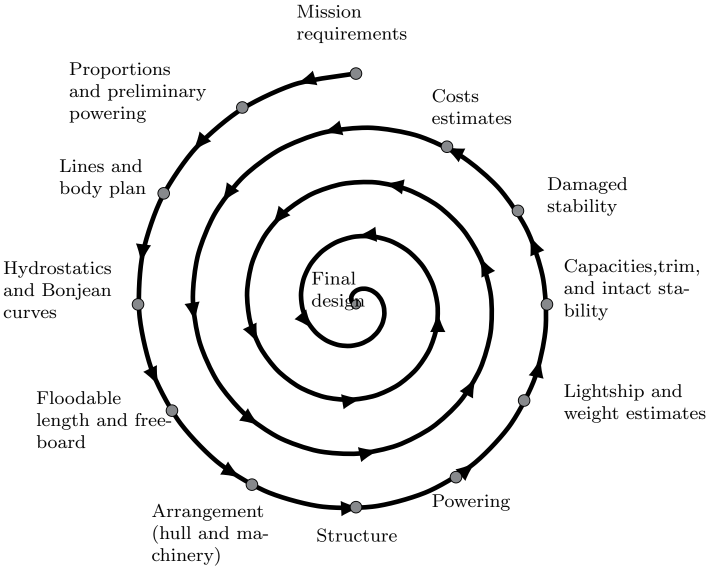

Figure 3.1: Design spiral from *Evans* [128]

As the design of a ship is progressing along the spiral, the structure becomes more and more complex. Nonetheless, the structure of a ship hull may be seen as an assembly of panels that are transversely and/or longitudinally stiffened. Various elements enter in the composition of a ship hull (local reinforcement, patch...). When evaluating at the predesign stage the ship crashworthiness or the crash performance of an alternative design, the detail level of input data is generally limited to the main structural components of the vessel. In ship bottom grounding analysis, only the following structural members are generally modelled:

- Outer / inner bottom plating
- Transverse floors
- Longitudinal girders

As ship side grounding is concerned, it is usual to consider the following structural members:

- Side / inner side shell
- Decks
- Transverse frames and bulkheads

Secondary stiffeners are often smeared into the supporting structural member in such a way that their contribution is approximated by increasing the thickness of the latter - see for instance *Paik* [129]. Widely used in ship grounding analysis, the smearing approach has proven to be efficient to account for secondary and tertiary stiffeners - see [110, 130, 131]. It is also worth mentioning that specific analytical solutions have been developed for secondary stiffeners - see example [123, 124, 132]. In the same way, transverse frames are generally reduced by cutouts for weight saving purpose. For simplicity, they are often considered as a bare homogeneous flat plate, with an effective thickness adjusted by considering both the cutouts and tertiary stiffeners. Such approach is always used when dealing with simplified formulations - see for instance *Simonsen* [11].

The theoretical models developed in the framework of the present PhD thesis will be validated considering different ship grounding scenarios. The validation strategy includes the following steps:

- Calibration of NLFEA parameters from numerical simulation of scaled experiments reported in the literature.
- Setup of the finite model of a given ship bottom structure. Parameters calibrated in previous step are re-used and a mesh convergence analysis is systematically performed.
- Numerical simulation of different grounding scenarios, varying for instance the rock dimensions, the vertical indentation of the rock inside the structure and the friction coefficient.
- Confrontation of the results obtained with the proposed analytical model to the numerical results.

The two first steps are presented in the current chapter.

3.2 Finite element analysis

As presented in Chapter 2, the quality and accuracy of finite element results are extremely sensitive to both the finite element size in the crushed areas and the failure criterion. The validation strategy of the NLFEA parameters such as element type and size, behaviour law, failure criterion, contact method, etc. consists in comparing numerical simulations to experimental results and includes the following steps:

- Mesh convergence analysis considering the deck folding experiment from ASIS [133].
- Mesh convergence analysis considering a ship bottom sliding scenario.
- Calibration of the failure criterion proposed by *Lehmann* & *Peschmann* [87] from the numerical simulation of the NSWC grounding experiment reported by *Rodd* & *Sikora* [70].

3.2.1 ASIS deck crushing

In 1993, a series of experiments were conducted by the ASIS (Association of Structural Improvement of Shipbuilding Industry) in Japan with the aim of investigating the response of the side of a ship subject to a collision. The ASIS model test was a 1:2 scale side structure of VLCC impacted by a rigid sphere of radius $500mm$. The finite element model of the undamaged structure is depicted in Figure 3.2. The impact was set between two adjacent transverse webs. Quasi-static as well as dynamic tests were performed, details on the experimental setup and results may be found in *Ohtsubo et al.* [133].

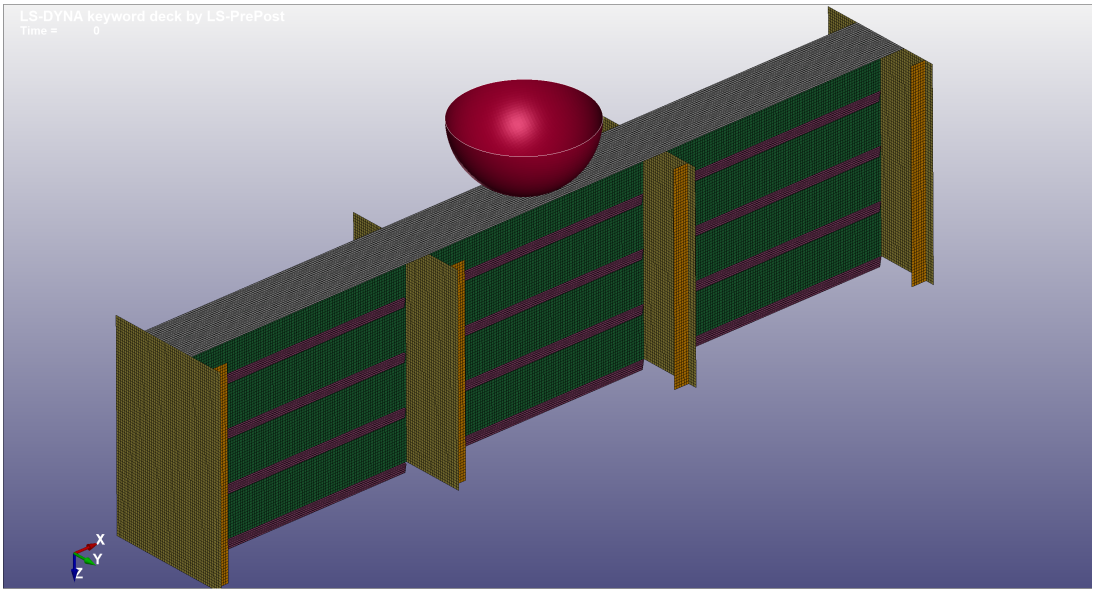

Figure 3.2: ASIS model - View of the finite element model

In the dynamic tests, the bow model fell freely from a height of $4.8m$ above the initial position of the outer hull, leading to an impact velocity of $9.7m/s$. The test was repeated four times until a permanent deformation of $900mm$ was reached.

Regarding the quasi-static test, the bow model was smoothly pushed down by a hydraulic piston. The structure was first indented up to 450mm, then pushed again up to a permanent indentation of $900mm$. Figure 3.3 illustrates the damaged structure after dynamic and quasi-static impacts.

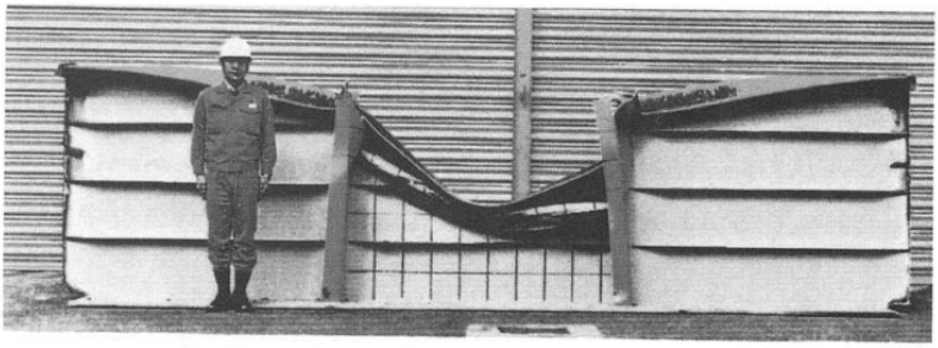

Dynamic Test

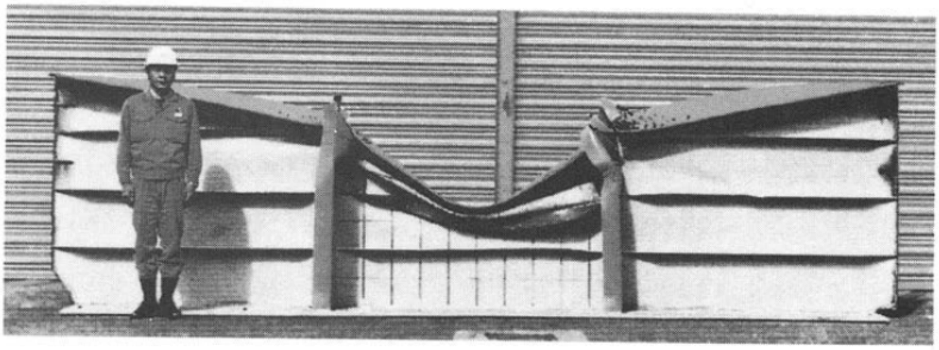

Static Test

Figure 3.3: ASIS deck crushing experiment - From *Ohtsubo et al.* [133]

For ship collision analysis involving plate structural folding, a fine mesh is required to correctly grasp the folding process. According to *Paik* [134], a minimum of 8 shell elements must be used to mesh half length of one structural fold. Based Zhang's formulation [37], the half folding length may be estimated as:

$$H_f = 0.838 b^{2/3} t_h^{1/3} \tag{3.1}$$

Where $b = 2000mm$ is the spacing between two webs and $t_h = 7mm$ is the deck plating thickness. The half folding wave length is then estimated as $H_f = 254.5mm$ which leads to a critical element size of $l = 254.5/8 \approx 32mm$. In *Paik et al.* [135], critical element size was calculated based on *Wierzbicki & Abramowicz* [136] formulation giving a value around $40mm$. In the present study, four different meshes are investigated: $l = 10$, 20, 40 and $80mm$. The plastic behaviour of the constitutive material is modelled using a classical power law:

$$\sigma = K\varepsilon^n \tag{3.2}$$

Where $K = 800\, MPa$ and $n = 0.25$ are the coefficients proposed by *Tørnqvist* [88] for mild steel. Principal dimensions and characteristics of the structure are resumed in appendix A.1.

In Figure 3.4, the resisting forces obtained with the different element sizes are compared to the one measured during the static test.

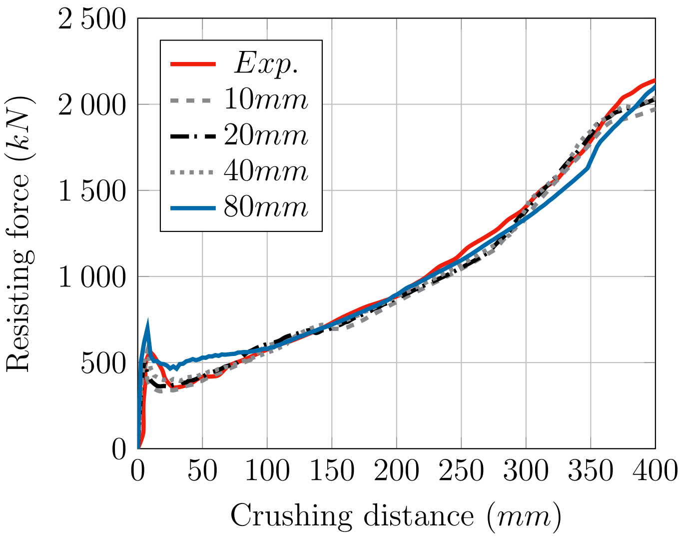

Figure 3.4: Comparison of the resisting force for different mesh sizes - ASIS experiment

The coarse meshed model ($80mm$) appears to be stiffer than the test structure, especially at the beginning of the denting process. Then, after some indentation, the model seems to be too flexible compared to the real structure. On contrary, finer meshes (10, 20 and $40mm$) allow for a good fitting with the experimental curve. This demonstrates that a mesh involving around 8 elements in half folding wave length is fine enough to correctly capture the crushing mechanism.

3.2.2 Ship bottom sliding analysis

The previous experiment was concerned with ship side collision but since the present thesis focuses on the response of a ship hull in powered grounding, a mesh convergence analysis is also performed for the simulation of a ship bottom running aground on a large rounded rock.

Let us consider a longitudinal girder attached to a piece of outer shell plating. The expected involved mechanisms are outer shell membrane straining and bending, girder crushing and friction. The structure FE model, shown in Figure 3.5, is $16m$ long, $1.6m$ high and $2m$ wide. It is meshed using Belytschko-Tsai shell elements [137] with 4 different element sizes: 120, 60, 30 and $15mm$. The thickness of plating and girder is respectively $15mm$ and $20mm$ and 5 integration points are used through thickness.

The mild steel constitutive material is represented by a bi-linear law and its principal characteristics are resumed in Table 3.1. A large rounded rock with coefficient $C = 0.3$ and $E = 0.3$ (see Eq.1.1) is used with an a imposed velocity V_x of $5m/s$. The vertical penetration of the rock into the structure is $0.4m$ and the friction coefficient between the rock and the outer shell is set to 0.3.

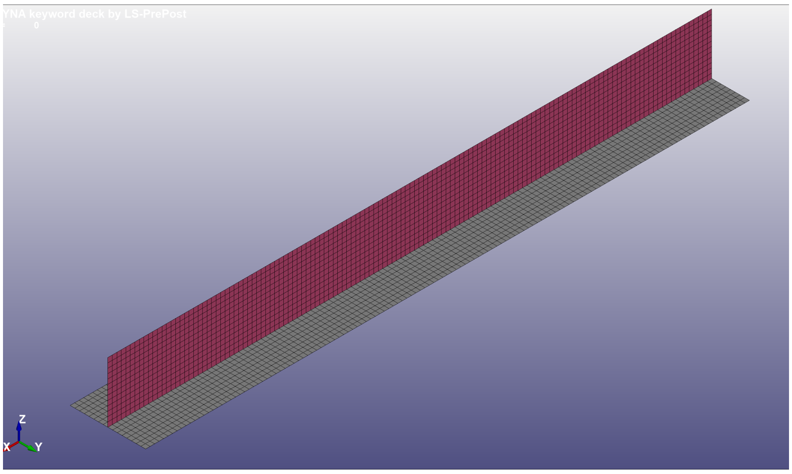

Figure 3.5: F.E model for ship sliding convergence analysis (element size = 120 mm)

Material properties		
Yield stress	σ_y (MPa)	240
Poisson's ratio	ν	0.33
Density	ρ (kg/m^3)	7850
Young modulus	E_{young} (MPa)	210 000
Tangent modulus	E_{tan} (MPa)	1018

Table 3.1: Material properties of mild steel

Figure 3.6 compares the girder internal energy obtained from the different meshes and Table 3.2 presents the overall dissipated energies (internal + friction) post-processed at the end of the simulations. It clearly appears that an element size of $30mm$ is sufficient to correctly capture the girder crushing. Such mesh fineness will thus be adopted in all numerical simulations performed in the framework of this research work. It is also worth noting that similar convergence analysis carried out by *Hong & Amdahl* [112] led to the same element size.

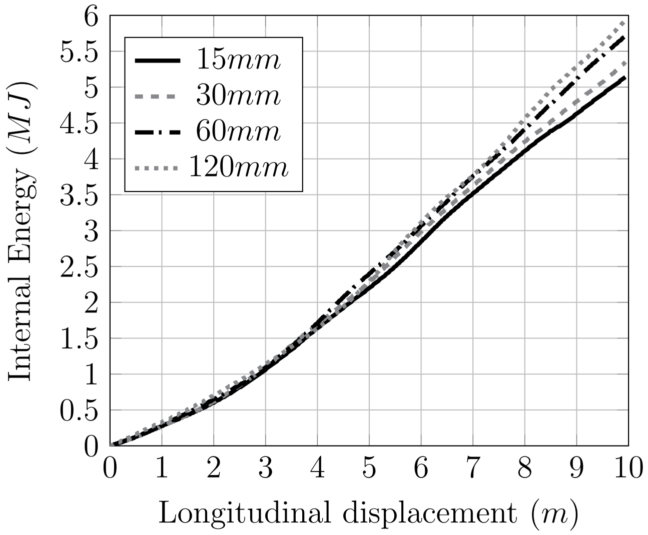

Figure 3.6: Evolution of internal energy - Mesh convergence analysis

Mesh (mm)	Girder Energy (MJ)	Deviation (%)
15	5.14	-
30	5.35	-4.0
60	5.72	-11.2
120	5.94	-15.5

Table 3.2: Girder dissipated energy - Mesh convergence analysis

3.2.3 Ship bottom raking analysis

As tearing of outer and possibly inner shell is expected in a grounding accident, the failure criterion as well as the failure strain ϵ_{rup} obtained from Eq. 2.10 must also be validated by confrontation with experimental results.

In the middle of the 1990s, the Naval Surface Warfare Centre in Virginia, USA performed several 1:5 scale grounding experiments with the objective to investigate the response of several ship bottom structures under grounding accidents [70]. The specimens were mounted on a railway attached to a vehicle of 223 tons and slightly inclined from the horizontal in order to progressively tear the structure. The rock was represented by a rigid cone making a semi apex angle of $\varphi = 45°$ and with a rounded apex of radius $R_r = 170mm$. At the instant of impact, the structure had reached a velocity of 6.17 m/s and the rock tip entered the specimens 50 mm below the inner shell.

Four different double bottom geometries were tested, but only the test related to the first specimen (conventional double bottom) is considered in the present validation. This specimen which geometry is displayed in Figure 3.7 is $7.36m$ long and $2.54m$ wide. Its main particulars are listed in Table A.2 and Table A.3 of appendix A.2. The corresponding finite element model contains 1 320 000 Belytschko-Tsay under-integrated shell elements with an average size of $9mm$ [137].

The behaviour of the ASTM constitutive material is modelled using Eq. 3.2 where $K = 600\ MPa$ and $n = 0.22$ are the coefficients of the power law as given by *Brubak et al.* [79].

As the friction between the rock and the grounded structure was not explicitly measured in the NSWC experiment, a friction coefficient of 0.35 is considered in the present numerical study, on the basis of the value assumed by *Brubak et al.* [79]. It is also worth noting that steel plate rupture in ship grounding may be challenging to model as the failure criterion to be used can vary depending whether the plate is stretched or torn or stretched-and-torn. Nevertheless, the classical criterion proposed by *Lehmann* & *Peschmann* [87] and given by Eq. 2.10 is considered.

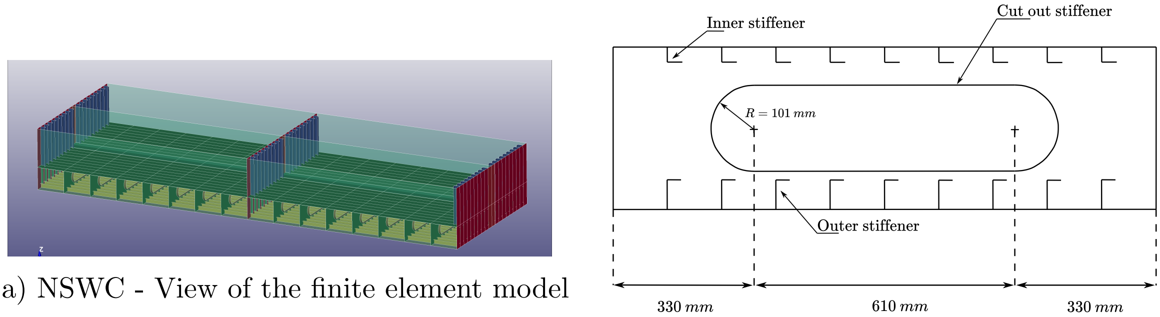

(a) NSWC - View of the finite element model

(b) NSWC - Transverse floor dimensions

Figure 3.7: NSWC model description

Longitudinal and vertical resistant forces as well as dissipated energy post-processed from *Ls-Dyna* numerical simulation are compared to experimental results in Figure 3.9, while damage extent from numerical simulation is depicted on Figure 3.8

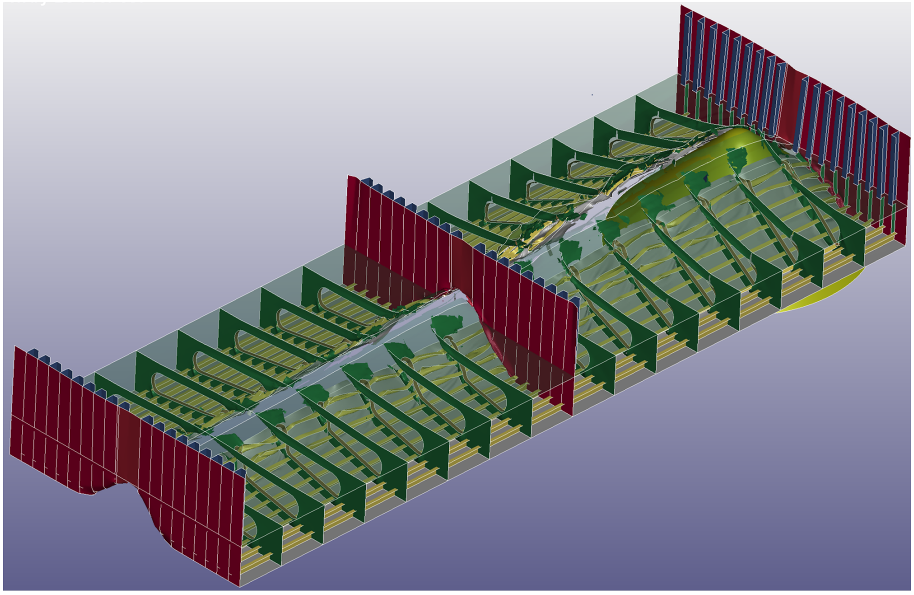

Figure 3.8: NSWC - Damage extent from numerical simulation

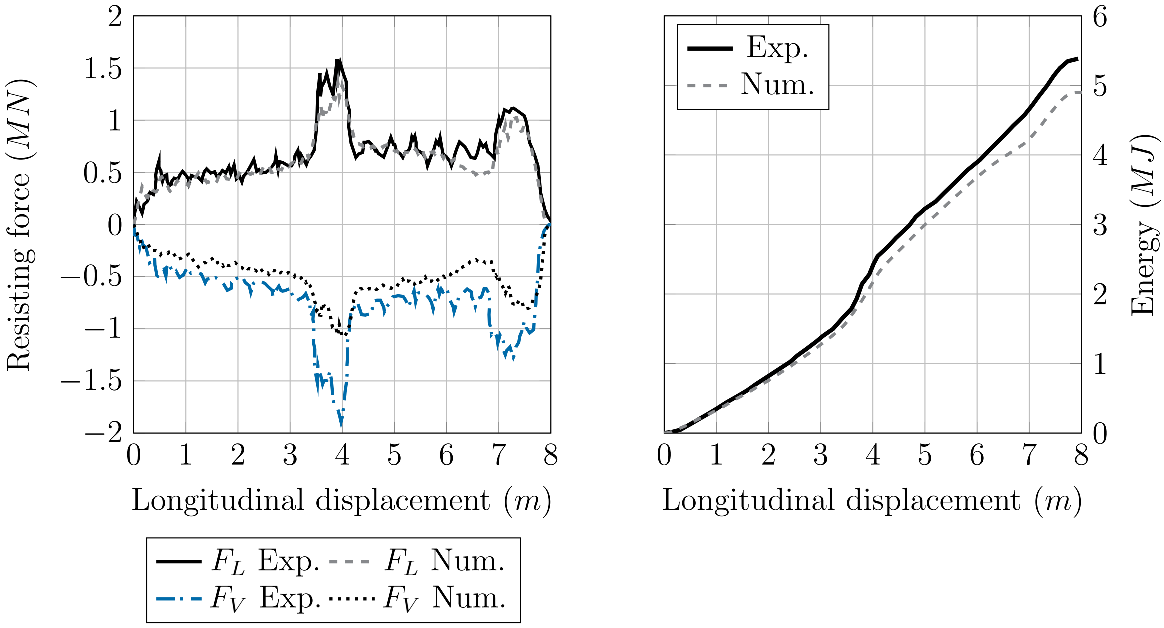

Figure 3.9: NSWC grounding test : comparison of resistant forces (left) and dissipated energy (right)

According to Figure 3.9, the longitudinal force F_L is fairly well reproduced by the numerical model, while the vertical component F_V is slightly underestimated, except when a transverse bulkhead is crushed (at $3.5m$). In this case, the deviation is more pronounced (around 50%). As the dissipated energy is concerned, the discrepancy between numerical and experimental results do not exceed 8.2%. The reason of such deviation may be attributed to the choice of the (unknown) friction coefficient. Nevertheless, the ability of the numerical model to reproduce the experiment may be considered as acceptable. More specifically, the relevance of the chosen modelling parameters including the failure criteria is demonstrated. Note that the computation for this finite element model takes 20 days.

3.3 Conclusion

In this chapter, several *Ls-Dyna* simulations have been presented and compared to experimental results. The influence of the mesh size and the applicability of a classical shear failure criterion have been investigated. As a result, $30mm$ long Belytschko-Tsay shell elements with five integration points through thickness are used in the numerical simulations presented in the next chapters. The contact between the outer shell and the rock is treated using the *Automatic surface to surface* card with a static friction coefficient. The steel material is represented by a bi-linear law with the characteristics resumed in Table 3.1 and the failure strain is computed according to Eq. 2.10. Note also that the strain rate effect is not considered, following *Çerik & Choung* [99] who recently demonstrated that at such velocity, its influence on the resulting breach is limited. This is also in accordance with the work of *Jones* [92] who claimed that the strain rate effect may be neglected as far as the impact velocity remains lower than 45 knots ($23m/s$).

Part II

Derivation of simplified models

Chapter 4

Ship sliding

4.1 Introduction

The present chapter is dedicated to the development of a simplified model for the problem of a ship sliding over a paraboloid shaped rock. The resisting force of the bottom main structural components will be analytically derived and compared with numerical simulations.

At the start of a grounding event and as far as the plastic strain in the outer shell remains small, the ship slides over the rock without tearing. The mode of deformation is referred to as *"sliding"*. Even though the outer shell is not perforated and no compartment gets flooded, the ship bottom damage may be severe, yielding a decrease of the bending moment capacity of the hull girder and, in some cases, premature collapse of the vessel. Residual strength capacity will not be discussed in the present thesis but some information may be found in *Smith & Dow* [138] or *Bin et al.* [139].

As discussed in Chapter 2, the raking response of a ship has long been the focus of research. On contrary, earlier ship sliding experimental tests were realised during June 1994 to April 1995 in the framework of the Joint MIT-Industry Tanker Safety Program. As reported by *Turgeon* [18], the specimen was a scaled model of VLCC's single hull with transverse stiffeners. Figure 4.1 illustrates a deformed single hull. Additional experiments were conducted by *Muscat-Fenech* [69] on unstiffened plating impacted by spherical indentor. However, apart from those two experiments and to the author's knowledge, no other experimental tests were carried out on the response of a ship hull in sliding configuration.

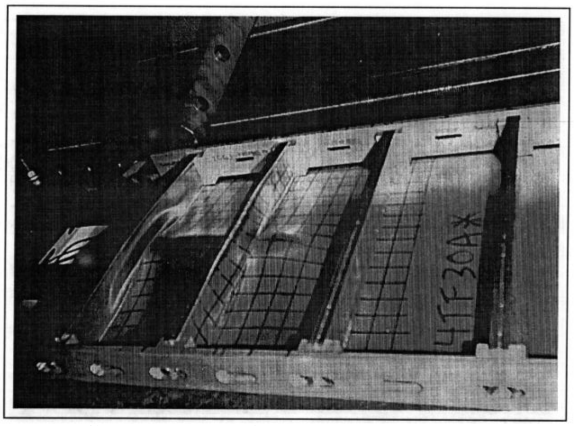

Figure 4.1: Ship hull deformation - From *Turgeon* [18]

The responses of the main individual structural members, i.e., outer shell plating, transverse floors and longitudinal girders as well as the effect of friction are discussed in the following sections.

4.2 Effect of friction

According to *Turgeon* [18], *Simonsen* [11], *Nguyen et al.* [15] or *Hong & Amdahl* [19], evaluating the contribution of friction is a major issue as almost 50 % of the ship initial kinetic energy is dissipated via friction during a grounding event.

In Eq. 2.15, the effect of friction is introduced through a tangential stress $\tau = \mu p$, where p is the pressure distribution on the contact surface and V_{rel} the relative velocity between the structure and the rock.

If the contact angle between the rock and a plate element is denoted by α, the relative velocity is:

$$V_{rel} = \frac{V}{cos(\alpha)} \tag{4.1}$$

The same expression may be found in *Hong & Amdahl* [19, 112]. Nevertheless, unlike *Hong & Amdahl* who dealt with truncated pyramidal rocks, here the contact angle α is not constant anymore but varies according to the following expression:

$$\alpha(x) = atan(2Cx) \tag{4.2}$$

Solving the integral in Eq. 2.15 comes to determine the pressure evolution along the contact line, i.e, for x varying in $[0, a_0]$. For this purpose, two different pressure distributions are assumed, namely a symmetric distribution (Figure 4.2a), which corresponds to the normal case of a plate sliding on a smooth rock, and a non-symmetric distribution where the pressure is maximum in a_0 (Figure 4.2b). This last case corresponds to the situation in which a transverse floor is impacted by the rock.

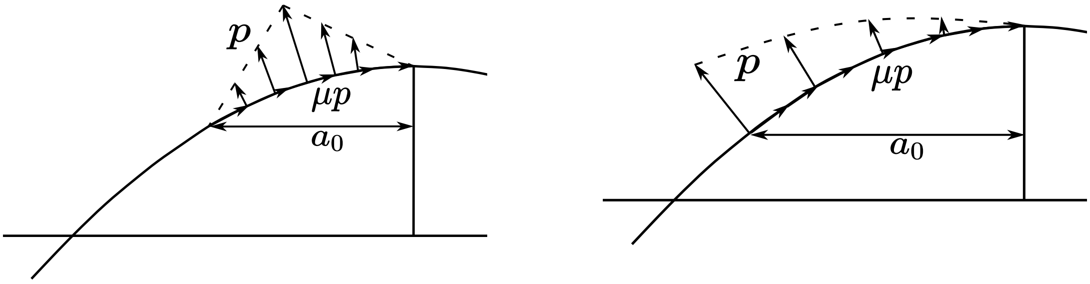

(a) Symmetric pressure distribution

(b) Non symmetric pressure distribution

Figure 4.2: Assumed pressure distribution in sliding

Force equilibrium in longitudinal and vertical direction writes:

$$F_L = \int_0^{a_0} p(x)(sin(\alpha) + \mu cos(\alpha))\sqrt{1 + 4C^2x^2}dx \tag{4.3}$$

$$F_V = \int_0^{a_0} p(x)(cos(\alpha) - \mu sin(\alpha))\sqrt{1 + 4C^2x^2}dx \tag{4.4}$$

Using Eqs. 2.15, 4.3 and 4.4, the friction factor $g_f = F_L/F_P$ and the ratio $K_v = F_V/F_L$ may be calculated using the following expressions:

$$g_f = \left(1 - \frac{\int_0^{a_0} \mu \frac{p(x)}{cos(\alpha)} \sqrt{1+4C^2x^2}dx}{\int_0^{a_0} p(x)(sin(\alpha) + \mu cos(\alpha))\sqrt{1+4C^2x^2}dx}\right)^{-1} \tag{4.5}$$

$$K_v = \frac{\int_0^{a_0} p(x)(cos(\alpha) - \mu sin(\alpha))\sqrt{1+4C^2x^2}dx}{\int_0^{a_0} p(x)(sin(\alpha) + \mu cos(\alpha))\sqrt{1+4C^2x^2}dx} \tag{4.6}$$

Assuming that the pressure is zero at $x = 0$ and $x = a_0$ and symmetric with respect to $x = a_0/2$ (Figure 4.2a), good approximations of Eqs. 4.5 and 4.6 are given by:

$$\frac{F_L}{F_P} = \left(1 - \frac{\mu}{sin(\alpha)cos(\alpha) + \mu cos(\alpha)^2}\right)^{-1} = g_f \tag{4.7}$$

$$\frac{F_V}{F_L} = \frac{1 - \mu tan(\alpha)}{\tan(\alpha) + \mu} = K_v \tag{4.8}$$

Where $\alpha = atan(2Ca_0/2) = atan(Ca_0)$.

When a transverse floor is impacted by the rock, the contact pressure is not symmetric anymore but is supposed to be maximum at point a_0 as illustrated in Figure 4.2b. In that case, the angle α is defined as $\alpha = atan(\frac{4}{3}Ca_0)$.

To summarise, the angle α is defined as:

$$\begin{cases} \alpha = atan(Ca_0) & \text{for symmetric pressure distribution.} \\ \alpha = atan(\frac{4}{3}Ca_0) & \text{for non symmetric pressure distribution.} \end{cases} \tag{4.9}$$

Figure 4.3 illustrates the difference between the integral forms of g_f and K_v (Eqs. 4.5 and 4.6) and their approximations (Eqs. 4.7 and 4.8). Eqs. 4.7 and 4.8 combined with Eq. 4.9 allow for an excellent approximation of Eqs. 4.5 and 4.6. Therefore, such approximations will be used in the following analytical developments. Note also that the expression of a_0 will be discussed later - see Section 4.3.

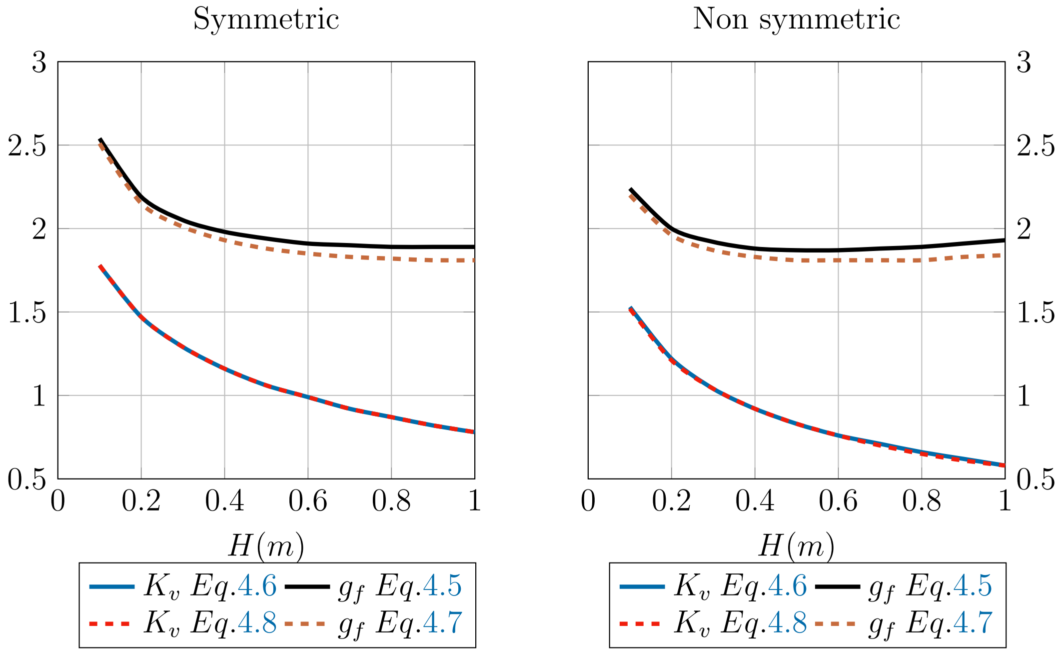

Figure 4.3: Approximation of g_f and K_v

4.3 Response of bottom plating

4.3.1 Literature review

The first elementary structure which is considered is an unstiffened horizontal plate representing either the outer or the inner shell of a ship bottom. The objective is to derive analytical expressions that relate the vertical penetration H of the rock to the longitudinal F_L and vertical F_V resisting forces. This problem has already been investigated by several authors for different rock shapes.

On the basis of small-scale experiments, *Turgeon* [18] investigated the response of a transversely stiffened plate impacted by a parabolic shaped rock. The plastic limit approach was used to derive a closed-form expression of the resisting force, for which the displacement field components u, v and w were approximated by trigonometric functions. According to *Turgeon* [18], one of the main challenges lies in the definition of the contact pressure distribution, given that the later may affect by up to 100% the final resisting force.

Furthermore, describing the seabed by a blunt conical rock, *Simonsen* [11] derived analytical expressions for the response of bottom plating, transverse floor, longitudinal girder as well as small longitudinal stiffeners. All the developments were performed under the punctual impact assumption and only the contribution of friction depended on the rock shape.

More recently, *Hong & Amdahl* [19] derived analytical expressions for the sliding response of the ship hull main components. The rock was idealised as a truncated pyramid making an angle α with the horizontal. The crushing resistance of secondary stiffeners attached to bottom plating, floors and girders has been investigated by *Yu et al.* [124] and *Hu et al.* [126]. On the basis of numerical simulations, *Nguyen et al.* [15] derived simple expressions giving vertical and longitudinal resisting forces for a paraboloid shaped rock. The vertical force in sliding condition was assumed to be half the punch force obtained in a stranding simulation.

Previous studies considered unstiffened plating. Nevertheless, in practice, bottom and double bottom shells are reinforced with small longitudinal stiffeners. These latter are often treated by a smearing method such as the one proposed by *Paik* [129]. By analysing the effect of smearing on the response of a ship hull, *Liu et al.* [140] concluded that this approach is an effective way of considering the contribution of longitudinals. Therefore, in the remaining, small stiffeners will not be explicitly modelled but their contribution will be added by increasing the bottom plating thickness, following the method proposed by *Paik* [129].

4.3.2 Analytical development

From both the literature and the analysis of numerical simulations, the energy absorption mechanism of the bottom plating may be split into four different contributions:

- Membrane straining that includes the stretching of transverse fibres and shearing
- Bending of longitudinal fibres
- Bending of transverse fibres
- Friction

A sketch of the deformation undergone by the bottom plating is depicted on Figure 4.4.

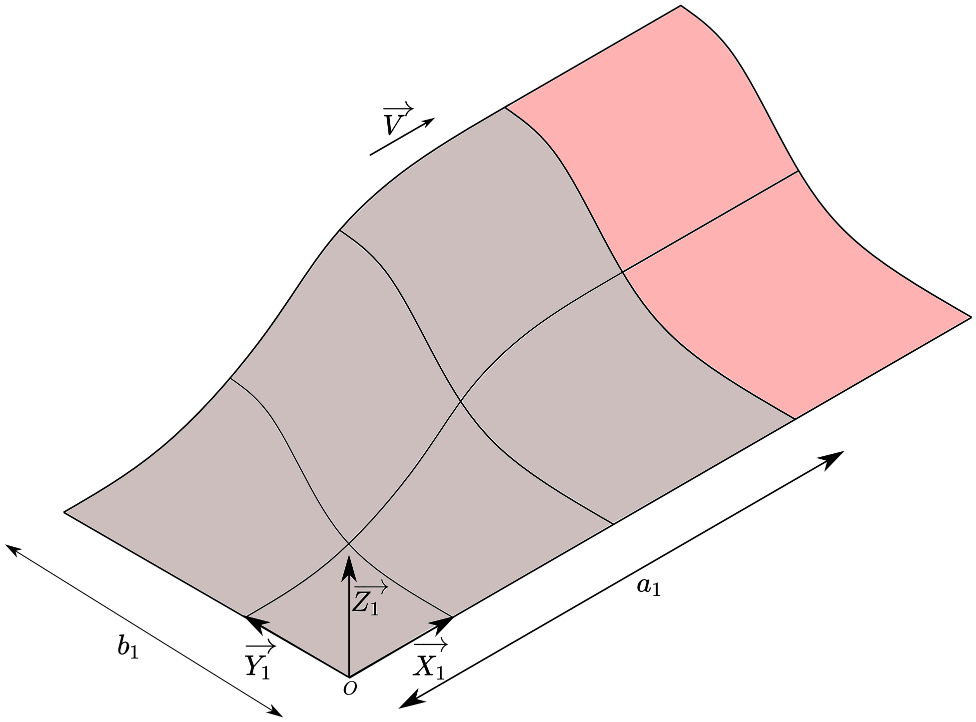

Figure 4.4: Overall bottom deformation process

4.3.2.1 Membrane straining

Let us consider a transverse fibre located at $x = a_1$. When the ship is moving forward, the fibre undergoes an out-of-plane displacement w, which can be broken down into two different displacement fields w_1 and w_2, as shown in Figure 4.5.

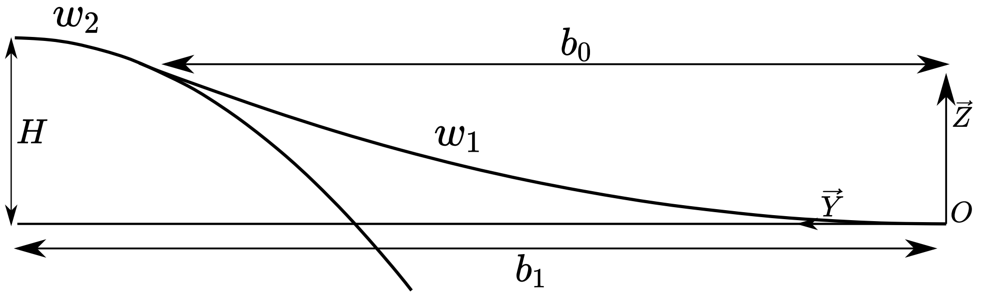

Figure 4.5: Transverse fibre out of plane displacement - Bottom plating

In the vicinity of the longitudinal symmetry plane, the outer shell is supposed to fit the shape of the rock so w_2 is given by:

$$w_2(y) = H - E\left(y - b_1\right)^2 \qquad y \in [b_0, b_1] \tag{4.10}$$

As for w_1, a polynomial function is chosen so as to comply with the following conditions: $w_1(0) = 0$, $w_1'(0) = 0$, $w_1(b_0) = w_2(b_0)$ and $w_1'(b_0) = w_2'(b_0)$

$$w_1(y) = \frac{H}{b_1 b_0} y^2 \qquad y \in [0, b_0] \tag{4.11}$$

Where $b_0 = b_1 - \frac{H}{E b_1}$

For illustration purpose, the assumed transverse displacement field (Eqs. 4.11 and 4.10) is compared on Figure 4.6 to the one post-processed from numerical simulations.

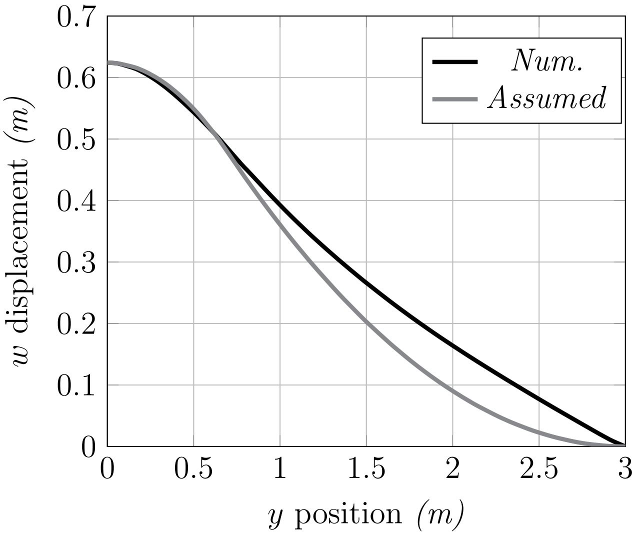

Figure 4.6: Comparison of assumed and numerical transverse displacement fields for the bottom plating

Once the displacement field is defined, the elongation v_0 of the transverse fibre can be calculated as:

$$v_0 = \int_0^{b_0} \frac{1}{2}\left(\frac{\partial w_1}{\partial y}\right)^2 dy + \int_{b_0}^{b_1} \frac{1}{2}\left(\frac{\partial w_2}{\partial y}\right)^2 dy = \frac{2}{3}\frac{H^2}{b_1} \tag{4.12}$$

Let us now look at the elongation of the longitudinal fibre located at $y = b_1$. During the sliding process, the deformed area extends to the next transverse member, so its length varies with the ship displacement. For $x \in [a_1 - a_0, a_1]$, the bottom plating displacement field f_2 follows the shape of the rock while for $x \in [0, a_1 - a_0]$, its displacement field f_1, illustrated in Figure 4.7 is approximated as follows:

$$f_1 = A x^p \tag{4.13}$$

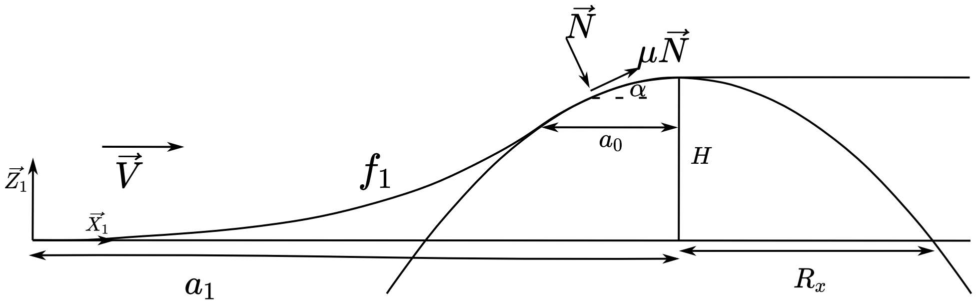

Figure 4.7: Transverse cut sliding process - Bottom plating

Considering the following conditions: $f_1(0) = 0$, $f_1'(0) = 0$ and taking into account the necessary continuity between f_1 and f_2 at $x = a_1 - a_0$, Eq. 4.13 becomes:

$$f_1 = \frac{H - Ca_0^2}{(a_1 - a_0)^p} x^p \tag{4.14}$$

With $p = 2Ca_0(a_1 - a_0)/(H - Ca_0^2)$.

The longitudinal fibre elongation u_0 is then calculated through numerical integration of the following expression:

$$u_0 = \int_0^{a_1 - a_0} \sqrt{1 + A^2 p^2 x^{2p-2}} dx + \int_{a_1 - a_0}^{a_1} \sqrt{1 + 4C^2 (x - a_1)^2} dx - a_1 \tag{4.15}$$

According to *Simonsen* [11] or *Hong & Amdahl* [112], straining of plate longitudinal fibre is unlikely to occur. Using trigonometric functions and moderately large deflections theory, *Turgeon* [18] succeeded in quantifying membrane straining but doing this led to a cumbersome expression. Moreover, from numerical simulations, it may be observed that the bottom plating remains almost flat after passing the rock, indicating that shearing is more likely to occur than longitudinal straining. Longitudinal straining is therefore neglected, which means that $\varepsilon_x = 0$.

Finally, the non zero strains write:

$$\begin{cases} \varepsilon_y = \frac{\partial v}{\partial y} = \frac{\partial}{\partial y}\left[v_0 \left(\frac{y}{b_1}\right)^2 \right] = 2v_0 \frac{y}{b_1^2} \\ \\ \varepsilon_{xy} = \frac{1}{2}\frac{\partial u}{\partial y} + \frac{1}{2}\frac{\partial v}{\partial x} = \frac{u_0 y}{b_1^2} + \frac{1}{2}\frac{v_0}{a_1}\left(\frac{y}{b_1}\right)^2 \end{cases} \tag{4.16}$$

Combining Eqs. 2.22, 4.12, 4.15 and 4.16, the membrane internal energy rate for half the outer shell plating may be expressed as:

$$\dot{E}_m = \frac{2}{\sqrt{3}} \sigma_0 t_h V_x \frac{1}{b_1^2} \int_0^{b1} \sqrt{4v_0^2 y^2 + y^2 \left(u_0 + \frac{1}{2}\frac{v_0}{a_1} y \right)^2} dy \tag{4.17}$$

Deriving a closed-form solution gets very complicated so the membrane energy rate is preferably calculated by numerical integration of Eq. 4.17.

4.3.2.2 Transverse fibre bending

The energy dissipated through transverse fibre bending is directly related to curvature radii of the fibres. From the definition of bending curvature radius and considering Eq. 2.23, the plastic bending energy rate of transverse fibres is expressed as :

$$\dot{E}_{bT} = M_0 V_x \int_0^{b_1} \frac{\frac{\partial^2 w}{\partial y^2}}{\left(1 + \left(\frac{\partial w}{\partial y}\right)^2\right)^{3/2}} dy \tag{4.18}$$

Replacing w by w_1 and w_2 leads to the following expressions:

$$\dot{E}_{bT1} = M_0 \frac{2H}{\sqrt{b_1^2 + 4H^2}} V_x \tag{4.19}$$

$$\dot{E}_{bT2} = M_0 \frac{2E(b_1 - b_0)}{\sqrt{1 + 4E^2(b_1 - b_0)^2}} V_x \tag{4.20}$$

Noting that $b_1 - b_0 = \frac{H}{Eb_1}$, this last equation can be rewritten as:

$$\dot{E}_{bT2} = M_0 \frac{2H}{\sqrt{b_1^2 + 4H^2}} V_x \tag{4.21}$$

Finally, for half the model, the bending energy rate of transverse fibres may be calculated as:

$$\dot{E}_{bT} = \dot{E}_{bT1} + \dot{E}_{bT2} = M_0 \frac{4H}{\sqrt{b_1^2 + 4H^2}} V_x \tag{4.22}$$

4.3.2.3 Longitudinal fibre bending

Longitudinal fibres located at the front of the rock are also subjected to bending deformation. By denoting R_m the bending curvature radius of a dy-wide longitudinal fibre (see Figure 4.8), the corresponding energy rate may be calculated as:

$$d\dot{E}_{bL} = M_0 V_x \frac{4}{R_m} \tag{4.23}$$

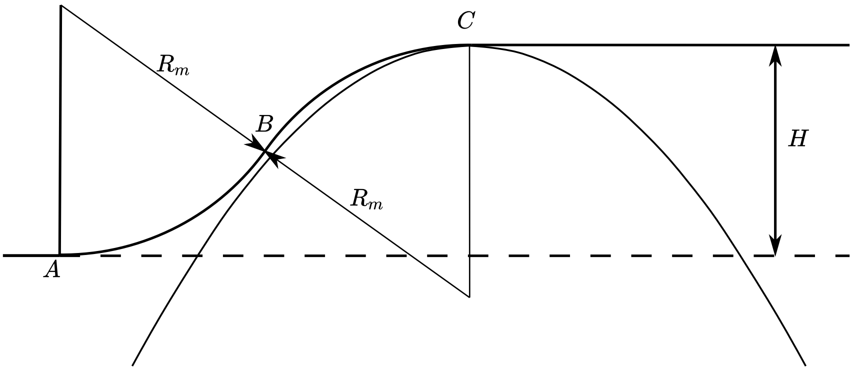

Figure 4.8: Longitudinal bending - Bottom plating

For a blunt conical rock, *Simonsen* [11] found that longitudinal fibre bending does not depend on the rock shape. On the other side, for a large contact surface, *Yu et al.* [113] found that the bending curvature radius is greatly influenced by the contact angle α proposed the following expression for the bending radius:

$$R_m = \frac{1}{\alpha} \tag{4.24}$$

Where α is the average contact angle defined by Eq. 4.9. As bending deformation is maximum at $y = b_1$ and vanishes at $y = 0$, the energy rate is expressed as :

$$\dot{E}_{bL} = M_0 V_x \frac{4}{R_m} \int_0^{b_1} \left(\frac{y}{b_1} \right)^2 dy = M_0 \frac{4}{3} \frac{b_1}{R_m} V_x \tag{4.25}$$

4.3.2.4 Total plastic energy rate

The total plastic energy rate is obtained by summing all the contributions given by Eqs. 4.17, 4.22 and 4.25:

$$\dot{E}_T = 2\left(\dot{E}_m + \dot{E}_{bT} + \dot{E}_{bL}\right) \tag{4.26}$$

The plastic resistant force F_P is finally obtained by dividing the expression 4.26 by V_x and the longitudinal and vertical forces F_L and F_V are calculated from the ratios g_f and K_v given by Eqs. 4.7 and 4.8 respectively.

Up to now, a_0 from Eq. 4.9 has not been defined. Following the approach proposed by *Hong & Amdahl* [19], it is found by minimising the discrepancy between finite element and analytical results. As it depends only on friction coefficient μ and distance a_0, the ratio $K_v = F_V/F_L$ is chosen as the quantity to fit. From various comparisons and for a given rock shape, it appears that K_v is a linear function of the longitudinal radius R_x, a_0 was found to also varies linearly with R_x and may be written as:

$$a_0 = \lambda R_x \tag{4.27}$$

Where the proportionality factor λ has to be defined.

Considering various simulations involving different rocks, friction coefficients and penetration depths, the best fitting is obtained by taking $\lambda = 0.55$. In that case, an average discrepancy of 6.8% is found between numerical and analytical values of K_v. It is worth to mention that the influence of the bottom thickness on a_0 was also investigated. It appeared that this parameter does not influence the ratio K_v. In other words, whatever the outer shell thickness, the value of a_0 remains equal to $0.55Rx$.

All previous analytical developments hold as far as no longitudinal girder is involved in the deformation process. However, if the impact is located just under a longitudinal girder and since this latter is relatively stiff, the outer shell is supposed to remain almost entirely stuck to the rock. Besides, this hypothesis is confirmed by numerical simulations. As a consequence, the proportionality factor λ in Eq. 4.27 has to be reevaluated and, at the same time, the influence of the girder thickness on the value of λ must be investigated. Figure 4.9 illustrates the evolution of K_v as a function of the girder thickness t_{hg} for a given rock and for two different friction coefficients. As expected, the ratio K_v decreases when the girder thickness increases, because this latter is getting stiffer and stiffer.

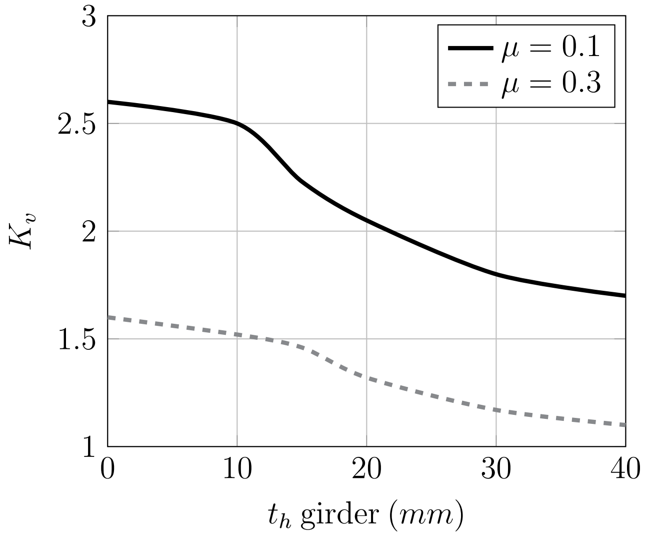

Figure 4.9: Evolution of K_v ratio for different girder thicknesses

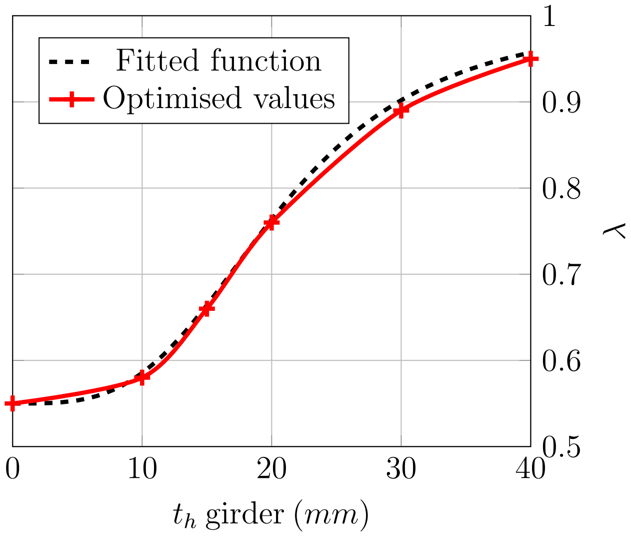

Figure 4.10: Fitted law and optimised values for λ

The proportionality factor λ is again obtained by minimising the discrepancy between K_v ratios extracted from analytical and numerical simulations. As K_v depends on the girder thickness, the following law is obtained for λ considering different scenarios:

$$\lambda(t_{hg}) = 1 - \frac{0.45}{1 + \left(\frac{t_{hg}}{20.6}\right)^{3.4}} \tag{4.28}$$

The relevancy of the proposed law is shown on Figure 4.10 where optimised values of λ extracted from the simulations are compared with the fitted function given by Eq. 4.28. It is worth noting that when no girder is involved in the deformation, i.e., $t_{hg} = 0$, we find $\lambda = 0.55$.

Apart from the proportionality factor λ, the elongation of the longitudinal fibres u_0 also changes and becomes:

$$u_0 = \int_0^{R_x} \left(\sqrt{1 + \left(\frac{\partial w}{\partial x}\right)^2} - 1 \right) dx = \int_0^{R_x} \left(\sqrt{1 + 4C^2x^2} - 1 \right) dx \approx \frac{2}{3} C^2 R_x^3 \tag{4.29}$$

Using these new expressions for a_0 and u_0, the response of the outer shell can be calculated from the theoretical model previously derived in Section 4.3.

4.3.3 Numerical validation

In an attempt to validate previous analytical model, the results obtained from simplified formulations are confronted to those post-processed from finite element simulations. Several grounding scenarios involving various rocks, penetrations and friction coefficients are modelled and simulated with *Ls-Dyna* finite element solver.

The mild steel which constitutes the ship bottom structure is represented by the *Mat.024-piecewise linear plasticity* behaviour law selected from *Ls-Dyna* library [137]. Its characteristics are resumed in Table 3.1. An *Automatic surface to surface* contact is set between the bottom structure and the rock with a static friction coefficient varying from 0.1 to 0.3. The rock is supposed to move with a constant penetration height H in a range of $[0.3;\, 0.6]\, m$ and at a constant velocity of $5m/s$. As the analytical model is concerned, the flow stress σ_0 is taken equal to the yield stress $\sigma_y = 240MPa$.

Three different rock shapes are considered by varying coefficients C and E of Eq. 1.1 according to the values listed in Table 4.1. Resulting transverse sections are compared in Figure 4.11. In all the simulations, the rock is assumed to be perfectly rigid.

A $16m$ long, $6m$ wide, and $15mm$ thick unstiffened bottom plating is considered. The rock is supposed to slide with a first contact located at the plate centre, i.e., at $b_1 = 3m$. It should be emphasised that the following simulations are run without considering the effect of transverse floors or longitudinal girders. The response of these components will be investigated in section 4.4 and 4.5 respectively.

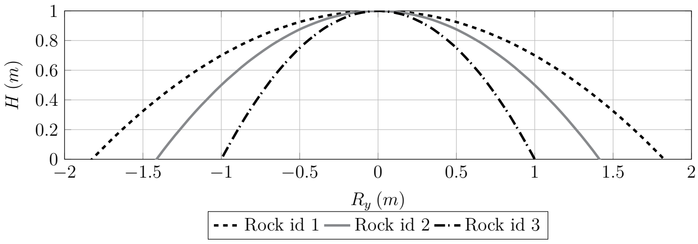

Figure 4.11: Transverse sections of the three different rocks

Rock id	$C\,[m^{-1}]$	$E\,[m^{-1}]$
1	0.3	0.3
2	0.5	0.5
3	1	1

Table 4.1: Rock parameters - Sliding

Discrepancies between analytical and numerical results are estimated as follows:

$$E_r = \frac{V_{Num} - V_{Ana}}{V_{Num}} \tag{4.30}$$

Where V_{Num} and V_{Ana} are the values retrieved from numerical and analytical models respectively.

Ls-Dyna first simulations showed that as expected, the outer shell rupture initiates at different penetrations H depending on the rock shape. For the shallowest rocks (id=1,2), the structure slides on the rock without rupture as far as the penetration does not exceed $H = 1.2m$ and $H = 0.85m$ respectively. In the parametric analyses presented hereafter, H is varied from $0.3m$ to $0.6m$ so bottom failure never occurs.

As the sharpest rock (n°3) is concerned, the rupture of the ship outer shell is triggered at $H \approx 0.45m$. As this chapter focuses on the response of a non perforated ship hull and for comparison purpose, the numerical failure criteria is intentionally omitted in the numerical simulations as suggested by *Hong & Amdahl* [112]. However, when the outer shell fails, corresponding scenarios are marked with an "*" in Table 4.2.

Combining the aforementioned parameters namely friction coefficients, rock shapes and impact heights leads to the study of 24 different scenarios. The mean values of F_L and F_V given by the proposed model are compared to the mean values extracted from *Ls-Dyna* simulations in Table 4.2.

Case id	μ	Rock id	H	F_L $Num.(MN)$	F_V $Num.(MN)$	F_L $Ana.(MN)$	F_V $Ana.(MN)$	Deviation F_L	Deviation F_V
1	0.3	1	0.3	0.63	1.31	0.70	1.42	-10.5%	-8.5%
2	0.3	1	0.4	0.99	1.94	1.05	2.02	-5.9%	-3.9%
3	0.3	1	0.5	1.42	2.63	1.47	2.67	-3.2%	-1.7%
4	0.3	1	0.6	2.00	3.40	1.95	3.39	2.7%	0.2%
5	0.3	2	0.3	0.62	1.10	0.67	1.22	-8.6%	-10.8%
6	0.3	2	0.4	0.99	1.65	1.00	1.70	-0.9%	-2.7%
7	0.3	2	0.5	1.41	2.26	1.39	2.22	1.3%	1.8%
8	0.3	2	0.6	1.98	3.00	1.84	2.79	6.9%	7.1%
9	0.3	3	0.3	0.68	1.00	0.68	1.03	0.1%	-2.7%
10	0.3	3	0.4	1.10	1.50	1.00	1.39	8.7%	7.5%
11*	0.3	3	0.5	1.50	2.00	1.39	1.78	7.5%	11.1%
12*	0.3	3	0.6	2.00	2.50	1.83	2.20	8.6%	12.1%
13	0.1	1	0.3	0.35	1.32	0.38	1.42	-11.0%	-7.7%
14	0.1	1	0.4	0.55	1.96	0.60	2.02	-8.5%	-2.8%
15	0.1	1	0.5	0.86	2.67	0.86	2.67	0.6%	-0.1%
16	0.1	1	0.6	1.14	3.42	1.16	3.39	-1.6%	0.8%
17	0.1	2	0.3	0.35	1.15	0.39	1.22	-11.4%	-6.0%
18	0.1	2	0.4	0.57	1.70	0.60	1.70	-5.4%	0.3%
19	0.1	2	0.5	0.89	2.30	0.86	2.22	3.8%	3.5%
20	0.1	2	0.6	1.22	3.00	1.15	2.79	5.5%	7.1%
21	0.1	3	0.3	0.40	0.99	0.43	1.03	-6.3%	-3.7%
22	0.1	3	0.4	0.67	1.50	0.64	1.39	3.9%	7.5%
23*	0.1	3	0.5	1.00	2.00	0.91	1.78	9.5%	11.1%
24*	0.1	3	0.6	1.35	2.50	1.21	2.20	10.6%	12.1%

Table 4.2: Ship bottom resistant force: comparison of numerical and analytical results

From Table 4.2, it is observed that discrepancies between numerical and analytical results do not exceed 12% for longitudinal and vertical forces, while the average deviation remains lower than 6% for both forces. It also emerges that for low penetration heights, the analytical model tends to overestimate the resisting forces. As reported by *Simonsen* [11], elastic contribution may be significant when the penetration depth is low, thus the use of rigid-plastic model is questionable. Anyway, the prediction given by the proposed model is judged to be reasonably good considering the different simplifications made and the benefit obtained in term of computation time.

Changing the friction coefficient from 0.3 to 0.1 reduces the longitudinal force by 60%, while the vertical force remains constant. In fact, for a given penetration depth, the vertical force defined as $F_V = F_P g_f K_v = F_P / tan(\alpha)$ is free of friction, which is confirmed by the numerical simulations.

Figure 4.12 illustrates the evolution of the breakdown between membrane and bending energies versus the penetration height H. As the rock penetration increases, the bending contribution decreases. Such result is in accordance with the observations of both *Turgeon* [18] and *Simonsen* [11] who found that bending deformation can be neglected when the rock penetration is significant.

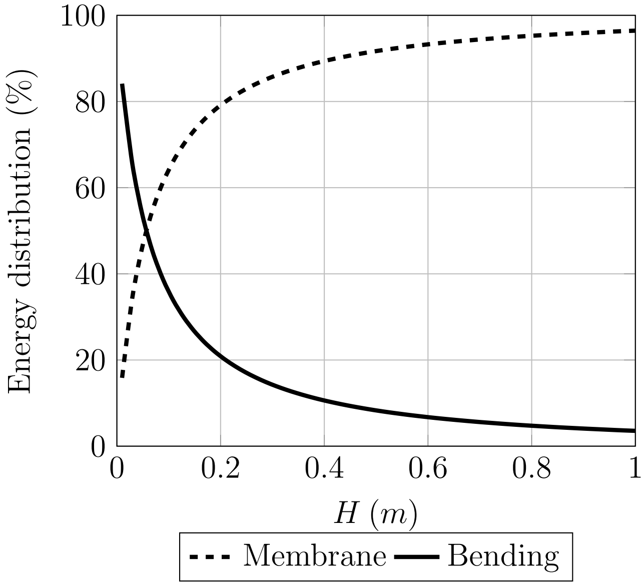

Figure 4.12: Membrane & bending share of energy

Based on previous analysis and neglecting bending contribution, *Turgeon* [18] proposed to estimate the membrane plastic resistant force (tension and shear) as:

$$F_P = 2.25\sigma_0 t_h \frac{H^2}{b_1} \tag{4.31}$$

On the other hand *Simonsen* [11], neglecting bending and shear contributions, succeeded in expressing the plastic force as:

$$F_P = 1.15\sigma_0 t_h \frac{H^2}{b_1} \tag{4.32}$$

As the present analytical derivation is concerned, neglecting bending as well as shear effects leads to:

$$F_P = 1.54\sigma_0 t_h \frac{H^2}{b_1} \tag{4.33}$$

The difference between the coefficient involved in equations 4.32 and 4.33 can be explained by the choice of the displacement field: linear in Simonsen's model and quadratic in the current one.

Including the effect of shear would lead to:

$$\begin{cases} F_P = 1.77\sigma_0 t_h \frac{H^2}{b_1} & \text{for } C = 0.3 \\ F_P = 1.82\sigma_0 t_h \frac{H^2}{b_1} & \text{for } C = 0.5 \\ F_P = 1.95\sigma_0 t_h \frac{H^2}{b_1} & \text{for } C = 1 \end{cases} \tag{4.34}$$

The difference regarding the coefficients involved in Eq 4.34 can be related to the different rock shapes. Moreover, it is worth noting these coefficients also vary with the distance a_1, which depends on the position of the rock with respect to the next impacted floor - see Figure 4.7. Finally, it is interesting to observe that Eqs. 4.33 and 4.34 are similar to those proposed by *Turgeon* [18] and *Simonsen* [11], the difference lying in the value of the coefficient.

Friction coefficient

In ship grounding analyses, the friction coefficient μ is often selected between 0.1 and 0.3 - see for instance [12, 19, 141]. That is why only these two values have been considered in the numerical simulations. Nevertheless, taking advantage of its rapidity, the proposed simplified model is now used to investigate the influence of μ on the dissipated energy. Figure 4.13 represents the evolution of the energy ratio E_T/E_P with μ, where E_T is the dissipated energy for a given μ (plastic + friction) and E_P is the one obtained with $\mu = 0$ (which corresponds in this case to the plastic deformation energy).

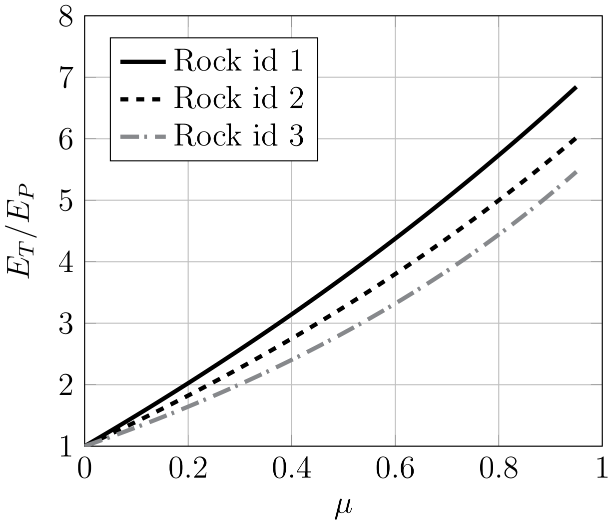

Figure 4.13: Influence of friction coefficient on total dissipated energy

It is observed that E_T/E_P varies almost linearly with the friction coefficient and, as expected, the wider the rock, the more pronounced the variation. Figure 4.13 confirms the observations made by various authors on the major role of friction in ship sliding.

4.4 Response of transverse floors

4.4.1 Literature review

The response of transverse floors has been examined by many authors and the deformation mechanisms are very well known. The first attempt to describe the folding mechanism of a structure submitted to axial compressive load was done by *Alexander* [142] on tubular members. The deformation patterns exhibited by a tube and a plate are illustrated on Figures 4.14 and 4.15 respectively.

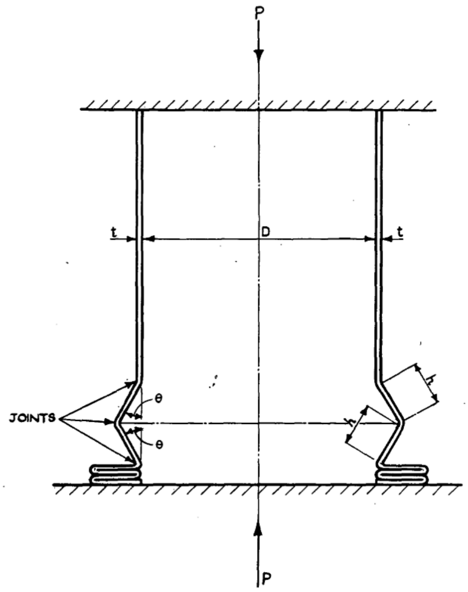

Figure 4.14: Folding of tubular member from *Alexander* [142]

Figure 4.15: Web crushing from *Zhang* [37]

Since these pioneer works, different authors like *Simonsen & Ocakli* [143], *Hong & Amdahl* [14], *Buldgen* [94] or *Gao et al.* [144] have studied experimentally, numerically or analytically the response of small scale web girders / decks / transverse bulkheads under compressive loads. The case of oblique impacts was in particular investigated by *Buldgen et al.* [107] and *Wang et al.* [101]. From all the experimental works, it appears that the response is quite insensitive to the indenter shape. Therefore, the assumption of a concentrated load is justified regarding the development of simplified formulations. Two main mechanisms are responsible for the plastic energy dissipation: the membrane straining of transverse fibres and the plastic bending related to the rotation of hinge lines.

As ship grounding is concerned, the response of transverse structures was investigated by *Simonsen* [11] and *Hong & Amdahl* [112]. Among other things, the authors concluded that the crushing response of a floor in ship sliding/stranding is similar to the crushing response of a web or a deck in ship collision. The influence of the presence of stiffeners has also been examined by *Chen et al.* [64]. It appears that horizontal stiffeners attached to a web girder significantly influences both the resisting force and the global response of the structure. On the other side, vertical stiffeners tend to trigger the rupture more rapidly.

4.4.2 Analytical developments

When a transverse floor is forced to pass over the rock, it undergoes a deformation similar to the concertina-like splitting of a deck collided by a ship bow [37]. According to numerical simulations performed on several double bottom configurations, two folds are formed such as depicted in Figure 4.16. The impact energy is thus dissipated through both transverse fibre stretching and plastic hinge bending.

The membrane energy rate related to half floor transverse fibre stretching may be written as:

$$\dot{E}_m = \frac{2}{\sqrt{3}}\sigma_0 t_h \int_S \dot{\varepsilon}_y dS \tag{4.35}$$

Where $S = 2H_f b$ in the stretched area and $\dot{\varepsilon}_y$ is the average membrane strain rate of a transverse fibre. In a similar way to Eq. 4.12, the elongation of a transverse fibre submitted to a vertical out of plane displacement χ writes:

$$v = \frac{2}{3}\frac{\chi^2}{b_1} \tag{4.36}$$

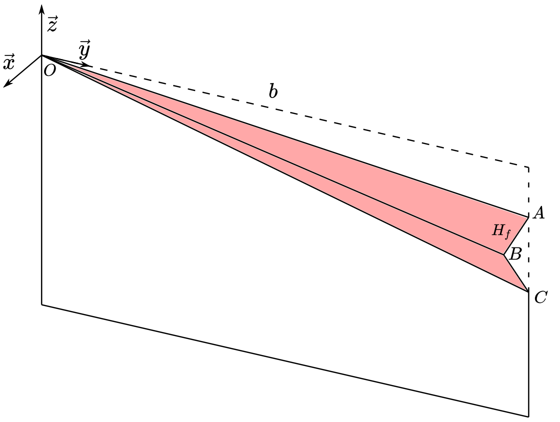

Figure 4.16: Floor crushing mechanism

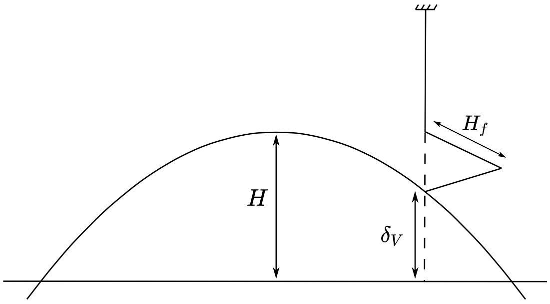

Figure 4.17: Floor crushing - side view

Let us consider the three points A,B and C depicted in Figure 4.16. Their initial position flagged by subscript "0" may be expressed as follows:

$$A_0 = \begin{bmatrix} 0 \\ b \\ 0 \end{bmatrix} \quad B_0 = \begin{bmatrix} 0 \\ b \\ -H_f \end{bmatrix} \quad C_0 = \begin{bmatrix} 0 \\ b \\ -2H_f \end{bmatrix} \tag{4.37}$$

Their final position after vertical crushing of the floor, flagged by subscript "1", is:

$$A_1 = \begin{bmatrix} 0 \\ b + \frac{2}{3}\frac{\left(2H_f\right)^2}{b} \\ 0 \end{bmatrix} \quad B_1 = \begin{bmatrix} H_f \\ b + \frac{2}{3}\frac{H_f^2}{b} \\ -H_f \end{bmatrix} \quad C_1 = \begin{bmatrix} 0 \\ b \\ -2H_f \end{bmatrix} \tag{4.38}$$

The elongation of transverse fibres OA, OB and OC is thus:

$$\begin{cases} v_A = \|OA_1\| - \|OA_0\| = \frac{8}{3}\frac{H_f^2}{b} \\ v_B = \|OB_1\| - \|OB_0\| \approx \frac{2}{3}\frac{(2H_f)^2}{b} = \frac{8}{3}\frac{H_f^2}{b} = v_A \\ v_C = 0 \end{cases} \tag{4.39}$$

The average elongation over the surface $S = 2H_f b_1$ is therefore only 3/4 of v_A. Similar results were found by *Simonsen* [11]. The energy dissipated by plastic membrane deformation of a half floor is thus:

$$E_m = \frac{8}{\sqrt{3}}\sigma_0 t_f \frac{H_f^3}{b} \tag{4.40}$$

As plastic bending is concerned, the energy is dissipated along three plastic hinges of length b and becomes:

$$E_b = \pi \frac{\sigma_0 t_f^2}{\sqrt{3}} b \tag{4.41}$$

Finally, the total energy which is absorbed by plastic deformation of the floor is:

$$E_P = \frac{8}{\sqrt{3}}\sigma_0 t_f H_f^3 \left(\frac{1}{b_{01}} + \frac{1}{b_{02}}\right) + \frac{\pi \sigma_0 t_f^2}{\sqrt{3}}(b_{01} + b_{02}) \tag{4.42}$$

The value of H_f can be taken as $H/2$ as only two folds are formed. The extent of the plastic area b_{01} and b_{02} along transverse direction may be obtained by minimising the total plastic energy E_p (Eq. 4.42) and resulting optimum value writes:

$$b_{opti} = \frac{1}{\sqrt{\pi}} H \sqrt{\frac{H}{t_f}} \approx 0.564 H \sqrt{\frac{H}{t_f}} \tag{4.43}$$

Note also that b_{opti} should not be larger than the distance b_1, respectively b_2, which are the distances between the rock apex and the edges of the floor along the transverse direction. Since the energy is dissipated by vertical crushing over the height H, the mean plastic force corresponds to the mean vertical reacting force F_V of the entire floor as :

$$F_V = F_P = \frac{E_P}{H} = \frac{1}{\sqrt{3}}\sigma_0 t_f H^2 \left(\frac{1}{b_{01}} + \frac{1}{b_{02}}\right) + \frac{\pi \sigma_0 t_f^2}{\sqrt{3}} \frac{b_{01} + b_{02}}{H} \tag{4.44}$$

Where b_{01} and b_{02} are given by:

$$\begin{cases} b_{01} = min\left(0.564 H \sqrt{\frac{H}{t_f}}\ ;\ b_1\right) \\ b_{02} = min\left(0.564 H \sqrt{\frac{H}{t_f}}\ ;\ b_2\right) \end{cases} \tag{4.45}$$

If we denote δ_V as the instantaneous vertical penetration of the rock into the floor - see Figure 4.17 - the instantaneous crushing force may be expressed as:

$$F_V = F_P = 4M_0 \frac{b_{01}+b_{02}}{H_f} \frac{1}{\sqrt{1-\left(1-\frac{\delta_V}{2H_f}\right)^2}} + 4N_0 H_f \left(\frac{1}{b_{01}}+\frac{1}{b_{02}}\right) \delta_V \tag{4.46}$$

Once the vertical resistant force is known, the longitudinal one F_L can be obtained from the ratio K_v given by Eq. 4.8 as $F_L = F_V/K_v$.

4.4.3 Numerical validation

With the aim to validate the simplified expressions derived above, various finite element simulations were performed. The finite element model set up to simulate the response of a transverse member impacted by a rock located between two girders is represented (without the mesh) in Figure 4.18. The main particulars of the modelled structure are displayed in Table 4.3.

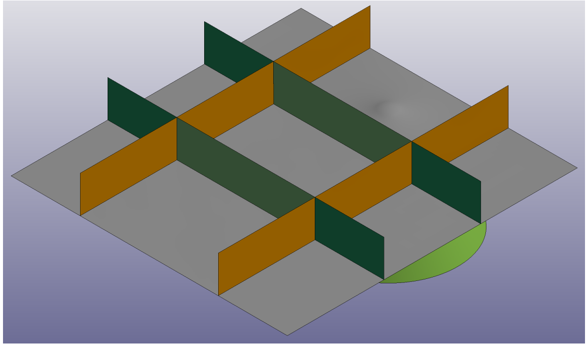

Figure 4.18: Floor impact - Finite element model

Item	Value (mm)
Outer hull thickness	15
Floor thickness	15
Girder thickness	20
Inner hull thickness	10
Height floor	1600
Floor spacing	4200
Girder spacing	6000

Table 4.3: Main characteristics

Since the energy absorbed by floor deformation does not depend on friction coefficient, only 12 scenarios (corresponding to the three rock shapes and four impact heights) are considered in this second validation. Resulting internal energies are compared in Table 4.4.

Case id	Rock id	H	Internal Energy Num. (kJ)	Internal Energy Ana. (kJ)	Deviation
25	1	0.3	340	302	11.1%
26	1	0.4	500	474	5.2%
27	1	0.5	660	649	1.6%
28	1	0.6	830	854	-2.8%
29	2	0.3	345	302	12.4%
30	2	0.4	485	474	2.3%
31	2	0.5	640	649	-1.4%
32	2	0.6	800	854	-6.7%
33	3	0.3	340	302	11.1%
34	3	0.4	500	474	5.2%
35	3	0.5	660	649	1.6%
36	3	0.6	830	854	-2.8%

Table 4.4: Floor internal energy comparison

From Table 4.4, it is observed that for a given penetration height, the floor internal energy does not vary much in relation to the rock shape. This confirms the point load assumption. Secondly, the analytical model generally tends to slightly underestimate the internal energy. Nevertheless, considering the 12 cases, the average discrepancy is around 5.4%. In Figure 4.19 compares analytical and numerical results together with the internal energies calculated from the expression proposed by *Simonsen* [11]. Since this later does not take into a account the extension due to the curvature imposed on the floor, the resulting absorbed energy is lower whatever the rock penetration.

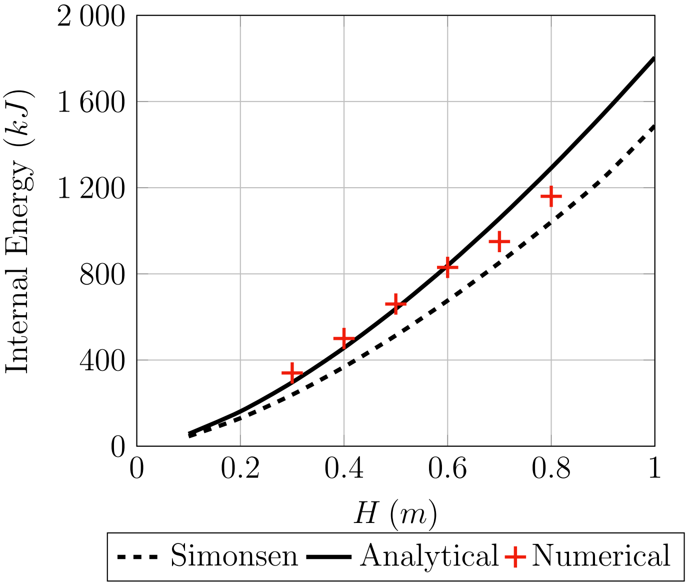

Figure 4.19: Floor internal energy comparison

4.5 Response of longitudinal girders

4.5.1 Literature review

The third and last structural component to be investigated are the longitudinal girders. Unlike the response of transverse floors, the girders in ship grounding behave differently than horizontal frames (like decks or stringers) in ship-ship collision.

In ship-ship collision, horizontal frame is crushed and its response is similar to the one of a transverse floor in grounding. However, in a grounding situation, the bottom girder is crushed vertically and the developed fold switches from one side to another thus forming a wave-like pattern as the ship moves along the surge direction. Figure 4.20 illustrates the crushing and wave-like pattern undergone by a longitudinal girder.

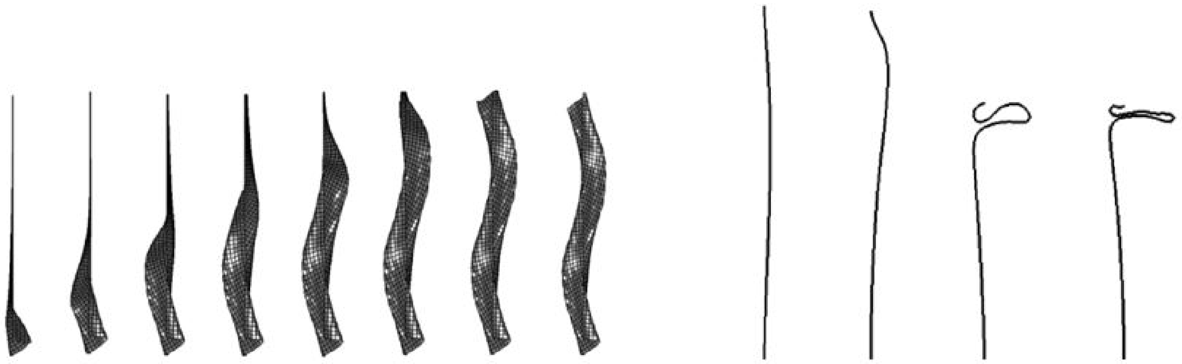

Figure 4.20: Web girder wave pattern deformation - From *Hong & Amdahl* [112]

Various authors proposed theoretical models for the response of longitudinal girders in ship grounding. Assuming that the only significant energy dissipation process comes from shearing, *Simonsen* [11] proposed a theoretical model based on the global deformation of the hull. A few years later, finite element simulations performed by *Hong & Amdahl* [112] and *Yu et al.* [124] demonstrated that the bending deformation may also have a significant contribution in the energy absorption process, especially when the penetration of the rock into the ship bottom remains moderate.

In the simplified model proposed by *Hong & Amdahl* [112], shearing, membrane stretching and bending deformations were considered. The wave periodicity was shown to mainly depend on both the contact angle α (between the rock and the bottom plating) and the vertical penetration H. Such conclusions were drawn from finite element simulations in which only the girders were represented. In other words, the influence of the transverse floors was not considered. This effect was latter investigated numerically by *Yu et al.* [124]. The authors concluded that although the periodicity tends to decrease when α increases, it remains almost constant and close to the gap between two adjacent transverse floors.

4.5.2 Analytical developments

Based on the observation of numerical simulations including both girders and floors, a slightly different folding mechanism illustrated by Figure 4.21 is proposed in the present section. The analytical model considers bending, shearing and transverse stretching deformations.

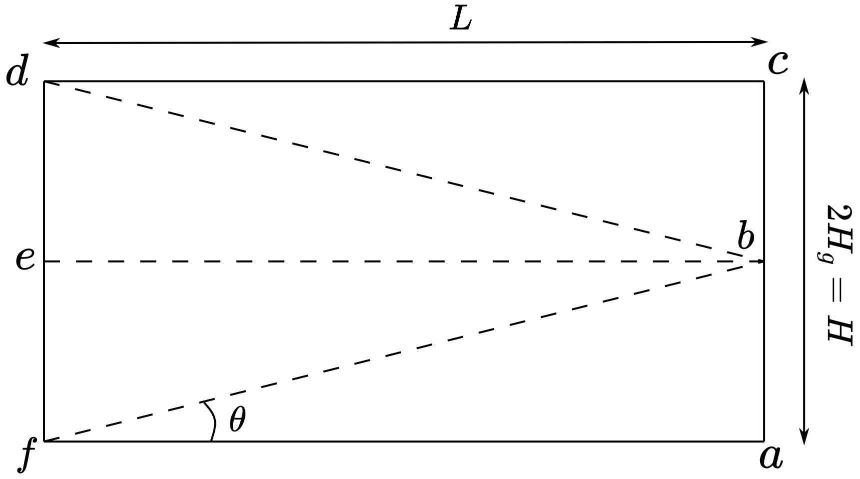

Figure 4.21: Girder paper folding deformation mechanism

First, the triangle abf is bent over the diagonal bf. Then, the rectangle $bcde$ is bent over the dashed line eb and finally the triangle bcd line is bent over the diagonal bd. It should be noted that af and cd lines are bent to the two sides of the rectangle. After the folding process, points a and c, respectively overlap with points d and f.

Figure 4.22 illustrates the straining mechanism between two adjacent folding waves. Point a from the first wave and point f_2 from the second are in connection at the bottom. Since no rupture is supposed to occur, the gap bae_2 has to accommodate. Junction between b and e_2 is supposed to appear at point g.

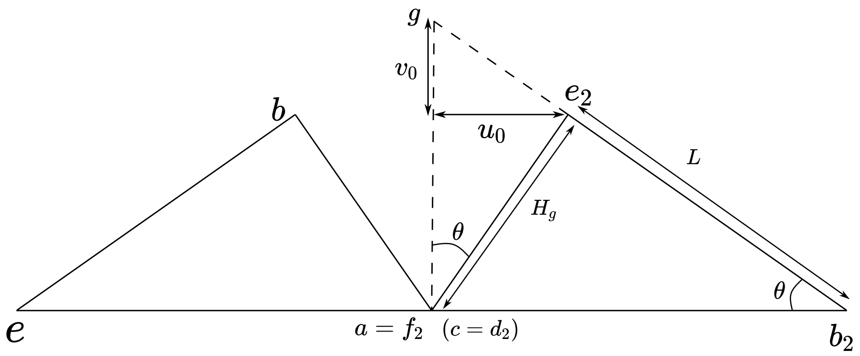

Figure 4.22: Girder connection between two adjacent folding waves

From geometrical considerations, one can write:

$$tan(\theta) = \frac{H_g}{L} \tag{4.47}$$

In plane displacement fields u_0 and v_0 are then given by:

$$u_0 = H_g sin(\theta) \tag{4.48}$$

$$v_0 = u_0 tan(\theta) \tag{4.49}$$

From these displacement fields, membrane strain components may be calculated as:

$$\begin{cases} \varepsilon_x = 0 \\ \varepsilon_y = \frac{\partial v}{\partial y} = \frac{v_0}{H_g} \\ \varepsilon_{xy} = \frac{1}{2}\frac{\partial u}{\partial y} = \frac{1}{2}\frac{u_0}{H_g} \end{cases} \tag{4.50}$$

Finally, the rate of energy absorbed by membrane deformation of the rectangle *acdf* is obtained from Eq. 2.22. The integration, performed over the deformed region $H_g L/2$ (see Figure 4.21) and considering the symmetries, leads to the following expression:

$$\dot{E}_m = 2N_0 V_x \sqrt{v_0^2 + \frac{1}{4}u_0^2} = N_0 V_x H sin(\theta)\sqrt{\frac{1}{4} + tan^2(\theta)} \tag{4.51}$$

As for the bending energy rate, it is obtained by considering the bending of the successive hinge lines:

$$\dot{E}_b = 2\pi \left(1 + \sqrt{1 + tan^2(\theta)}\right) M_0 V_x \tag{4.52}$$

The last remaining unknown is the angle θ or the length L. A first attempt would be to minimise Eq. 4.52 with respect to θ. However, this may lead to $\theta = 0$. Another way such as proposed by *Hong & Amdahl* [112] consists in deriving an empirical law from the experiment. Nevertheless, according to *Yu et al.* [124], the periodicity appears to be almost constant and equal to the gap χ_t between two adjacent transverse floors. Therefore one can write:

$$L = \frac{\chi_t}{4} \tag{4.53}$$

The plastic force associated to this deformation mode is obtained by dividing the total plastic energy rate by the surge velocity V_x:

$$F_P = \frac{\dot{E}_m + \dot{E}_b}{V_x} = 2M_0\pi \left(1 + \sqrt{1 + tan^2(\theta)}\right) + N_0 H sin(\theta)\sqrt{\frac{1}{4} + tan^2(\theta)} \tag{4.54}$$

Once the plastic resistant force has been obtained, longitudinal and vertical components F_L and F_V may be deduced from Eqs. 4.7 and 4.8.

In addition to the girder wave deformation pattern, when an intersecting floor is pushed upwards by the rock, the girder deformation mode should switch to the so-called *intersection* mode which will be detailed hereafter.

Aforementioned authors did not consider this effect but supposed that the response of the girder remains the same. Nevertheless, a closer look to the internal energy dissipated through plastic deformation clearly shows a change in behaviour. Figure 4.23 illustrates the evolution of the absorbed energy versus the longitudinal crushing distance δ post-processed from numerical simulation. Dashed red lines correspond to the instant when the rock enters in contact with a transverse floor, while dashed blue lines correspond to the instant when the rock is no longer in contact with the floor. Whereas the steady state process appears to dissipate around 10% of the energy over 1 m, the presence of one floor has the effect of dissipating around 20 % of energy over the same distance, indicating a changes in the deformation process of the longitudinal girder.

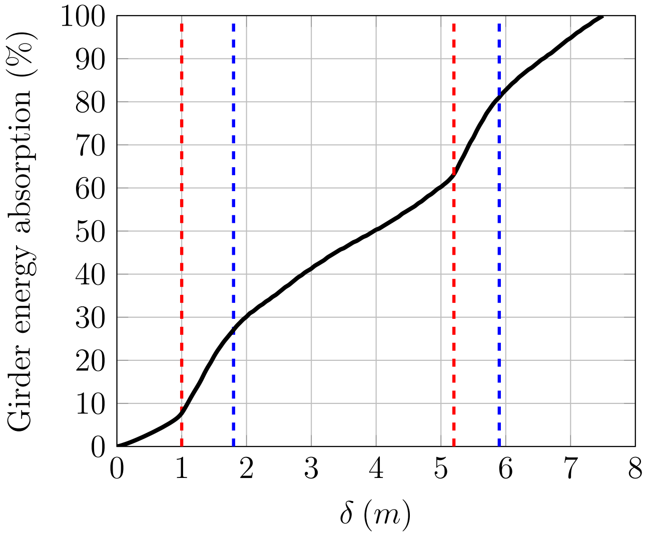

Figure 4.23: Energy dissipated by longitudinal girder retrieved from numerical simulation

4.5.2.1 Response at the intersection between a girder and a floor

Let us now consider a floor/girder intersection that is pushed upwards by the rock. As observed in the numerical simulations, a strong interaction exists between the deformation mechanisms of the intersected floor and girder so the previous analytical solutions no longer hold.In this thesis the, the model derived by *Zhang* [37] for intersection in ship-ship collision is considered. The energy absorbed during axial crushing of the intersection is given by:

$$E = 2\sigma_0 t_h \left(1.8138 t_h b + 1.4896 \frac{H^2}{4} + 1.5396 \frac{H^3}{4} \frac{1}{2b - KH}\right) \tag{4.55}$$

The transverse extent of the damaged area b is found by minimising Eq. 4.55, which yields the following expression: $b = min\left(\frac{K}{2}H + 0.3258H\sqrt{\frac{H}{t_h}}\ ,\ b_1\right)$ where $K = 0.5733$

Since the energy is dissipated through the work of a vertical force, resulting plastic vertical force may be written as:

$$F_P = F_V = \frac{E}{H} = \frac{2\sigma_0 t_f \left(1.8138 t_f b + 1.4896 \frac{H^2}{4} + 1.5396 \frac{H^3}{4} \frac{1}{2b-KH}\right)}{H} \tag{4.56}$$

Finally, the longitudinal force F_L is obtained as : $F_L = F_V / K_v$. Equation 4.55 applies for both the transverse floors and longitudinal girders.

4.5.3 Numerical validation

With the aim to validate the previous analytical developments, the simplified formulations were compared to a series of numerical simulations. The structure shown in Figure 4.24 together with characteristics listed in Table 4.3 have been considered for the numerical model. As the girders are $20mm$ thick, a proportionality factor λ of 0.76 is obtained from Eq. 4.28 was used in the analytical model.

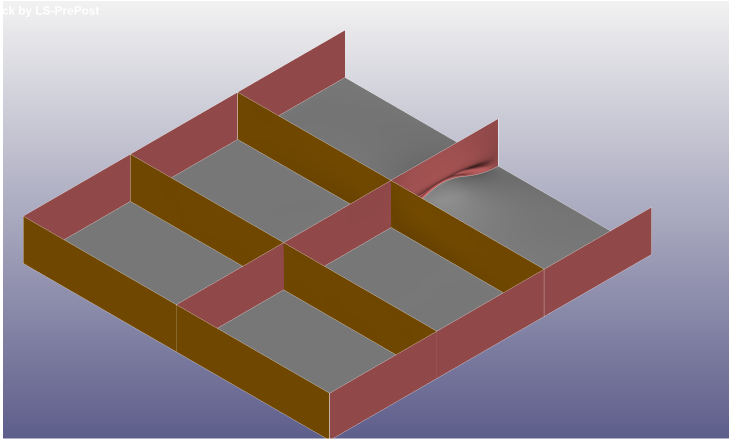

Figure 4.24: Finite element model (without the mesh)

Three different rocks, two friction coefficients and four impact heights are investigated. Nevertheless, since the plastic energy dissipated by a longitudinal girder does not depend on the friction coefficients μ, only 12 scenarios were simulated as resumed in Table 4.5.

Case id	Rock id	H	Internal Energy Num. (MJ)	Internal Energy Ana. (MJ)	Deviation Energy
61	1	0.3	4.2	3.8	8.7%
62	1	0.4	5.0	5.0	-0.5%
63	1	0.5	6.1	6.5	-6.8%
64	1	0.6	6.9	8.3	-20.5%
65	2	0.3	4.7	4.1	13.5%
66	2	0.4	5.3	5.3	-0.3%
67	2	0.5	6.5	6.9	-6.4%
68	2	0.6	7.2	8.9	-23.2%
69	3	0.3	5.3	4.3	19.6%
70	3	0.4	6.0	5.6	5.8%
71	3	0.5	7.0	7.5	-7.0%
72	3	0.6	7.9	9.7	-23.3%
72	3	0.6	7.9	9.7	-23.3%

Table 4.5: Girder internal energy comparison

The analysis of Table 4.5 reveals that the amount of energy dissipated by the longitudinal girder increases with the rock parameters (C, E) and penetration height. For a vertical penetration of $H = 0.6\,m$, the discrepancy between numerical and analytical results exceeds 20% whatever the rock shape. Such discrepancy may be explained as follows:

1. It is observed in the numerical simulation that only three half-waves (instead of four) are formed for this configuration. By changing $L = \chi_t/3$ in Eq. 4.53, the deviation for cases 64, 68 and 72 drops below 13%.

2. The numerical simulation also shows that both the longitudinal girder and the inner bottom undergo a global vertical motion. This indicates the presence of global bending deformation.

Further analytical developments should consider the gap between transverse floors since the latter behave as a boundary condition regarding the initiation and ending of the wave folding pattern. In addition a global bending mechanism may be derived following the work of *Buldgen* [94]. Anyway, despite some imperfections, one can conclude the proposed analytical model allows for an adequate representation of the girder crushing process.

4.6 Overall double hull

Now that the elementary responses of bottom plating, transverse floors and longitudinal girders have been individually validated, the next step focused on validating the proposed theoretical model on a full ship bottom section.

4.6.1 Impact between two longitudinal girders

Starting with the response of bottom and floors, the stiffened hull structure presented in Figure 4.18 together with the characteristics listed in Table 4.3 were considered. The same 24 grounding scenarios defined from the 3 different rock shapes, the 2 friction coefficients and the 4 penetration heights were simulated.

As the distance between the rock and the next floor decreases, the outer shell plating located in front of the rock tends to be more and more constrained. At a certain distance (a_{crit}) from the floor, Eq. 4.13 cannot be satisfied anymore ($p > 1$). A *critical* distance is then defined as:

$$a_{crit} = \frac{H + Ca_0^2}{2Ca_0} \tag{4.57}$$

As soon as the distance a_1 between the rock tip and the next floor becomes lower than a_{crit}, the displacement field in front of the rock is simply taken as a straight line defined by the function :

$$f_1(x) = \frac{H - Ca_{0(t-1)}^2}{a_{0(t-1)} - a_1}(x - a) \tag{4.58}$$

Where a is the length of the bottom plating. The new distance a_0 is thus given by:

$$a_0(t) = \frac{-K_1 + \sqrt{K_1^2 + 4C(H + K_1 a_1)}}{2C} \tag{4.59}$$

With $K_1 = \frac{H - Ca_{0(t-1)}^2}{a_{0(t-1)} - a_1}$.

The distance a_0 is therefore determined through a step-by-step process, as illustrated in Figures 4.25a and 4.25b.

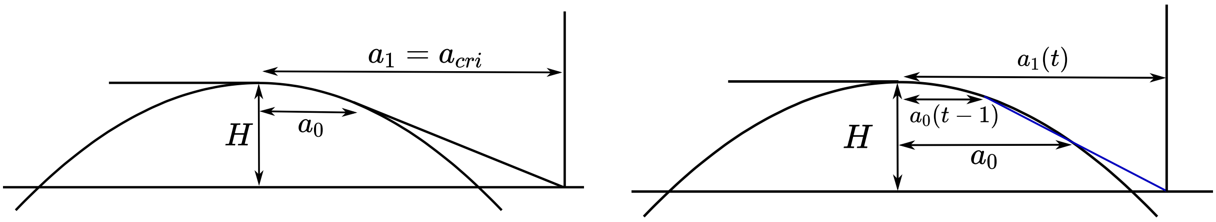

(a) a_0 Step 1

(b) a_0 Step 2

Figure 4.25: Calculation of a_0 near a transverse floor

When the floor is impacted by the rock, the contact pressure is assumed to be maximum under the floor and its unsymmetrical distribution is similar to the one depicted in Figure 4.2b. Therefore, a_0 is taken as the distance between the rock tip and the impacted floor position, while a_1 refers to the distance between the rock tip and the next floor - see Figure 4.26.

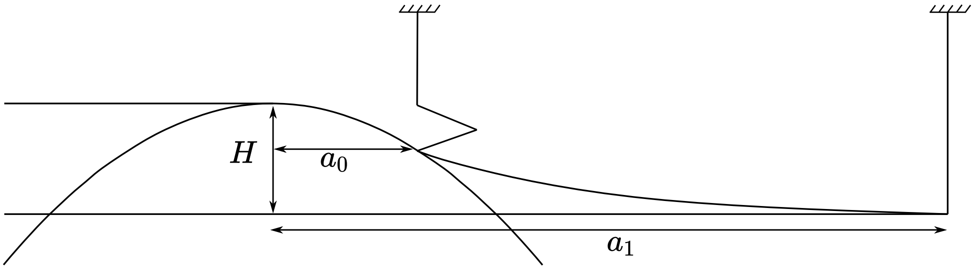

Figure 4.26: Bottom displacement field when a floor is impacted

Table 4.6 lists the energies post-processed from analytical and numerical simulations of the 24 scenarios (Cases 37 to 60). Longitudinal and vertical resisting forces versus crushing distance obtained for the scenario 43 are compared in Figure 4.27. Note that the crushing distance corresponds to the longitudinal displacement of the ship bottom with respect to the rock.

Case id	Rock id	H	μ	Bottom Num. (MJ)	Floor Num. (MJ)	Sliding Num. (MJ)	Total Num. (MJ)	Bottom Ana. (MJ)	Floor Ana. (MJ)	Sliding Ana. (MJ)	Total Ana. (MJ)	Dev. Bottom	Dev. Floor	Dev. Sliding	Dev. Total
37	1	0.3	0.3	2.0	0.6	4.8	7.4	2.0	0.6	4.3	7.0	-1.2%	6.5%	9.6%	6.4%
38	1	0.4	0.3	3.3	0.9	6.7	10.9	3.3	0.9	6.1	10.3	-0.3%	-0.6%	8.9%	5.3%
39	1	0.5	0.3	4.7	1.2	8.6	14.4	4.9	1.3	8.0	14.2	-3.9%	-9.2%	6.4%	1.7%
40	1	0.6	0.3	6.4	1.5	10.7	18.6	6.7	1.7	10.1	18.5	-4.6%	-13.7%	5.3%	0.4%
41	2	0.3	0.3	2.5	0.6	4.4	7.6	2.3	0.6	3.9	6.8	9.0%	4.7%	12.2%	10.5%
42	2	0.4	0.3	3.9	0.9	6.0	10.9	3.7	0.9	5.4	10.1	6.7%	-5.3%	9.8%	7.5%
43	2	0.5	0.3	5.8	1.2	8.0	15.0	5.3	1.3	7.2	13.8	7.5%	-8.2%	10.1%	7.6%
44	2	0.6	0.3	7.7	1.5	10.0	19.2	7.3	1.7	9.1	18.1	5.8%	-13.1%	8.4%	5.7%
45	3	0.3	0.3	3.5	0.6	4.3	8.4	2.8	0.6	3.5	6.9	20.6%	5.5%	17.8%	18.0%
46	3	0.4	0.3	5.3	0.9	5.9	12.2	4.3	0.9	5.0	10.2	19.1%	-1.9%	16.4%	16.2%
47*	3	0.5	0.3	7.8	1.3	8.1	17.1	6.1	1.3	6.6	14.1	21.3%	-4.0%	17.8%	17.8%
48*	3	0.6	0.3	10.4	1.6	10.2	22.2	8.3	1.7	8.5	18.5	20.5%	-7.4%	16.5%	16.6%
49	1	0.3	0.1	2.0	0.6	1.6	4.2	2.0	0.6	1.3	3.9	-2.2%	5.3%	18.7%	6.8%
50	1	0.4	0.1	3.2	0.9	2.1	6.3	3.3	0.9	1.8	6.0	-2.2%	-1.7%	16.6%	4.3%
51	1	0.5	0.1	4.6	1.2	2.7	8.5	4.9	1.3	2.3	8.5	-6.1%	-10.5%	15.2%	0.2%
52	1	0.6	0.1	6.3	1.5	3.4	11.2	6.7	1.7	2.9	11.3	-6.3%	-13.7%	15.0%	-0.7%
53	2	0.3	0.1	2.5	0.6	1.4	4.5	2.3	0.6	1.1	4.0	7.6%	3.8%	19.4%	10.7%
54	2	0.4	0.1	3.8	0.9	1.9	6.6	3.7	0.9	1.6	6.2	4.5%	-6.7%	18.8%	7.1%
55	2	0.5	0.1	5.6	1.2	2.6	9.4	5.3	1.3	2.0	8.7	5.6%	-10.0%	20.4%	7.7%
56	2	0.6	0.1	7.5	1.5	3.2	12.2	7.3	1.7	2.5	11.5	3.3%	-15.4%	19.9%	5.3%
57	3	0.3	0.1	3.4	0.6	1.3	5.3	2.8	0.6	1.0	4.3	18.3%	3.7%	25.7%	18.5%
58	3	0.4	0.1	5.1	0.9	1.8	7.9	4.3	0.9	1.4	6.6	16.3%	-3.9%	26.0%	16.3%
59*	3	0.5	0.1	7.5	1.2	2.5	11.2	6.1	1.3	1.8	9.2	18.0%	-6.6%	27.6%	17.4%
60*	3	0.6	0.1	10.0	1.6	3.1	14.6	8.3	1.7	2.3	12.2	17.0%	-10.2%	27.6%	16.4%

Table 4.6: Comparison dissipated energy - Impact between girder

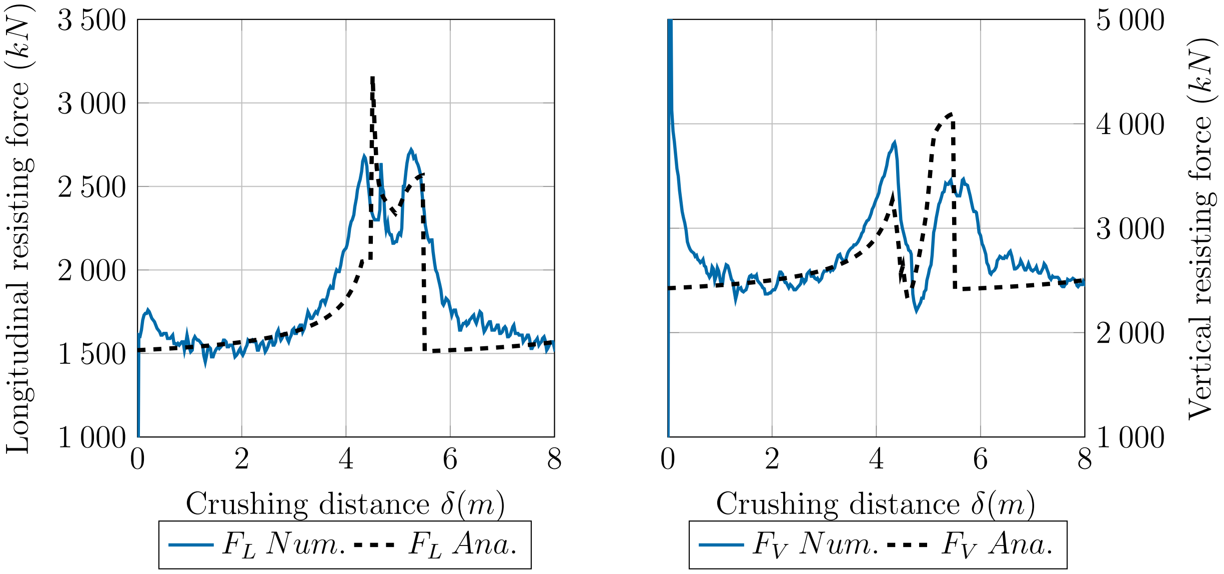

Figure 4.27: Comparison of longitudinal and vertical resisting forces for scenario 43

The major discrepancies observed in Table 4.6 are related to the sliding energy, especially when the structure grounds over the sharpest rock, i.e., rock n°3. The proposed model systematically underestimates the energy dissipated by friction. Several reasons might explain such deviations:

1. First of all, the deviation cannot be attributed to the choice of a_0. Indeed, considering the scenario 47 from Table 4.6 for instance, the average ratio K_v (i.e. when the rock is located between two successive floors) given by numerical and analytical models are 1.3 and 1.28 respectively. It is rather related to the treatment of the transverse floor impact. In fact, when a floor begins to deform, the contact pressure is assumed to be maximum just under the floor and zero at the rock's apex. In reality, the pressure distribution under the floor is more complex and the angle α given by Eq. 4.9 is probably overestimated. As already mentioned, the pressure distribution affects by up to 100% the final results - see *Turgeon* [18].

2. Second, in the analytical model, once the floor has been vertically crushed over a height H, it is assumed that only the bottom plating continues to dissipate energy. As a result, the resistant force drops abruptly (see Figure 4.27), while the numerical simulation shows a slow decrease until the steady state is reached. That is also a reason why the analytical model generally underestimates the overall dissipated energy. Moreover, the numerical simulations have shown that just before the rock enters in contact with the transverse floor, buckling of this latter occurs and stresses inside the bottom suddenly release, explaining the drop of the numerical curve at $4.3m$ - see Figure 4.27 (left). However, such buckling is not considered in the analytical model.

3. Finally, the deformation mechanisms considered when deriving the energy rates seem to work better with wide than sharp rocks. No doubt that the proposed model should be further improved to better capture the bottom response when it is impacted by a sharp rock.

Anyway from Table 4.6, it can be seen that the deviation on the total dissipated energy does not exceed 20%. All in all, the average discrepancies for bottom plating, transverse floor, sliding and total energies are respectively 9.5%, 7.2%, 16.2 % and 9.4%. Figures 4.28a and 4.28b show how the dissipated energy is distributed, respectively when $\mu = 0.3$ (cases 37-48) and $\mu = 0.1$ (cases 49-60). It appears that whatever the friction coefficient, the energy dissipated through deformation of transverse floors remains less than 13% of the total energy. Similar conclusions were drawn by *Heinvee* [20] on the contribution of the floors in the dissipation process. As expected, the share of sliding energy increases with the friction coefficient. Note that when $\mu = 0.3$, more than half of the energy is dissipated through friction between the rock and the bottom plating.

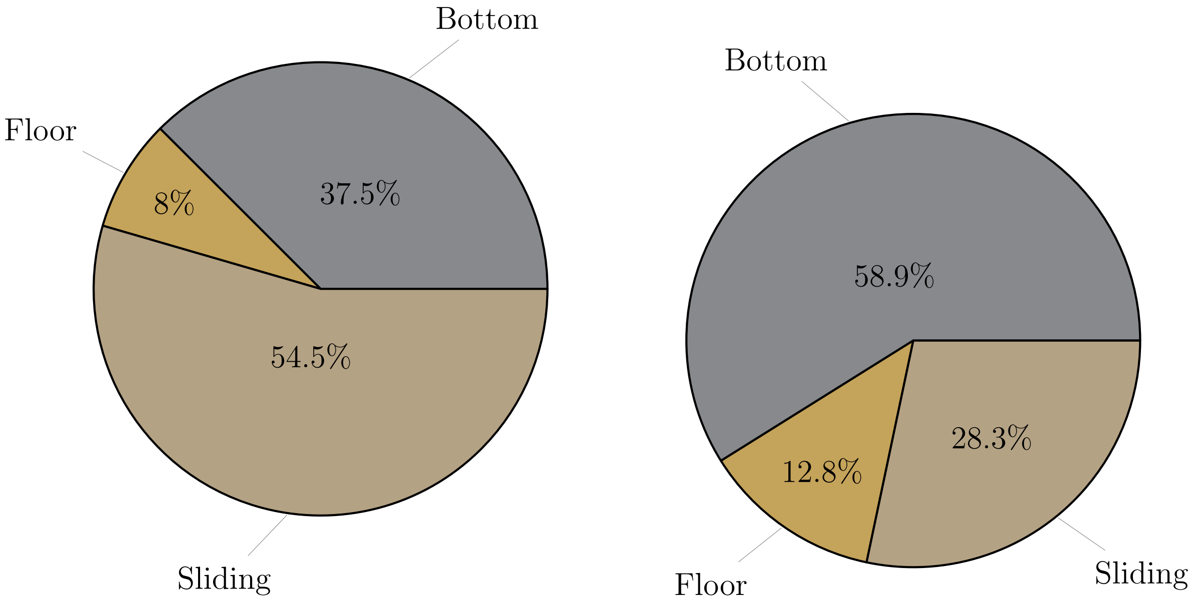

(a) $\mu = 0.3$ (b) $\mu = 0.1$

Figure 4.28: Energy distribution for an impact between two girders

4.6.2 Impact under a longitudinal girder

With the aim of validating the analytical expressions giving the resistance of the bottom plating, floors and girders, let us consider the grounding scenario and the stiffened hull structure depicted in Figure 4.24. Here, the outer shell is supposed to ground on the rock just below a girder. Resulting bottom, floor and girder internal energies are compared in Table 4.7 while sliding and total dissipated energies are confronted in Table 4.8.

Case id	Rock id	H	μ	Bottom Num. (MJ)	Floor Num. (MJ)	Girder Num. (MJ)	Bottom Ana. (MJ)	Floor Ana. (MJ)	Girder Ana. (MJ)	Dev. Bottom	Dev. Floor	Dev. Girder
61	1	0.3	0.3	3.3	1.1	4.2	3.1	0.9	3.8	6.0%	17.6%	8.7%
62	1	0.4	0.3	4.7	1.6	5.0	4.8	1.5	5.0	-2.6%	8.9%	-0.5%
63	1	0.5	0.3	6.7	2.1	6.1	6.8	2.2	6.5	-2.3%	-1.5%	-6.8%
64	1	0.6	0.3	8.4	2.6	6.9	9.1	3.0	8.3	-8.8%	-17.4%	-20.5%
65	2	0.3	0.3	4.3	1.0	4.7	3.8	0.9	4.1	10.8%	8.4%	13.5%
66	2	0.4	0.3	6.2	1.4	5.3	5.9	1.5	5.3	5.0%	-2.1%	-0.3%
67	2	0.5	0.3	8.7	2.0	6.5	8.2	2.2	6.9	5.4%	-10.2%	-6.4%
68	2	0.6	0.3	11.1	2.5	7.2	10.9	3.0	8.9	1.5%	-20.8%	-23.2%
69	3	0.3	0.3	6.4	0.9	5.3	5.2	0.9	4.3	18.7%	6.0%	19.6%
70	3	0.4	0.3	9.1	1.4	6.0	7.9	1.5	5.6	13.0%	-6.4%	5.8%
71	3	0.5	0.3	12.7	1.9	7.0	11.0	2.2	7.5	13.3%	-17.5%	-7.0%
72	3	0.6	0.3	16.0	2.4	7.9	14.5	3.0	9.7	9.4%	-25.3%	-23.3%
73	1	0.3	0.1	3.1	1.1	4.2	3.1	0.9	3.8	0.9%	19.2%	9.0%
74	1	0.4	0.1	4.5	1.6	5.0	4.8	1.5	5.0	-7.9%	7.8%	-1.5%
75	1	0.5	0.1	6.1	2.2	5.9	6.8	2.2	6.5	-11.5%	-0.6%	-10.3%
76	1	0.6	0.1	7.8	2.6	6.0	9.1	3.0	8.3	-17.6%	-17.4%	-38.4%
77	2	0.3	0.1	4.1	0.9	4.7	3.8	0.9	4.1	6.0%	7.7%	13.1%
78	2	0.4	0.1	5.7	1.5	5.3	5.9	1.5	5.3	-2.7%	0.0%	-0.5%
79	2	0.5	0.1	8.0	1.9	6.2	8.2	2.2	6.9	-3.4%	-11.9%	-12.0%
80	2	0.6	0.1	10.2	2.6	7.3	10.9	3.0	8.9	-7.2%	-16.6%	-23.0%
81	3	0.3	0.1	5.9	0.9	5.3	5.2	0.9	4.3	11.4%	3.2%	18.7%
82	3	0.4	0.1	8.3	1.4	5.9	7.9	1.5	5.6	5.3%	-5.7%	4.5%
83	3	0.5	0.1	11.6	1.9	6.9	11.0	2.2	7.5	5.1%	-16.8%	-8.1%
84	3	0.6	0.1	14.6	2.4	7.8	14.5	3.0	9.7	0.7%	-28.0%	-24.4%

Table 4.7: Comparison of internal energies - Impact below a girder

Case id	Rock id	H	μ	Sliding Num. (MJ)	Total Num. (MJ)	Sliding Ana. (MJ)	Total Ana. (MJ)	Dev. Sliding	Dev. Total
61	1	0.3	0.3	10.9	19.5	10.5	18.3	3.5%	5.8%
62	1	0.4	0.3	13.1	24.4	13.3	24.6	-1.7%	-1.0%
63	1	0.5	0.3	15.8	30.7	16.6	32.2	-5.4%	-4.7%
64	1	0.6	0.3	18.1	36.0	20.4	40.9	-12.7%	-13.7%
65	2	0.3	0.3	10.0	19.9	9.7	18.5	2.5%	7.2%
66	2	0.4	0.3	12.4	25.3	12.6	25.2	-1.6%	0.2%
67	2	0.5	0.3	15.4	32.6	15.9	33.3	-3.4%	-2.1%
68	2	0.6	0.3	18.1	38.9	19.8	42.6	-9.3%	-9.5%
69	3	0.3	0.3	10.0	22.6	9.3	19.6	6.5%	13.0%
70	3	0.4	0.3	12.6	29.1	12.4	27.4	1.3%	5.5%
71	3	0.5	0.3	15.9	37.4	16.4	37.0	-2.9%	1.1%
72	3	0.6	0.3	18.8	45.2	21.0	48.2	-11.2%	-6.8%
73	1	0.3	0.1	3.4	11.8	3.2	11.0	7.6%	7.4%
74	1	0.4	0.1	4.2	15.2	3.9	15.2	7.0%	-0.1%
75	1	0.5	0.1	4.9	19.1	4.7	20.2	4.3%	-5.8%
76	1	0.6	0.1	5.6	22.0	5.7	26.2	-1.2%	-19.1%
77	2	0.3	0.1	3.2	12.8	2.9	11.6	9.7%	9.6%
78	2	0.4	0.1	3.9	16.3	3.6	16.2	7.5%	0.6%
79	2	0.5	0.1	4.7	20.8	4.4	21.8	7.0%	-4.4%
80	2	0.6	0.1	5.6	25.6	5.3	28.2	4.2%	-10.2%
81	3	0.3	0.1	3.0	15.0	2.6	13.0	12.2%	13.6%
82	3	0.4	0.1	3.9	19.5	3.4	18.4	12.3%	5.7%
83	3	0.5	0.1	4.8	25.2	4.3	25.0	9.9%	0.8%
84	3	0.6	0.1	5.7	30.5	5.4	32.6	5.6%	-7.0%

Table 4.8: Comparison of sliding and total energies - Impact below a girder

Except from rare cases, it is observed that the proposed model allows for a good prediction of both sliding and total dissipated energies. Among the 24 scenarios, average discrepancies are 5.7 % , 11.5 %, 12.0 % and 6.6 % for bottom, floors, girder and sliding respectively. It is also worth noting that due to the fineness of the mesh, the computational time of one *Ls-Dyna* simulation is around 27 hours[1], while the analytical model provides results in less than 4 seconds.

For illustration purpose, the evolution of numerical and analytical energies with respect to the crushing length δ is plotted on Figure 4.29 for case 67. It is observed that the energy absorbed by the bottom plating deformation varies almost linearly. On contrary, the curves related to the girder internal energy clearly illustrates the alternation between wave-like and girder-floor intersection mechanisms.

---

[1] Computation time obtained using 8 SMP thread on Intel Xeon CPU E5-2680 V4 at 2.88 GHz

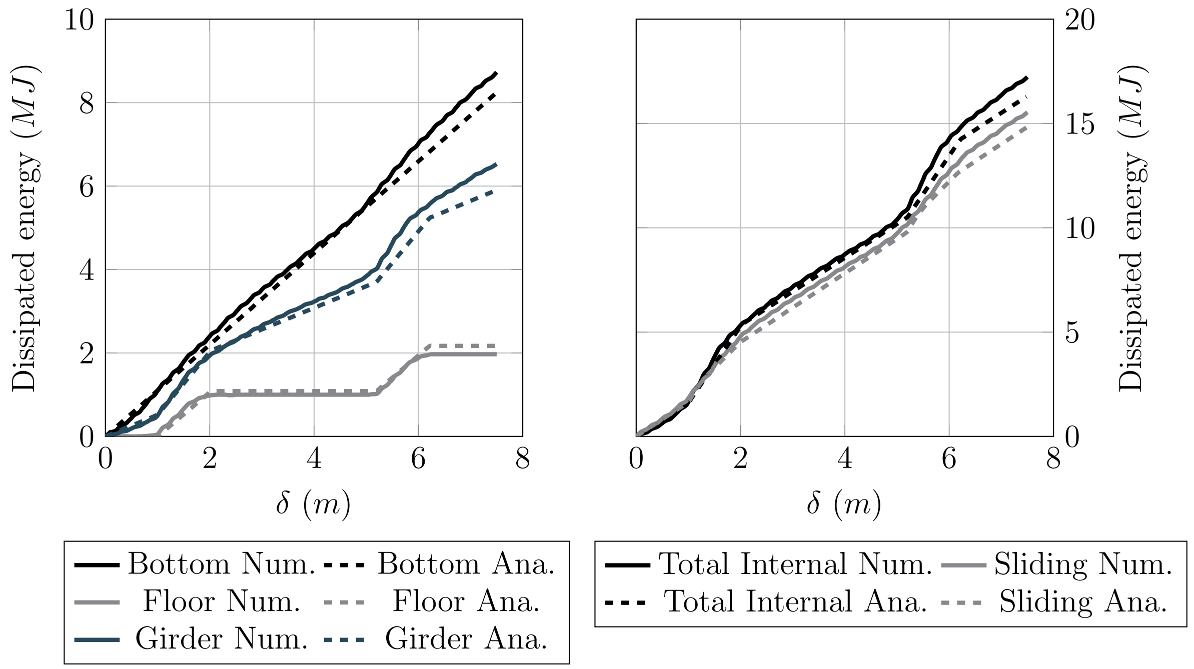

Figure 4.29: Comparison of dissipated energies scenario 67

The energy distributions obtained for $\mu = 0.3$ (cases 61-72) and $\mu = 0.1$ (cases 73-84) are depicted in Figures 4.30a and 4.30b respectively. It is seen that the energy dissipated by floor plastic deformation does not exceed 9% of the total dissipated energy. Note also that whatever the friction coefficient, girders and bottom contribute almost equally to the deformation energy. Finally, sliding forces contribute again significantly as almost half of the energy is dissipated by friction when $\mu = 0.3$.

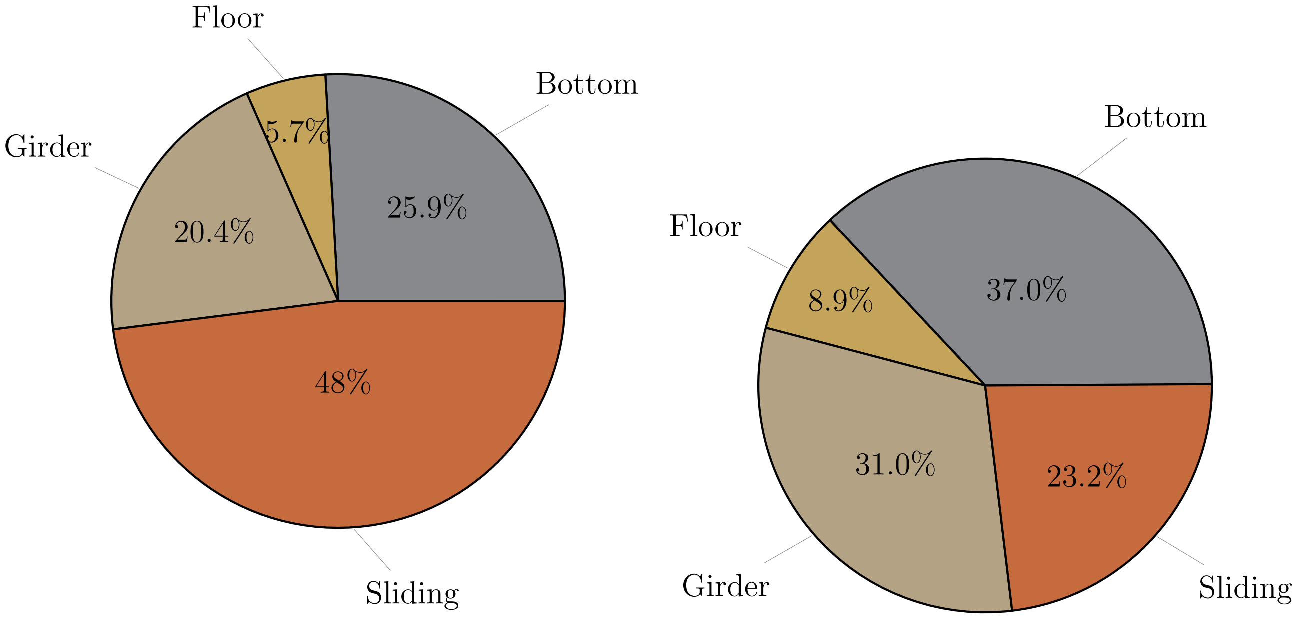

(a) $\mu = 0.3$

(b) $\mu = 0.1$

Figure 4.30: Energy distribution for an impact below a girder

4.7 Analysis considering a real rock

In this chapter, several analytical models have been derived to assess the response of a ship hull impacted by a paraboloid shaped rock and successfully confronted to finite element simulations. However, the real seabed is undoubtedly much more complex than a simple paraboloid shape.

In 2016, *Sormunen et al.* [145] succeeded in extracting real rock shapes from a sonar scan campaign carried out in the two busiest tanker harbours in Finland. Thanks to the data kindly provided by Prof. Hirdaris and Dr. Sang-Jin Kim from Aalto University, the study presented in this section aimed to compare finite element simulations of a ship grounding on such real rocks with the predictions given by the previously developed analytical model. Predictions provided by another model based on truncated pyramid shaped rocks will also be included in the comparison.

For this purpose, a smooth rock was selected from Sormunen's paper, it is illustrated in Figure 4.31.

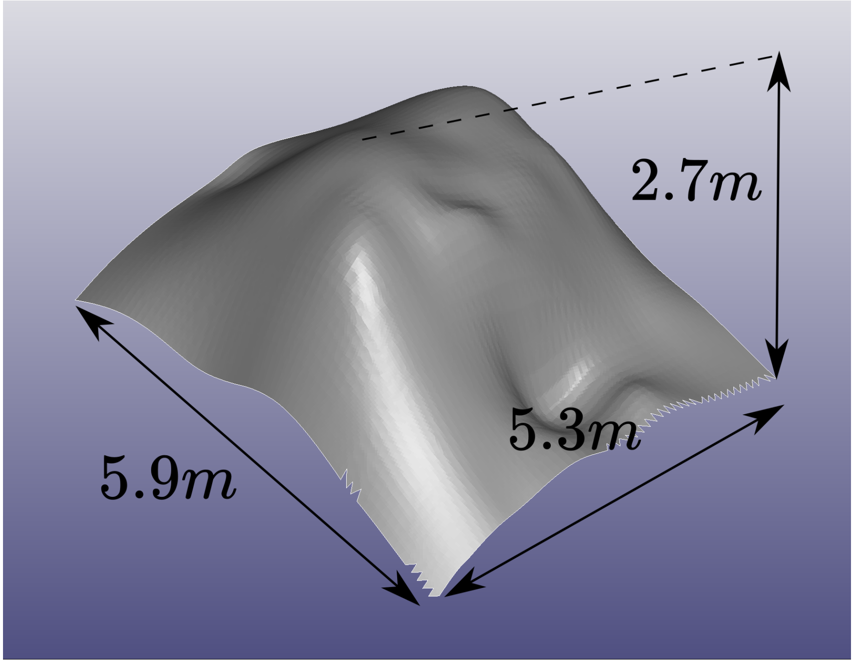

Figure 4.31: Smooth rock - from *Sormunen et al.* [145]

According to the literature, a large rock may be approximated as a truncated pyramid or a paraboloid. Thus, only these two shapes will be investigated for the smooth rock case. In the following subsections, *Para.* will refer to paraboloid shaped rock while *Trun.* will designate a truncated pyramid shape.

4.7.1 Rock approximation

First and foremost, the parameters defining the main dimensions of both paraboloid and truncated pyramid shaped rocks have to be determined. Regarding the paraboloid shape, coefficients $C = 0.4$ and $E = 0.36$ are found to give the best fit with the shape of the rock presented in Figure 4.31. As the truncated pyramid shape is concerned, the best fit is obtained taking a contact angle $\alpha = 60°$, a width of the shoulder $= 1.3m$ and a lateral angle $\beta = 40°$. All these values are resumed in Table 4.9 and illustrated on Figure 4.32 for the pyramid shape.

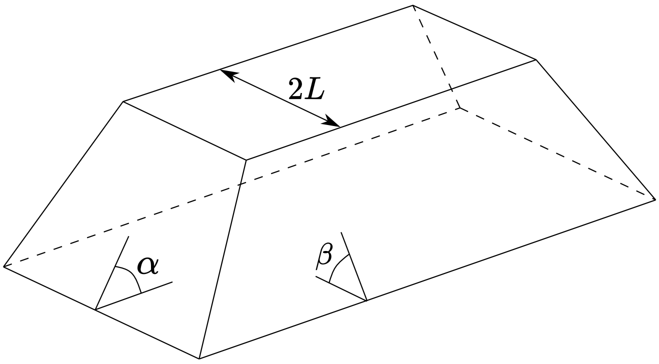

Figure 4.32: Pyramidal approximation and parameters

Parameters	Trun.	Para.
α	60°	-
$2L$	$1.3m$	-
β	40°	-
C	-	$0.4\ m^{-1}$
E	-	$0.36\ m^{-1}$

Table 4.9: Model parameters for the smooth real rock

4.7.2 Unstiffened bottom plating

At first instance, the response of a simple unstiffened bottom plating is discussed. The plate considered is $5.7m$ width, $13m$ long and $15mm$ thick and is meshed with $30mm$-sized shell elements. Numerical and analytical calculations based on either the developed model or the model proposed by Hong and Amdahl [19] are run considering four penetration heights in a range of $H \in [0.3;\ 0.6]\ m$ as well as two friction coefficients $\mu = 0.1$ and $\mu = 0.3$.

Longitudinal and vertical forces post-processed from numerical and analytical simulations are compared in Table 4.10.

Case id	H	μ	F_L Num. (MN)	F_V Num. (MN)	F_L Para. (MN)	F_V Para. (MN)	F_L Trun. (MN)	F_V Trun. (MN)	Dev. F_L Para.	Dev. F_V Para.	Dev. F_L Trun.	Dev. F_V Trun.
1	0.3	0.3	0.66	1.38	0.63	1.21	2.53	0.60	4%	13%	-286%	57%
2	0.4	0.3	1.09	2.00	0.93	1.67	3.21	0.76	14%	16%	-195%	62%
3	0.5	0.3	1.56	2.66	1.33	2.26	3.99	0.94	15%	15%	-155%	65%
4	0.6	0.3	2.07	3.17	1.79	2.90	4.78	1.13	13%	9%	-131%	64%
5	0.3	0.1	0.37	1.40	0.36	1.21	1.33	0.60	1%	14%	-263%	57%
6	0.4	0.1	0.62	2.00	0.55	1.67	1.68	0.76	12%	16%	-171%	62%
7	0.5	0.1	0.92	2.68	0.80	2.26	2.09	0.94	13%	16%	-126%	65%
8	0.6	0.1	1.31	3.34	1.10	2.90	2.51	1.13	16%	13%	-91%	66%

Table 4.10: Energies dissipated by a unstiffened plate sliding on a smooth rock

It is seen that the model based on a paraboloid shaped rock always underestimates both resisting force components but the highest deviation does not exceed 16 % and average discrepancies observed on F_L and F_V are respectively 11.2% and 14%. Second, the truncated pyramid model appears to overestimate the longitudinal force and underestimate the vertical one. Average discrepancies are much more significant (around 180% for F_L and 62% for F_V) and in some cases, the gap with numerical results rises to 285% for F_L

and 66% for F_V.

The share of deformation energy in the overall dissipated energy is illustrated in Figure 4.33. It appears that all models give similar results so the high deviations observed in Table 4.10 for the truncated pyramid model can not be attributed to a different distribution between sliding and deformation energies.

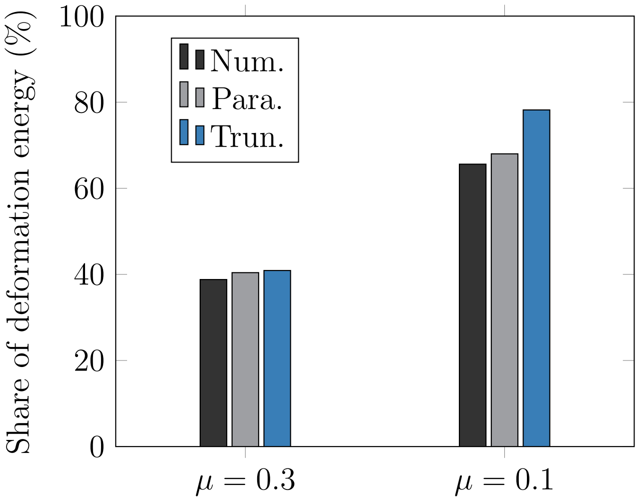

Figure 4.33: Share of deformation energy - smooth rock

However, since the prediction may greatly depend on the rock dimensions, a sensitivity analysis is performed by slightly varying (±20%) the dimensional parameters of both rocks. New dimensional values as well as variations of F_L and F_V are presented in Table 4.9, given that all simulations have been performed considering a friction coefficient $\mu = 0.3$.

	Parameters				Variation	
	Case	C	E	α	F_L	F_V
Paraboloid	-20%	0.32	0.288	-	4.6%	10.4%
	+20%	0.48	0.432	-	-3.1%	-7.6%
Pyramid	-20%	-	-	48°	-32.2%	35.5%
	+20%	-	-	72°	744%	19%

Table 4.11: Sensitivity of the resisting force to rock dimensional parameters

As far as the paraboloid rock is concerned, it is observed that the longitudinal force is almost insensitive to the change of rock dimensions, while the vertical one appears to be slightly more sensitive. All in all, resulting variations do not exceed 11%.

To define the truncated pyramid shape, three coefficients are needed. A first sensitivity analysis shows that the rock width $2L$ and the angle β influence the force prediction by only 1% and 10% respectively.

As shown in Table 4.11, the effect of angle α is much more pronounced. Indeed, increasing α by 20% causes a rise of F_L of 744%. Such huge and nonphysical increase comes from the factor g_f, which becomes infinite when $\alpha = 73.3°$. Consequently, with $\alpha = 72°$, the

g_f factor no longer makes sense. On the other hand, decreasing the contact angle by 20% yields a variation of the resistant force components by more than 30%.

To summarise, the truncated pyramid model appears to be extremely sensitive to the contact angle α, which constitutes its main limitation. Moreover, for the sliding cases studied in this thesis, the deviation from the numerical results is significant. On contrary, the model based on a paraboloid shaped rock seems to be more robust and correlates fairly well with numerical results.

Now that the response of a simple unstiffened plate has been discussed, let us check the paraboloid model on the response of full double bottom section impacted by the real smooth rock.

4.7.3 Double hull structure

The validation of the analytical model is performed considering the same double hull structure as the one presented in subsection 4.5.3. Two friction coefficients $\mu = 0.1$ and $\mu = 0.3$ combined with two penetration heights $H = 0.3m$ and $H = 0.6m$ are considered. Moreover, two impact locations are analysed: one between two longitudinal girders and one just under a girder. In total, the validation process involves 8 different scenarios.

Table 4.12 compare's the sliding and deformation energies retrieved from *Ls-Dyna* and analytical calculations. Cases 9 to 12 correspond to the impact between two longitudinal girders, while cases 13 to 16 are the cases where a girder is directly involved in the deformation process.

Case id	H	μ	Sliding Num. (MJ)	Int. Num. (MJ)	Total Num. (MJ)	Sliding Ana. (MJ)	Int. Ana. (MJ)	Total Ana. (MJ)	Dev. Sliding	Dev. Internal	Dev. Total
9	0.3	0.3	5.1	3.2	8.3	4.0	2.8	6.8	21%	12%	18%
10	0.6	0.3	10.5	8.8	19.3	9.5	8.7	18.2	10%	1%	6%
11	0.3	0.1	1.6	3.1	4.7	1.2	2.8	4.0	24%	10%	15%
12	0.6	0.1	3.2	8.5	11.8	2.7	8.7	11.4	17%	-2%	3%
13	0.3	0.3	11.2	9.5	20.7	10.2	8.4	18.6	9%	11%	10%
14	0.6	0.3	18.2	20.6	38.8	19.2	21.1	40.3	-6%	-2%	-4%
15	0.3	0.1	3.5	9.2	12.7	3.0	8.4	11.4	14%	9%	10%
16	0.6	0.1	5.7	19.4	25.1	5.2	21.1	26.3	8%	-9%	-5%

Table 4.12: Energies dissipated by a double bottom sliding on a smooth rock

The different results presented in Table 4.12 show that the highest discrepancies are observed on the sliding energy. In fact, the surface roughness of the real rock cannot be accurately captured by the simplified model as the later is based on a simplified smooth shape. Moreover, it seems unrealistic to consider such level of details in the analytical derivations. Finally, recalling that friction is very sensitive to the contact angle α, it is not surprising to observe some differences between numerical and analytical results. Nevertheless, the average discrepancies for sliding, internal and total dissipated energies are respectively 12.1%, 3.8% and 6.6%, indicating a surprisingly good performance of the analytical model.

4.7.4 Conclusion regarding the real rock shape

The response of a ship bottom sliding on a real smooth rock has been investigated and numerical simulations have been compared with two simplified models: the one developed in this thesis and one proposed by *Hong & Amdahl* [19], based on a truncated pyramid shaped rock.

The study demonstrates a surprising good performance of the paraboloid solution with an average deviation about 13%, while the model proposed by *Hong & Amdahl* [19] leads to an overestimation of around 120% (on average). Furthermore, a sensitivity analysis of the results has been conducted by slightly varying the rock particulars for each rock shape. The results obtained from the paraboloid model appears to vary only slightly with the dimensional parameters, indicating that the proposed formulation is quite robust. On contrary, the model based on a truncated pyramid shape appears to be very sensitive to the contact angle. Finally, although the model developed in this thesis does not account for the actual roughness of the rock and consequently underestimates the sliding energy, one can conclude that it seems to be a wise choice for rapidly assessing the resistant force of a ship hull sliding on a large smooth rock.

4.8 Impact on an inclined ship bottom or a bilge

Probabilistic damage stability analysis of a grounded ship requires to consider many grounding scenarios, varying ship velocity, rock shape, penetration depth and impact location. Consequently, some scenarios where the offset of the rock with respect to the ship's centerline is important have to be investigated. Such scenarios may lead either to the impact of a bilge if any or to inclined platind due to a significant roll motion of the ship. In such cases, the model developed in sections 4.3 to 4.5 for an horizontal bottom is no longer appropriate. To the author's knowledge, the literature dealing with inclined bottom grounding models is very scarce, not to say nonexistent. This section focuses on the derivation of an analytical model able to simulate the particular case of an inclined bilge-like inclined bottom under a sliding grounding scenario.

4.8.1 Response of bottom plating

First, let us consider a plate making an angle γ with the horizontal plan such as the one depicted in Figure 4.34. The rock apex (S) is situated on (b_R, H_R) in the reference frame $\mathcal{R}_1 = (O, \overrightarrow{Y}, \overrightarrow{Z})$.

Second, to simplify the analytical derivation, let us assume that a point M of the plate is only subjected to a displacement w perpendicular to its plane. In the second reference frame $\mathcal{R}_2 = (O, \overrightarrow{Y_P}, \overrightarrow{Z_P})$ associated to the inclined bottom plating, the out-of-plane displacement field is therefore $w(y_p)\overrightarrow{Z_P}$.

As for the horizontal bottom plating, the initial kinetic energy is supposed to be dissipated through the following mechanisms:

- Membrane straining
- Bending of transverse fibres
- Bending of longitudinal fibres
- Friction

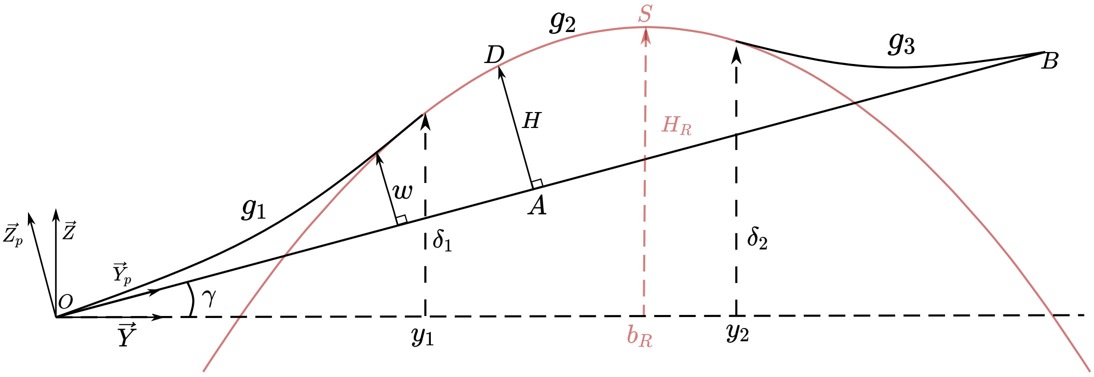

Figure 4.34: Inclined bottom plating - Displacement field

4.8.1.1 Membrane straining

Coming back to the frame $(O, \overrightarrow{Y}, \overrightarrow{Z})$, the plate displacement field $w(y)$ may be split into three different functions namely $g_1(y)$ for $y < y_1$, $g_2(y)$ for $y \in [y_1; y_2]$, and $g_3(y)$ for $y > y_2$.

For $y \in [y_1; y_2]$, the plate is supposed to take the shape of the rock so g_2 may be written as:

$$g_2(y) = H_R - E\left(y - b_R\right)^2 \tag{4.60}$$

The function g_1 has to comply with the following conditions:

$$\begin{cases} g_1(0) = 0 \\ \frac{\partial g_1}{\partial y}(0) = tan(\gamma) \\ g_1(y_1) = g_2(y_1) = \delta_1 \end{cases} \tag{4.61}$$

Taking g_1 as a second order polynomial function, one obtain:

$$g_1 = \delta_1 \left(\frac{y}{y_1}\right)^2 + tan(\gamma)y \tag{4.62}$$

$$\delta_1 = H_R - E\left(y_1 - b_R\right)^2 - tan(\gamma)y_1 \tag{4.63}$$

Denoting by $b = OB$ the width of the plate, the function g_3 must satisfy the following conditions:

$$\begin{cases} g_3(b) = bsin(\gamma) \\ \frac{\partial g_3}{\partial y}(b) = tan(\gamma) \\ g_3(y_3) = g_2(y_2) = \delta_2 \end{cases} \tag{4.64}$$

Following the same approach as for g_1, the function g_3 is thus defined as:

$$g_3(y) = \delta_2 \left(\frac{y - bcos(\gamma)}{y_2 - bcos(\gamma)}\right)^2 + tan(\gamma)y \tag{4.65}$$

$$\delta_2 = H_R - E\left(y_2 - b_R\right)^2 - tan(\gamma)y_2 \tag{4.66}$$

To complete the definitions of g_1, g_2 and g_3, the expressions of y_1 and y_2 are determined by writing the compatibility of the slopes between g_1 and g_2:

$$y_1 = \frac{2Eb_R^2 - 2H_R}{2Eb_R - tan(\gamma)} \tag{4.67}$$

and between g_2 and g_3:

$$y_2 = \frac{bsin(\gamma) - 2Eb_R(bcos(\gamma) - b_R) - 2H_R}{2E(b_R - bcos(\gamma)) - tan(\gamma)} \tag{4.68}$$

Finally, let us denote by D the first contact point between the ship bottom and the rock as illustrated by Figure 4.34. In the reference frame $\mathcal{R}_2$, we denote by b_1 the distance OA, by $b_2 = b - b_1$ the distance AB and by H the out-of-plane displacement of point D. H and b_1 are given by:

$$H = \left(H_R - b_R tan(\gamma) + \frac{tan(\gamma)^2}{4E}\right) cos(\gamma) \tag{4.69}$$

$$b_1 = \left(b_R - \frac{tan(\gamma)}{2E}\right) \frac{1}{cos(\gamma)} \tag{4.70}$$

Once functions g_1, g_2 and g_3 are known, the corresponding displacement fields $w_{i,i=1,2,3}$ are obtained by:

$$w_i(y_p) = (g_i(y_s) - tan(\gamma)y_s)\, cos(\gamma) \tag{4.71}$$

Where y_s is the solution of the following equation:

$$g_i(y_s) = -\frac{y_s}{tan(\gamma)} + \frac{y_p}{sin(\gamma)} \tag{4.72}$$

Solutions for the three displacement fields w_1, w_2 and w_3 are detailed in Appendix B.

Once the displacement fields are known, the elongations v_{01} and v_{02} of the transverse fibres may be calculated as :

$$v_{01} = \int_0^{b_1} \frac{1}{2} \left(\frac{\partial w}{\partial y_p}\right)^2 dy_p \tag{4.73}$$

$$v_{02} = \int_{b_1}^{b-b_1} \frac{1}{2} \left(\frac{\partial w}{\partial y_p}\right)^2 dy_p \tag{4.74}$$

For sake of clarity, resulting expressions of v_{01} and v_{02} are also given in Appendix B.
In a similar way to the case of a non-inclined plating, the longitudinal straining ε_{xx} is neglected, thus the non-zero strain components write:

$$\varepsilon_y = v_0 \frac{\partial \eta}{\partial y_p} \tag{4.75}$$

$$\varepsilon_{xy} = \frac{1}{2} u_0 \frac{\partial \eta}{\partial y_p} + \frac{1}{2} \frac{v_0}{a_1} \eta \tag{4.76}$$

Where η is defined as:

$$\eta(y_p) = \begin{cases} \left(\frac{y_p}{b_1}\right)^2 & if \quad y_p \leq b_1 \\ \\ \left(\frac{y_p-b}{b-b_1}\right)^2 & else \end{cases} \tag{4.77}$$

And where u_0 is still given by Eq. 4.15.

The energy rate related to the plate membrane deformation is finally obtained from Eq. 2.22. However, due to the inclination angle γ, deriving a closed-form solution gets very complicated so the membrane energy rate is preferably found by numerical integration of Eqs. 4.78 and 4.79.

$$\dot{E}_{m1} = \frac{2}{\sqrt{3}}\sigma_0 t_h V_x \frac{1}{b_1^2}\int_0^{b_1}\sqrt{4v_{01}^2 y_p^2 + y_p^2\left(u_0 + \frac{1}{2}\frac{v_{01}}{a_1}y_p\right)^2}\,dy_p \tag{4.78}$$

$$\dot{E}_{m2} = \frac{2}{\sqrt{3}}\sigma_0 t_h V_x \frac{1}{(b-b_1)^2}\int_{b_1-b}^{0}\sqrt{4v_{02}^2 y_p^2 + y_p^2\left(u_0 + \frac{1}{2}\frac{v_{02}}{a_1}y_p\right)^2}\,dy_p \tag{4.79}$$

Finally, the total membrane energy is the sum of the two previous contributions:

$$\dot{E}_m = \dot{E}_{m1} + \dot{E}_{m2} \tag{4.80}$$

4.8.1.2 Transverse bending

Transverse bending contribution might be calculated by the use of Eq. 4.18. Nonetheless doing so leads to cumbersome equations.For simplicity, the bending deformation of transverse fibres is supposed to concentrate on local plastic hinges (O, D, B). Plastic bending energy rate is thus expressed as:

$$\dot{E}_{bT} = 2M_0\left(\beta_1 + \beta_2\right)V_x \tag{4.81}$$

Where expressions of angles β_1 and β_2 are:

$$\beta_1 = atan\left(\frac{AD}{OA}\right) = atan\left(\frac{H}{b_1}\right) \tag{4.82}$$

$$\beta_2 = atan\left(\frac{AD}{AB}\right) = atan\left(\frac{H}{b-b_1}\right) \tag{4.83}$$

4.8.1.3 Longitudinal fibres bending

Longitudinal fibres located in front of the rock are still subject to a change of curvature. Based on Eq. 4.25, the resulting bending energy rate for the entire plate is given by:

$$\dot{E}_{bL} = M_0 V_x \frac{4}{3}\frac{b}{R_m} \tag{4.84}$$

4.8.1.4 Total plastic energy rate

The rate of total plastic energy absorbed by the inclined outer plating is finally obtained by summing the contributions given by Eqs. 4.80, 4.81 and 4.84:

$$\dot{E} = \dot{E}_m + \dot{E}_{bL} + \dot{E}_{bT} \tag{4.85}$$

As for the horizontal bottom, the plastic resistant force of the inclined structure F_P is deduced by dividing the total plastic energy rate $\dot{E}$ by V_x. It is worth noting that, unlike the case of horizontal plating, the transverse component F_T of the resistant force is not zero anymore.

Once F_P is known, longitudinal, transverse and vertical resisting force components can be determined using the following expressions:

$$\begin{cases} F_L = F_P g_f \\ \\ F_T = -tan(\gamma) F_V = -\frac{tan(\gamma)}{tan(\alpha)} F_P \\ \\ F_V = F_L K_v = \frac{1}{tan(\alpha)} F_P \end{cases} \tag{4.86}$$

Where the expressions of g_f and K_v are given by Eqs. 4.7 and 4.8 respectively. The definition of a_0 remains the same, i.e., $a_0 = \lambda R_x$. However, due to the inclination of the structure, the definition of R_x changes to:

$$R_x = \sqrt{\frac{H}{C}\frac{1}{cos(\gamma)}} \tag{4.87}$$

4.8.1.5 Numerical validation

To corroborate the analytical formulae previously derived, an inclined bottom or bilge plating is considered for validation with the following dimensions: length=16m, width=6m and thickness=15mm. Two inclination angles $\gamma = 15°$ and $\gamma = 30°$ as well as two friction coefficients $\mu = 0.3$ and $\mu = 0.1$ are considered. Simulating the impact of three different rocks leads to the 12 scenarios (Cases 85 to 96) listed in Table 4.13. In this table, the resistant forces F_L, F_T and F_V given by the theoretical model are compared to the mean values post-processed from the finite element simulations. The agreement is shown to be pretty good as discrepancies between numerical and analytical results do not exceed 10 %.

Scenario id	Rock id	γ	μ	H_R	b_R	F_L Num. (MN)	F_T Num. (MN)	F_V Num. (MN)	F_L Ana. (MN)	F_T Ana. (MN)	F_V Ana. (MN)	Dev. F_L	Dev. F_T	Dev. F_V
85	1	15	0.1	1.7	3.5	2.1	-1.3	5.3	2.0	-1.4	5.1	4.3%	-4.8%	4.1%
86	1	15	0.3	1.7	3.5	3.4	-1.3	5.3	3.2	-1.4	5.1	4.8%	-4.8%	3.2%
87	1	30	0.1	2.4	3.5	1.1	-1.7	3.1	1.1	-1.8	3.1	-0.7%	-5.4%	-3.0%
88	1	30	0.3	2.4	3.5	1.9	-1.7	3.0	1.8	-1.8	3.1	2.9%	-6.6%	-4.7%
89	2	15	0.1	1.6	3.0	1.9	-1.1	4.0	1.7	-1.0	3.8	7.0%	4.7%	5.9%
90	2	15	0.3	1.6	3.0	2.9	-1.0	3.9	2.7	-1.0	3.8	5.2%	1.0%	3.5%
91	2	30	0.1	2.4	3.0	1.8	-2.0	3.7	1.7	-2.1	3.6	5.0%	-4.5%	2.1%
92	2	30	0.3	2.4	3.0	2.8	-2.0	3.6	2.7	-2.1	3.6	5.5%	-4.4%	-0.3%
93	3	15	0.1	1.3	3.0	1.0	-0.5	2.0	0.9	-0.5	1.8	7.1%	3.2%	9.8%
94	3	15	0.3	1.3	3.0	1.5	-0.5	1.9	1.4	-0.5	1.8	7.7%	3.2%	5.0%
95	3	30	0.1	2.3	3.0	1.3	-1.3	2.2	1.2	-1.2	2.1	5.2%	1.5%	3.0%
96	3	30	0.3	2.3	3.0	1.9	-1.3	2.2	1.8	-1.2	2.1	4.7%	1.5%	2.2%

Table 4.13: Inclined bottom plating - Comparison of F_L, F_T & F_V

As the angle γ decreases down to zero, the analytical solution previously developed should tend toward the solution developed in section 4.3 for horizontal shell plating. This may be verified by testing the inclined solution with decreasing inclination angles. To do that, the rock n°2 from Table 4.1 is considered with the following fixed parameters: $H_R = 1$, $b_R = 2.5$, $a_1 = 8\,m$ and $\mu = 0.1$.

Figure 4.35 presents the evolution of the resistant force components F_L, F_T and F_V for different value of γ $(5°, 10°, 15°, 20°)$. In this figure, the subscript *"i"* refers to the inclined plating while horizontal plating solutions are marked by a circle, triangle and a cross. The figure clearly confirms that the solution derived for the bilge plating actually converges towards the horizontal plating solution when γ decreases down to zero. In addition, this graph demonstrates the high dependency of the forces to the inclination. Indeed, an angle of 10° is sufficient to decrease by 2/3 the longitudinal resistant force and by 1/2 the vertical one.

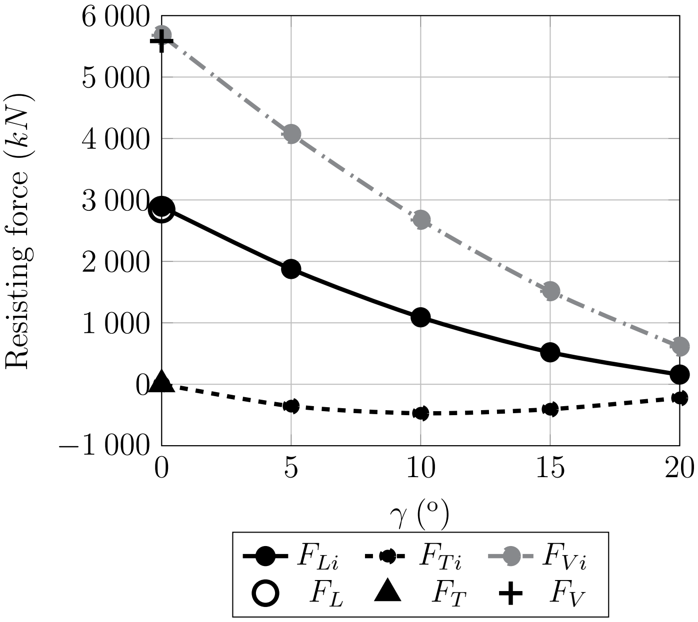

Figure 4.35: Evolution of the resisting forces with the inclination angle

4.8.2 Response of transverse floors

When impacted by the rock, an inclined transverse member deforms in a similar way as the vertical one, that is following the concertina splitting mechanism illustrated in Figures 4.16 and 4.17. Therefore, the following expression, similar to Eq. 4.42, allows to calculate the related plastic energy:

$$E_P = \frac{1}{\sqrt{3}}\sigma_0 t_f H^3 \left(\frac{1}{b_{01}} + \frac{1}{b_{02}}\right) + \frac{\pi\sigma_0 t_f}{\sqrt{3}}\left(b_{01} + b_{02}\right) \tag{4.88}$$

Where H, defined by Eq. 4.69, is the vertical penetration of the rock into the inclined outer plating located just below the floor. The plastic resistant force thus becomes:

$$F_P = \frac{1}{\sqrt{3}}\sigma_0 t_f H^2 \left(\frac{1}{b_{01}} + \frac{1}{b_{02}}\right) + \frac{\pi\sigma_0 t_f}{\sqrt{3}}\frac{b_{01} + b_{02}}{H} \tag{4.89}$$

Where the transverse fibre extension b_{01} and b_{02} may be calculated as:

$$b_{01} = min\left(0.564H\sqrt{\frac{H}{t_h}}, b_1\right) \tag{4.90}$$

$$b_{02} = min\left(0.564H\sqrt{\frac{H}{t_h}}, b_2\right) \tag{4.91}$$

4.8.2.1 Numerical validation

To verify the theoretical model, various numerical simulations are performed using *Ls-Dyna* finite element solver. Two inclination angles $\gamma = 15°$ and $\gamma = 30°$ are investigated, which leads to only 6 scenarios (Cases 97 to 102) since the resulting absorbed energy does not depend on the friction coefficient μ.

Table 4.14 compares the energies absorbed by the floor deformation and shows that the deviation between numerical and analytical values does not exceed 12%, which appears satisfying regarding the assumptions made.

Case id	Rock id	γ	H_R	b_R	Int. energy Num. (MJ)	Int. energy Ana. (MJ)	Deviation
97	1	15	2	3	1.12	1.32	-12%
98	1	30	2	4	0.77	0.78	-0.6%
99	2	15	2	3	1.17	1.3	-11.1%
100	2	30	2	3	1.0	1.1	-11%
101	3	15	1	3	0.64	0.63	1.3%
102	3	30	2	3	0.74	0.76	-3.3%

Table 4.14: Inclined floor - Comparison of the energies absorbed by inclined floors

Once again, considering the following fixed parameters: $H_R = 1$ and $b_R = 2.5$, one can verify that the solution converges toward the horizontal case when the inclination vanishes, as demonstrated in Figure 4.36.

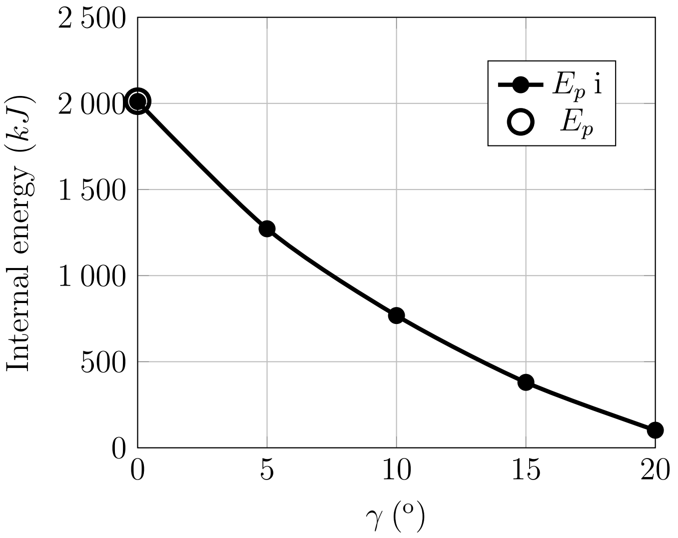

Figure 4.36: Evolution of floor dissipated energy with angle γ

4.8.3 Overall inclined double hull

Once elementary responses of bottom plating and transverse members have been validated, the next step is concerned with the validation of the proposed method on a full double bottom structure. The hull model is the one depicted in Figure 4.18. Considering 3 rock shapes, 2 friction coefficient and 2 inclination angle leads to the study of 12 scenarios (Cases 103 to 114). Results in term of internal energy, sliding energy and total dissipated energy are confronted in Table 4.15.

Case id	Rock id	γ	μ	H_R	b_R	Int. Num. (MJ)	Sliding Num. (MJ)	Total Num. (MJ)	Int. Ana. (MJ)	Sliding Ana. (MJ)	Total Ana. (MJ)	Dev. internal	Dev. sliding	Dev. total
103	1	15	0.3	2.1	6	6.1	8.9	15.0	6.3	8.0	14.3	-2.7%	9.7%	4.6%
104	1	30	0.3	3.8	5.8	8.4	11.9	20.3	8.8	10.4	19.1	-5.0%	12.9%	5.5%
105	2	15	0.3	2.2	6	8.7	9.7	18.4	8.4	8.5	16.9	4.4%	12.2%	8.5%
106	2	30	0.3	3.8	5.8	6.9	8.5	15.3	7.1	7.6	14.7	-3.8%	10.1%	3.8%
107	3	15	0.3	2.2	6	10.9	9.3	20.2	8.7	7.4	16.1	20.2%	20.4%	20.3%
108	3	30	0.3	3.8	5.8	7.4	7.1	14.4	6.2	5.7	12.0	15.0%	18.5%	16.7%
109	1	15	0.1	2.1	6	6.1	2.9	8.9	6.3	2.3	8.6	-3.7%	18.3%	3.3%
110	1	30	0.1	3.8	5.8	8.2	3.8	12.0	8.8	3.1	11.9	-6.9%	18.8%	1.3%
111	2	15	0.1	2.2	6	8.5	3.1	11.6	8.4	2.4	10.7	2.2%	21.6%	7.3%
112	2	30	0.1	3.8	5.8	6.7	2.7	9.4	7.1	2.2	9.4	-6.3%	16.0%	0.0%
113	3	15	0.1	2.2	6	10.4	2.8	13.3	8.7	2.0	10.7	17.0%	29.3%	19.7%
114	3	30	0.1	3.8	5.8	7.2	2.1	9.3	6.2	1.7	7.9	12.7%	20.0%	14.4%

Table 4.15: Inclined ship double bottom - Comparison of internal, sliding and total energies

For the case of a non inclined ship hull, the major discrepancies are observed on the scenarios related to the sharpest rock, i.e., rock n°3 from Table 4.1. This confirms that both the deformation and sliding mechanisms would need to be improved for the sharpest rocks. Nonetheless, the results are very encouraging given that the deviation on the total dissipated energy does not exceed 10% for rocks n°1 and n°2 from Table 4.1.

The energy distribution between bottom plating, transverse floor and sliding energy is plotted on Figure 4.37a and 4.37b. As expected, the results are similar to those obtained for the horizontal bottom. The floors dissipate a very few amount of energy compared to the outer shell and the sliding energy represents a significant amount of the total dissipated energy, especially when $\mu = 0.3$.

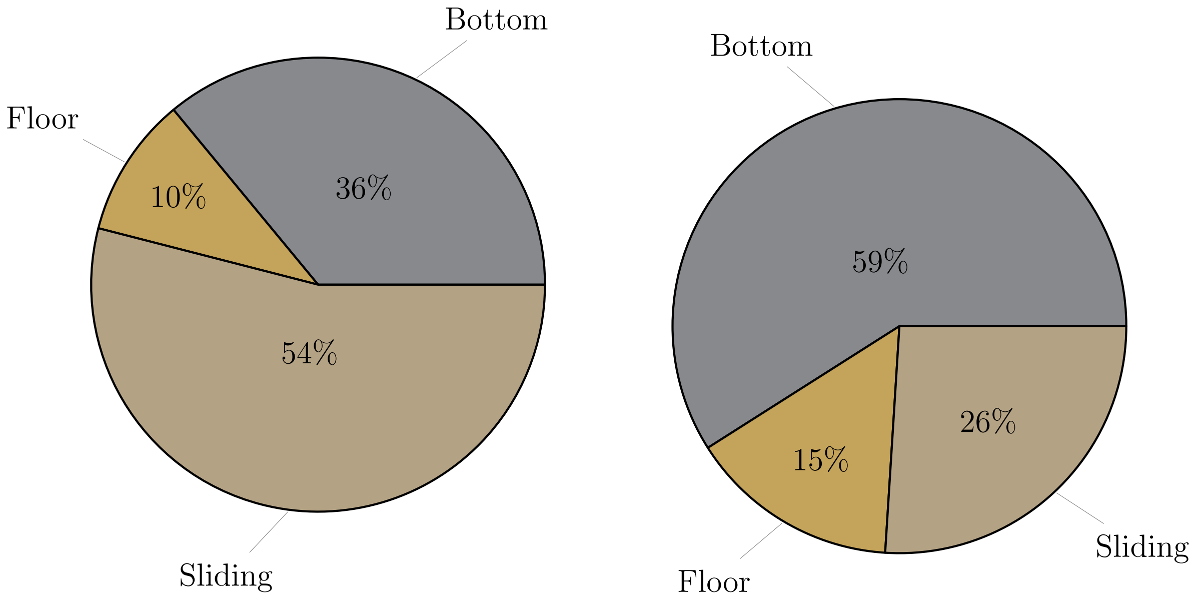

(a) $\mu = 0.3$ (b) $\mu = 0.1$

Figure 4.37: Inclined structure - Energy distribution for an impact between two girders

Several additional numerical simulations are carried out on a double structure but this time, the longitudinal girders are involved in the deformation. The results in term of dissipated energies (internal, sliding and total) are given in Table 4.16.

Case id	Rock id	γ	μ	H_R	b_R	Int. Num. (MJ)	Sliding Num. (MJ)	Total Num. (MJ)	Int. Ana. (MJ)	Sliding Ana. (MJ)	Total Ana. (MJ)	Dev. Internal	Dev. Sliding	Dev. Total
115	1	15	0.3	2	6	12.7	14.5	27.2	11.5	12.8	24.3	9.4%	11.9%	10.7%
116	1	30	0.3	3.6	5.4	18.4	20.4	38.8	19.6	19.4	38.9	-6.1%	5.0%	-0.2%
117	2	15	0.3	2	6	13.5	13.0	26.5	12.2	11.6	23.8	9.4%	11.1%	10.2%
118	2	30	0.3	3.6	5.3	19.6	18.2	37.8	20.8	17.7	38.5	-5.9%	2.6%	-1.8%
119	3	15	0.3	2	5.85	18.8	14.2	33.0	15.6	12.1	27.7	16.9%	14.7%	16.0%
120	3	30	0.3	3.6	5.3	22.3	16.8	39.1	21.2	16.3	37.5	4.8%	3.0%	4.0%
121	1	15	0.1	2	6	12.5	4.6	17.1	11.5	3.5	15.0	7.9%	23.6%	12.1%
122	1	30	0.1	3.6	5.4	18.0	6.4	24.4	19.6	5.6	25.1	-8.9%	13.1%	-3.1%
123	2	15	0.1	2	6	13.0	4.0	17.0	12.2	3.1	15.3	6.1%	23.6%	10.2%
124	2	30	0.1	3.6	5.3	19.0	5.7	24.6	20.8	4.8	25.6	-9.4%	14.7%	-3.9%
125	3	15	0.1	2	5.85	17.7	4.2	22	15.6	3.0	18.6	12.0%	29.6%	15.4%
126	3	30	0.1	3.6	5.3	21.0	5.0	26.0	21.1	4.3	25.4	-0.6%	14.1%	2.2%

Table 4.16: Inclined ship double bottom - Girder impact - Comparison of internal, sliding and total energies

It can be concluded from Table 4.16 that considering the complexity of the problem, the agreement between theoretical and numerical results is fairly good. The major discrepancies are observed for the lower friction coefficient $\mu = 0.1$. Evaluation of the attack point on the rock becomes quite complex when the inclination of the hull is considered. In addition, the presence of a floor/girder intersection tends to modify the pressure distribution, which changes the contribution of friction to the dissipation process, explaining the important deviation observed for the case 125. Nevertheless, considering the 12 cases, the average discrepancies for internal, sliding and total energies are respectively 8.2%, 13.8% and 7.5%.

Figure 4.38 illustrates the evolution of resisting forces F_L, F_T and F_V for case 115. A good agreement is observed on the three forces F_L, F_T, and F_V for the *steady state* part, that is when the rock slides between two transverse floors. However, when a floor/girder intersection is crushed, the longitudinal force is underestimated by approximately 30% compared to *Ls-Dyna* result, indicating that further research is undoubtedly needed to better assess the response of an inclined intersection during ship grounding.

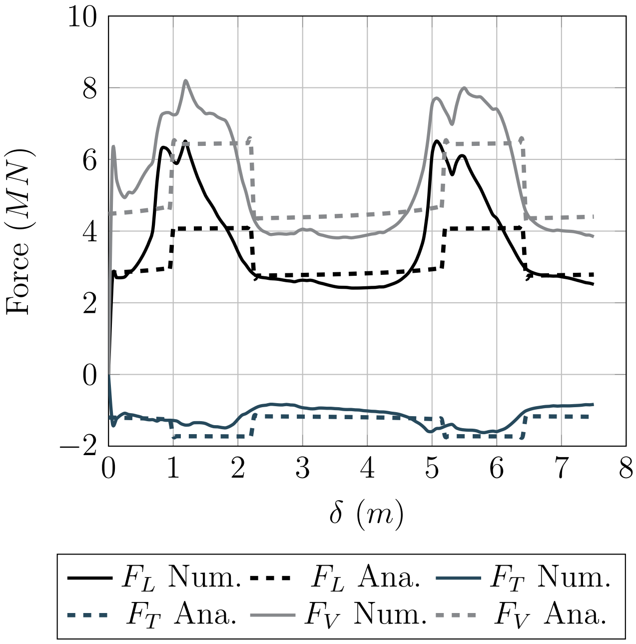

Figure 4.38: Comparison of energies scenario 115 - Inclined sliding

The energy distribution between the different components and the sliding energy is very similar to the case of a non-inclined hull: bottom plating and girder dissipate almost the same amount of energy while transverse floors are seen to dissipate less than 10% of the total energy.

4.9 Conclusion

The purpose of this chapter was the derivation of analytical solutions for the problem of a ship bottom structure sliding over an elliptic paraboloid-shaped rock.

To achieve this goal, in a first part, nonlinear finite element simulations were carried out considering the main substructures of a ship bottom i.e., outer shell, floors and girders. From these simulations, the main mechanisms of energy absorption were identified. Using the Upper-bound theorem, closed-form expressions were derived to evaluate the resisting force of each component. Both horizontal and inclined bilge-like bottoms were investigated as well as impacts between and onto girders. The developments realised for an inclined hull may be seen as a generalisation of the horizontal hull case ($\gamma = 0°$).

Considering 126 different scenarios, the results obtained from the proposed analytical models were systematically confronted to numerical simulations and, in general, a pretty good agreement was obtained. The highest discrepancies were mainly observed when the rock is very sharp. In such case, the dissipated energy is systematically underestimated by the analytical model (by up to around 20%). Moreover, numerical simulations show that such sharp rock initiates plating rupture at low penetration height so the hull response response rapidly switches from sliding to raking mode. This highlights the necessity of defining a criterion to trigger the initiation of the rupture. Such criterion will be discussed in Chapter 6. From numerical and analytical simulations, the following observations were made:

- Most energy - absorbing parts are respectively the bottom plating and the girders, while the floors absorb less than 10 % of the energy.
- Friction has a significant influence on the results. Changing the coefficient from 0.1 to 0.3 leads to the doubling of the frictional energy. This demonstrates the importance of a sensitivity analysis on this parameter when simulating ship sliding events. On the contrary, the vertical reaction force is found to be independent of the friction coefficient.
- The inclination of the bottom with respect to the horizontal plane has also a significant influence on the results. Indeed, an inclination of 10° is sufficient to decrease by 2/3 the longitudinal force and by 1/2 the vertical one. This also stresses the importance of modelling accurately the external dynamics of a grounding ship and especially its roll motion.

From the various comparisons, it was shown that even if the response of the bottom plating is quite well captured, further studies seem necessary to better model the mechanisms involved in the crushing of the longitudinal girders. More specifically, the influence of transverse floors and rock shape on the girder wave-like deformation pattern should be further investigated.

Finally, although imperfect, the proposed simplified model can be advantageously used to rapidly assess the response of a ship sliding on a seabed idealised as a paraboloid-shaped rock.

Once the outer shell has fractured, the ship enters the so-called "raking" deformation mode. The response of the main ship bottom components in raking mode are investigated in the next chapter.

Chapter 5

Ship raking

5.1 Introduction

After a certain level of penetration, the rock starts to tear the outer shell plating and the ship enters the so-called *raking* mode. A lot of experimental work has been performed to better understand the mechanics involved in this tearing/cutting mode, which may be split into two distinct phases:

- In the so-called *transient* phase, the plate resisting force increases as long as the rock/wedge penetrates into the plate. Two flaps are created on each side of the indenter. This phase ends as soon as the shoulder of the rock/wedge is in contact with these flaps.
- At that time, the plating resisting force stabilises around an average value and the plate is said to be in the *steady state* mode.

According to the literature on plate tearing, different deformation patterns may be observed:

- The so-called *clean cut* mode corresponds to a stable tearing as illustrated in Figure 5.1*A*. Two flaps are created on each side of the rigid wedge used as indentor. Such "ideal" tearing mode is generally observed in grounding events.
- In the *braided cut* mode, the plate also splits into two flaps at the tip of the wedge but, at the same time, the sheet appears to buckle from one direction to another resulting in a sinusoidal force, as illustrated in Figure 5.1*B*. Each peak of the force corresponds to a periodic change of direction of the buckles.
- Finally, when the indentor is large compared to the plate width, the *concertina* tearing mode illustrated in Figure 5.1*C* may occur. Successive folds are formed and the plate tears along its edges. Although this mode may be observed in real grounding events, it is more commonly observed in ship collision events, for instance when a deck is crushed by a ship bow. A simplified model was derived by *Wierzbicki* [93] for predicting the mean resisting force associated to the concertina tearing mode. Unlike the two previous modes, the force was shown to not depend on the friction coefficient.
- A last but rather rare tearing mode has been reported by *Muscat-Fenech* & *Atkins* [121]. Here, two tears are formed by the wedge and a chip-like spiral band of metal develops in front of the indentor - see Figure 5.2.

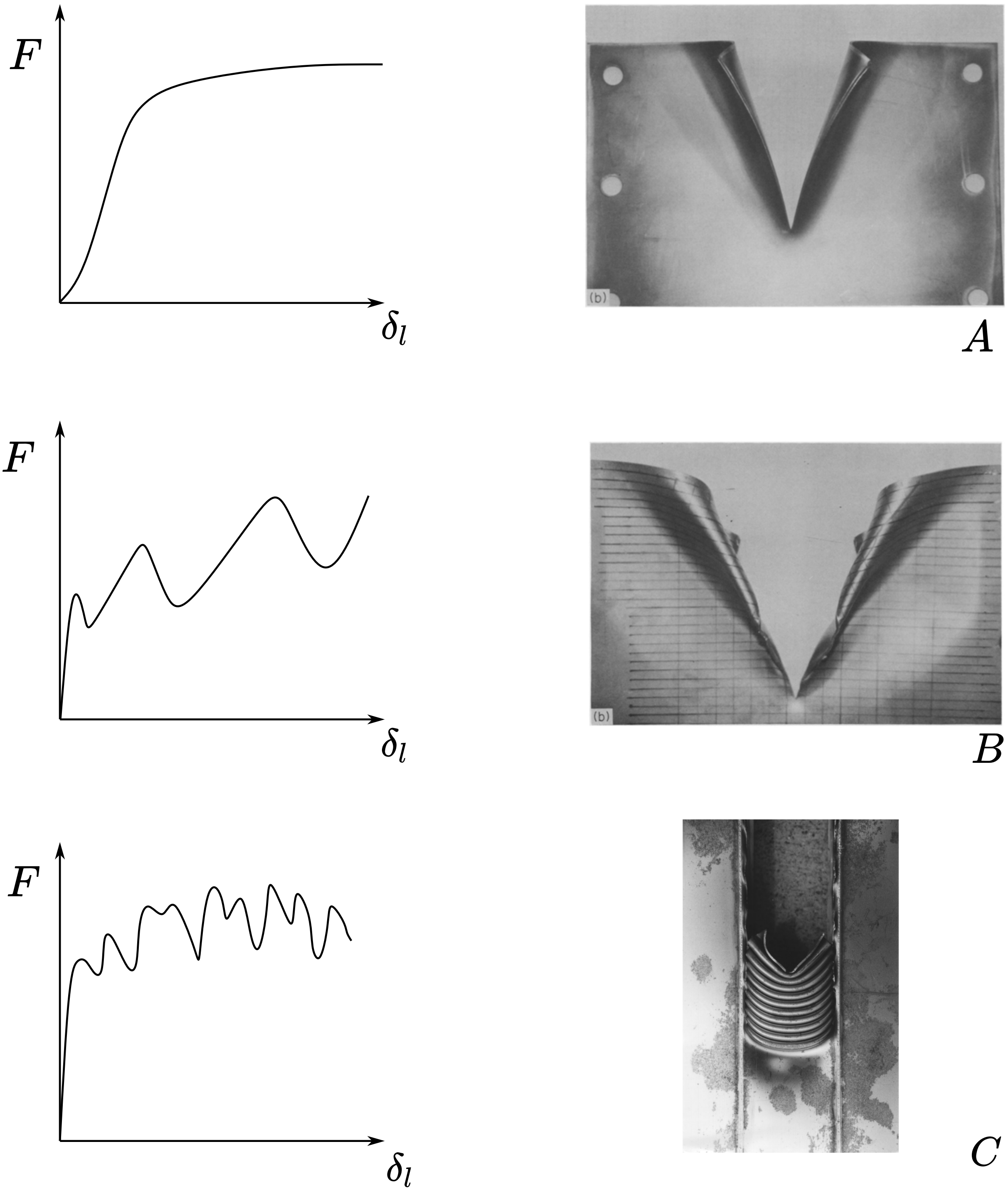

Figure 5.1: Different tearing mode - *A* & *B* from *Lu* & *Calladine* [71] - *C* from *Zhang* [37]

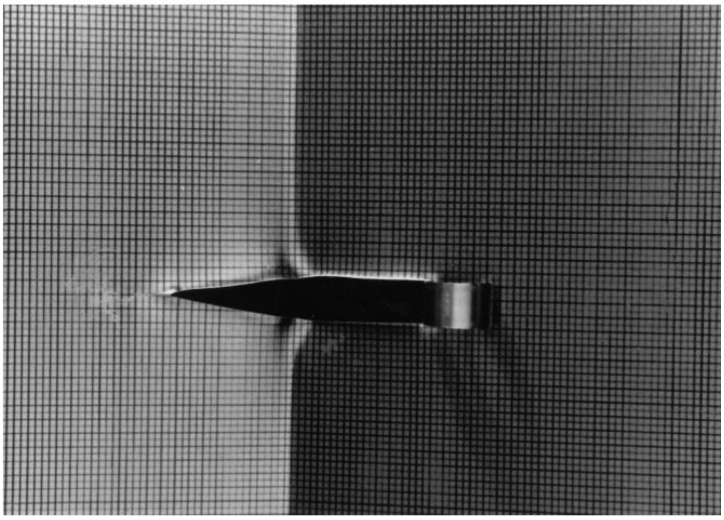

Figure 5.2: Double tear from *Muscat-Fenech* & *Atkins* [121]

Although the outer shell is often considered as the most energy-dissipating part of the ship, transverse floors and longitudinal girders also absorb energy through different mechanisms of deformation. The objective of the work presented in this chapter is therefore to derive analytical expressions giving the resisting force of the bottom (or double bottom) plating, the floors and the girders in raking conditions.

5.2 Response of bottom plating

5.2.1 Literature review

As for ship sliding problem, the outer/inner shell is modelled by an horizontal unstiffened plate. Since the problem of plate tearing has been widely investigated over the past decades, a brief summary of literature is presented.

In one of the first experiments conducted by *Akita et al.* [146], steel plates were teared by two rigid wedges with split angles $\theta = 30°$ and $40°$. A first attempt for modelling the plate resisting force was made by the authors but the developed analytical model did not result in good agreement with experimental tests. Based on experimental results extracted from Akita's paper, *Vaughan* [147, 148] proposed an empirical expression for the resisting force. The energy was supposed to be dissipated through plastic bending and fracture. Following the example of Vaughan, *Woisin* [149], *Jones & Jouri* [150] or *Lu & Calladine* [71] developed various empirical solutions for a plate cut by a rigid wedge. The latter discussed the effect of friction on the resisting force. It is noteworthy that friction influence on dissipated energy is still today a subject of research - see *Zhou et al.* [63] for instance. *Wierzbicki et al.* [118] were among the first to derive an analytical solution for the initiation phase based on a kinematic deformation mechanism. The two flaps created during this phase were assumed to deform taking a cylindrical shape. Resulting deformation mechanisms were membrane stretching at the tip wedge and plastic bending of the flaps. The effect of friction was also included in the model.

Solutions for steady state tearing mode were later derived by *Zheng* [151] and *Simonsen* [11] considering a rigid wedge indentor. However, one major issue when dealing with a wedge shape is the dissipation mechanism at the opening tip and the choice between pure plastic flow or fracture is not obvious. In the experimental tests carried out by *Vaughan* [147, 148] and *Lu & Calladine* [71], the crack was seen to remain in front of the tip, indicating that the separation process was coming from plastic flow. On contrary, in the test documented by *Rodd* [152], a blunt rock was used and the crack was observed to run ahead of the rock indicating a fracture mode. Moreover, in this last experiment, the crack suddenly propagated to transverse structures and a general theory covering those two aspects appeared to be a major difficulty.

Some raking experimental tests involving a cone shaped rock were realised on a unstiffened plate by *Muscat-Fenech* [69] and on a double bottom structure by *Rodd* [152]. *Simonsen* [141] and later *Zeng et al.* [12] developed simplified models to assess the resisting force of a plate cut by a conical shape indentor. The case of paraboloid shaped rocks was investigated by *Heinvee* [20], *Heinvee & Tabri* [78], and *Heinvee et al.* [153] who performed numerical simulations. From curve fitting analysis, the authors proposed a simple expression to estimate the mean resisting force of three different types of tankers.

The response of longitudinal stiffened panels subjected to tearing was investigated by *Paik* [129] and *Bracco* [110]. The contribution of small longitudinal stiffeners was accounted for by defining an equivalent plate thickness:

$$t_{eq} = t_h + \frac{S}{b} \tag{5.1}$$

Where t_h is the plating initial thickness, S the cross section area of the stiffeners and b the spacing between two adjacent stiffeners. Such smearing method was shown to be effective in including the resistance of small longitudinals. The problem of transversely stiffened panels was discussed experimentally and analytically by *Little* [116] and *Pippenger* [117]. A sudden raise in force was reported when the cutting wedge was closed to a transverse member, indicating a strong coupling between plate and transverse member behaviours. The authors concluded that transverse members like floors should be explicitly modelled rather than smeared into the plating thickness. Recently, *Sun et al.* [13] reported from numerical simulations that the presence of transverse floors tends to stop the propagation of the plate fracture. Just behind the floor, the bottom plating firstly forms a fold (see Figure 5.3) then, after a certain level of indentation, it comes back to the tearing mode.

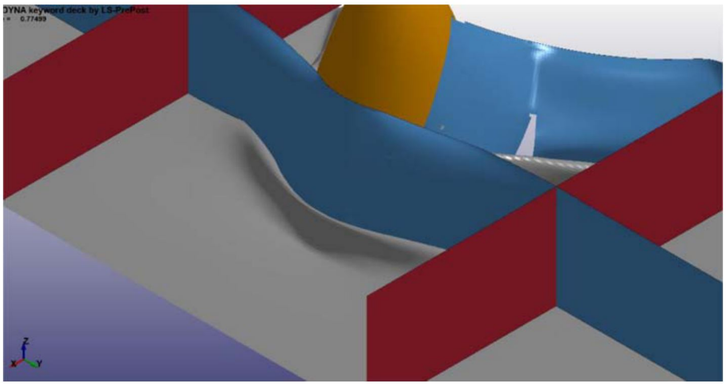

Figure 5.3: Bottom folding after a transverse floor

5.2.2 Analytical development

The mechanisms involved during plate tearing and considered in this work are the following ones:

- Plastic membrane straining
- Plastic bending
- Crack propagation
- Friction between the rock and the bottom plating

Assuming the ship heave and sway velocities are zero, Eq. 2.15 becomes:

$$F_L V_x = \dot{E}_p + \dot{E}_f = F_P V_x + \int_S \mu p V_{rel} \, dS \tag{5.2}$$

Where F_L is the resistant force along longitudinal direction, F_P is the plastic resistance, μ is the friction coefficient, p is the contact pressure between the rock and the plate element of surface dS and V_{rel} is the relative velocity between the plate and the rock in the contact area.

Supposing that the problem is symmetric with respect to the vertical plane passing through the rock apex S - see Figure 5.4 - only one-half of the plate deformation will be described.

The idealised model splits the deformed plate into two cylindrical $KQTB$ and $QDFM$ and two planar BTJ and MFI areas. The radius of the cylindrical parts are respectively R_1 and R_2. *Wierzbicki et al.* [118] reported that other surface shapes are unlikely to occur as they would consume more energy.

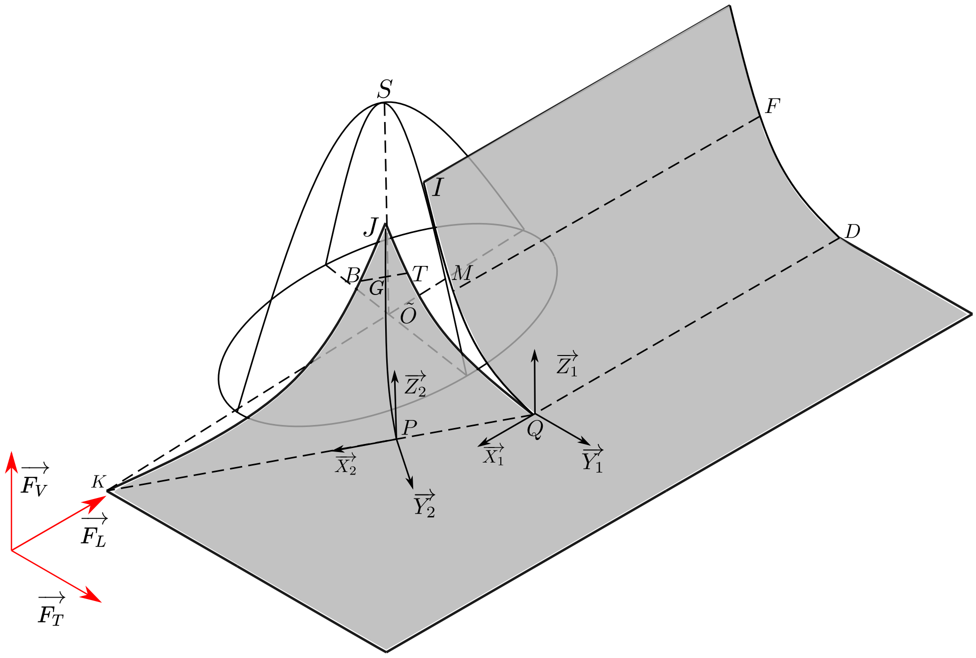

Figure 5.4: Plate tearing overall process - 3D

The fracture mechanism is concentrated at the centre line (point K) and plastic bending occurs along KQ and BT lines. It can be observed from numerical simulations that the plate does not tear on its side. Consequently, the gap $QJ - QI$ must accommodate by membrane straining.

When a plate element passes through the line KQ, its curvature changes from 0 to $1/R_2$ then the element is stretched in the plane BTJ or MFI with a zero curvature. Along the lines BT or MF, the curvature of an element comes to zero. The BT/MF lines are respectively parallel to the KQ/QD lines. Moreover, as illustrated on Figure 5.5, the rock and the deformed plate are tangent at point G and M. It is worth noting that the rock is supposed to have a constant vertical indentation H into the plate.

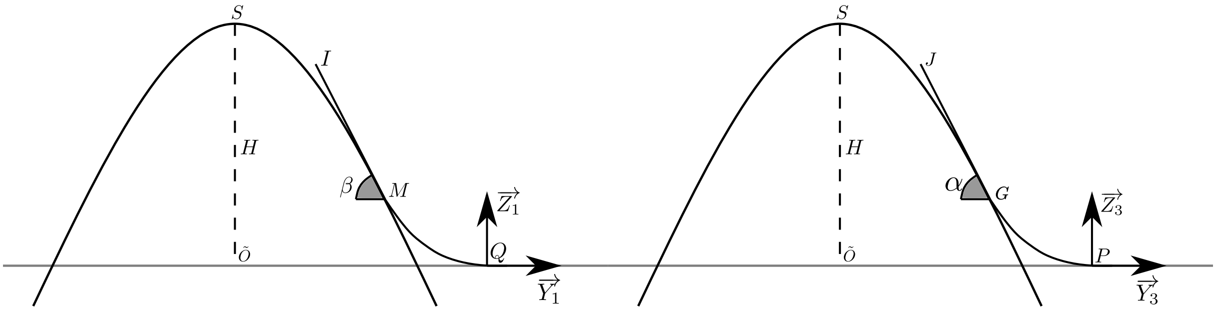

(a) Contact angle β

(b) Contact angle α

Figure 5.5: Raking cross section contact angles

On opposition to the problem of ship sliding, evaluation of the relative velocity might be difficult. For this reason, the relative velocity is supposed to be equal to the surge velocity, i.e., V_{rel}=V_x. By denoting N as the force obtained by integration of the contact pressure over surface dS (N will act in the normal direction of the rock at the contact point G), Eq. 5.2 becomes :

$$F_L V_x = F_P V_x + \mu N V_x \tag{5.3}$$

Writing the force equilibrium related to the deformation of the half plate depicted in Figures 5.4, 5.5 and 5.6 leads to:

$$F_L = N\left(sin\alpha sin\psi + \mu\left(sin\xi sin\psi cos\alpha + cos\psi cos\xi\right)\right) \tag{5.4}$$

$$F_V = N\left(cos\alpha - \mu sin\xi sin\alpha\right) \tag{5.5}$$

$$F_T = \pm N\left(sin\alpha cos\psi + \mu\left(sin\xi cos\psi cos\alpha - sin\psi cos\xi\right)\right) \tag{5.6}$$

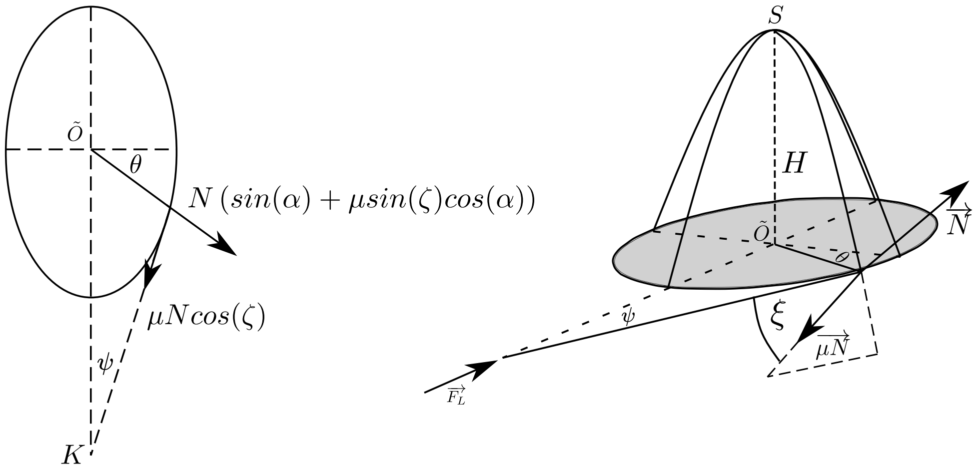

Figure 5.6: Raking top and 3D views - Contact forces

In previous equations, θ is the angle of contact between the rock and the plate, ψ is the angle giving the length of the crack during the steady state process and α represents the slope of the rock in P$\widetilde{O}$S plane - see Figure 5.5. The angle ξ traduces the direction of the relative motion between the rock and the plate. The sign ± of Eq. 5.6 comes from either left or right flap is considered. However, since the deformation is supposed to be symmetric, the resultant force acting along $\vec{y_1}$ axis is zero. Using Eqs. 5.3, 5.4 and 5.5, the resisting forces F_L and F_V may be expressed as:

$$F_L = F_p\left(1 - \frac{\mu}{sin\alpha sin\psi + \mu\left(sin\xi sin\psi cos\alpha + cos\psi cos\xi\right)}\right)^{-1} = F_p.g_f \tag{5.7}$$

$$F_V = F_L\left(\frac{cos\alpha - \mu sin\xi sin\alpha}{sin\psi sin\alpha + \mu\left(sin\xi sin\psi cos\alpha + cos\psi cos\xi\right)}\right) = F_L.k_v \tag{5.8}$$

The rate of plastic energy $\dot{E}_p$ related to the three aforementioned deformation mechanisms are now derived.

5.2.2.1 Fracture energy rate

As the rock has not a sharp cutting edge, ductile rupture (Mode I) is most likely to occur. Identical hypothesis were made by *Simonsen* [141] and *Zeng et al.* [12]. Denoting by R_c the material ductile rupture coefficient and by t_h the plate thickness, the rate of energy dissipated by plate fracture at the tip of the rock is :

$$\dot{E}_c = R_c t_h V_x \tag{5.9}$$

5.2.2.2 Membrane straining energy rate

In a similar way to the sliding process, straining of plate longitudinal fibre is unlikely to occur for the two following reasons: (i) longitudinal stiffeners attached to the bottom plating prevent the fibre from straining along longitudinal direction and (ii) from experiments and numerical simulations, the flaps appear to be almost plane after leaving the rock, indicating that shearing rather stretching occurs. Nonetheless, it is obvious that the strain field is more complicated than a pure shearing mode and some longitudinal stretching may also be present. While *Simonsen* [141] neglected the contribution of stretching, *Zeng et al.* [12] considered its effect. Integrating the effect of stretching leads to a difference of less than 5% on the resisting force. Therefore, in the present analysis, the contribution of stretching deformation is neglected so the membrane energy rate becomes :

$$\dot{E}_m = 2\sigma_0 t_h V_x \int_{y=0}^{y=W_{de}} \varepsilon_{eq}(y)dy = \frac{2}{\sqrt{3}}\sigma_0 t_h u_0 V_x \tag{5.10}$$

Where the distance u_0 between points I and J may be expressed as:

$$u_0 = \sqrt{(X_J - X_I)^2 + (Y_J - Y_I)^2 + (Z_J - Z_I)^2} \tag{5.11}$$

Where $\overrightarrow{OI}$ and $\overrightarrow{OJ}$ are given as :

$$\overrightarrow{OI} = \begin{bmatrix} 0 \\ -R_1 sin(\beta) - (W_{de} - R_1\beta)\, cos(\beta) \\ R_1\,(1 - cos(\beta)) + (W_{de} - R_1\beta)\, sin(\beta) \end{bmatrix} \tag{5.12}$$

$$\overrightarrow{OJ} = \begin{bmatrix} W_{de} sin(\psi) cos(\psi) - l_J sin(\psi) \\ -W_{de} sin^2(\psi) - l_J cos(\psi) \\ R_2\,(1 - cos(\alpha)) + cos(\psi)\,(W_{de} cos(\psi) - R_2\alpha) \end{bmatrix} \tag{5.13}$$

With l_J, R_2 and W_{de} defined as :

$$l_J = R_2 sin\alpha + cos\alpha\,(W_{de} cos\,(\psi) - R_2\alpha) \tag{5.14}$$

$$R_2 = \frac{W_{de} cos\,(\psi) - R_y}{tan\,\left(\frac{\alpha}{2}\right)} \tag{5.15}$$

$$W_{de} = R_y + R_1 tan\left(\frac{\beta}{2}\right) \tag{5.16}$$

Where $R_y = \sqrt{H/E}$ is the transverse radius in the plate.

5.2.2.3 Bending energy rate

The material in the area $QJ - QI$ undergoes a significant membrane stretching to close the gap, thus the energy dissipated by plastic bending in this region will be limited. It is then supposed that all bending energy is due to curvature change along the KQ line. With a length of the hinge line $l_n = W_{de}/sin(\psi)$, a change of curvature $K_n = 1/R_2$ and a normal velocity of $V_n = V_x sin\,(\psi)$, the bending energy writes:

$$\dot{E}_b = 2M_0 l_n V_n K_n = 2M_0 V_x \frac{W_{de}}{R_2} \tag{5.17}$$

5.2.2.4 Total plastic energy rate

The total plastic energy rate $\dot{E}_p$ is obtained by summing all the previous contributions, i.e., Eqs. 5.9, 5.10 and 5.17.

$$\dot{E}_p = \left(2M_0 \frac{W_{de}}{R_2} + N_0 u_0 + R_c t_h\right) V_x \tag{5.18}$$

Finally, the plastic force is obtained by dividing Eq. 5.18 by the ship surge velocity V_x:

$$F_P = 2M_0 \frac{W_{de}}{R_2} + N_0 u_0 + R_c t_h \tag{5.19}$$

For a paraboloid shaped rock, angles α and β are not constant. Indeed, they should be chosen consistently according to the position of the points M and N on the rock. However, the points M and N depend on angles α and β. To break the deadlock, α and β angles are supposed to be the same as the rock angles at $z = 0$. This assumption allows to define the following expressions :

$$\alpha = atan\left(2\frac{H}{d}\right) \tag{5.20}$$

$$\beta = atan\,(2ER_y) \tag{5.21}$$

$$d = \sqrt{\frac{tan(\theta)^2 H}{E + Ctan(\theta)^2}\frac{E - C}{E} + \frac{H}{E}} \tag{5.22}$$

Finally ψ is related to θ by:

$$\psi = atan\left(\frac{C}{E} tan(\theta)\right) \tag{5.23}$$

5.2.2.5 Resisting force

The definition of angles ξ and θ is now discussed. As mentioned by *Simonsen* [141] or *Zeng et al.* [12], the angle ξ can be taken equal to either $\psi/2$ or ψ. In the current development, ξ is taken equal to ψ. Note that taking $\xi = \psi/2$ instead of $\xi = \psi$ leads to a difference of only 2% on the dissipated energy.

In the coordinate system $\mathcal{R}_1 = \left(Q, \overrightarrow{X_1}, \overrightarrow{Y_1}, \overrightarrow{Z_1}\right)$, the resistant force vector for one flap may be written as:

$$\overrightarrow{F_R} = \begin{bmatrix} F_L \\ F_T \\ F_V \end{bmatrix}_1 \tag{5.24}$$

In a coordinate system $\mathcal{R}_3$ having as main axes the direction of the forces $\overrightarrow{N}$ and $\mu\overrightarrow{N}$, the resisting force vector writes:

$$\overrightarrow{F_R} = \begin{bmatrix} N \\ \mu N \\ 0 \end{bmatrix}_3 \tag{5.25}$$

Where N may be expressed as:

$$N = \frac{F_P}{2}.\left(sin\alpha sin\theta + \mu\left(sin\xi sin\theta cos\alpha + cos\theta cos\xi - \mu\right)\right)^{-1} \tag{5.26}$$

Finally, it is postulated that θ adjusts itself to give the lowest resistant force. In other words, θ is determined numerically by minimising the norm of $\overrightarrow{F_R}$ vector that is:

$$\left\|\overrightarrow{F_R}\right\| = N\sqrt{1+\mu^2} \tag{5.27}$$

To conclude, considering the kinematic compatibility, i.e., $R_1 > 0$ and $R_2 > 0$, the following conditions may be written:

$$\begin{cases} 0 \leq \theta \leq min\left(\theta_1, atan\left(\frac{E}{C}tan(\theta_1)\right)\right) \\ \theta_1 = acos\left(\frac{R_y}{R_1 tan(\beta/2)+R_y}\right) \\ R_1 = \frac{R_y}{\beta - tan(\beta/2)} \end{cases} \tag{5.28}$$

5.2.3 Numerical validation

In an attempt to validate the proposed theoretical model, various raking scenarios on an unstiffened bottom plating are simulated using the non-linear finite element solver *Ls-Dyna*. The plate considered is $8.4m$ long, $5.7m$ wide and $15mm$ thick. Simulations parameters are set in accordance to Chapter 3 and the sensitivity of the results to the friction coefficient is investigated by varying μ from 0.1 to 0.3. The rock is assumed to be perfectly rigid and five different rocks are considered in the analysis, which parameters are listed in Table 5.1. In order to trigger the plate tearing at the front of the rock, it is assumed that the rock is more elongated in the longitudinal direction, which means that $C < E$. However, the rock n°5 is taken as axisymmetric to verify the proposed theoretical model for the limit case $C = E$. Moreover, as raking is unlikely to occurs with wide rocks, the coefficients C and E are selected in such a way that only sharp rocks are considered. As the resistant forces depend on the rock vertical indentation H into the plate, three impact heights $H = 0.75 - 1 - 1.4$ are considered for a sensitivity analysis. Combining the 5 different rock geometries with aforementioned parametric values leads to the study of 30 scenarios.

Rock id	C (m^{-1})	E (m^{-1})
1	2	4
2	3	6
3	2.5	5
4	1	2
5	2	2

Table 5.1: Rock parameters for raking validation

According to *Atkins* [154], the ductile rupture coefficient R_C for mild steel varies from 200-1000 kJ/m^2. Here, R_C is then taken as the mean value, i.e. 600 kJ/m^2. Nevertheless, its influence on the response will be discussed later on.

A clean cut of the plate post-processed from *Ls-Dyna* simulation is shown on Figure 5.7 and the associated longitudinal and vertical forces post-processed from numerical and analytical calculations are plotted on Figure 5.8. The mean values of forces F_L and F_V obtained numerically are computed varying the horizontal crushing length δ from 0 to $5m$ and are compared in Table 5.2. In the same way, the total energies (deformation + friction) dissipated during the tearing process for a crushing length $\delta = 5m$ are compared in Table 5.3. The percentage of the energy absorbed by plastic deformation and dissipated by friction is also given. Discrepancies are estimated according to Eq. 4.30.

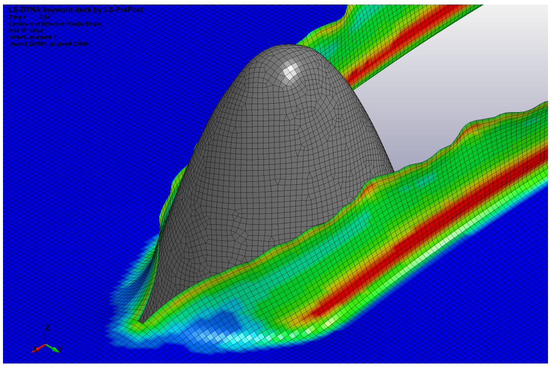

Figure 5.7: Clean cut from plate tearing simulation

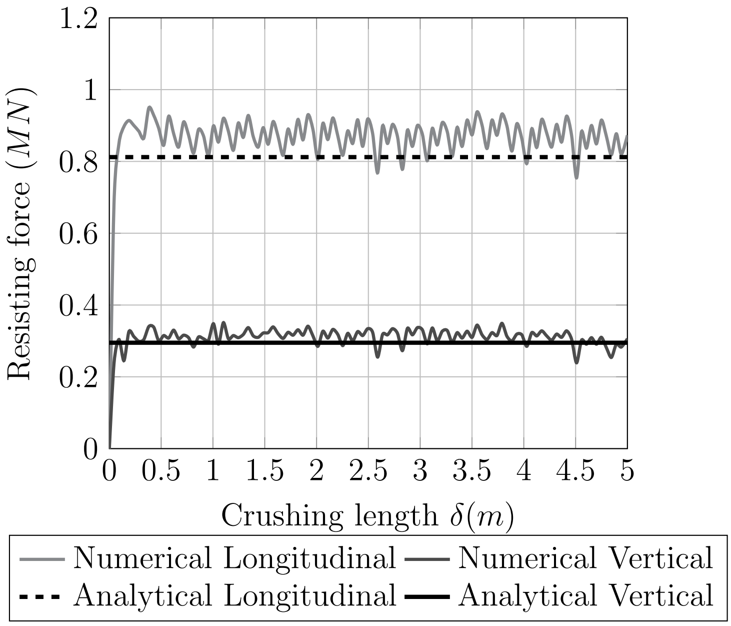

Figure 5.8: Resisting force for raking case 1

Case id	Rock id	H	μ	Num. F_L (MN)	Num. F_V (MN)	Ana. F_L (MN)	Ana. F_V (MN)	Deviation F_L	Deviation F_V
1	1	0.75	0.3	0.87	0.30	0.83	0.28	5%	9%
2	1	1.0	0.3	1.06	0.30	0.97	0.28	8%	9%
3	1	1.4	0.3	1.31	0.29	1.16	0.27	12%	8%
4	1	0.75	0.1	0.56	0.37	0.58	0.35	-3%	6%
5	1	1.0	0.1	0.65	0.38	0.67	0.36	-3%	5%
6	1	1.4	0.1	0.74	0.36	0.79	0.37	-7%	-2%
7	2	0.75	0.3	0.91	0.21	0.77	0.18	16%	14%
8	2	1.0	0.3	1.09	0.20	0.88	0.17	19%	14%
9	2	1.4	0.3	1.26	0.17	1.04	0.16	17%	1%
10	2	0.75	0.1	0.59	0.29	0.54	0.25	9%	13%
11	2	1	0.1	0.66	0.29	0.62	0.25	7%	11%
12	2	1.4	0.1	0.76	0.28	0.72	0.26	5%	9%
13	3	0.75	0.3	0.90	0.25	0.80	0.22	11%	13%
14	3	1	0.3	1.06	0.24	0.92	0.22	13%	11%
15	3	1.4	0.3	1.21	0.21	1.09	0.21	10%	0%
16	3	0.75	0.1	0.57	0.32	0.55	0.29	3%	8%
17	3	1	0.1	0.65	0.32	0.64	0.30	2%	7%
18	3	1.4	0.1	0.74	0.31	0.75	0.30	-2%	3%
19	4	0.75	0.3	0.88	0.52	0.94	0.50	-7%	4%
20	4	1	0.3	1.06	0.54	1.11	0.52	-5%	2%
21	4	1.4	0.3	1.39	0.52	1.35	0.55	2%	-6%
22	4	0.75	0.1	0.57	0.58	0.63	0.58	-10%	-1%
23	4	1	0.1	0.67	0.61	0.75	0.62	-11%	-1%
24	4	1.4	0.1	0.80	0.61	0.90	0.65	-12%	-7%
25	5	0.75	0.3	0.99	0.53	0.91	0.52	8%	3%
26	5	1	0.3	1.17	0.34	1.08	0.55	8%	-61%
27	5	1.4	0.3	1.68	0.44	1.31	0.57	22%	-29%
28	5	0.75	0.1	0.64	0.59	0.62	0.57	2%	4%
29	5	1	0.1	0.76	0.59	0.73	0.61	4%	-3%
30	5	1.4	0.1	1.02	0.61	0.88	0.65	14%	-7%

Table 5.2: Comparison of resisting force - Raking bottom plating

Case id	Rock id	Num. internal (MJ)	Num. sliding (MJ)	Num. total (MJ)	Ana. total (MJ)	Total energy Deviation
1	1	2.4 (56%)	1.9 (44%)	4.3	4.2	2.3%
2	1	2.7 (52%)	2.5 (48%)	5.2	4.9	5.8%
3	1	3.3 (51%)	3.2 (49%)	6.5	5.8	10.8%
4	1	2.2 (79%)	0.6 (21%)	2.8	2.9	-3.6%
5	1	2.5 (78%)	0.7 (22%)	3.3	3.32	-0.6%
6	1	2.9 (76%)	0.9 (24%)	3.7	3.9	-5.4%
7	2	2.5 (55%)	2.0 (45%)	4.5	3.8	15.6%
8	2	2.9 (54%)	2.5 (46%)	5.4	4.4	18.5%
9	2	3.4 (55%)	2.8 (45%)	6.2	5.2	16.1%
10	2	2.3 (80%)	0.6 (20%)	2.9	2.7	6.9%
11	2	2.6 (78%)	0.7 (22%)	3.3	3.1	6.1%
12	2	2.9 (77%)	0.9 (23%)	3.8	3.6	5.3%
13	3	2.5 (55%)	2.0 (45%)	4.5	4	11.1%
14	3	2.8 (53%)	2.5 (47%)	5.3	4.6	13.2%
15	3	3.4 (54%)	2.8 (46%)	6.2	5.5	11.3%
16	3	2.3 (80%)	0.6 (20%)	2.9	2.8	3.4%
17	3	2.6 (78%)	0.7 (22%)	3.3	3.2	3.0%
18	3	2.9 (77%)	0.9 (23%)	3.7	3.8	-2.7%
19	4	2.3 (54%)	2.0 (46%)	4.4	4.7	-6.8%
20	4	2.7 (51%)	2.6 (49%)	5.3	5.6	-5.7%
21	4	3.6 (53%)	3.2 (47%)	6.8	6.81	-0.1%
22	4	2.3 (79%)	0.6 (21%)	2.9	3.2	-10.3%
23	4	2.6 (77%)	0.8 (23%)	3.3	3.7	-12.1%
24	4	3.0 (75%)	1.0 (25%)	4	4.5	-12.5%
25	5	2.4 (54%)	2.0 (46%)	4.4	4.6	-4.5%
26	5	3.2 (60%)	2.1 (40%)	5.2	5.4	-3.8%
27	5	4.4 (60%)	2.9 (40%)	7.3	6.6	9.6%
28	5	2.3 (79%)	0.6 (21%)	2.9	3.1	-6.9%
29	5	2.7 (78%)	0.7 (22%)	3.4	3.7	-8.8%
30	5	3.6 (80%)	0.9 (20%)	4.5	4.4	2.2%
30	5	3.6 (80%)	0.9 (20%)	4.5	4.4	2.2%

Table 5.3: Comparison of dissipated energy - Raking bottom plating

Table 5.2 and Figure 5.8 show a relatively good agreement of the proposed model with numerical simulations. In general, the discrepancy on longitudinal and vertical forces does not exceed 20%. However, for some cases such as cases 9, 15 and 27, the discrepancy is higher. For these cases, numerical simulations did not lead to clean but rather braided cut, as shown in Figure 5.9a. As for the case 26, after some indentation, tearing initiates on both rock edges and only one flap of the plate remains in contact with the indenter - see Figure 5.9b. This might explain the large discrepancy observed on the vertical force for this case. In addition, from *Ls-Dyna* simulations, non-clean cuts were observed mainly when both the friction coefficient and the vertical indentation were the highest ($\mu = 0.3$ and $H = 1.4$). In fact, the lower the coefficient of friction, the more the rock will easily slide along the flaps. The bottom plating therefore remains less stuck to the rock, which leads to a clean cut mechanism. This assumption is confirmed by *Brubak et al.* [79] who reported that the failure mode may change with the friction coefficient.

Anyway, despite some differences observed on the tearing mode, the developed model still gives acceptable results. This may be also observed in Table 5.3 where the discrepancy between numerical and analytical dissipated energies does not exceed 15%, except for cases 8 and 9.

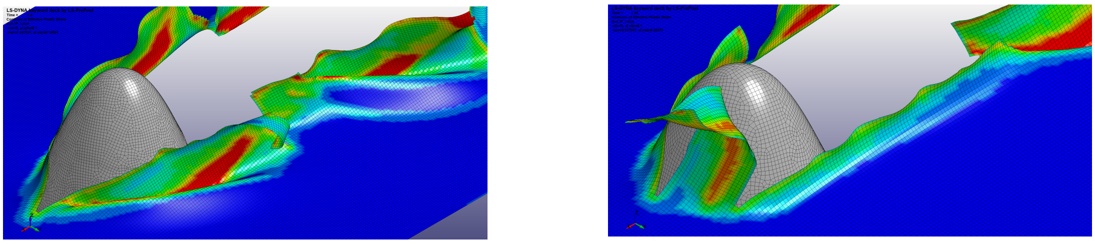
(a) Braid cut (b) Double tearing

Figure 5.9: Non clean cut simulations

5.2.4 Sensitivity analyses

The purpose of this section is to perform a sensitivity analysis on different parameters using the proposed analytical model and to observe their influence on the longitudinal and vertical resistant forces.

Ductile rupture coefficient

Since the ductile fracture coefficient R_c has been chosen arbitrarily in previous section, a sensitivity analysis is performed by varying R_c from 200 to 1000 kJ/m^2 and selecting rock n°1 as example.

Figure 5.10 reveals that only the horizontal resistant force is sensitive to the coefficient R_c but the difference between the lowest and highest values remain small (less than 5%). In addition, the energy dissipated at the fracture tip is small compared to membrane stretching and plastic bending energies (less than 5% of the total plastic energy). One can thus conclude that it is not necessary to identify precisely R_c.

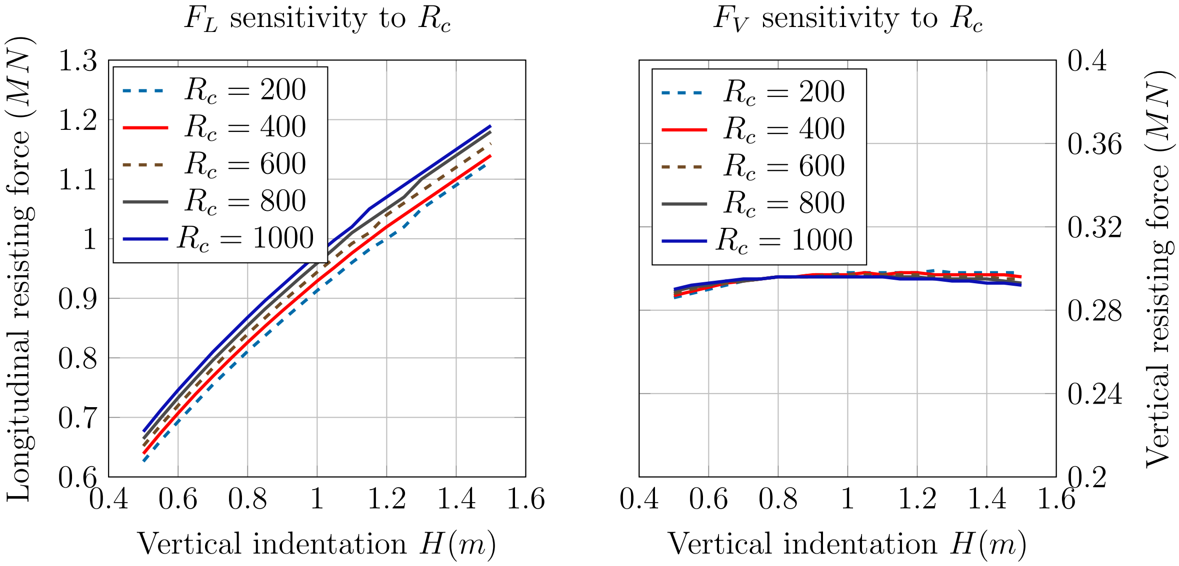

Figure 5.10: R_c Sensitivity - $\mu = 0.3$

Friction coefficient

In view of the results given by the Table 5.3, the friction coefficient μ plays an important role in the tearing process. Therefore, the purpose of this subsection is to determine to what extent forces F_L and F_V are sensitive to μ.

For this purpose, the simplified model is used considering four different friction coefficients μ in the interval $[0.1, 0.4]$. Figure 5.11 clearly shows that both the forces F_L and F_V greatly depend on coefficient μ. When the later is multiplied by 4, the longitudinal force is multiplied by around 1.7. On the other hand, a closer attention to Eq. 5.5 reveals that for a given angle, F_V is a decreasing function of μ. It is therefore concluded that friction should require much attention when analysing the plate tearing problem.

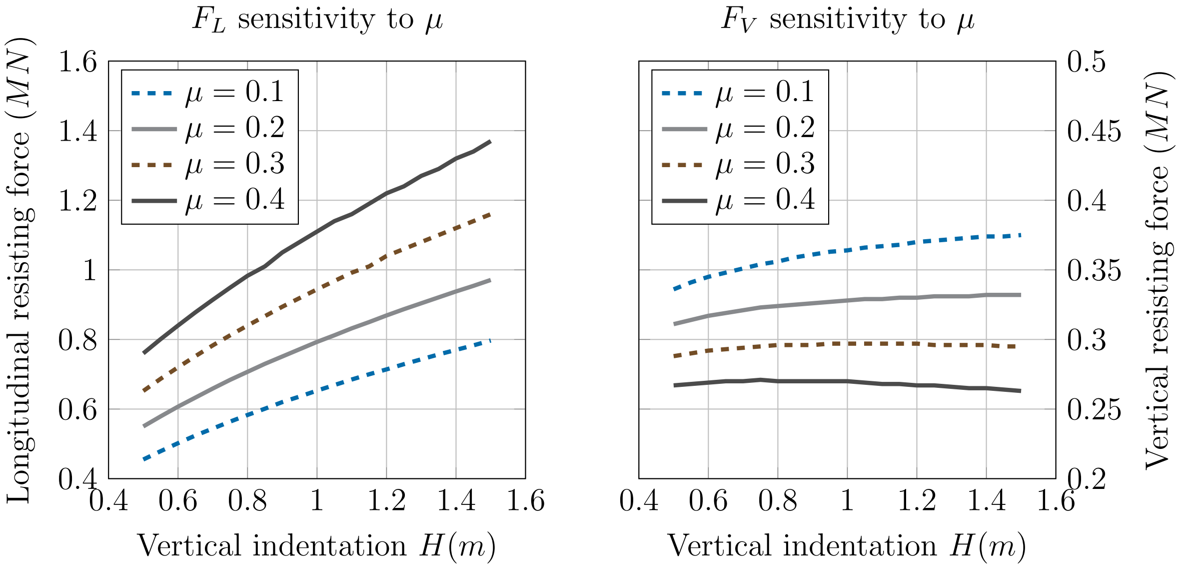

Figure 5.11: μ Sensitivity - $R_c = 600kJ/m^2$

Penetration depth

Since the rock section in contact with the plate increases with H, the longitudinal force and vertical one should also increase. Figure 5.12 illustrates the evolution of both F_L and F_V with H. It is observed that F_L increases non-linearly while the vertical force is almost constant. To explain this phenomenon, the evolution of angles α and β with respect to H are also plotted in Figure 5.12. It is shown that both angles tend rapidly toward a value closed to 90°. The closer α and β to 90°, the more the flaps are subjected to bending and membrane straining and, consequently, the higher the plastic resistant force. However, at the same time, as the normal reaction force tends to have a direction parallel to y-axis, the vertical force might decrease. From numerical simulations and analytical calculations, it appears that both effects tend to offset each other, which results in an almost constant vertical force.

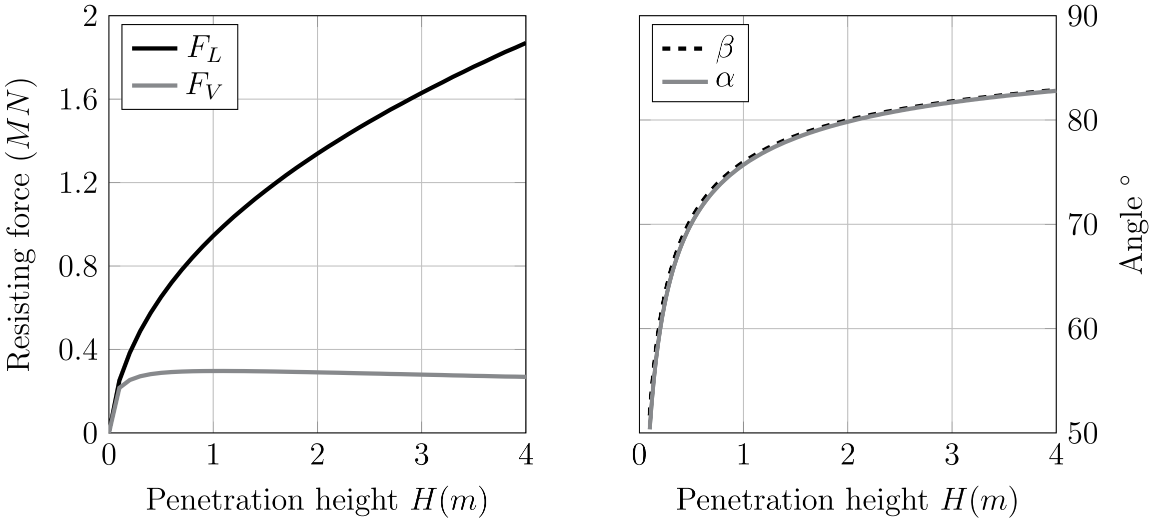

Figure 5.12: Evolution of F_L & F_V and α & β with H

Influence of the rock shape

As presented at the beginning of the chapter, the majority of published analytical developments are related to wedge or conical shape indenters. That is why this paragraph aims to illustrate the difference in term of resisting force between a conical and paraboloid shaped rock.

As demonstrated by *Sormunen et al.* [155], the choice of the rock shape is of crucial importance. In fact, as the real rock (extracted from sonar scan) depicted in Figure 5.13 is not axisymmetric, the area in contact with the ship structure may differ whether the front or the side part of the rock is impacted.

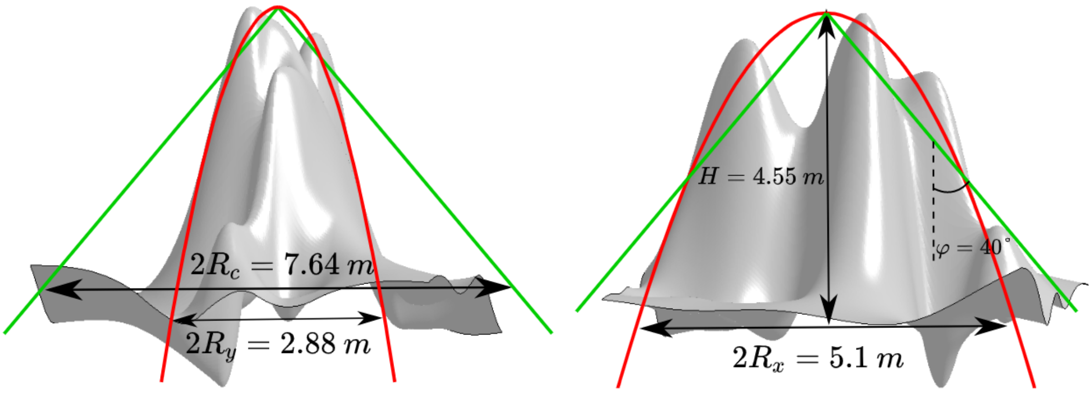

Figure 5.13: Raking top and 3D views - Contact forces

A paraboloid rock has been defined using Eq. 1.1 where coefficients $C = 0.7$ and $E = 2.2$ have been chosen to fit the best as possible with the real rock shape (in width and length). On the other side, a conical rock with a semi-apex angle of 40° was found by *Sormunen et al.* [155] to fit the best with the real rock. In Figure 5.14, horizontal and vertical components of the resistant force obtained from the analytical model proposed by *Simonsen* [141] (based on a conical shape) are compared with the forces given by the model presented in subsection 5.2.2.

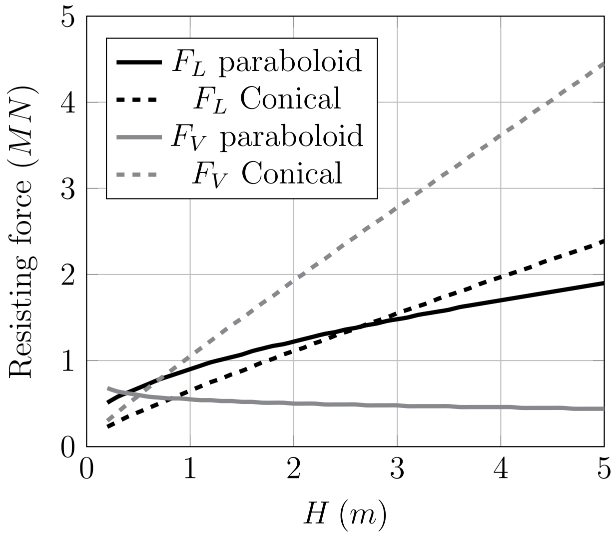

Figure 5.14: Paraboloid vs Conical shaped rock

Although the deformation mechanisms are similar, the figure clearly shows that the resistant force (especially its vertical component) differs significantly when the penetration height exceeds $1m$, meaning that the damage extent may greatly differ if the rock is approximated by a conical or paraboloid shape. The influence of the rock shape will be more deeply discussed in Section 5.6.

5.3 Response of transverse floors

5.3.1 Literature review

As a continuation to the previous work, the response of transverse members is now investigated. Unlike the case of ship sliding for which all the authors agree on the deformation modes, there does not appear to be any consensus on the response of transverse members in a raking deformation mode.

Puente [119] reported that the main difficulty lies in treating the welded intersection between outer / inner bottom and transverse floors. According to him, the response of transverse floors may be decomposed into three steps:

1. When the lower edge of the floor comes in contact with the rock, the floor mainly resists through membrane stretching.
2. After some indentation, fracture appears at the junction between floor and bottom and a vertical crack rapidly propagates as the rock penetrates into the floor.
3. Once the opening is large enough to clear the rock, the floor no more contributes to the energy dissipation process.

According to *Wang et al.* [17], as the floor is subjected to significant transverse indentation, in plane membrane forces mainly govern its response. Therefore, bending deformation can be neglected and a beam model is used to model the response. On its side, from the analysis of the NSWC test described in subsection 3.2.3, *Simonsen* [11] assumed the floor to be crushed vertically due to the creation of the two flaps on the bottom plating. The deformation mode is then similar to the floor crushing mechanism presented in section 4.4, except that a vertical crack propagates into the floor. The energy is thus mainly absorbed through plastic bending and crack propagation. A sketch of the deformation mode assumed by *Simonsen* [11] is depicted in Figure 5.15.

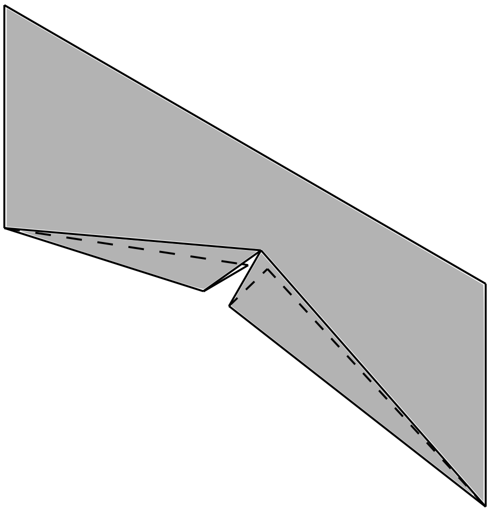

Figure 5.15: Deformation mode assumed by *Simonsen* [11]

On the other side, from parametric studies, *Zhang* [156] proposed to smear the floor into the bottom plating thickness to estimate the total resisting force a ship hull. More recently, *Sun et al.* [13] performed a number of finite element simulations on a double bottom structure and derived analytical solutions for the response of transverse floors.

The latter were assumed to mainly suffer from membrane straining due to large out of plane displacement. Finally, from the observation of the NSWC test, Rodd [70] reported that the crack tends to propagate rapidly from the outer shell to the transverse floor. A vertical crack develops inside the floor and further propagates to the inner shell.

It transpires from all aforementioned studies that the crushing mechanism of transverse floors is quite complex. Although *Heinvee* [20] stated that transverse members contribution in ship raking remains moderate compared to outer and inner shells, the response of the floors will be analytically investigated in the next subsection considering a paraboloid shaped rock.

5.3.2 Analytical developments

In this subsection, it is also assumed that the floors are mainly subjected to membrane stretching and plastic bending. However, during a grounding event, the deformation of transverse members is usually large and it is commonly assumed that bending contribution can be neglected. To avoid any redundancy, the formulation will focus on one side of the floor, i.e. $y \in [0, a_1]$ but the contribution of the other side may be easily obtained by replacing a_1 by $a_2 = a - a_1$ in subsequent formulae.

The floor is supposed to be made of independent fibres oriented along the η and ζ axes without any shearing as depicted on Figure 5.16. Such plate strip assumption has also be made by various authors like *Wierzbicki* & *Simonsen* [157] or *Buldgen et al.* [158] for instance. Assuming moderately large deflection, strain-displacement relations may be written as:

$$\varepsilon_\eta = \frac{1}{2}\left(\frac{\partial u}{\partial y}\right)^2 \tag{5.29}$$

$$\varepsilon_\zeta = \frac{1}{2}\left(\frac{\partial u}{\partial z}\right)^2 \tag{5.30}$$

Where $u(y, z)$ is the plate out-of-plane displacement field, defined as the product of functions $f(y)$ and $g(z)$ illustrated in Figure 5.17. As shown in Figure 5.17, $f(y)$ is decomposed into two parts denoted by f_1 and f_2.

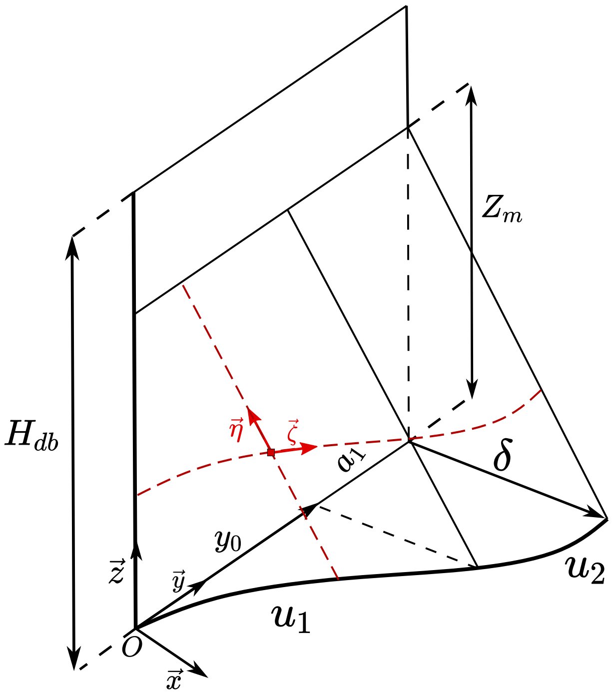

Figure 5.16: Displacement fields u_1 and u_2

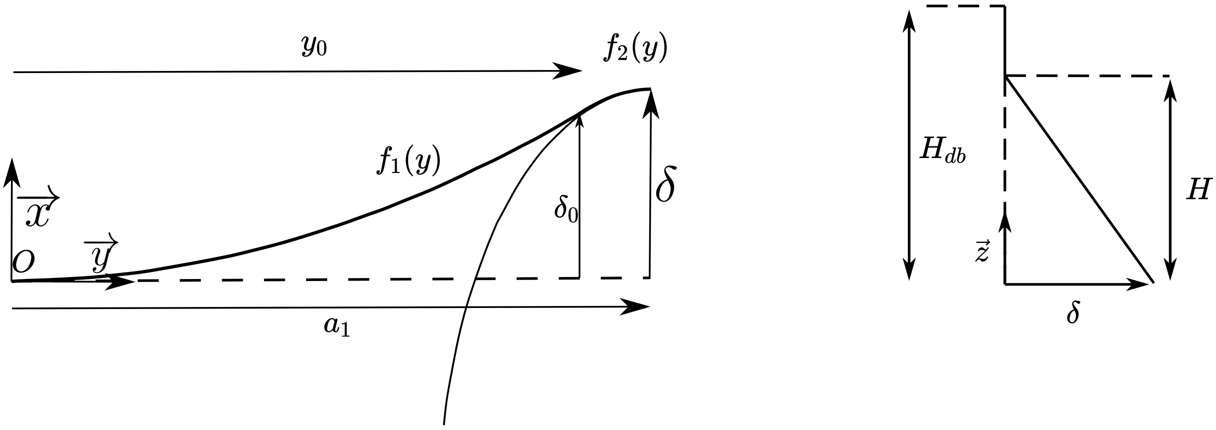

Figure 5.17: Function $f(y)$ (left) - Function $g(z)$ (right)

At the intersection of the floor with the girder - point O ($y = 0$), the plate is supposed to be clamped and at $y = y_0$, f_1 and f_2 must be continuous. Such conditions lead to the following relations:

$$\begin{cases} f_1(0) = 0 \\ \frac{\partial f_1(0)}{\partial y} \\ f_1(y_0) = f_2(y_0) \\ \frac{\partial f_1(y_0)}{\partial y} = \frac{\partial f_2(y_0)}{\partial y} \end{cases} \tag{5.31}$$

Function f_1 is assumed as a 2^{nd} order polynomial function defined in the interval $y \in [0, y_0]$:

$$f_1(y) = \delta_0 \left(\frac{y}{y_0} \right)^2 \tag{5.32}$$

Function f_2 is defined in the interval $y \in [y_0, a_1]$ and reflects the fact that the floor matches the shape of the rock:

$$f_2(y) = \delta - R_x + \frac{R_x}{R_y} \sqrt{R_y^2 - (y - a_1)^2} \tag{5.33}$$

Along the vertical axis, the floor is supposed to deform linearly such as:

$$g(z) = 1 - \frac{z}{z_m} \quad \text{with } z_m = min\,(H, H_{db}) \tag{5.34}$$

Finally, the resulting displacement fields u_1 and u_2, illustrated in Figure 5.16, may be written as:

$$u_1(y,z) = \delta_0 \left(\frac{y}{y_0} \right)^2 \left(1 - \frac{z}{z_m} \right) \tag{5.35}$$

$$u_2(y,z) = \left(\delta - R_x + \frac{R_x}{R_y} \sqrt{R_y^2 - (y - a_1)^2} \right) \left(1 - \frac{z}{z_m} \right) \tag{5.36}$$

In Eq. 5.36, R_x and R_y represent the longitudinal and transverse radii of the rock at the level of the outer plate, and are calculated as $R_x = \sqrt{H/C}$ and $R_x = \sqrt{H/E}$.
So far, y_0 has not been defined. y_0 is found by solving Eq. 5.37, which traduces the compatibility of the slope at $y = y_0$ for u_1 and u_2. As such equation is not easily hand-tractable, a numerical approach is used to find y_0.

$$2 \left(\delta - R_x + \frac{R_x}{R_y} \sqrt{R_y^2 - (y_0 - a_1)^2} \right) = \frac{R_x}{R_y} \frac{y_0 (a_1 - y_0)}{\sqrt{R_y^2 - (y_0 - a_1)^2}} \tag{5.37}$$

Once the displacement field is known, resisting forces are obtained by integrating the respective contributions of longitudinal and vertical fibres:

$$F_\zeta = \sigma_0 t_f \int_y \int_z \frac{\partial u}{\partial y} \frac{\partial^2 u}{\partial \delta \partial y} dydz \tag{5.38}$$

$$F_\eta = \sigma_0 t_f \int_y \int_z \frac{\partial u}{\partial z} \frac{\partial^2 u}{\partial \delta \partial z} dydz \tag{5.39}$$

Where t_f is the floor thickness. Finally, the floor longitudinal resisting force F_L is simply the sum of Eqs. 5.38 and 5.39. More details about the derivation of F_ζ and F_η are given in Appendix C.1.

For a given value δ^*, the rock is supposed to enter in contact with the upper edge of the floor if $H \geq H_{db}$ - see Figure 5.18. The upper edge of the plate must then conform to the rock shape. The displacement field is thus linearly interpolated between the amplitude function at $z = 0$, $f_0(y)$ and $z = H_{db}$, $f_{H_{db}}(y)$.

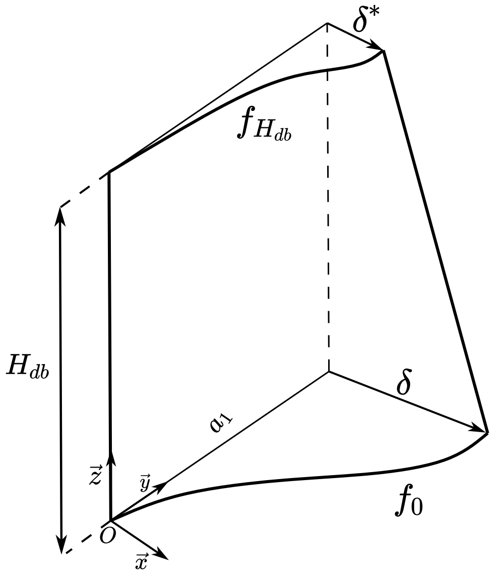

Figure 5.18: Double impact on floor

$$u(y, z) = f_0(y)\left(1 - \frac{z}{z_m}\right) + f_{H_{db}}(y)\frac{z}{H_{db}} \tag{5.40}$$

The procedure to find the floor resisting force in this case is as follows:

1. Solve Eq. 5.37 with $R_x = \sqrt{H/C}$, $R_y = \sqrt{H/E}$ and $\delta = \delta$.
2. Compute the resisting force using Eqs. C.1 to C.7
3. Solve Eq. 5.37 with $R_x = \sqrt{(H - H_{db})/C}$, $R_y = \sqrt{(H - H_{db})/E}$ and $\delta = \delta - \delta^*$.
4. Compute the resisting force using Eqs. C.1 to C.7
5. Sum the elementary forces to obtain F_L

All the previous developments are valid as far as there is no failure in the transverse member. However, after a certain level of penetration, the resulting large elongation leads to material rupture. When the strain ε_η (respectively ε_ζ) becomes larger than a threshold failure strain value ε_c, the corresponding resistant force is set to zero.

$$\varepsilon_\zeta = 2Ay_0^2 \quad \geq \ \varepsilon_c \quad \Rightarrow \ F_\zeta = 0 \tag{5.41}$$

$$\varepsilon_\eta = \frac{1}{2}\left(\frac{\delta}{Z_m}\right)^2 \ \geq \ \varepsilon_c \quad \Rightarrow \ F_\eta = 0 \tag{5.42}$$

According to *Zhang* [37], *Lützen et al.* [159] or *Buldgen et al.* [160], the threshold value ε_c should be taken in a range of 6% to 12%. In this study, a threshold value of 12% is found from numerical simulations based on the failure criteria proposed by *Lehmann & Peschmann* [87].

5.3.3 Numerical validation

For the purpose of validating the simplified formulations, several ship raking scenarios are simulated with the non-linear finite element solver *Ls-Dyna*. The ship double bottom considered is $12m$ long and $17.1m$ wide. A mesh size of $30mm$ is chosen for the crushed areas to comply with the mesh convergence results presented in Chapter 3.

An "Automatic surface to surface" contact is set between the plate and the rock with a static friction coefficient of 0.3. The bottom structure is illustrated in Figure 5.19 while its main particulars are listed in Table 5.4. Longitudinal secondary stiffeners attached to bottom plating are intentionally omitted. However, they can be taken into consideration using a smearing approach based on the stiffeners cross-sectional area and spacing.

The rock is assumed to be perfectly rigid and is moved horizontally into structure with a constant speed of $5m/s$. Five different rocks are considered in the analysis, which parameters are listed in Table 5.1. Finally, four impact heights $H = 0.75m - 1m - 1.4m - 3m$ are considered. As the height of the double bottom is $1.6m$, both outer and inner shells are crushed when $H = 3m$. Combining the 5 different rock geometries with different rock penetrations leads to the study of 20 scenarios (numbered 31 to 50 hereafter).

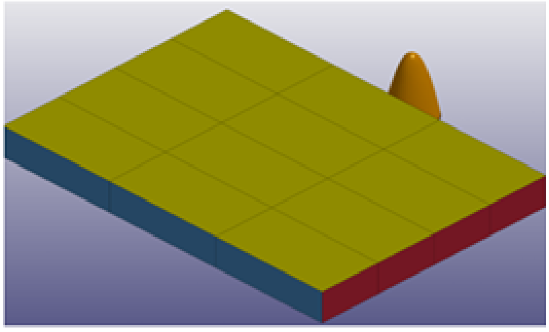

Figure 5.19: Finite element model for raking validation (without the mesh)

Item	Value (mm)
Outer bottom plating thickness (t_b)	15
Inner bottom plating thickness (t_i)	10
Floor thickness (t_f)	15
Girder thickness (t_g)	20
Double bottom height (H_{db})	1600
Floor spacing (χ_f)	3000
Girder spacing (χ_g)	5700

Table 5.4: Ship characteristics for raking accident

For each scenario, the dissipated energy calculated by the proposed analytical model is compared in Table 5.5 to the corresponding numerical result and the deviation is calculated according to Eq. 4.30.

Case id	Rock id	μ	H (m)	Internal energy Num. (MJ)	Internal Ana. (MJ)	Deviation
31	1	0.3	0.75	0.5	0.55	-10.0%
32	1	0.3	1	0.7	0.82	-17.1%
33	1	0.3	1.4	1.05	1.2	-14.3%
34	1	0.3	3	1.86	1.45	22.0%
35	2	0.3	0.75	0.45	0.5	-11.1%
36	2	0.3	1	0.65	0.73	-12.3%
37	2	0.3	1.4	1.02	1.12	-9.8%
38	2	0.3	3	1.65	1.43	13.3%
39	3	0.3	0.75	0.5	0.52	-4.0%
40	3	0.3	1	0.65	0.76	-16.9%
41	3	0.3	1.4	1.02	1.18	-15.7%
42	3	0.3	3	1.64	1.43	12.8%
43	4	0.3	0.75	0.6	0.63	-5.0%
44	4	0.3	1	0.7	0.82	-17.1%
45	4	0.3	1.4	1.2	1.25	-4.2%
46	4	0.3	3	1.88	1.52	19.1%
47	5	0.3	0.75	0.58	0.57	1.7%
48	5	0.3	1	1	0.87	13.0%
49	5	0.3	1.4	3.36	1.3	61.3%
50	5	0.3	3	2.3	1.62	29.6%

Table 5.5: Floor Raking - Comparison of dissipated energy

It is observed that except for cases 34, 49 and 50, the deviation does not exceed 20%. The large discrepancy observed for the case 49 may be explained by the tearing mode of the outer bottom plating observed in *Ls-Dyna* simulation, which is a concertina-like tearing cut rather than a clean cut, see Figure 5.20. The simplified model derived in this work is unable to capture the concertina tearing mechanism and using the simplified expression proposed by *Wierzbicki* [93] would probably improve the prediction of the dissipated energy for this particular case.

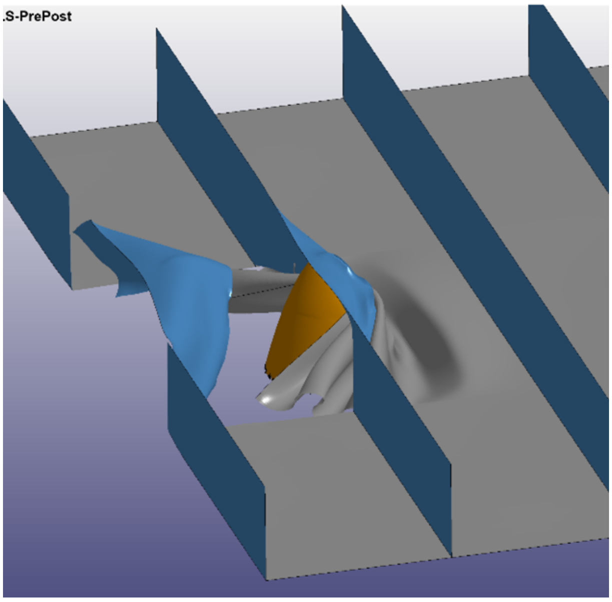

Figure 5.20: Concertina tearing in raking simulation

The discrepancy related to cases 34 and 50, higher than 20%, may be explained by a tear propagating along the floor / outer shell junction, as highlighted by the red rectangle depicted on the right-hand side of Figure 5.21. Consequently, the floor lower edge is free to deform, and the rupture of the transverse member appears later.

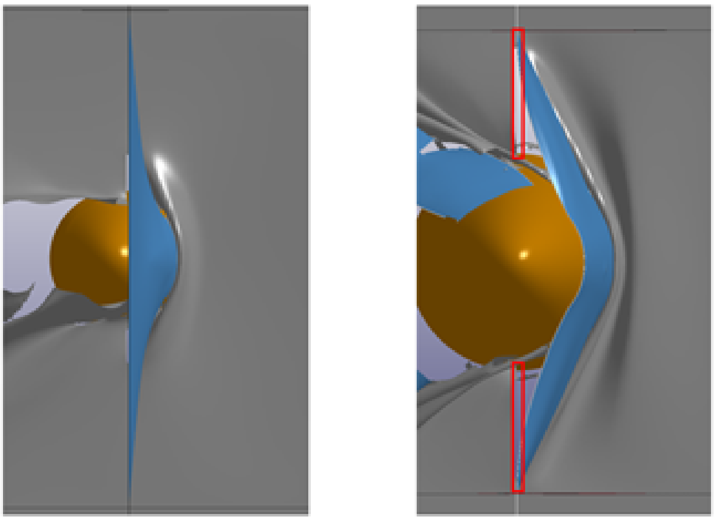

Figure 5.21: Deformation of floor from numerical simulations

It is worth noting that as expected, the amount of absorbed energy is very sensitive to the critical failure strain. For example, increasing by 10% the threshold value used in analytical calculations (12% → 13.2%) allows to decrease the deviation down to 13.9% for case 34 and 22.6% for case 50.

To conclude, one can say that the response of transverse members is quite difficult to model as there exists a strong coupling between the bottom plating and the floors. From numerical simulations, one observe that the next bottom plating section prevents the deformation of the floor. The deformation is thus mainly localised near the impact point.

Since the super-element approach assumes a complete decoupling between the neighbouring elements, the resistance force of the floor cannot be captured with the accuracy of the finite element method. Additionally, it should be emphasised that weld between bottom and floor are not considered neither in the numerical nor in the analytical calculation. Although imperfect, the simplified model provides a reasonable approximation of the energy dissipated by transverse components.

5.4 Response of longitudinal girders

5.4.1 Literature review

Although experimental research and numerical simulations have shown the importance of girders in the energy dissipation process for the case of sliding bottom, there are limited publications on the response of these main longitudinal stiffeners when the hull has fractured.

Based on the overall deformation process of the bottom, *Simonsen* [11] assumed that shearing is the only relevant absorbing energy process. *Samuelides et al.* [122] highlighted that when the rock is situated just below the girder, it behaves in the same way as when the shell is intact, i.e. a “wave” pattern is created. On its side, *Zhang* [156] proposed to smear their thickness into the bottom plating. Nevertheless, it is believed that a deep longitudinal girders cannot be treated using the smearing approach as they undergo very specific deformation modes. *Heinvee* [20] found out from numerical simulations that if the rock is located just under a longitudinal girder, the grounding force can be up to 50 % higher as compared to the situation when the rock is located between two girders. Moreover, when a girder is involved in the deformation, Heinvee reported that the rupture of the outer bottom is triggered almost instantly.

5.4.2 Analytical development

First numerical simulations performed in the frame of this thesis pointed out at least two different responses of longitudinal girders, depending on the rock shape. For wide rocks, the girder deformation is similar to the one observed in sliding condition and the analytical formulae derived in Chapter 4 may be applied. On contrary, a sharper rock does not stay under the girder but rather slides on its side, which leads to a different deformation mechanism. A sketch of the deformation undergone by a girder impacted by a sharp rock is illustrated on Figures 5.22a and 5.22b.

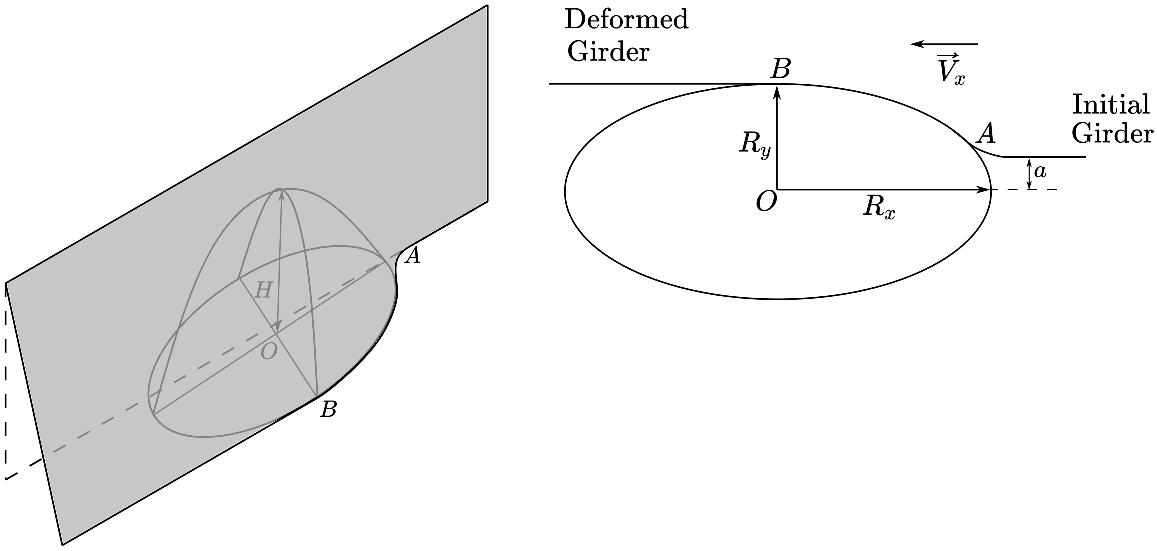

(a) Girder deformation raking - 3D view

(b) Girder deformation raking - Top view

Figure 5.22: Girder deformation with sharp rock

As the girder is forced to pass the rock, it is pushed transversely and conforms to the rock shape. The structure undergoes a shear strain u_0/H_{db} where H_{db} is the height of the girder and u_0 is the elongation of its lower edge expressed as:

$$u_0 = \int_0^{x_2} \sqrt{1 + \frac{R_y^2}{R_x^2}\frac{x^2}{R_x^2 - x^2}}\, dx - x_2 \tag{5.43}$$

Where x_2 is given as:

$$x_2 = R_x\sqrt{1 - \frac{a^2}{R_y^2}} \tag{5.44}$$

The parameter a simply traduces that rock and girder are necessarily aligned along the longitudinal direction. Unfortunately, Eq. 5.43 cannot be solved analytically as it involves an elliptic integral of second kind. A numerical integration is thus performed to calculate u_0 and the membrane energy rate is obtained by:

$$\dot{E}_m = \frac{2}{\sqrt{3}}\sigma_0 t_h V_x \int_0^{H_{db}} \frac{1}{2}\frac{u_0}{H_{db}} dz = \frac{1}{\sqrt{3}}\sigma_0 t_h u_0 V_x \tag{5.45}$$

Longitudinal and transverse bending contributions are added in the same way as for the response of bottom plating in sliding grounding.

$$\dot{E}_{bL} = \frac{4}{3} M_0 \frac{H_{db}}{R_m} V_x \tag{5.46}$$

Where R_m may be approximated as the average radii of the ellipse:

$$R_m = \frac{2R_x + R_y}{3} \tag{5.47}$$

And the transverse bending is accounted for by the following formulation:

$$\dot{E}_{bT} = 4M_0 \frac{R_y - a}{\sqrt{H_{db}^2 + 4\left(R_y - a\right)^2}} V_x \tag{5.48}$$

Once again, the total plastic force is obtained by dividing the total energy rate by V_x and writes:

$$F_P = \frac{1}{\sqrt{3}}\sigma_0 t_h u_0 + \frac{4}{3} M_0 \frac{H_{db}}{R_m} + 4M_0 \frac{R_y - a}{\sqrt{H_{db}^2 + 4\left(R_y - a\right)^2}} \tag{5.49}$$

Finally, longitudinal and vertical components of the resisting force are calculated as $F_L = F_P g_f$ and $F_V = F_L K_v$.

5.4.3 Numerical validation

To validate the previous formulations, numerical simulations are performed and compared to the analytical results. The rock is off-centred by a distance $a = 0.1\ m$. The model is similar to the one depicted on Figure 5.19. Six different simulations including three different rock shapes and two penetrations height are carried out. Result in terms of plastic force are listed in Table 5.6.

Case id	Rock id	H *(m)*	Plastic force Num. *(MN)*	Plastic force Ana. *(MN)*	Deviation
51	1	0.4	0.34	0.35	2.86%
52	1	0.9	0.58	0.48	17.2%
53	3	0.4	0.29	0.33	-13.8%
54	3	0.9	0.46	0.43	7.2%
55	4	0.4	0.52	0.45	13.4%
56	4	0.9	0.86	0.67	22.1%

Table 5.6: Girder plastic force in ship raking

Several conclusions may be drawn from the analysis of Table 5.6.

First, for a given rock shape, it is observed that the plastic force increases with the penetration depth H. The last column of Table 5.6 shows a relative good correlation between numerical and analytical predictions, with an average deviation of around 12.5%. Nevertheless, it is worth to remark that the welds between girders and bottom plating as well as between girders and floors are not considered in the models. That is why these results should be taken with caution since according to *Chen et al.* [64], the presence of welds may have a significant effect on the deformations process and increase the resisting forces.

5.5 Overall double hull

Now that the elementary responses of bottom plating, transverse members and longitudinal girder have been individually validated, the proposed theoretical model is compared to numerical simulations of a full ship bottom section running aground a paraboloid shaped rock.

5.5.1 Impact between two longitudinal girders

At first instance, the case of a double bottom impacted between two longitudinal girders by a paraboloid shape rock is considered. Analytical and numerical results are then compared in terms of dissipated energy. The finite element model considered in Section 5.3 and presented in Figure 5.19 is used for the validation. The friction coefficient μ is set to 0.3.

For each scenario, the total dissipated energy calculated as the sum of internal and sliding energies is post-processed from *Ls-Dyna* simulations. Then, the dissipated energy given by the present model (referred as *Model* in Table 5.7) is confronted not only to the numerical results but also to the ones obtained from two additional analytical models:

- The first one consists in smearing the floors into the outer bottom plating by increasing the thickness of the latter. In Table 5.7, this model is referred as *smeared*.
- The second model is the one proposed by *Zhang* [156] and referred as *Zhang* in Table 5.7.

Regarding the so-called *smeared* model, the equivalent plate thickness of the outer bottom plating is calculated according to Eq. 5.1, giving a value of $23mm$.

When the double bottom is impacted, tearing formulation is applied in a similar way to the inner shell using $H - H_{db}$ instead of H. The values of dissipated energies post-processed from the different models are compared in Table 5.7 and the deviations listed in the three last columns are always expressed with respect to numerical results.

Case id	Rock id	H	Num. (MJ)	Model (MJ)	Smeared (MJ)	Zhang (MJ)	Model Deviation	Smeared Deviation	Zhang Deviation
57	1	0.75	9.7	9.2	12.7	11.4	6.0%	-30.3%	-16.9%
58	1	1	12.3	11.2	14.7	12.1	8.9%	-19.9%	1.9%
59	1	1.4	16.4	14.1	17.4	12.9	14.6%	-6.3%	21.5%
60	1	3	29.8	28.2	31.8	20.2	5.5%	-6.4%	32.1%
61	2	0.75	9.6	8.4	11.7	10.9	12.9%	-22.0%	-13.1%
62	2	1	11.6	10.2	13.5	11.5	12.6%	-16.3%	0.6%
63	2	1.4	14.7	12.8	15.8	12.3	12.8%	-8.0%	15.9%
64	2	3	25.3	24.9	28.3	19.4	1.8%	-11.7%	23.5%
65	3	0.75	9.74	8.7	12.2	10.5	10.3%	-24.7%	-7.8%
66	3	1	11.2	10.6	14.1	11.1	5.4%	-25.2%	0.8%
67	3	1.4	14.0	13.4	16.6	11.9	3.9%	-18.3%	15.0%
68	3	3	26.3	26.2	29.8	18.6	0.1%	-13.4%	29.0%
69	4	0.75	11.6	10.3	14.1	13.1	11.3%	-21.4%	-12.4%
70	4	1	13.9	12.6	16.7	13.9	9.3%	-20.3%	0.40%
71	4	1.4	19.3	15.9	20.2	14.8	17.3%	-5.1%	23.1%
72	4	3	33.5	34.8	38.2	23.3	-3.8%	-13.7%	30.7%
73	5	0.75	12.4	9.9	13.9	13.1	19.7%	-11.8%	-5.5%
74	5	1	16.5	12.3	16.4	13.9	25.3%	0.7%	16.0%
75	5	1.4	88.8	15.6	19.8	14.8	82.2%	77.5%	83.2%
76	5	3	37.7	34.6	36.8	23.2	8.1%	2.4%	38.3%

Table 5.7: Double bottom structure raking - Comparison dissipated energy

It is observed that apart from cases 73, 74 and 75, the discrepancy between the proposed model and finite element simulations keeps under 18%, showing the relatively good accuracy of the simplified method to estimate the energy absorbed during plastic deformation of a grounded ship double bottom. Excluding theses cases, the average deviation calculated on the 17 remaining scenarios is around 8.5%.
From numerical simulations, it also appears that when the rock impacts a floor at a height close to the double bottom ($H = 1.4m$), the inner shell tends sometimes to deform vertically. For instance, in scenario n°71, the deflection of the inner shell is around 13 cm at the middle of the junction between floors and inner bottom. This illustrates the strong interaction that may occur between floors and double bottom plating, which is not considered by the analytical model.

Cases 73, 74 and 75 correspond to the rock n°5, for which transverse and longitudinal radii are the same ($C = E = 2$). As shown in Figures 5.20 and 5.23, the relatively large width of this rock causes the formation of concertina-like folds in the outer shell. As for cases n°73 and n°74, these folds start to form in the outer shell just behind the crushed floors, together with a non-centred rupture that propagates - see Figure 5.23. This rupture leads to the formation of additional folds (braided cut) that absorb a quite significant amount of energy.

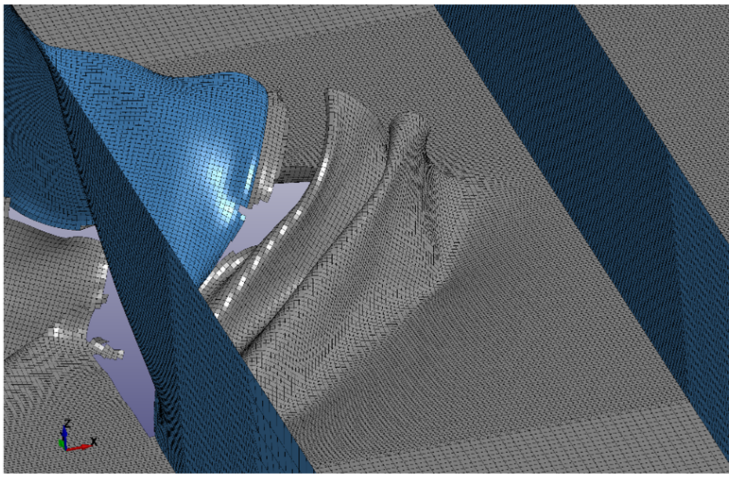

Figure 5.23: Non centred rupture and additional folding

Compared to the numerical simulations, the *smeared* model is found to overestimate the dissipated energy by 15% in average, while Zhang's model either overestimates or underestimates the energy with an average deviation of 17%. However, for scenarios where the double bottom is involved in the deformation, Zhang's model tends to underestimate the dissipated energy by almost 30%.

Finally, both numerical and analytical simulations reveal that the energy dissipated by transverse members is less than 20% of the total dissipated energy. That is why, as proposed by *Heinvee et al.* [153], transverse members may be omitted in a preliminary calculation since they dissipate a small portion of the initial kinetic energy.

5.5.2 Impact under a longitudinal girder

As a continuation of the previous part, the case of an impact involving a longitudinal girder is now investigated. For this purpose, different finite element simulations are performed using the model depicted in Section 5.4. The energies dissipated by bottom plating, girders and floors deformation as well as friction, retrieved from numerical and analytical simulations, are compared in Table 5.8.

Case id	Rock id	H *(m)*	Total dissipated energy *(MJ)* Num.	Total dissipated energy *(MJ)* Ana.	Deviation
77	1	0.4	11.7	9.1	22.4%
78	1	0.9	18.3	15.4	15.8%
79	3	0.4	10.8	8.1	24.9%
80	3	0.9	17.7	13.1	26.2%
81	4	0.4	13.7	12.6	7.8%
82	4	0.9	22.2	21.6	3.0%

Table 5.8: Total dissipated energy - Girder full raking event

The discrepancy is around 16.7% in average and the deviation reaches 26% for the case 80, which is quite significant. The main reason is that the girder drastically constraints the deformation of the bottom plating (especially the formation of the flap) as illustrated on Figure 5.24. Indeed, one observe that only one flap is created and the deformation pattern of the outer shell is no longer symmetric. The simplified model is thus unable to correctly capture the coupled deformations of the outer shell and girder. Fortunately, it is worth noting that the model always underestimates the dissipated energy, which is conservative regarding the damage extent.

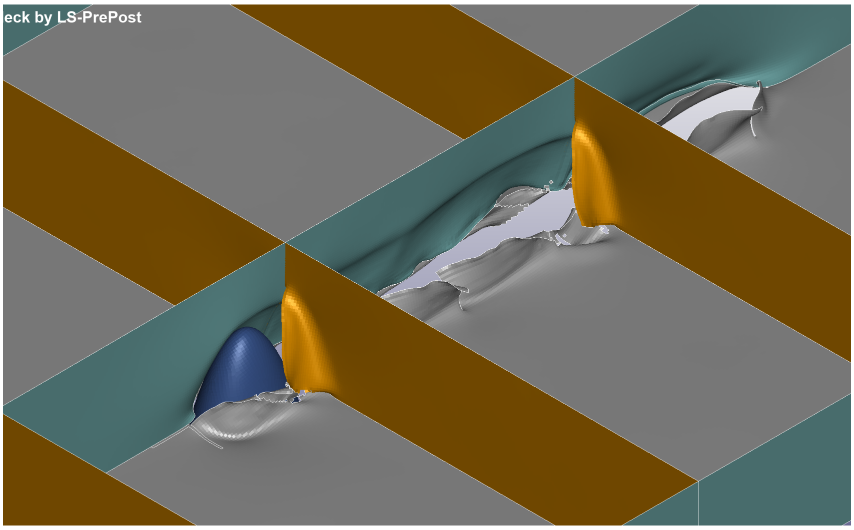

Figure 5.24: Hull deformation girder impact

Both numerical and analytical simulations reveal that the dissipated energy is equally distributed between longitudinal girders and bottom plating, which demonstrate the important role played by the girders in ship grounding. On the other side, the transverse floors are found to dissipate less than 5% of the total kinetic energy.

5.6 Analysis considering a real rock

In the same way as in Chapter 4, the simplified analytical models are now compared with finite element simulations of a ship raking on a real rock. Predictions provided by other model based on conical shaped rocks are also included in the comparison.

The real sharp rock which was again selected from Sormunen's paper [155] [1] is illustrated in Figure 5.25.

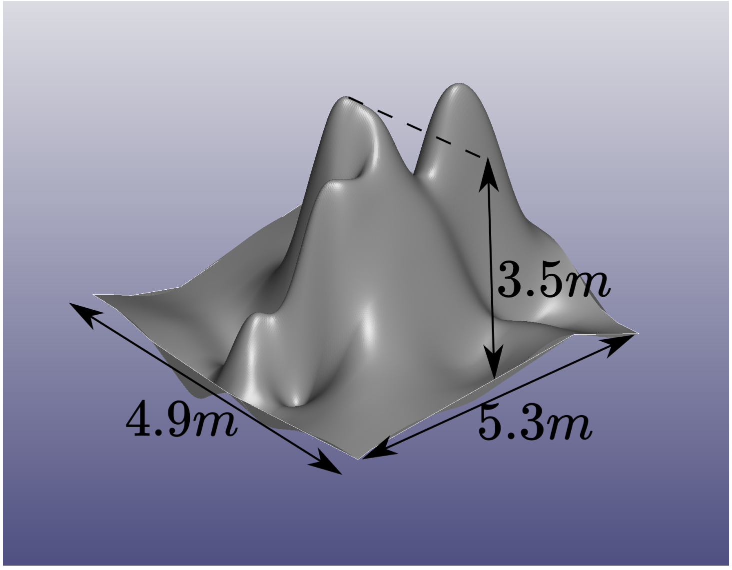

Figure 5.25: Sharp rock - from *Sormunen et al.* [155]

According to the literature, sharp rocks may be approximated as conical, paraboloid or wedge shapes. However, the latter is rather used in small scale tearing experiments than in simplified models for hard grounding analysis so only the simplified models based on conical and paraboloid shapes will be considered in this section. The objective is to confront the model developed in the frame of this thesis with both finite element simulations and conical shape based model proposed by *Simonsen* [141].

Looking at Figure 5.25, several "*peaks*" form the real sharp rock. Since the response of a raking plate is mainly governed by the rock width at outer shell level and by the splitting angle θ, it appears reasonable to assume in a first step that the plate is mainly torn by the front peak, that is the first impacted protuberance. The cone angle and paraboloid dimensional parameters that allow for the best fits with the front peak of the real rock are listed in Table 5.9.

Parameters	Conical	Paraboloid
φ	17.5°	-
C	-	3.7
E	-	6

Table 5.9: Real sharp rock - Simplified rock shape parameters

---

[1] Thanks again to Prof. Hirdaris and Dr Kim from Aalto University who provided the CAD file.

5.6.1 Unstiffened bottom plating

As for the smooth rock, the response of a single unstiffened bottom plating is first investigated. The plate considered is $5.7m$ width, $13m$ long and $15mm$ thick. Regarding the definition of the scenarios, four penetration heights in a range of $H \in [1.5\,;\,3]m$ as well as two friction coefficients ($\mu = 0.1 - 0.3$) are analysed. Numerical and analytical results in term of longitudinal and vertical forces are compared in Table 5.10, where $Para.$ and $Coni.$ refer to paraboloid and conical shape based models respectively.

Case id	H	μ	F_L Num. (MN)	F_V Num. (MN)	F_L Para. (MN)	F_V Para. (MN)	F_L Coni. (MN)	F_V Coni. (MN)	Dev. F_L Para.	Dev. F_V Para.	Dev. F_L Coni.	Dev. F_V Coni.
83	1.5	0.3	1.00	0.20	0.94	0.19	0.60	0.39	6%	4%	40%	-95%
84	2.0	0.3	1.22	0.33	1.11	0.18	0.76	0.53	9%	45%	37%	-60%
85	2.5	0.3	1.30	0.40	1.25	0.17	0.93	0.67	4%	57%	29%	-67%
86	3.0	0.3	1.31	0.45	1.38	0.16	1.08	0.80	-5%	64%	17%	-78%
87	1.5	0.1	0.70	0.29	0.66	0.27	0.28	0.49	6%	9%	59%	-70%
88	2.0	0.1	0.80	0.39	0.77	0.27	0.35	0.65	4%	31%	56%	-69%
89	2.5	0.1	0.90	0.51	0.86	0.26	0.41	0.81	4%	49%	54%	-57%
90	3.0	0.1	0.88	0.56	0.94	0.26	0.47	0.96	-7%	53%	46%	-71%

Table 5.10: Model comparison for real sharp rock

A first analysis of above table shows that the longitudinal component F_L is much better estimated by the model based on the paraboloid shaped rock. Among the height scenarios, the average discrepancy on F_L is 5.6% for this model and 42.5% for the model based on a conical shaped rock.

However, the vertical components F_V given by both simplified models do not correlate with numerical results. The average deviation is around 37.6% for the paraboloid rock and 69.5% for the conical one. To explain such results, let us have a deeper look on the tearing process. As shown by Figure 5.26, *clean* and *non clean* tearing modes are observed in numerical simulations, depending on the rock penetration depth. Note that the non clean cut depicted in Figure 5.26 (Right) is similar to the one observed by *Muscat-Fenech & Atkins* [121] and illustrated in Figure 5.2.

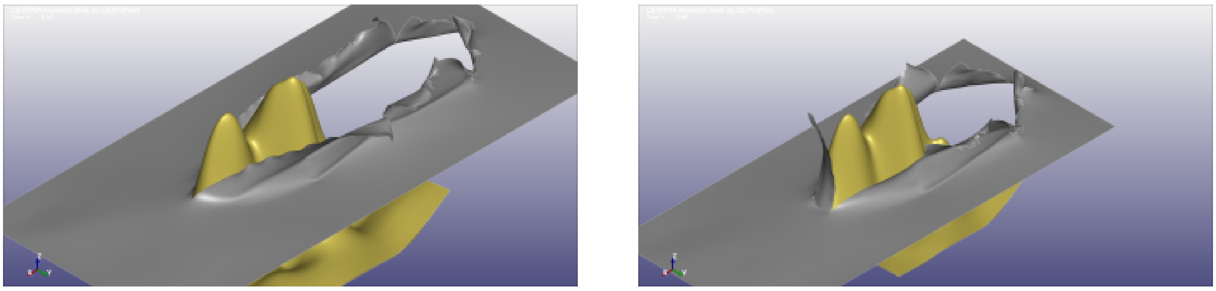

Figure 5.26: Two different tearing modes - Left: clean cut (case 83) - Right: Non clean cut (case 86)

The effect of friction on the resistant force is now discussed. When μ switches from 0.3 to 0.1, the deviation observed on F_L remains lower than 10% for the paraboloid shape based model while it increases by around 50% when the rock is represented by a cone. To explain this, the share of deformation energy post-processed from the three sets of simulations is compared on Figure 5.27. While it is similar in numerical and paraboloid shape based models, it is significantly underestimated by the model based on a conical rock. Consequently, when numerical simulations are run with $\mu = 0.1$, plastic deformation energy is by far predominant compared to sliding energy. On contrary, as the conical shape based model significantly underestimates the share of deformation energy, switching from $\mu = 0.3$ to $\mu = 0.1$ accentuates the deviation observed on F_L.

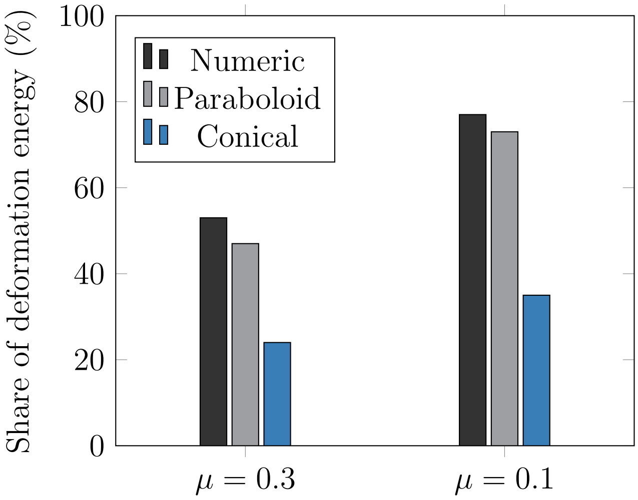

Figure 5.27: Share of deformation energy - Real sharp rock

Finally, it is noteworthy that a non zero transverse force F_T was also post-processed from finite element simulations.

There are many reasons for the discrepancies observed between numerical and analytical results:

1. As the real rock is not symmetric, the plate deformation is not symmetric so the transverse resistant force F_T is non zero. This is a limitation of both simplified models that are based on symmetric rock shapes, which implies that F_T is always zero.

2. The second peak of the real rock is wider than the first one. This causes a second contact to occur between the plate and the rock, which increases the plastic strain on the plate and dissipates additional energy. Figure 5.28a and Figure 5.28b illustrate the increase of plastic strain once the second contact has occurred (inside the red frame). The red frame also points out the dissymmetry of the rock as much plastic strain is visible on the right flap of the plate.

3. On the second peak, the real rock slope is less pronounced, as shown by Figure 5.29. Moreover, the rock slope in its lower part (left side) almost vanishes. As a consequence, when the penetration height H increases, the vertical resistant force F_V also increases. Such particularity is obviously not captured by the simplified models.

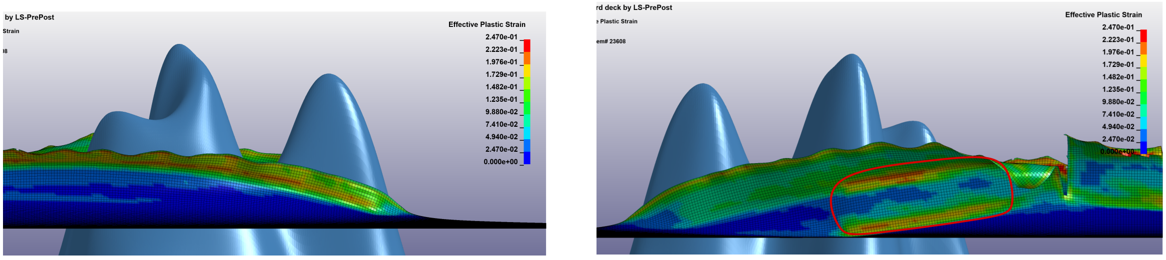

(a) Left flap (b) Right flap

Figure 5.28: Plastic strain distribution in both plate flaps - Sharp real rock

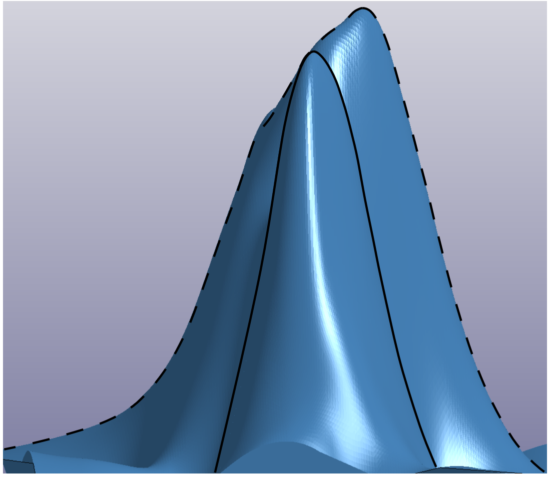

Figure 5.29: Front view of the sharp rock: left and right slopes are highlighted with dashed lines

Numerical simulations are then rerun considering only the front peak (the other peak is removed from the contact card). Resulting forces are post-processed considering the 8 (case 91 to 98) aforementioned scenarios and plotted in Figure 5.30, as well as the forces obtained for the entire rock and the forces given by the simplified model based on the paraboloid shaped rock.

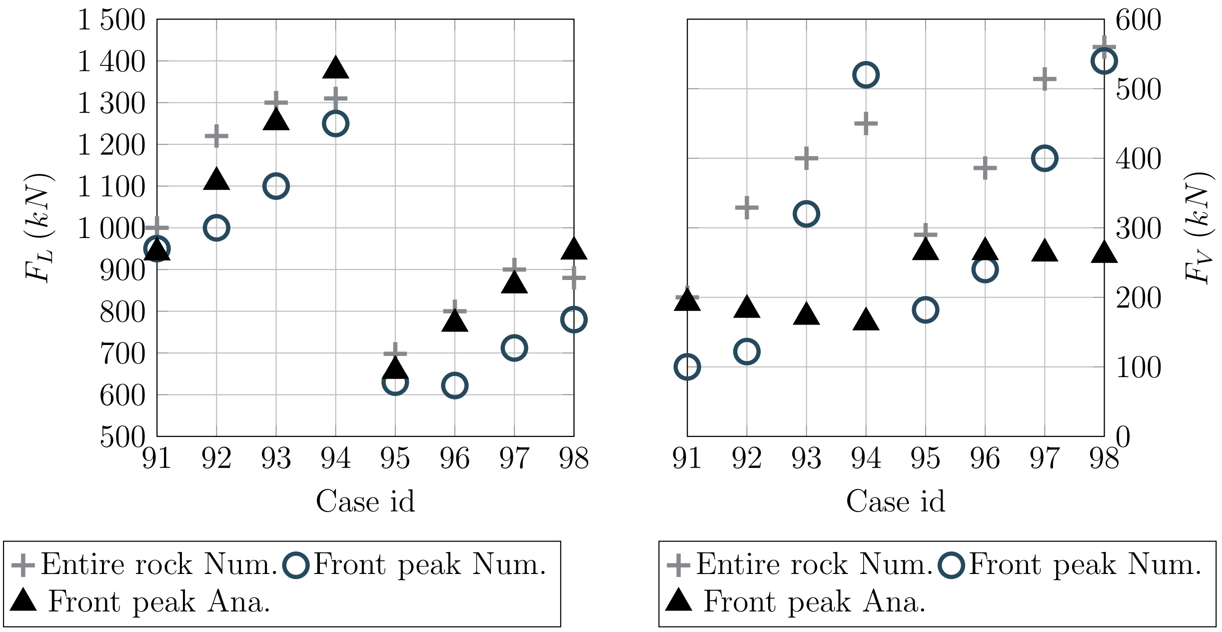

Figure 5.30: Sharp rock first peak comparison

In light of above figures, the longitudinal force F_L appears to be minimally affected by the absence of the second peak, while the vertical one F_V looses around $100N$ in the majority of the cases. This confirms that the plate response is mainly governed by the impact against the front peak. As expected, considering only this latter in the numerical simulations leads most of the time to a drop of both longitudinal and vertical forces since the contact with the second one does not occur anymore. However, although the longitudinal force is fairly well predicted by the “front peak” simplified approach, the vertical one still remains significantly underestimated.

Table 5.11 resumes the dissipated energy (plastic + sliding) post-processed once the plate has been torn along $5m$. The average discrepancy between analytical and numerical results post-processed from the model based on the full real rock is around 5.6%. The average discrepancy is higher, around 13.3%, with the results retrieved from the front peak numerical model. This last observation may appear contradictory with all above remarks. In fact, the paraboloid model slightly overestimates the resisting force, resulting in analytical predictions are luckily closer to the numerical results based on the full rock model. In other words, at least for this particular case, notwithstanding the underestimation of the vertical force, the dissipated energy is seen to be quite well predicted by the simplified approach.

Case id	H (m)	μ	Entire rock Num. (MJ)	Front peak Num. (MJ)	Front peak Ana. (MJ)	Deviation Entire rock	Deviation Front peak
91	1.5	0.3	5.00	4.75	4.71	5.9%	0.9%
92	2	0.3	6.10	5.00	5.55	9.0%	-11.0%
93	2.5	0.3	6.50	5.50	6.27	3.6%	-13.9%
94	3	0.3	6.55	6.25	6.89	-5.1%	-10.2%
95	1.5	0.1	3.49	3.15	3.29	5.9%	-4.3%
96	2	0.1	4.00	3.11	3.85	3.8%	-23.8%
97	2.5	0.1	4.50	3.56	4.31	4.2%	-21.1%
98	3	0.1	4.40	3.90	4.72	-7.2%	-20.9%

Table 5.11: Dissipated energy real sharp rock comparison

As for the real smooth rock, the sensitivity of the results to the rock dimensional parameters is now investigated. Rather than modelling only the front peak, a second way is to use a conical or paraboloid shape that fits the best as possible with the entire real rock. To do that, *Sormunen et al.* [155] proposed to use a cone having half apex angle $\varphi = 40°$. In Chapter 5, a paraboloid shape was defined taking $C = 0.7$ and $E = 2.2$, where E was found to give the best fit with the second peak width. If the front peak is also considered, the mean width of the rock is obtained taking $E = (2.2 + 6)/2 = 4.1$. Figure 5.31 illustrates the real sharp rock as well as fitted conical and paraboloid shapes.

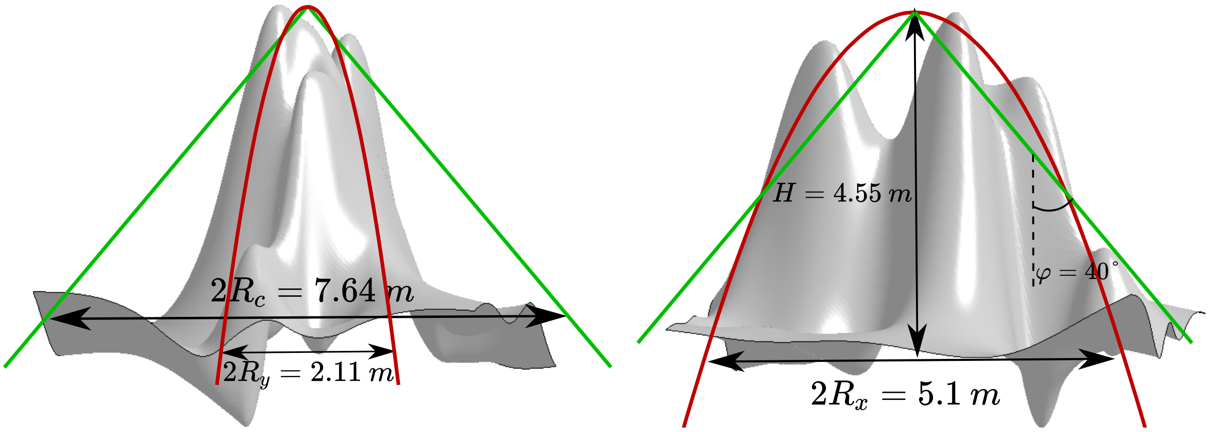

Figure 5.31: Sharp rock - global fitting

Table 5.12 illustrates the effect of fitting the full rock rather than only the front peak on the resisting forces over the 8 raking scenarios. The variation on forces are calculated with respect to the initial rock fit i.e., rock coefficients given in Table 5.9, while the deviation are expressed with respect to numerical results presented in Table 5.10.

Rock shape	Variation F_L	Variation F_V	Average deviation F_L	Average deviation F_V
Paraboloid	15.8%	140 %	14%	48%
Conical	23%	200%	30%	415%

Table 5.12: Real rock shape model influence

It is shown that the resistant force is globally increased when the entire rock is considered, the vertical force F_V is especially affected. However, both simplified models fail to correctly predict this latter.

Several conclusions may be drawn from above analysis:

1. First, the raking response of the hull appears to be mainly governed by the front peak of the rock which initiates the plate rupture. Therefore, it is more relevant to find a shape that fits rather the front peak than the entire rock.
2. Second, both conical and paraboloid shapes are unable to correctly predict the vertical force F_V. To better capture the vertical force exerted by this sharp rock, it would probably be necessary to better model the slope change at the lower part of the rock, using for instance a new approximation function.
3. Due to the dissymmetry of the real rock, the transverse force F_T appears to be of the same magnitude than F_V. This points out another limitation of the simplified models that are based on symmetric rock shapes, which implies that F_T is always zero.
4. Despite the above limitations, the energy dissipated during the grounding event is fairly well predicted by the simplified model developed in the frame of this thesis. In fact, this result conforms with the results obtained for the longitudinal force F_L because the plastic deformation energy mainly correspond to the work of F_L. The paraboloid model predicts F_L with a deviation of 5.6% (on average) with numerical results, while the model proposed by *Simonsen* [141] underestimates the longitudinal force by around 42.5%, which may be attributed to an overestimation of the sliding energy.

5.6.2 Double hull structure

The response of a double hull structure is now investigated and again the paraboloid shape based model is confronted to numerical simulations based on the real rock. The double hull structure considered in this subsection has already been presented in this chapter - see Figure 5.19. The friction coefficient μ varies from 0.3 to 0.1 and two penetration heights $H = 1.4 - 3m$ are considered. The ship is supposed to ground on the rock between two adjacent girders.

As a continuation to the previous work, two different numerical models have been set up. In the first model referred as "F_R", the full rock is considered while in the second one referred as "P_R", only the front peak is modelled. Dissipated energies at the end of the simulations are resumed in Table 5.13.

Scenario id	H	μ	Energy F_R Num. (MJ)	Energy P_R Num. (MJ)	Energy F_R Ana. (MJ)	Energy P_R Ana. (MJ)	Deviation F_R	Deviation P_R
99	1.4	0.3	19.2	12.5	13.9	10.9	27.6%	12.8%
100	1.4	0.1	14	9.3	8.55	7.8	38.9%	16.1%
101	3	0.3	31.2	24.3	25	24.4	19.9%	-0.4%
102	3	0.1	23.5	19.7	14.8	17.1	37.0%	13.2%

Table 5.13: Dissipated energy real rock double hull structure

Before comparing the results between numerical and analytical solutions, let us focus on the differences between the two numerical models F_R and P_R.

Table 5.13 reveals that the full rock numerical model dissipates more energy than the front peak one: +54% for cases 99-100 and +28% for cases 101-102. This is mainly due to the amount of energy absorbed by the bottom plating:
0.9 MJ/m in the F_R model versus 0.6 MJ/m in the P_R model for cases 99-100.

The classical deformation pattern of an unstiffened plate torn by a rock includes a cylindrical bent section (A to B) and a plane one (B to D), is drawn in blue on Figure 5.32. When the full bottom grounds on the real rock, an additional bent cylindrical section (F to D' in red) is formed. The material thus undergoes not only additional bending but also straining between B and F. This may explain that the energy absorbed by the structure is higher in the numerical simulation (+30 %) than in the simplified calculation. As such additional bent part was not observed for the unstiffened plate (subsection 5.6.1), one may conclude that some coupling seems to occur between transverse floors and bottom plating deformations.

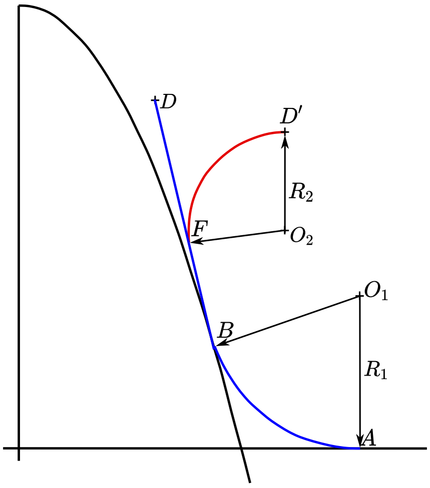

Figure 5.32: Real rock - Different observed deformations modes in raking

Note finally in Table 5.13 that the deviation between analytical and numerical results obtained when only the front peak of the rock is considered does not exceed 17%.

5.6.3 Conclusion regarding the real rock

The response of a ship hull grounding on a real sharp rock was investigated and simplified formulations developed in this chapter as well as analytical solutions proposed by *Simonsen* [141] considering a conical shaped rock were confronted to numerical results. Several conclusions may be drawn from this study. Starting with the conical shape, it appears that the internal dissipation rate is poorly modelled and the contribution of sliding energy is overestimated. Consequently, when the friction coefficient decreases, the error in term of total dissipated energy rapidly increases. In addition, the sensitivity study shows the great dependence of the predicting resisting force on the half top angle φ. On the other side, the simplified formulations based on a paraboloid shaped rock was found to give good predictions for the unstiffened bottom plating (the average deviation equals 5.6%). Moreover, the parameters C and E were found to have a limited effect on the response.

Nevertheless, it should be mentioned that neither of the two analytical models are able to accurately predict the vertical force F_V. Furthermore, since the real rock is clearly not symmetric, a non-zero transverse force F_T appears but both simplified models are unable to capture it.

The response of a double hull structure including floors and girders was also investigated. When the entire real rock was considered, a surprising new deformation mode was observed in the bottom plating. This new mechanism, depicted in Figure 5.32, absorbs more energy than the "classical" clean cut mode considered in the analytical developments. Despite this, a relative good agreement was found between numerical and paraboloid shape based models. Further research work seems however necessary since the analytical approach does not predict correctly both the vertical F_V and transverse F_T resisting forces. More complex non symmetric shapes should be considered to improve the prediction. This may be achieved by choosing two different coefficients C for left and right sides of the rock. Other mathematical function may also be used such as the exponential expression proposed by *Sormunen et al.* [145]:

$$z = Ae^{-x^2/B} \tag{5.50}$$

Where A and B are coefficients defining the height and the width of the rock respectively. Once again, non symmetrical rock may be easily created by imposing different value of B in left and right side of the rock - see Figure 5.33 for instance. This last representation, although more complex to handle analytically, is able to account for a change of curvature at the rock base, like the one observed on the real sharp rock - see Figure 5.29. Doing so may probably improve the prediction of both F_V and F_T.

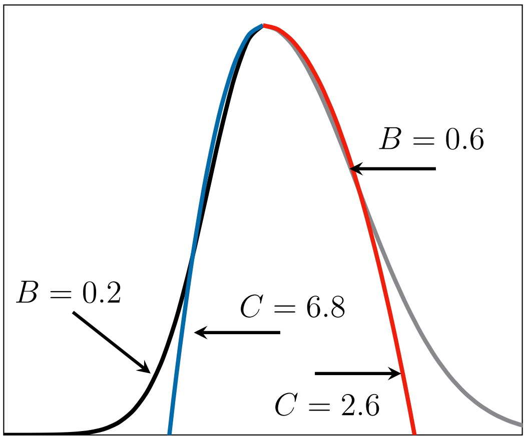

Figure 5.33: Non symmetric rock shape

5.7 Conclusion

A series of analytical expressions giving the resisting force of different ship bottom components in a raking event have been presented. The theoretical models derived in this chapter are based on the upper-bound theorem of plasticity associated with an idealised kinematic model.

First, an unstiffened bottom plating torn by a sharp rock has been studied. The main mechanisms of energy dissipation are friction, membrane straining, plastic bending, and crack propagation. Closed-form expressions derived for the plate tearing problem involve one free parameter, the so-called θ angle, which is supposed to adjust itself to give the lowest resisting force. The analytical model revealed that plate cutting is highly sensitive to the plate-rock friction coefficient μ as more than half of the total energy may be dissipated through friction. In addition, the vertical force was found to be almost insensitive to friction coefficient and vertical penetration depth.

The second analytical development focused on the response of transverse floors, which appears to be strongly coupled with the bottom plating. The presence of transverse floors tends to stop the propagation of the bottom plating opening. Behind the floor, the later is seen to fold before the crack re-initiates. The energy absorbed by transverse members is mainly dissipated through membrane straining. However, modelling their contribution with accuracy remains a challenge, knowing that they dissipate less than 20% of the initial kinetic energy.

The last components that have been investigated are the girders. The deformation undergone by these large longitudinal stiffeners was seen to highly depend on the rock shape. When a large rock is involved in the raking process, the girder deformation resembles the one undergone in a sliding process. However, when the rock becomes sharper, the girder no longer stays above the rock but rather slides on its edge. In this case, the energy is mainly dissipated by shearing as demonstrated by *Simonsen* [11].

In the majority of the raking scenarios investigated, analytical and numerical results are found to be in good agreement. In addition, the simplified model is most of the time conservative as it predicts a lower resisting force, resulting in a longer damage extent. Regarding the energy distribution, the mechanisms that contribute the most to energy dissipation are bottom plate tearing, longitudinal girders deformation and friction. All themselves, these mechanisms dissipate nearly 90% of the initial kinetic energy, the remaining 10% being absorbed by floor plastic deformation. As expressed by *Heinvee* [20], it is concluded that as a first approach, floors contribution can be omitted in the assessment of the ship damage extent.

Up to now, the ship was supposed to run aground over a rock following a prescribed horizontal trajectory with a constant penetration depth. However, in situations where the vessel is navigating in presence of waves, its oscillating heave motion sometimes leads to multiple breaches in the bottom plating, as observed by DNV-GL [29] and EMSA [161] in some real grounding events. Therefore, the effect of combined heave and surge velocities on the grounding response of a vessel will be investigated in the next chapter.

Chapter 6

Heave and surge combined motions

6.1 Introduction

In most of the literature available in grounding analysis (see for instance [20, 34, 162, 163]), the ship is supposed to run aground over a rock following a prescribed horizontal trajectory. As done in Chapters 4, 5, the bottom structure is often clamped on its edges and a moving rock is given horizontal displacement, which means that the action of hydrodynamic loads is totally ignored. In all simplified models found in the literature (see [97, 141] for instance), the ship heave motion is supposed to be negligible so only the instantaneous vertical penetration of the rock into the hull is considered. Simplified formulations derived for ship horizontal sliding in Chapter 4 or horizontal raking in Chapter 5 may thus be directly applied to estimate the response of the hull.

Recently, *Kim et al.* [51] and *Le Sourne et al.* [53] investigated the influence of ship rigid body motions on the grounded ship damage and demonstrated that even when the surge motion is predominant, the damage extent may be drastically affected by the hydrodynamic forces acting on the hull. Indeed, in situations where the vessel is navigating in presence of waves, her oscillating heave motion may lead to multiple breaches along the hull, as actually observed in some real grounding events [29, 161]. Recent numerical studies like the one performed by *Le Sourne et al.* [35] even showed that resulting overall damage can extend up to 4 times the one obtained by assuming only a horizontal movement for the ship. Resulting distribution of flooded compartments is thus likely to be greatly affected.

This chapter is focused on the derivation of specific analytical solutions considering both surge and heave velocities at the time the ship impacts the rock. Non fractured and fractured hull situations are considered and the criterion to switch from sliding to raking mode is discussed. In the following, “combined” grounding will refer to scenarios where the ship is giving both surge and heave initial speeds at the moment of impact.

6.2 Literature review

To the author's knowledge, there is no experimental, numerical or analytical studies of combined grounding problems reported in the literature. As a first approximation, ship combined grounding can in some way be analogous to ship oblique collision so a brief literature review on this topic is now presented.

Although right angle collision is the most studied scenario, several attempts have been made to derive simplified models for ship oblique collisions - see [37, 101, 107, 164–166] for instance.
Based on limit plastic approach, *Buldgen et al.* [107] succeeded in deriving simplified solutions for the response of ship components (side shell, transverse bulkheads, decks, secondary stiffeners) under oblique collision. The ship stem was represented by a parabolic shape but the simplified formulas were derived under the assumption of a punctual impact. A sensitivity analysis to the collision angle was then performed and the authors found that the worst case in term of damage extent was not necessarily the perpendicular impact but rather a 60° or 120° impact in situations where the initial struck ship velocity is non zero.

Recently, *Wang et al.* [101] extended some analytical solutions proposed by *Sun et al.* [167] to oblique collisions. The struck ship side components were supposed to be obliquely impacted by a raked bow.

From all previous studies, it transpires that friction plays an important role as a significant part of the initial kinetic energy is dissipated when the striking bow slides on the struck ship hull. This is all the more true since the collision angle φ is close to 0° or 180°. Although excellent agreement between analytical and numerical solutions was found by *Buldgen et al.* [107] or *Wang et al.* [101]), the proposed models have some limitations:

- They can correctly predict the response of a ship side an angle φ in a range of $[30°, 150°]$. Outside of this range, proposed solutions do not correctly capture the deformation and sliding mechanisms.
- They do not consider the shape of the impacting bow or bulb. However, it was shown in Chapters 4 and 5 that the response of the grounded hull is greatly dependent on the rock shape.

Considering typical V_z/V_x ratio expected in a combined grounding event (this ratio will be further discussed in Section 6.3), the angle φ usually lies in a range of $[0°, 20°]$, thus aforementioned solutions derived for ship-ship collisions no longer apply.

6.3 Quantification of initial ship velocities

First, it is necessary to have a more accurate idea about surge and heave initial speeds to consider in a cruise ship grounding simulation.

Youssef & Paik [4] performed a statistical analysis of real grounding accidents and found that the surge velocity at the moment of impact is related to the ship service velocity through a Weibull distribution expressed as :

$$\frac{V_{impact}}{V_{service}} = 3.84 \left(\frac{x+0.97}{1.7}\right)^{5.53} e^{-\left(\frac{x+0.97}{1.7}\right)^{6.53}} \tag{6.1}$$

Data extracted from *Youssef & Paik* [4] as well as the Weibull function are plotted on Figure 6.1.

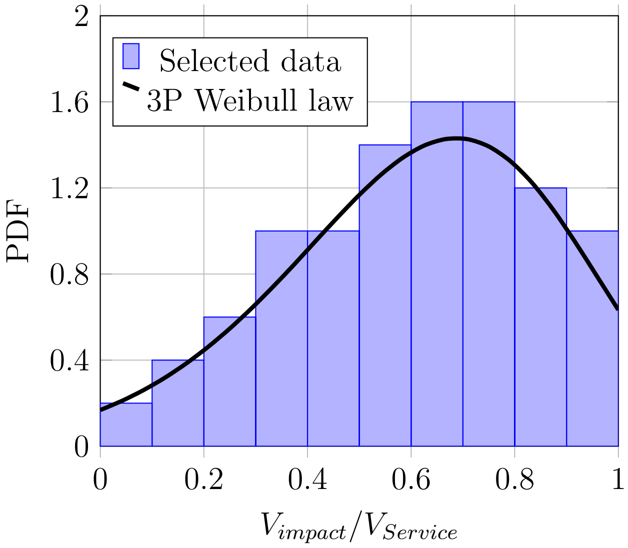

Figure 6.1: Relative ship velocity impact to ship service velocity

According to Eq. 6.1 and Figure 6.1, the average impact velocity is approximately 60% of the ship service speed. Considering a ship service velocity of round 20 knots, the initial surge velocity at impact may be estimated as $0.6V_{service} = 12$ knots $\approx 6\, m/s$.

On the other hand, the ship heave velocity is often disregarded and almost nothing has been published on expected heave velocity at the moment of impact, except the works of *Taimuri et al.* [109] and *Le Sourne et al.* [35]. Using a seakeeping code such as *HydroStar* from *Bureau Veritas*, the Response Amplitude Operator (RAO) obtained for the ship heave motion as well as resulting velocity at the ship's center of gravity may be estimated. As reported by *Le Sourne et al.* [35], Floodstand ship B heave velocity varies between 0 to $2m/s$ considering a maximum wave height of $4m$[1]. More details regarding *HydroStar* code will be given in Chapter 7.

---

[1] The author would like to thank Fabien Conti from Bureau Veritas (Nantes) who kindly provided these values extracted from *HydroStar* simulations

In summary, the expected initial surge velocity is about 12 knots while the heave velocity varies from 0 to 4 knots. Therefore, the collision angle $\varphi = atan(V_z/V_x)$ between the ship bottom and the rock may lie in a range of $[0°, 20°]$.

6.4 Response of bottom plating

6.4.1 Analytical development

As in Chapters 4 and 5, the response of the bottom plating is first investigated.

Let us consider a plate clamped on its edges, with a length a, a width b, and a thickness t_h. A coordinate system is attached to the plate at point O. At the beginning of the grounding event, the impact between the rock and the plate is located at $x = a_1$ and $y = b_1$ (gray color in Figure 6.2). After a while, the penetration of the rock into the bottom plating is equal to H and the distance between the rock apex S and the origin is now $a_1 + H/tan\left(\varphi\right)$ as illustrated on Figure 6.2.

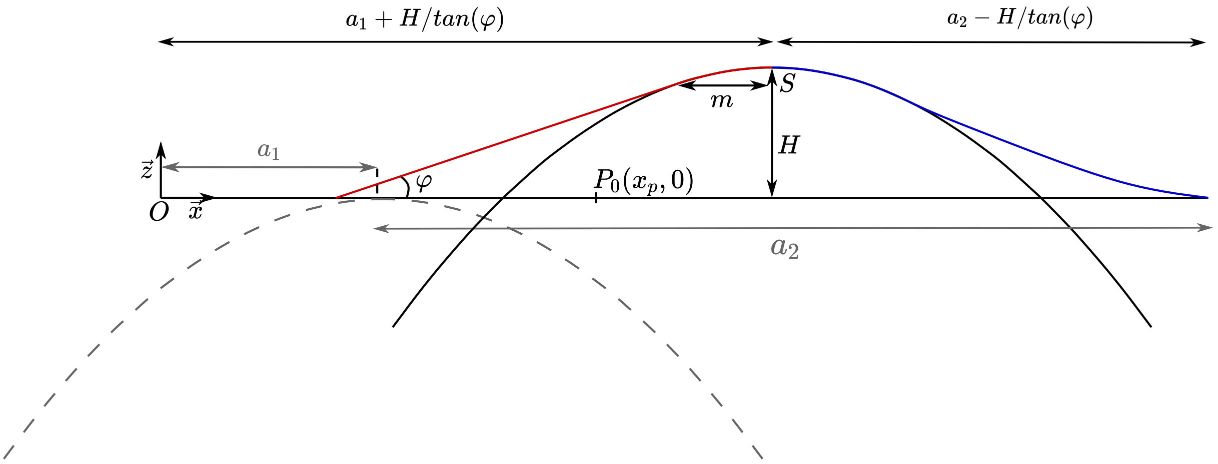

Figure 6.2: Assumed deformation of the bottom plating

To avoid any redundancy, derivations presented hereafter concern only the plate section delimited by $y \in [0; b_1]$. The contribution of the other side may be found by replacing b_1 by $b_2 = b - b_1$ in subsequent formulae.

For further clarification, the ship bottom damaged area is split into two different parts:

- The first one located at the rear part of the bottom and depicted in blue on Figure 6.2
- The second one, depicted in red, located at the front part of the bottom.

The energy is thus dissipated through different deformation mechanisms in the different areas of the damaged plating. Analytical derivations carried out for each mechanism are presented in the following subsections.

6.4.1.1 Energy dissipated by the rear part of bottom plating

Let us start with the derivation of the energy dissipated at the rear part of the bottom plating, i.e., $x \in \left[a_1 + H/tan\left(\varphi\right); a_1 + a_2\right]$ (blue line in Figure 6.2).

For simplification purposes, the displacement of the bottom plating is decomposed into two steps. First, the structure is moved to the left at a velocity V_x with a constant vertical penetration H, thus travelling a distance dx. Second, the structure is moved downward at a velocity V_z and travels a distance dz. All in all, the bottom plating travels a total distance $dl = \sqrt{dx^2 + dz^2}$ at each time step.

As long as the penetration H of the rock into the bottom plating remains constant, the ship horizontal motion may be considered as a pure sliding problem. Therefore, closed-form solutions developed in Chapter 4 can be applied. Resisting forces during the horizontal motion (dx) are expressed as:

$$\begin{cases} F_{L1} = g_{f1} F_{P1} \\ \\ F_{V1} = k_{v1} F_{L1} \end{cases} \tag{6.2}$$

Where F_{P1} is the plastic force derived in Section 4.3 and g_{f1} and k_{v1} are given by Eqs. 4.7 and 4.8.

During the vertical motion (dz), the situation is similar to a right angle collision. Based on the work of *Buldgen* [94] for a paraboloid ship bulb, the plastic force may be expressed as:

$$F_{P2} = \frac{8}{3\sqrt{C}} \sigma_0 t_h \frac{H^{1.5}}{b_1} \left(\frac{1}{3} + \frac{1}{5} \frac{C}{E} \right) \tag{6.3}$$

The application of the virtual work principle leads to:

$$\begin{cases} F_{L2} = 0 \\ \\ F_{V2} = F_{P2} \end{cases} \tag{6.4}$$

Recalling that at each time-step, the bottom plating travels a distance $dl = \sqrt{dx^2 + dz^2}$ and that the deformation process related to Eq. 6.2 only occurs along a displacement dx, Eq. 6.2 should be multiplied by $dx/dl = cos(\varphi)$. In the same way, as Eq. 6.4 only applies for a displacement dz, it should be multiplied by $dz/dl = sin(\varphi)$. Finally, the resisting force of the bottom plating rear part writes:

$$\begin{cases} F_{LR} = F_{L1} cos(\varphi) \\ \\ F_{VR} = k_{v1} F_{L1} cos(\varphi) + F_{V2} sin(\varphi) \end{cases} \tag{6.5}$$

6.4.1.2 Energy dissipated by the front part of bottom plating

Up to now, only the rear part of the bottom plating delimited by $x \in [a_1 + H/tan(\varphi); a_1 + a_2]$ has been considered in the energy dissipation process. However, when the impact angle $\varphi \neq 0°$, the front part delimited by $x \in [a_1; a_1 + H/tan(\varphi)]$ (red line on Figure 6.2) also dissipates some energy through plastic deformation and friction.
To quantify resulting dissipated energy, let us consider a point P located at a distance $x = x_p$ from the origin – see Figure 6.2. Its initial position is flagged by subscript "0" and may be defined as:

$$P_0 = \begin{bmatrix} x_p \\ 0 \\ 0 \end{bmatrix} \tag{6.6}$$

While its position when the rock apex S is at $x = x_p$ is expressed as:

$$P_1 = \begin{bmatrix} x_p \\ 0 \\ H = (x_p - a_1)tan(\varphi) \end{bmatrix} \tag{6.7}$$

The bottom plating front part deformed by the rock is depicted in red on Figure 6.3. Since $\varphi \neq 0°$ and considering the rock shape, the point P remains in contact with the rock even after the apex S has passed the position x_p. Denoted by m the distance between the apex and the split-off point, the bottom plating is supposed to slide on the rock over the region delimited by $x \in [a_1 + H/tan(\varphi) - m; a_1 + H/tan(\varphi)]$.

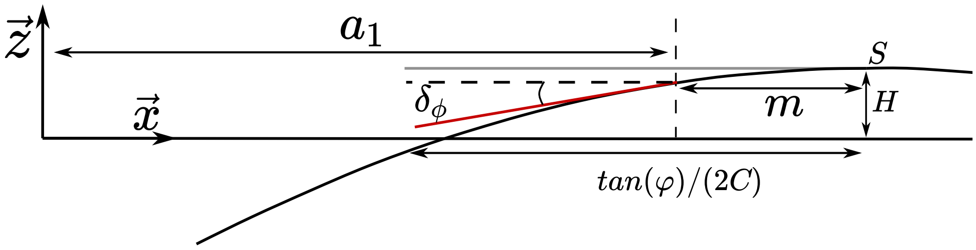

Figure 6.3: Deformation of the bottom plating at the rear part of the rock

At the first instant of grounding, m corresponds to the distance separating the rock apex and the initial contact point, that is:

$$m = a_1 + \frac{H}{tan(\varphi)} - a_1 = \frac{H}{tan(\varphi)} \tag{6.8}$$

The previous equation is only valid at the first instant of the grounding process. Since elastic deformation is neglected, the plate deformation is perfectly plastic so the plate deflection at point P cannot decrease. Given that, the maximum value of m may be expressed as:

$$m = \frac{tan(\varphi)}{2C} \tag{6.9}$$

Combining Eqs. 6.8 and 6.9, the distance m may be finally defined as:

$$m = min\left(\frac{H}{tan(\varphi)} ; \frac{tan(\varphi)}{2C}\right) \tag{6.10}$$

The total out-of-plane displacement of a point located at a distance $x \geq a_1$ from the origin is:

$$H_T(x) = (x - a_1)\tan(\varphi) + \delta_H \tag{6.11}$$

With δ_H expressed as:

$$\delta_H = \frac{m}{2}tan(\varphi) \tag{6.12}$$

Figure 6.4 compares the measured maximum out-of-plane displacement (H_T) retrieved from *Ls-Dyna* simulations and the one obtained from Eq. 6.11 with $a_1 = 2.05m$, $\varphi = 14°$ and $C = E = 0.3m^{-1}$.

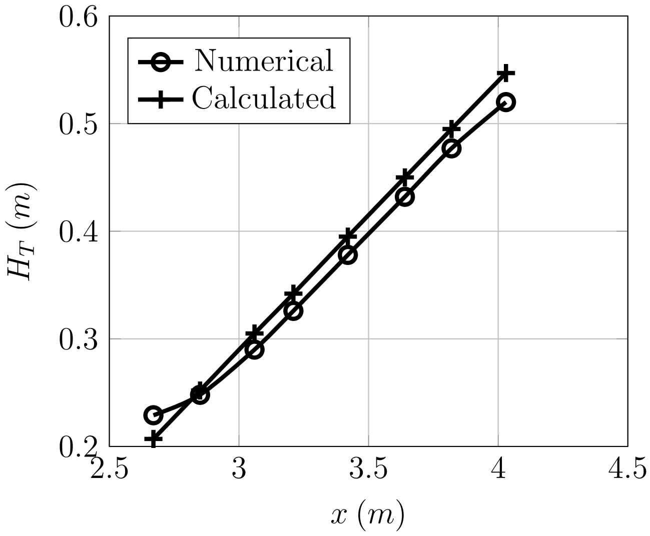

Figure 6.4: Measured and calculated maximum out of plane displacement

It is observed that Eq. 6.11 slightly overestimates the maximum out-of-plane displacement, but the discrepancy does not exceed 5%.

Knowing the plate deflection, the next step consists in calculating the rate of energy dissipated by plastic deformation. It is worth to recall that for now, the bottom plating is supposed to slide over the rock without rupturing.

Membrane energy rate

Accounting for the rock shape, the elongation of plate longitudinal fibre δ_{u0} is given by:

$$\delta_{u0} = \int_0^m \frac{1}{2}\left(\frac{\partial w}{\partial x}\right)^2 = \frac{2}{3}C^2 m^3 \tag{6.13}$$

Using Eq. 4.12, the elongation of transverse fibre δ_{v0} may be expressed as:

$$\delta_{v0} = \frac{2}{3}\frac{(H+\delta_H)^2}{b_1} - \frac{2}{3}\frac{H^2}{b_1} = \frac{2}{3}\frac{\delta_H}{b_1}\left(\delta_H + 2H\right) \tag{6.14}$$

Assuming that longitudinal fibres are not stretched, i.e., $\varepsilon_{xx} = 0$ but rather sheared, the non-zero strains may be expressed as:

$$\begin{cases} \varepsilon_{yy} = \frac{\partial v}{\partial y} = \frac{\partial}{\partial y}\left(\delta_{v0}\left(\frac{y}{b_1}\right)^2\right) = 2\frac{\delta_{v0}}{b_1^2}y \\ \\ \varepsilon_{xy} = \frac{1}{2}\frac{\partial u}{\partial y} + \frac{1}{2}\frac{\partial v}{\partial x} = \frac{y}{b_1^2}\left(\delta_{u0} + \frac{1}{2}\frac{\delta_{v0}}{m}y\right) \end{cases} \tag{6.15}$$

Combining Eqs. 2.22 and 6.15, the membrane energy rate writes:

$$\dot{E}_{m3} = N_0 \frac{V_x}{b_1^2} \int_0^{b_1} \sqrt{4\delta_{v0}^2 y^2 + y^2 \left(\delta_{u0} + \frac{1}{2}\frac{\delta_{v0}}{m} y\right)^2} \, dy \tag{6.16}$$

This expression is calculated by numerical integration.

Longitudinal bending energy rate

In a horizontal sliding process, when a point of the plating leaves the rock, the plate curvature becomes zero. On contrary, in a surge and heave combined motion, as the rock penetration increases, some of the plating front part remains in contact with the rock and the curvature at a given point P changes according to the rock shape until the point separates from the rock. The plate rotation angle δ_ϕ illustrated on Figure 6.3 is therefore:

$$\delta_\phi = atan(2Cm) \tag{6.17}$$

Since the longitudinal bending deformation reaches its maximum at $y = b_1$ and vanishes at $y = 0$, resulting energy rate writes:

$$\dot{E}_{bL3} = M_0 V_x \int_0^{b_1} \delta_\phi \left(\frac{y}{b_1}\right)^2 dy = \frac{b_1}{3} \operatorname{atan}(2Cm) M_0 V_x \tag{6.18}$$

Transverse bending energy rate

Following the way used to obtain the transverse bending contribution in Chapter 4, the energy dissipated by bending of transverse fibres for an increment of vertical penetration δ_H may be calculated as:

$$\dot{E}_{bT1} = 4M_0 V_x \left(\frac{H + \delta_H}{\sqrt{b_1^2 + 4(H + \delta_H)^2}} - \frac{H}{\sqrt{b_1^2 + 4H^2}} \right) \tag{6.19}$$

As δ_H is small compared to H, Eq. 6.19 may be further simplified to:

$$\dot{E}_{bT3} = 4M_0 \frac{b_1^2}{(b_1^2 + 4H^2)^{3/2}} \delta_H V_x \tag{6.20}$$

Bottom plating front part resistance

Finally, the total plastic force of the front part of bottom plating is given by :

$$F_{P3} = \frac{\dot{E}_{PT3}}{V_x} = \frac{\dot{E}_{m3} + \dot{E}_{bL3} + \dot{E}_{bT3}}{V_x} \tag{6.21}$$

It is worth noting that for the limit case $\varphi = 0°$ which corresponds to a horizontal sliding mode, $\delta_H = 0$ so the plastic force $F_{P3} = 0$. This result is consistent with the derivation performed in section 4.3 where it was found that the plating front part does not dissipate any energy.

As for horizontal pure sliding, contribution of friction is simply added using Eqs. 4.7 and 4.8 and replacing with α expressed as:

$$\alpha = atan(Cm) \tag{6.22}$$

The longitudinal and vertical resisting forces of the bottom plating front part are finally calculated as:

$$\begin{cases} F_{L3} = g_{f3} F_{P3} \\ F_{V3} = k_{v3} F_{L3} \end{cases} \tag{6.23}$$

6.4.2 Overall resisting force and dissipated energy

During the combined sliding process, longitudinal and vertical resisting forces are finally obtained by summing the contributions of the bottom plating rear part (Eq. 6.5) and front part (Eq. 6.23):

$$\begin{cases} F_L = F_{L1} cos(\varphi) + g_{f3} F_{P3} \\ F_V = k_{v1} F_{L1} cos(\varphi) + F_{V2} sin(\varphi) + k_{v3} F_{L3} \end{cases} \tag{6.24}$$

The amount of overall energy dissipated during the combined sliding process is then calculated as:

$$E_I = \int_0^{\chi} F_L dx + \int_0^{H} F_V dz \tag{6.25}$$

Where χ and H are respectively the longitudinal and vertical displacements of the rock into the bottom plating.

All previous closed-form expressions hold until tearing of the outer shell plating occurs. After a certain vertical penetration of the rock into the bottom plating, the latter fractures and the grounded ship enters the so-called raking phase. At that time, the plating begins to tear and outer shell strains are released. In the analytical models developed for ship-ship oblique collisions, once the side shell is fractured, the resisting force is usually set to zero - see for instance [37, 101, 107]. However, a significant part of the initial kinetic energy may be dissipated by plate tearing. Therefore, once the plate is fractured, it is assumed that two flaps are created on each side of the rock (this hypothesis will be confirmed by numerical simulations). The deformation process is then similar to the problem of plate tearing in ship grounding and closed-form solutions developed in Chapter 5 may be directly applied. The amount of energy dissipated in the raking phase is then calculated as:

$$E_{II} = \int_0^{\chi} F_L dx \tag{6.26}$$

In summary, when the ship bottom plating first slides on the rock and then ruptures, the total energy dissipated during the combined grounding event is obtained by adding E_I and E_{II} given by Eqs. 6.25 and 6.26 respectively.

6.4.3 Rupture triggering

Among all the different information available in ship grounding, plate failure is perhaps one of the most interesting.

In the present work, it is assumed that tearing occurs when the outer shell plastic strain reaches a given threshold value ε_c. According to the literature [37, 65, 94, 106], ε_c should be chosen in a range of 5-12% for steel-like materials commonly used in ship building industry. On the other hand, according to *Hill* [168], the necking (rapidly followed by the failure) of a plate appears when the sum of minor and major strains reaches a certain threshold value which depends on the hardening exponent of the material. Here, given that $\varepsilon_{xx} = 0$, the rupture condition is :

$$\frac{1}{2}\left(\frac{\partial w}{\partial y}\right)^2 + zk = \varepsilon_c \tag{6.27}$$

Where z denotes the distance from the plate mid-surface and k is the curvature of the transverse fibre expressed as:

$$k = \frac{\frac{\partial^2 w}{\partial y^2}}{\left(1+\left(\frac{\partial w}{\partial y}\right)^2\right)^{3/2}} \tag{6.28}$$

Eq. 6.27 corresponds in fact to the maximum strain along transverse direction. Using Eqs. 6.27 and 6.28 and considering the paraboloid shape of the rock, the failure condition calculated from the maximum strain may be expressed as:

$$2\left(\frac{H}{b_1}\right)^2 + t_h \frac{E}{\left(1+\frac{4H^2}{b_1^2}\right)^{3/2}} = \varepsilon_c \tag{6.29}$$

Denoting the membrane strain by χ, Eq. 6.29 becomes:

$$\chi + t_h \frac{E}{(1+2\chi)^{3/2}} = \varepsilon_c \tag{6.30}$$

With χ :

$$\chi = 2\left(H/b_1\right)^2 \tag{6.31}$$

Correctly triggering the outer shell rupture is essential to properly simulate a ship grounding accident. Unfortunately, simplified formulations are developed under the assumption of a global displacement field. Since rupture is a local problem, finding a unique failure strain able to correctly trigger the tearing of the plate for a large variety of rocks is complex. Here, a simple approach is proposed and may be summarised as follows:

- Numerical simulations are performed for different rock shapes, distance b_1 and plate thickness t_h.
- At rupture, the vertical penetration H_N of the rock into the plating is post-processed from the numerical simulation.

- The value of H_N is introduced into Eq. 6.31 giving the threshold for the membrane strain ε_M.
- A simplified law is obtained for $\bar{\chi}\left(E, b_1, t_h\right) = \varepsilon_M$ from curve fitting varying the parameters E, b_1 and t_h.
- The simplified law $\chi\left(E, b_1, t_h\right)$ is included into Eq. 6.30 to obtain the failure threshold value ε_c.

A total of 60 numerical simulations were performed considering different rock dimensions, lateral impact distance b_1 and plate thickness t_h and the following fitted law was found for the critical failure strain $\bar{\chi}$:

$$\bar{\chi} = \frac{2.2 + 85e^{-1.1Eb_1}}{100}\left(\frac{t_h}{15}\right)^{1.2} \tag{6.32}$$

Where the plate thickness t_h is expressed in millimetre and the lateral impact distance b_1 in meter. The different values considered for b_1, t_h and E are summarised in Table 6.1.

Parameter	Values
b_1 (m)	2, 3, 3.5 and 4.5
t_h (mm)	5, 10, 15 and 20
E (m^{-1})	0.3, 0.5, 1 and 2

Table 6.1: Parametric values considered for the fitted law for failure depth

Then, from Eqs. 6.30 and 6.32, the failure of the plate is assumed to occur as soon as:

$$2\left(\frac{H}{b_1}\right)^2 + t_h\frac{E}{\left(1+\frac{4H^2}{b_1^2}\right)^{3/2}} \geq \bar{\chi} + t_h\frac{E}{\left(1+2\bar{\chi}\right)^{3/2}} \tag{6.33}$$

Figure 6.5 illustrates the penetration depth at failure obtained in numerical simulations as well as the prediction using Eq. 6.33. The figure shows a quite good accordance between the numerical and fitted results.

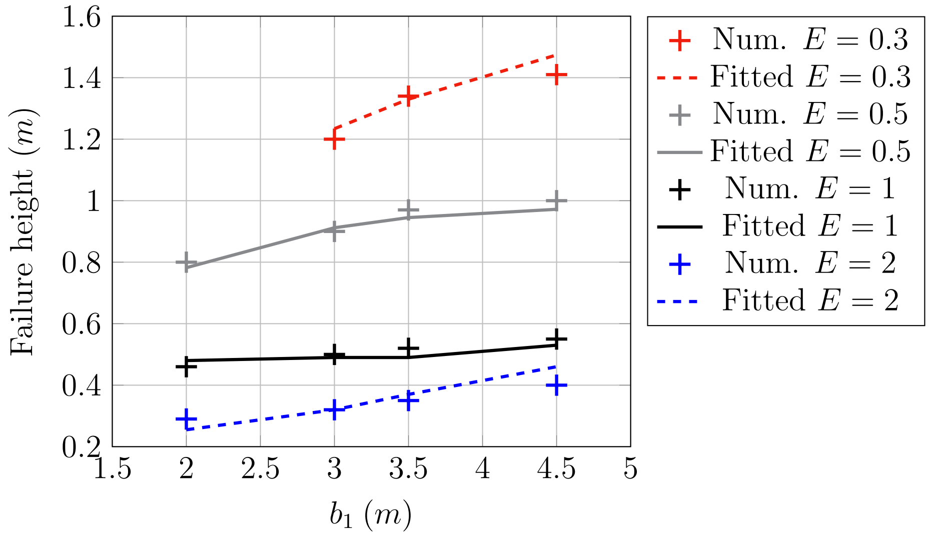

Figure 6.5: Failure height - Numerical and fitted law for $t_h = 15mm$

It should be mentioned that from various configurations of the plate (length and width), the rupture was always triggered by excessive straining of transverse fibres ε_{yy} which is coherent with Eq. 6.27. Consequently, the fitted law given by Eq. 6.32 does not depend on a_1 or a_2. Moreover, in the various tested configurations, b_1 was always chosen as the smallest distance between the rock apex and the clamped edge, i.e., $b_1 \leq b_2$. Finally, only the coefficient E was selected since it defines the rock shape in the yz plane, that is in the transverse direction.

It is worth noting that *Heinvee* [20] also investigated the numerical response of three different tankers grounded on paraboloid shaped rocks. The author highlighted that when no girder is involved in the deformation, bottom plating failure depends on both the ship breath and rock dimensions, which is consistent with the previous observations and fitted law.

6.4.4 Numerical validation

The analytical derivations presented in previous subsections are now confronted to numerical simulations. To do this, a 12.6m long, 6m width and 15mm thick unstiffened plate as well as the three rock shapes presented in Chapter 4 are considered. Moreover, two friction coefficients $\mu = 0.1$ and $\mu = 0.3$ are set to quantify the influence of friction on the response. Finally, the three collision angles φ resumed in Table 6.2 are tested. Combining all the items leads to the study of 18 scenarios. Note also that the failure strain used in numerical simulations is calculated according to Eq. 2.10.

V_x (m/s)	V_z (m/s)	φ (°)
6	0.75	7.12
6	1.5	14.0
3	1.0	18.4

Table 6.2: Surge and heave velocities used in combined scenarios

Table 6.3 compares the dissipated energies (plastic + sliding) retrieved from numerical and analytical calculations. For comparison purpose, the results are saved when the vertical penetration of the rock into the plate reaches $1m$. The deviation between numerical and analytical results is calculated according to Eq. 4.30.

Case id	Rock id	μ	φ (^{o})	Energy Num. (MJ)	Energy Ana. (MJ)	Deviation
1	1	0.3	7.1	21.8	21.1	3.4%
2	1	0.3	14.0	14.1	13.9	1.5%
3	1	0.3	18.4	12.3	12.5	-1.3%
4	2	0.3	7.1	16.3	15.8	2.8%
5	2	0.3	14.0	9.8	9.9	-0.9%
6	2	0.3	18.4	8.6	8.7	-0.3%
7	3	0.3	7.1	7.9	7.3	7.9%
8	3	0.3	14.0	4.6	4.1	11.2%
9	3	0.3	18.4	4.0	3.3	17.0%
10	1	0.1	7.1	14.2	13.8	2.3%
11	1	0.1	14.0	9.4	10.0	-6.3%
12	1	0.1	18.4	8.5	9.4	-11.8%
13	2	0.1	7.1	11.0	10.5	4.9%
14	2	0.1	14.0	7.0	7.2	-2.5%
15	2	0.1	18.4	6.1	6.5	-7.0%
16	3	0.1	7.1	5.2	4.8	6.7%
17	3	0.1	14.0	3.1	2.8	8.8%
18	3	0.1	18.4	2.8	2.4	14.9%

Table 6.3: Comparison of numerical and analytical dissipated energies

Several observations may be done from above table:

- First, for a given rock shape and friction coefficient, the dissipated energy decreases with the collision angle, indicating that the horizontal resisting force contributes more to dissipate the energy than the vertical one.
- Second, for a given rock shape, the amount of dissipated energy decreases with the value of μ. According to Table 6.3, varying μ from 0.3 to 0.1 decreases by around 30% the amount of dissipated energy.
- Third, as the rock gets sharper, the total dissipated energy decreases. In fact, the rupture occurs rapidly with a sharp rock and since the resisting force is much lower in raking mode, the energy dissipated by meter also decreases.

Despite some imperfections, the last column of Table 6.3 shows that the maximal discrepancy between analytical and numerical results does not exceed 17%. Moreover, the average deviation considering the 18 simulation cases is around 6.2%, which is acceptable regarding the different assumptions made.

The evolution of F_L and F_V forces post-processed from numerical and analytical simulations of case 5 is compared in Figure 6.6. The sudden drop of both longitudinal and vertical resisting forces is obviously due to the outer shell failure. Analytical and numerical results are shown to be in good agreement, except the vertical force after rupture for which a discrepancy of around $0.8MN$ is observed. For comparison purposes, analytical solutions developed by *Buldgen et al.* [107] for ship-ship oblique collision are also plotted. Since the model was developed under the assumption of a punctual load and for large collision angle ($\varphi \geq 30°$), it is not surprising to obtain such a large deviation.

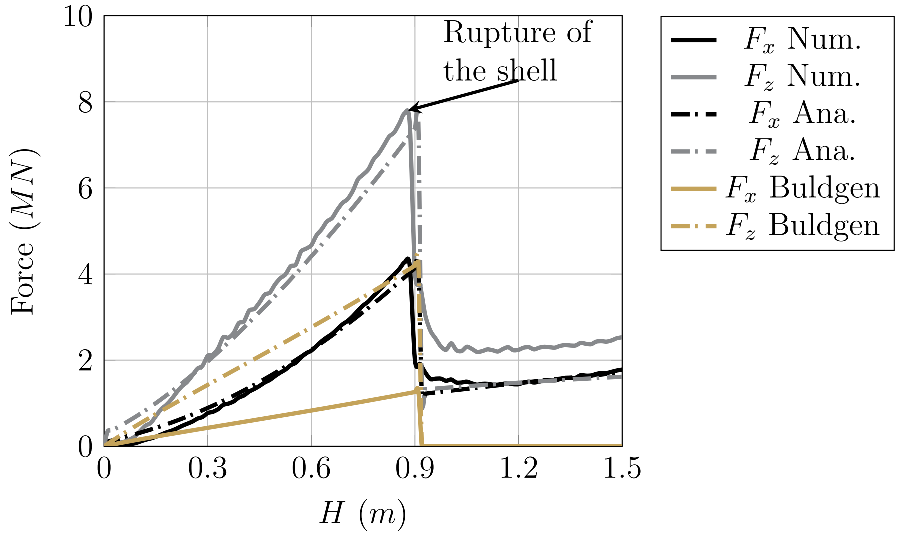

Figure 6.6: Evolution of numerical and analytical forces for case 5

It should be emphasised that the analytical solution proposed for the raking mode has been developed under the assumption of a constant rock vertical penetration. However, in a combined grounding mode, the ship heave motion goes on after outer shell failure, amplifying the bending of the two flaps created and dissipating additional energy. Figure 6.7 illustrates the deformation of the plate before and after rupture.

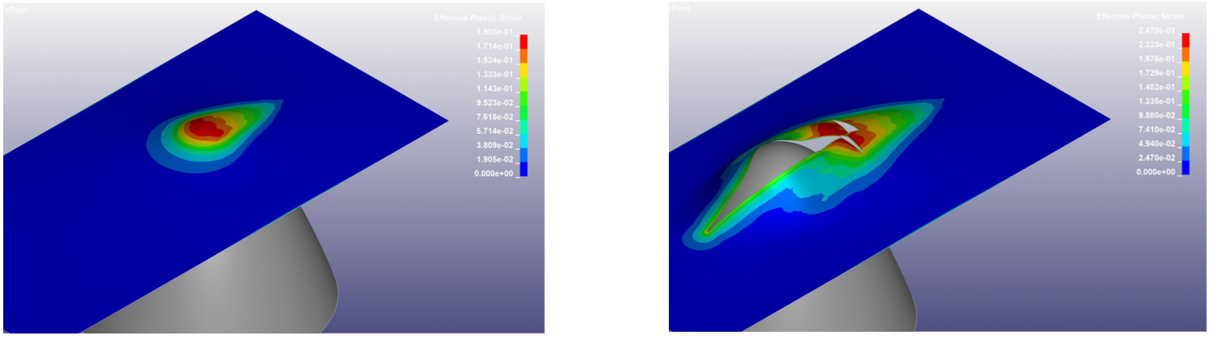

Figure 6.7: Plate deformation before and after rupture from case 5 - Numerical simulation

Such bending mode and resulting friction mechanism have been investigated for rounded conical shape in [169–174] for instance. Nevertheless, integrating such solutions in the case of combined grounding with consistency with all the previous analytical solutions is complex. Therefore, additional bending and sliding of the flaps have not been considered in the present analysis, and this may explain why the vertical resisting force is observed to be underestimated after rupture in Figure 6.6.

Let us now compare the energy (E_{sli}) dissipated by the pure (horizontal) sliding model, (Eq. 6.2) to the energy (E_{comb}) calculated through the combined grounding solutions (Eqs. 6.2, 6.4 and 6.23). Figure 6.8 illustrates the evolution of $(E_{comb} - E_{slid})/E_{comb}$

for different impact angles. In fact, $(E_{comb} - E_{slid})/E_{comb}$ corresponds to the proportion of the energy dissipated by the outer shell rear part during the heave motion (Eq. 6.4) and the energy related to the front part resistance (6.23). The ratio is calculated after a grounding time of 1.4 seconds. Two rocks are considered, namely rocks 1 and 3.

Starting with the widest one (rock 1), the contribution of resistant forces given by Eqs. 6.4 and 6.23 is seen to increase with the collision angle as expected. Over the range [0°; 25°], the heave motion contributes in average by around 35% to the total dissipated energy, which is significant. As the sharpest rock is concerned (rock 3), one may observe that $(E_{comb} - E_{slid})/E_{comb}$ rapidly decreases when φ increases. This is because the higher the impact angle, the earlier the rupture of the plate. After rupture, the plate enters a raking mode and the energy is mainly dissipated through raking mechanisms (tearing, bending, friction), decreasing the ratio since mechanisms are similar between pure raking and combined grounding in the current simplified model.

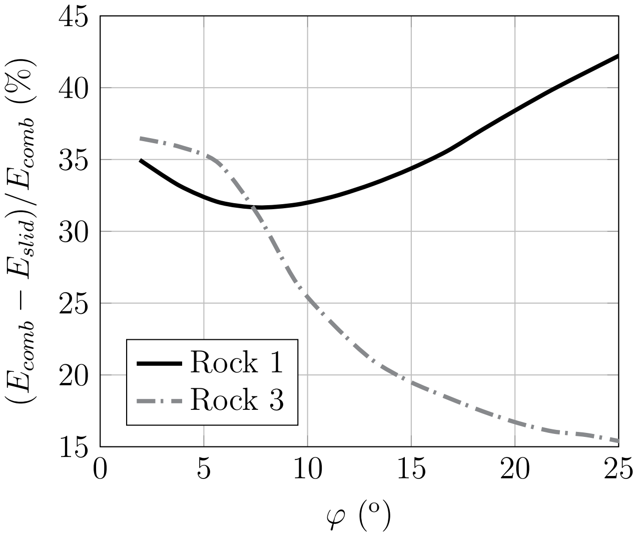

Figure 6.8: Evolution of $(E_{comb} - E_{slid})/E_{comb}$ with the impact angle

From Figure 6.8, it can be concluded that the energy dissipated by the plate deformation due to the heave motion and the one dissipated in the rear part of the plating are significant, especially when the rock is wide. Although imperfect, the proposed model may be confidently used to rapidly assess the response of the outer/inner bottom running aground over a rock in a combined surge and heave movement.

6.5 Response of transverse floors

As continuation to the previous work, the response of transverse floors are now investigated. In a similar way to the bottom plating, two situations have to be distinguished:

- If the bottom plating is not fractured, the response of the floor is supposed to be the same as in the sliding mode - see Chapter 4.
- Once the bottom plating has been perforated, the response of the floor is assumed to be the same as in the raking mode - see Chapter 5

6.5.1 Numerical validation

With the aim of validating the response of a ship hull in combined grounding, several numerical simulations are carried out. The finite element model includes outer and inner bottoms, transverse floors and longitudinal girders. Grounding parameters are the ones considered in Section 6.4 so 18 different scenarios (scenarios 19 to 36) are investigated.

First simulations reveal the presence of a second collapse mode for the transverse floor once the outer shell is opened. The deformation pattern is rather similar to the one observed in the sliding mode. The floor is seen to be vertically crushed and two folds are created on each side of the rock. However, unlike the case of sliding where the floor does not rupture, here a vertical crack initiates and propagates through the transverse member as illustrated in Figure 6.9.

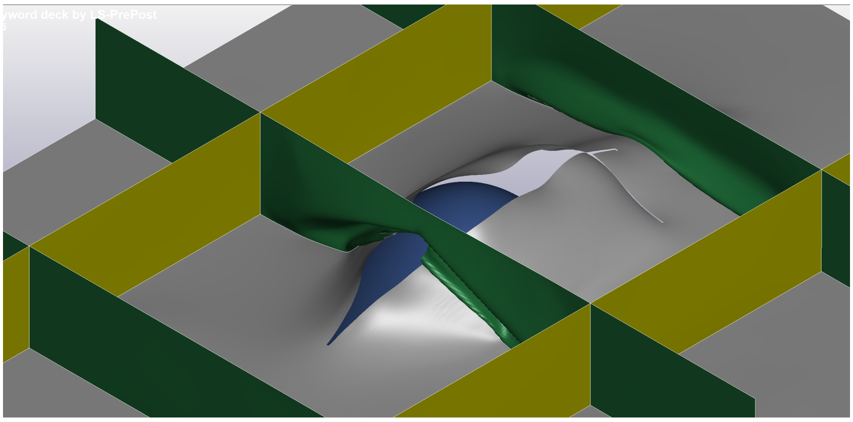

Figure 6.9: Floor alternative collapse mode - Combined grounding

This deformation mode has also been reported by *Simonsen* [11] from the analysis of NSWC ship grounding experiments [152]. According to Simonsen, the energy is mainly dissipated by plastic bending and crack propagation and may be calculated as:

$$E_P = R_c t_h min\left(H, H_{db}\right) + 2M_0\pi\left(\frac{1}{b_1}+\frac{1}{b_2}\right) \tag{6.34}$$

Where H is rock penetration into the outer plating, t_h the thickness of the transverse floor, H_{db} the height of the double bottom, M_0 the plastic bending moment capacity and b_1 or b_2 are the distances between the rock and the edges of the floor along the transverse direction.

The associated resisting force are then:

$$\begin{cases} F_L = \frac{1}{K_V} F_V \\ \\ F_V = \frac{E_P}{min(H, H_{db})} \end{cases} \tag{6.35}$$

It should be emphasised that this collapse mode was only observed for the two widest rocks (rock 1 and 2). Therefore, if the rock coefficient $C \leq 0.5$, Eq. 6.35 is preferred to the solution developed in Chapter 5 for the response of transverse floor when the bottom plating has been fractured.

Table 6.4 resumes the total dissipated energy retrieved from numerical and analytical simulations of the 18 scenarios. The discrepancy does not exceed 20% and is in average about 9.4%.

Case id	μ	Rock id	φ (°)	Total energy Num. (MJ)	Total energy Ana. (MJ)	Deviation energy
19	0.3	1	7.1	30.4	33.8	-11.1%
20	0.3	1	14	50	42.7	14.7%
21	0.3	1	18.4	25.1	25.2	-0.5%
22	0.3	2	7.1	22.9	21.3	6.9%
23	0.3	2	14	31.6	27.5	13.0%
24	0.3	2	18.4	13.45	13.8	-2.9%
25	0.3	3	7.1	12.67	10.4	18.2%
26	0.3	3	14	23.24	18.7	19.7%
27	0.3	3	18.4	8.52	7.5	11.9%
28	0.1	1	7.1	19.41	22.5	-16.0%
29	0.1	1	14	31.6	30.0	5.0%
30	0.1	1	18.4	16.92	18.2	-7.7%
31	0.1	2	7.1	15.34	13.6	11.5%
32	0.1	2	14	19.95	19.8	0.8%
33	0.1	2	18.4	10.84	9.6	11.9%
34	0.1	3	7.1	8.45	7.3	14.2
35	0.1	3	14	13.78	13.5	2.3
36	0.1	3	18.4	5.57	5.7	-1.4

Table 6.4: Comparison of numerical and analytical energies dissipated by the floors in a combined surge and heave motion

Figures 6.10 and 6.11 illustrate the evolution of F_L and F_V with respect to the vertical rock penetration H for cases 23 and 25 respectively. In Figure 6.10, one may observe that tearing occurs when the widest rock penetration $H \approx 0.9m$. When the rock gets sharper, tearing is triggered earlier ($H \approx 0.5m$) as shown by Figure 6.11. Red circles mark the vertical crushing of the transverse floor during the sliding mode while blue circles correspond to the floor response after rupture. While deformation mechanisms appear to be very well captured before rupture, horizontal and vertical resistant forces are significantly underestimated when the floor has fractured.

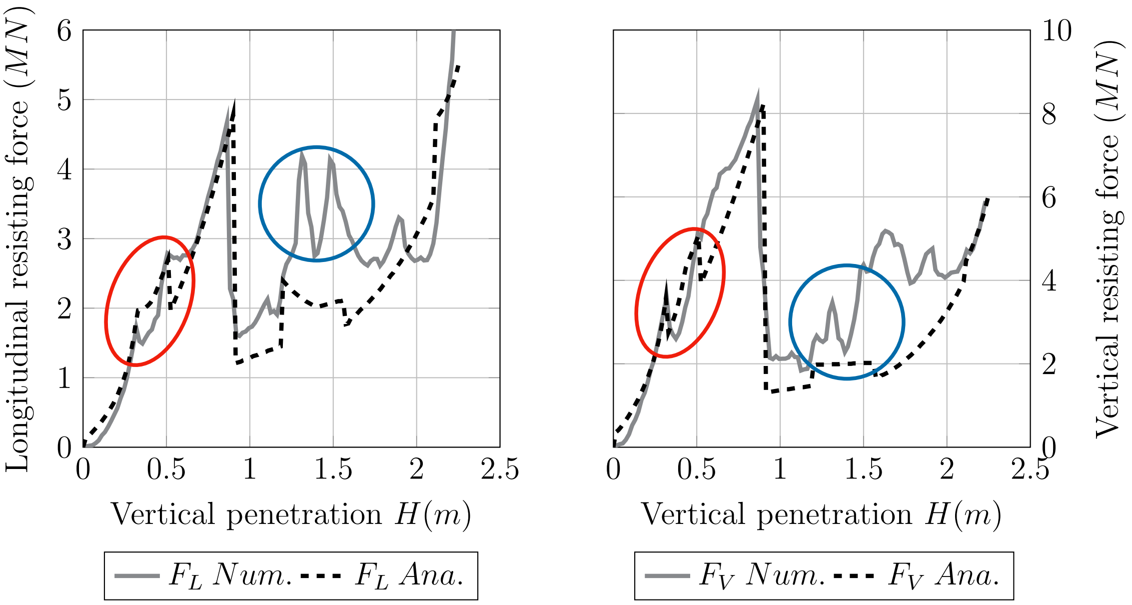

Figure 6.10: Comparison of longitudinal and vertical resisting forces for scenario 23

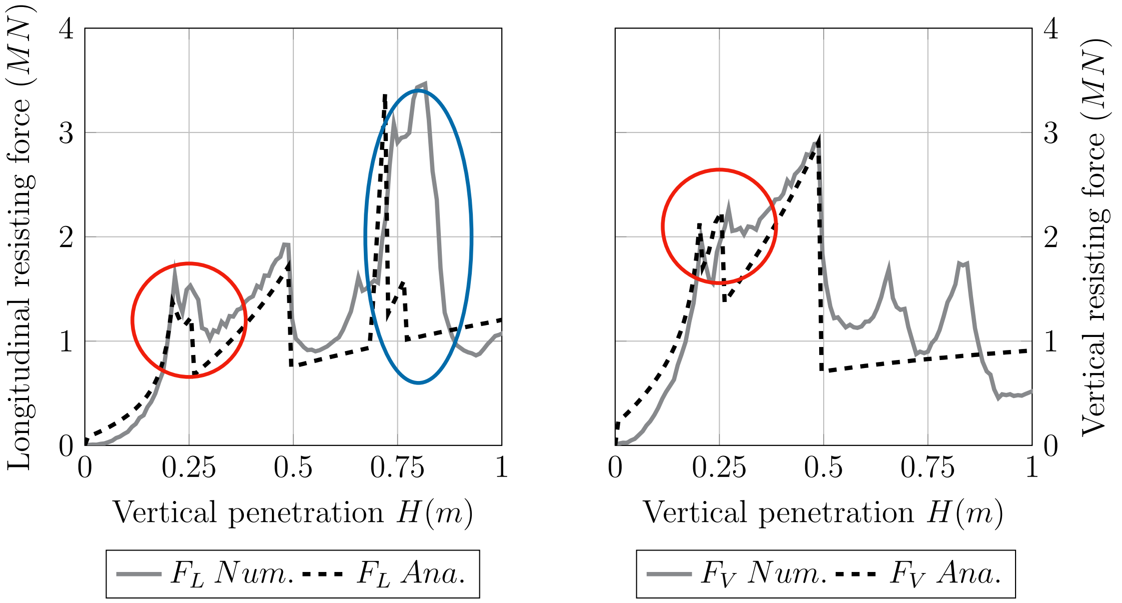

Figure 6.11: Comparison of longitudinal and vertical resisting forces for scenario 25

This may be attributed to the fact that membrane straining is underestimated by the proposed model once rupture has occurred. According to *Simonsen* [11] and Eq. 6.34, since a crack is present in the transverse structure, membrane straining is not considered. However, the crack does not propagate instantly along the vertical direction. As a consequence, some transverse straining remains, dissipating energy through plastic deformation. Figure 6.12 illustrates the plastic strain ε_{yy} post-processed from the numerical simulation of case 23. It clearly underlines that transverse fibre straining does not completely vanish after rupture. Nevertheless, since the proposed simplified method cannot provide information about the crack propagation, it appears impossible to accurately capture the energy dissipated by membrane straining after rupture.

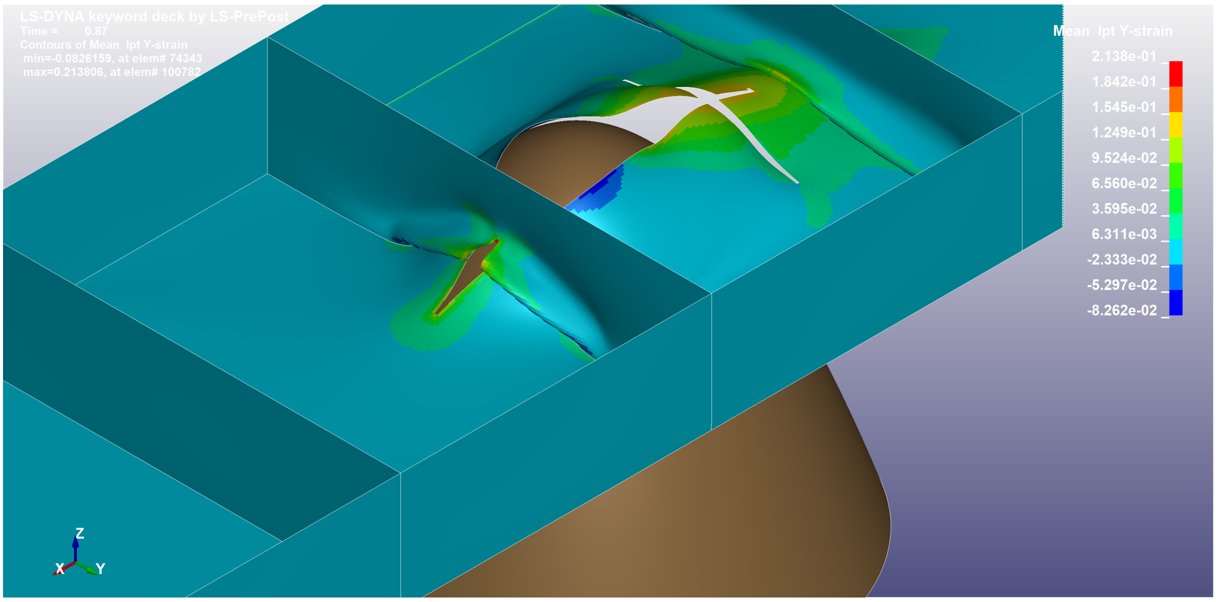

Figure 6.12: Transverse strain after floor rupture - Combined grounding

Despite this limitation, Figures 6.10 and 6.11 show a fairly good agreement between numerical and analytical results. Over the 18 scenarios considered in this study, the average discrepancy is around 9.4%, which appears acceptable. Note finally that the underestimation of the energy dissipated after rupture of the floors has a limited effect on the final grounding response as transverse floors absorb less than 20% of the total energy.

6.6 Response of longitudinal girders

6.6.1 Introduction

Following the same procedure, the response of longitudinal girders to a combined surge and heave motion of the ship is now investigated. *Heinvee* [20] recently highlighted two points:

- Longitudinal elements such as girders or longitudinal bulkheads have a significant influence on the resisting force.
- Numerical simulations show that girders tend to trigger almost instantly the rupture of the outer shell.

The latter behaviour was also observed from the numerical simulations carried out in the scope of this section. Outer shell rupture occurs just under the girder, after a rock vertical penetration of around $0.2m$, whatever the rock shape. Note however that the use of the failure criteria proposed by *Lehmann & Peschmann* [87] becomes questionable in this area as out-of-plane shear stresses predominate in the bottom plating just below the girder.

6.6.2 Analytical developments

As for the bottom plating, front and rear parts may be distinguished in the response of a girder. However, numerical simulations show that the energy is mainly dissipated by the rear part so the front part contribution will be neglected in the following developments.

As for the bottom plating, the deformation process is split into two steps. First, the ship moves along x direction with a constant penetration depth (H). Then, a vertical movement is imposed with a velocity V_z. During the first phase, the deformation is similar to the problem of bottom sliding, while in the second phase, the girder rather suffers in-plane crushing.

Using the expressions derived in Chapters 4 and 5 for girders, the resisting force during the horizontal motion of the ship is given by:

$$\begin{cases} F_{L1} = g_{f1} F_{P1} \\ \\ F_{V1} = k_{v1} F_{L1} \end{cases} \tag{6.36}$$

Where g_{f1}, K_{v1} and F_{P1} depend on both the outer hull state and rock dimensions. In the second phase, the girder is further pushed vertically so Eq. 4.44 may be used for the resistant forces:

$$\begin{cases} F_{L2} = 0 \\ \\ F_{V2} = \frac{\sigma_0 t_g}{\sqrt{3}} \frac{H^2}{R_x} + \pi \frac{\sigma_0 t_g^2}{\sqrt{3}} \frac{R_x}{H} \end{cases} \tag{6.37}$$

Where H is the penetration depth into the girder, t_g its thickness and $R_x = \sqrt{H/C}$ the longitudinal radius of the rock.

It should be emphasised that Eq. 6.37 is only valid for large rocks. As mentioned in Chapter 5, the girder rather slides on one edge of a sharp rock and is not vertically crushed. Thus, F_{V2} is set to 0 when $E > 1$. This allows to be consistent with previous analytical developments. Finally, the total resisting force is expressed by combining Eqs. 6.36 and 6.37 as:

$$\begin{cases} F_L = F_{L1}cos(\varphi) \\ \\ F_V = F_{V1}cos(\varphi) + F_{V2}sin(\varphi) \end{cases} \tag{6.38}$$

where $\varphi = atan(V_z/V_x)$ is the impact angle.

6.6.3 Numerical validation

As an attempt to validate the proposed model, 18 simulations are conducted (cases 37 to 54) with the finite element model used for the validation of the model developed for girders in Chapter 4. Again, three rock shapes, two friction coefficients and three impact angles are considered. For comparison purposes, the dissipated energies presented in Table 6.5 have been post-processed as soon as the vertical penetration reached $1m$. In addition, Figures 6.13 and 6.14 illustrate the evolution of F_L and F_V for cases 41 and 43.

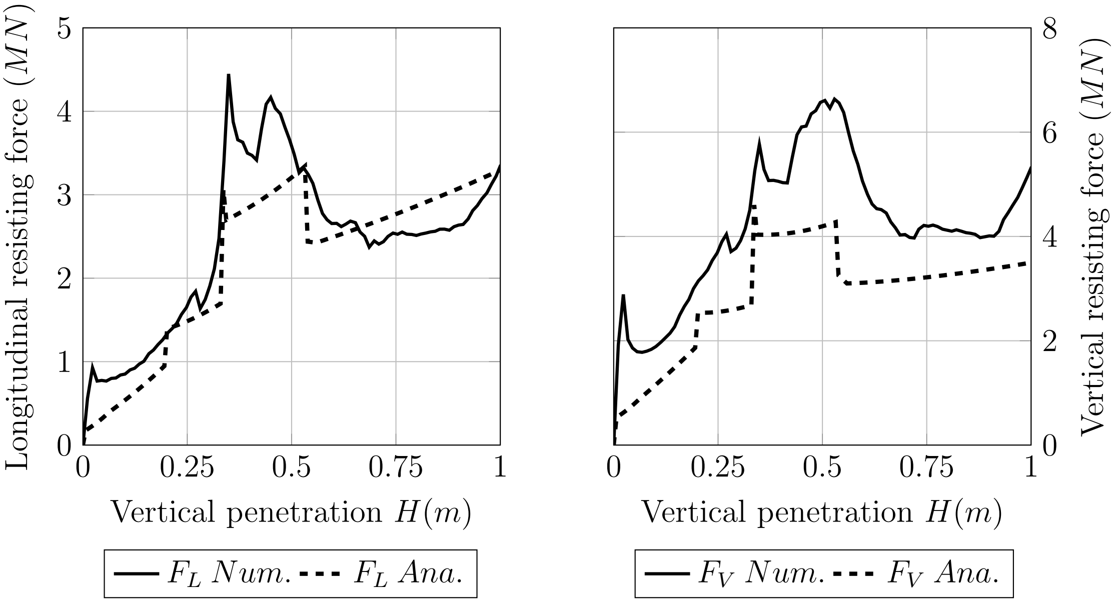

Figure 6.13: Comparison of longitudinal and vertical resisting forces for scenario 41

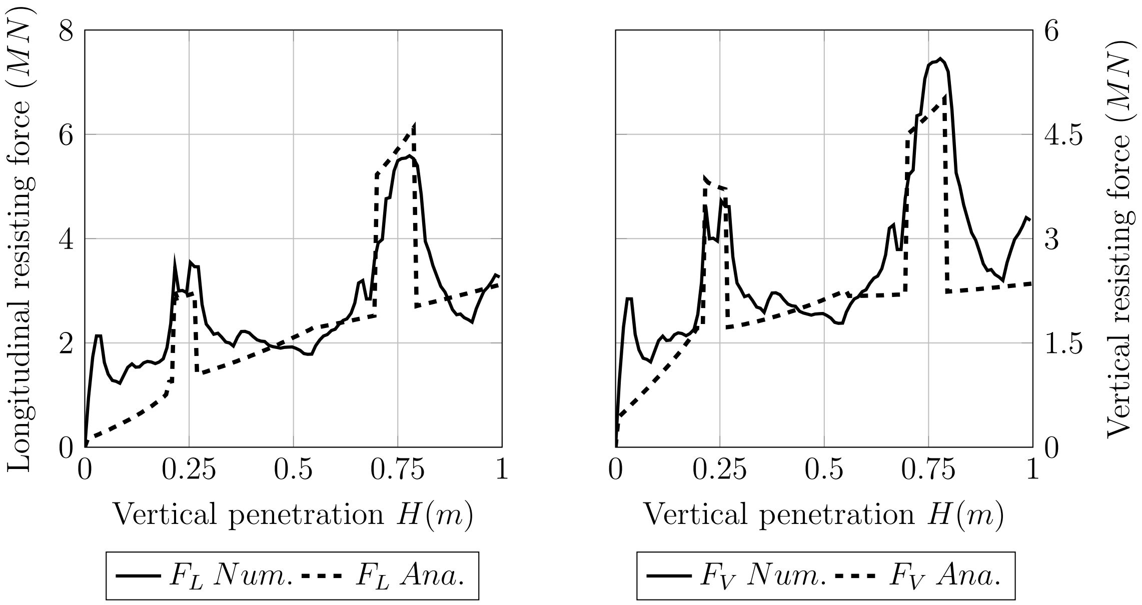

Figure 6.14: Comparison of longitudinal and vertical resisting forces for scenario 43

Case id	Rock id	μ	φ (°)	Dissipated energy Num. *(MJ)*	Dissipated energy Ana. *(MJ)*	Deviation
37	1	0.3	7.1	24.5	23.4	4.6%
38	1	0.3	14	15.71	13.0	17.4%
39	1	0.3	18.4	15.2	11.2	26.1%
40	2	0.3	7.1	22.52	22.0	2.2%
41	2	0.3	14	13.23	12.0	9.3%
42	2	0.3	18.4	13.07	10.5	19.8%
43	3	0.3	7.1	21.37	20.8	2.6%
44	3	0.3	14	12.55	11.1	11.9%
45	3	0.3	18.4	11.56	9.8	15.1%
46	1	0.1	7.1	16.45	15.6	5.2%
47	1	0.1	14	11.6	9.3	20.0%
48	1	0.1	18.4	10.64	8.3	21.9%
49	2	0.1	7.1	15.7	15.2	3.1%
50	2	0.1	14	9.55	8.7	8.4%
51	2	0.1	18.4	8.98	7.9	12.4%
52	3	0.1	7.1	15.07	14.6	2.8%
53	3	0.1	14	8.7	8.1	6.7%
54	3	0.1	18.4	8.54	7.4	13.7%

Table 6.5: Girder internal energy in combined grounding

Results presented in Table 6.5 show that the analytical model tends to underestimate the dissipated energy when φ increases and this effect is all the more visible on wide rocks (1 and 2). There are two main reasons for such discrepancies:

- As a reminder, additional bending of plate flaps during the vertical ship motion is not considered in the current analytical model. However, since the rupture of the outer shell is almost instantly triggered, the hole enlargement during to the vertical motion dissipates a significant amount of energy and more especially in case of large rocks.

- The raking solutions developed in Chapter 5 always underestimate the resisting forces for large rocks at low penetration depth. Indeed, in this situation, the created flaps are no longer flat as it was assumed in Chapter 5, but follow the rock shape - see Figure 6.15 for instance. Therefore, additional energy is dissipated through plastic bending and membrane straining. It should be stressed that such deformations were not observed in sections 6.4 and 6.5 since, for rock 1 and 2, the rupture was triggered at a higher penetration depth.

These explanations are confirmed by the fact that the deviation is generally smaller for the sharpest rock (id 3), even when the impact angle φ increases. Therefore, when the rock is large, the resisting force and especially its vertical component is underestimated as illustrated by Figure 6.13. Despite this, considering the 18 cases, the average deviation is 11.3% which appears reasonable.

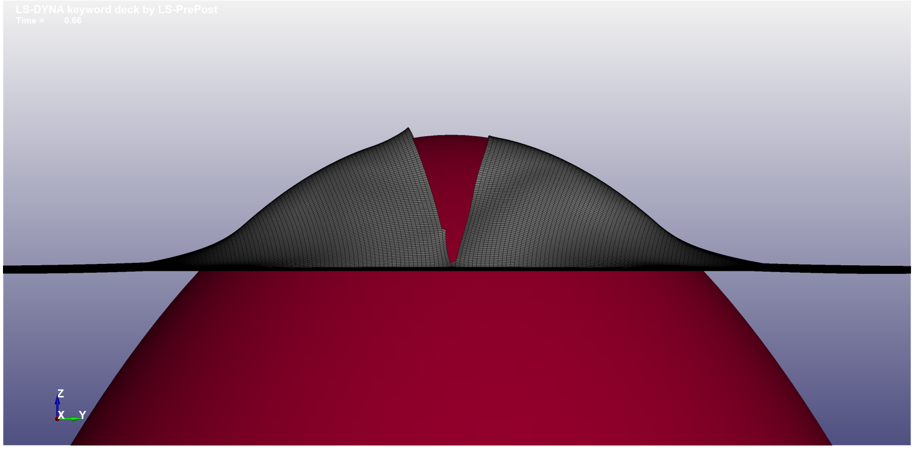

Figure 6.15: Tearing deformation for large rock - Combined grounding

The contribution of the different components and friction to the dissipated energy is given in Figures 6.16a and 6.16b. Once again, these figures confirm that the most energy absorbing parts are the bottom plating and the girders, while floors dissipate a very small amount of energy.

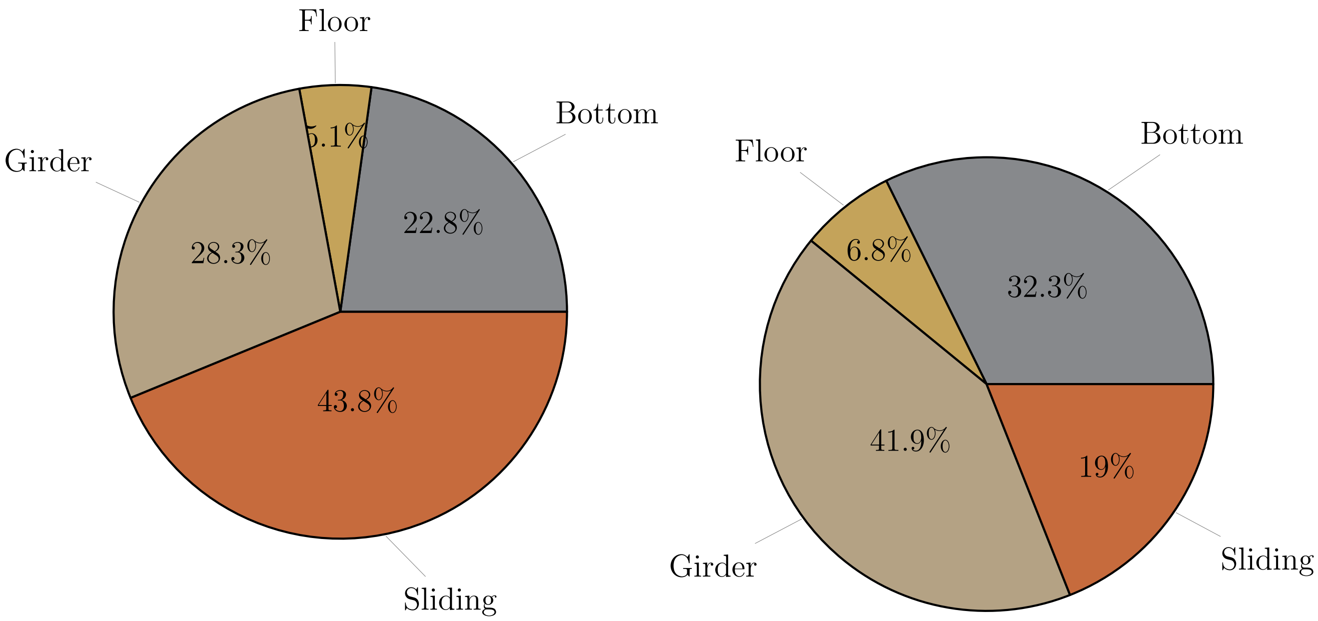

(a) $\mu = 0.3$ (b) $\mu = 0.1$

Figure 6.16: Energy distribution for an impact below a girder - Combined grounding

6.7 Conclusion

The work presented in this chapter aimed to derive a set of analytical solutions for the problem of a ship bottom running aground a paraboloid shaped rock through a combined surge and heave movement.

Various finite element simulations were carried out and simplified models were proposed to simulate both the sliding and raking deformations of outer/inner shell, floors and girders. The closed-form expressions proposed in this chapter are mainly based on derivations performed in Chapters 4 and 5.

From the observation of the numerical results, a simple failure criterion combining membrane straining and bending of the bottom plating was established to switch from the sliding to the raking mode. Considering in total 54 different scenarios, the results obtained from the proposed analytical models were systematically confronted to numerical simulations and, in general, a pretty good agreement was observed. However, the following limitations may be pointed out:

- When the ship hull is in a raking mode, the resistance of the floors is always underestimated by the simplified model. Fortunately, floors contribution to the total dissipated energy is small compared to outer shell, girders and friction contributions.
- As reported by *Heinvee* [20], the numerical simulation of situations where the rock impacts the ship just below a girder results in a premature rupture of the outer shell. However, the reliability of such simulations is questionable as the failure criteria used in the numerical models may no longer be suitable in areas where large out-of-plane shear strains dominate.
- When the ship bottom is raking over a large rock, the proposed model tends to underestimate the resistance of the bottom plating. In fact, with a large rock and a small penetration depth, the flaps created on the two edges of the rock are no longer straight but rather curved as they follow the rock shape. The bottom plating thus suffers additional bending and membrane straining deformations that are not captured by the analytical model.

Although imperfect and improvable, the proposed simplified approach results conservative in all studied scenarios and can be advantageously used to rapidly assess the response of a ship grounding over a paraboloid shaped rock through a combined surge and heave movement.

Part III

Ship grounding analysis tool

Chapter 7

Simplified tool FLAGS/MCOL

7.1 Introduction

The simplified formulations derived in Chapters 4, 5, and 6 have been validated individually by confrontation to numerical results, then mixed together to analyse the response of a full ship bottom stiffened section. To do this, the structures were systematically constrained on their edges and the rock was forced to follow a prescribed path into the structure. This means that hydrodynamic forces acting on the ship immersed hull and governing its rigid-body movements were totally ignored. To develop a complete calculation code, the simplified formulations have been implemented into a semi-analytical solver named *FLAGS* (**FLA**RE **G**rounding **S**olver) and the latter is coupled with the existing "fluid" external dynamics solver *MCOL* [175].

The present chapter includes:

- A general presentation of the *FLAGS/MCOL* tool (Input and output data, graphical interface).
- An explanation on its overall functioning (Interactions between the different modules).
- The validation of the tool by confrontation to numerical simulations for several grounding scenarios.
- Structural sensitivity analyses carried out with *FLAGS/MCOL* tool considering both bottom and side grounding events.

7.2 Overview of the simplified solver

The objective of this section is to briefly present the simplified program *FLAGS/MCOL*. The section presents the functioning of the solver, input and output data as well as the graphical user interface (GUI). Both *FLAGS* solver and its graphical interface were developed in Java language.

7.2.1 Input files

Data requested to fully define a ship grounding event is distributed in three different input files:

- *Ship.xml* which contains the description of the ship hull arrangement.
- *Ship.mco* which contains the hydrodynamic data of the ship.
- *Scenario.xml* which describes the grounding scenario.

Since the solver is based on simplified formulations, the ship description is limited to the main scantling of the hull i.e., spacing between floors and girders, double bottom height and structural thicknesses and materials. The ship hull is then divided into a finite number of Super-Elements, their position being expressed in an earth fixed reference frame. Note that the material description is limited to the flow stress and ductile rupture toughness in accordance with the rigid-plastic assumption.

The second file *Ship.mco* contains the ship mass, water added mass, wave radiation damping and hydrostatic restoring matrices. An example is given in Appendix E and more details regarding the definition of these matrices may be found in [6, 176]. In this work, *Hydrostar* seakeeping code from the *Bureau Veritas* has been used to calculate the hydrodynamic properties of Floodstand ship B cruise ship. This software is based on 3D diffraction/radiation potential flow theory for wave-body interactions taking into account multi-body interaction, effects of forward speed and dynamic effects of liquid motions in tanks. It is worth noting that the effect of progressive flooding on the ship hydrodynamic properties is not considered in this study. In addition, the influence of the rock on the velocity field of water particles is also disregarded. Such influence could be quantified by a CFD calculation for instance but doing this would not be coherent with the idea of developing a simplified and efficient tool.

Finally, the file *Scenario.xml* contains all the data relative to the grounding scenario i.e., initial position (XYZ) of the rock in the earth fixed frame, initial ship speeds, friction coefficient and rock parameters. An example is given in Figure 7.1, and Appendix E presents an example of *ship.mco* and *ship.xml* files..

```xml
<?xml version="1.0" encoding="UTF-8" standalone="yes"?>
<PROJECT>
    <GROUNDING Type="bottom_Grounding"> <!-- Grounding type -->
        <X>130</X>
        <Y>3</Y>
        <Z>1</Z>
        <Vx>2.572</Vx> <!-- Ship initial Surge, Sway and Heave velocity  -->
        <Vy>0</Vy>
        <Vz>0</Vz>
        <Friction>0.3</Friction> <!-- Ship / Rock friction coefficient -->
        <DeltaT>0.0</DeltaT> <!-- Specified timestep -->
        <C>0.7</C> <!-- Rock coefficients C - E -->
        <E>4.0</E>
    </GROUNDING>
</PROJECT>
```

Figure 7.1: Example of scenario input file

7.2.2 Output files

Once a simulation has been completed, several output files are created but only two are of interest:

- Results.csv
- Out.HMI

The output file *Results.csv* stores the time histories of resisting forces, energies dissipated by the structural components, ship kinematics, etc... The second file contains the list of impacted elements at each time step and is mainly used for graphical post-processing.

The *FLAGS/MCOL* graphical interface depicted in Figure 7.2 is constituted of three different areas. The first one (orange box) allows to select the project, create a video, change the camera angle etc... In the second area (blue rectangle), the impacted Super-Elements are highlighted in different colours depending on their state (non-impacted, impacted, ruptured, deleted) and the position (translation and rotation) of the ship is updated at each time step. Finally, in the third area (red box), the time evolution of resisting forces, dissipated energies, ship displacements, velocities and other quantities available in the *Results.csv* file are visualised.

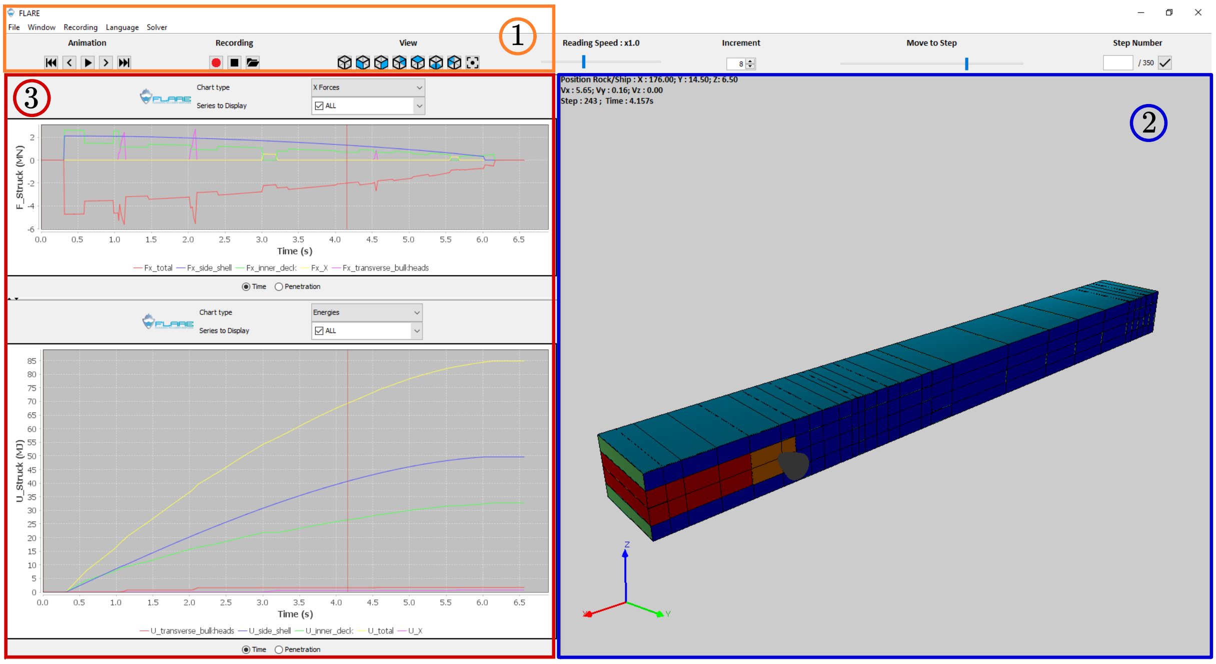

Reading Speed : x1.0

Increment 8

Step Number / 350

Position Rock/Ship : X : 176.00; Y : 14.50; Z: 6.50
Vx : 5.65; Vy : 0.16; Vz : 0.00
Step : 243 ; Time : 4.157s

Chart type: X Forces
Series to Display: ☑ ALL

● Time ○ Penetration

Chart type: Energies
Series to Display: ☑ ALL

● Time ○ Penetration

Figure 7.2: FLAGS/MCOL Graphical User Interface

7.2.3 Main program

Figure 7.3 resumes the general calculation procedure which includes the following steps:

- First, an *Hydrostar* calculation is performed to obtain the ship hydrodynamic properties needed by *MCOL*.
- Then, the input files presented in subsection 7.2.1 are read. The main loop of *FLAGS/MCOL* then begins.
- At each time step, a detection module is first activated. The impacted Super-Elements are identified and the penetration of the rock into each impacted Super-Element is computed. More details about element detection are given in subsection 7.2.4
- Then, for each Super-Element and depending on its type (bottom, floor, girder or intersection) and the state of the outer hull (ruptured or not), the resisting forces F_L, F_T and F_V are computed using the formulations presented in Chapters 4, 5 or 6.
- By summing up the contribution of each impacted element, the total resisting forces acting along longitudinal, transverse and vertical directions as well as resulting moments with respect to the ship CoG are computed. Forces and moments are then transferred to *MCOL* program which solves Eq. 2.2. The new X_G, Y_G, Z_G positions of the centre of gravity as well as the roll, pitch and yaw angles are calculated and transferred back to *FLAGS* for the next iteration.
- If the stopping criterion presented in subsection 7.2.6 is satisfied, the results are printed and the program stops. Otherwise, the position of all Super-Elements is updated according the translations and rotations of the ship CoG.

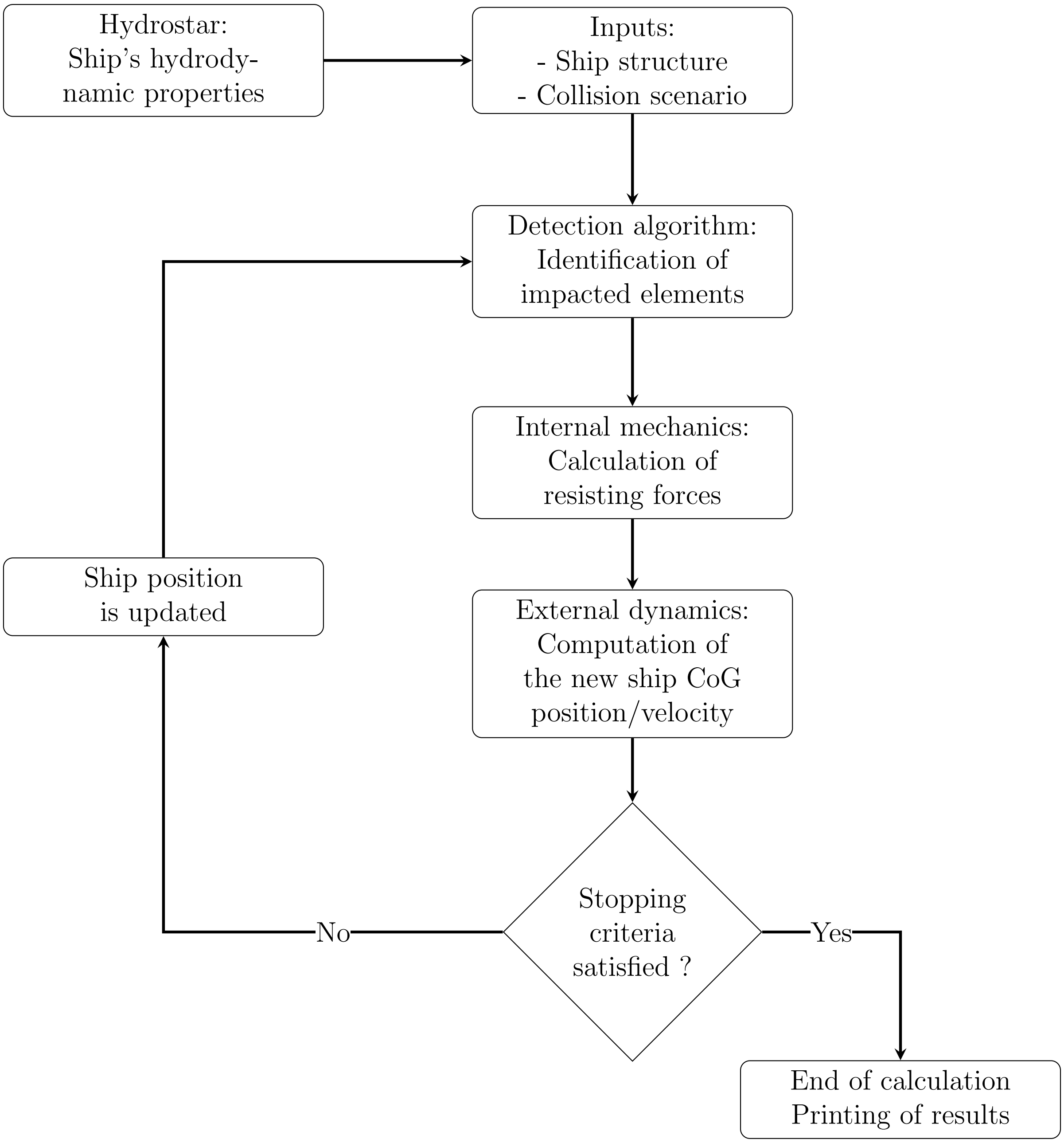

Figure 7.3: FLAGS Flowchart

7.2.4 Detection of impacted Super-Element

One possibility to obtain the list of the impacted elements might be to apply a detection algorithm to the entire ship structure. Nevertheless, since the bottom hull may contain hundreds of S.E, doing so would lead to a loss of efficiency in terms of computation time. Therefore, the Super-Elements located in the circle of radius R_d and centred at the rock apex R are first identified. They are highlighted in orange on Figure 7.4. Then, a detection algorithm is applied to these elements and various quantities such as the vertical penetration (H) of the rock into the element are calculated.

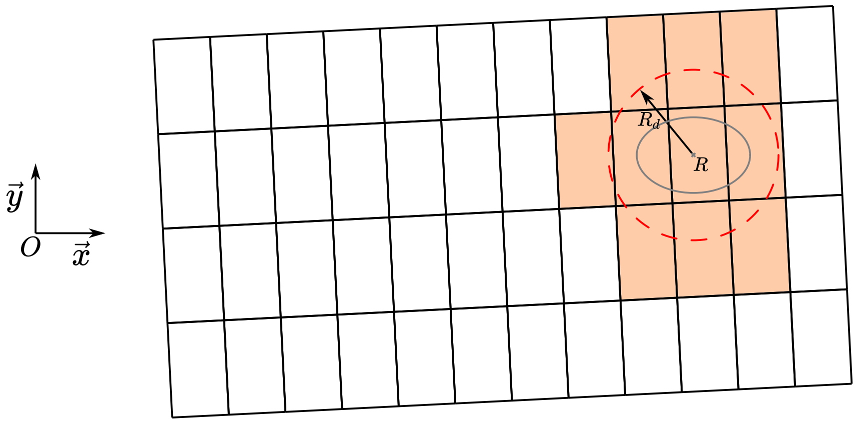

Figure 7.4: Pre-filter detection procedure

In the following, the equations are written for the case of an outer / inner bottom plating. However, the procedure may be easily adapted to floors and girders.

In the earth-fixed frame, the equation of the rock becomes:

$$z = Z_0 - C(x - X_0)^2 - E(y - Y_0)^2 \tag{7.1}$$

Where X_0, Y_0 and Z_0 are the initial coordinates of the rock apex provided in the *Scenario.xml* file. All the flat plate elements may be described by the following Cartesian equation:

$$ax + by + d + z = 0 \tag{7.2}$$

Where a, b and d are three coefficients depending on the connecting node coordinates (X, Y, Z). From Eqs. 7.1 and 7.2, the intersection of a Super-Element with the rock is given by the following quadratic form:

$$K_1x^2 + K_2xy + K_3y^2 + K_4x + K_5y + K_6 = 0 \tag{7.3}$$

Where $K_{i\ 1 \le i \le 6}$ are expressed as:

$$\begin{cases} K_1 = C \\ K_2 = 0 \\ K_3 = E \\ K_4 = -a - 2CX_0 \\ K_5 = -b - 2EY_0 \\ K_6 = CX_0^2 + EY_0^2 - d - Z_0 \end{cases} \tag{7.4}$$

Equation 7.3 may be rewritten in matrix form as:

$$\begin{pmatrix} x & y \end{pmatrix} \begin{pmatrix} K_1 & K_2 \\ K_2 & K_3 \end{pmatrix} \begin{pmatrix} x \\ y \end{pmatrix} + \begin{pmatrix} K_4 & 0 \\ 0 & K_5 \end{pmatrix} \begin{pmatrix} x \\ y \end{pmatrix} + K_6 = 0 \tag{7.5}$$

With a paraboloid rock shape, $K_2 = 0$ so Eq. 7.3 is :

$$K_1(x')^2 + K_3(y')^2 + K_7 = 0 \tag{7.6}$$

With :

$$\begin{cases} x' = x - \frac{1}{2}K_4/K_1 \\ y' = y - \frac{1}{2}K_5/K_3 \\ K_7 = K_6 - \frac{1}{K_1}\left(\frac{K_4}{2}\right)^2 - \frac{1}{K_3}\left(\frac{K_5}{2}\right)^2 \end{cases} \tag{7.7}$$

Finally, depending on the sign of K_7, one obtains:

$$\begin{cases} K_7 = 0 & \textit{Intersection is reduced to a point} \\ K_7 < 0 & \textit{Intersection is reduced to an ellipse} \\ K_7 > 0 & \textit{No intersection} \end{cases} \tag{7.8}$$

Since a Super-Element is a finite plane surface, a simple procedure is applied to check if the rock is actually inside the Super-Element when the intersection reduces to an ellipse or a point. Then, the centre of the ellipse as well the penetration into the S.E are calculated.

7.2.5 Time step computation

Defining the time step requires to find a compromise between a small time step that provides accurate results at the cost of an important computation effort, and a large time step that allows for rapid computation but with lower accuracy.

For ship grounding application, the time step Δt should be small enough to ensure that no transverse structure will be missed between two successive iterations. In addition, since the dissipated energy is calculated as the integral of the force-displacement curve, the time step should be small enough to integrate with sufficient accuracy. Based on several analyses, the time step has been set to:

$$\Delta t = \frac{R_x}{V_x}\frac{1}{10} \tag{7.9}$$

Where R_x and V_x are respectively the longitudinal radius of the rock into the outer shell and the ship surge velocity. Equation 7.9 ensures that 10 iterations are performed during the crushing of a transverse floor, which appears sufficient to accurately capture the evolution of the resisting forces. Besides, as the ship slows down, the surge velocity V_x decreases and consequently the time step interval Δt should be allowed to increase. Then, for sake of efficiency, the time step is reevaluated every 100 iterations based on the actual surge velocity $V_x(t)$. Figure 7.5 illustrates a typical evolution of the time step Δt with the number of iteration. It should be emphasised that the user can also define a constant time step in the *Scenario.xml* file.

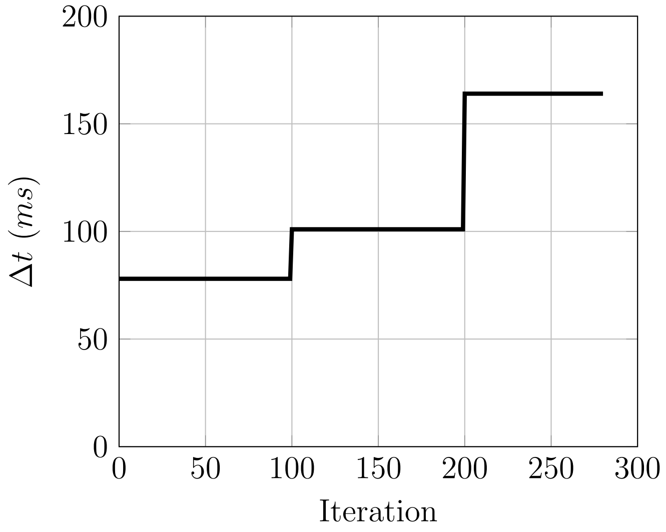

Figure 7.5: Typical evolution of time step interval

7.2.6 Stop criteria

The calculation procedure continues until one of the following stop criteria is satisfied:

1. $V_x = 0$
2. Out of ship

The first condition corresponds to the case where the entire kinetic energy has been dissipated through plastic deformation and friction. At the end of the calculation, the ship is at rest. The other case corresponds to a ship that has been entirely damaged (along its full length), or has "escaped" from the rock (after a heave, roll or sway movement for instance). The ship final kinetic energy is not necessarily zero but the calculation stops as soon as the ship is no longer in contact with the rock.

7.3 Application to bottom grounding

In this section the *FLAGS/MCOL* solver is validated by simulating full ship bottom grounding events and by comparing the results with *Ls-Dyna/MCOL* numerical simulations. In a second step, the solver is used to investigate the effect of various structural parameters on the ship damage extent.

7.3.1 Validation

To validate *FLAGS/MCOL* tool in bottom grounding, a benchmark that involves three partners of the FLARE project - Aalto University in Finland, Strathclyde University (MSRC[1]) in Scotland and ICAM Engineering School - has been conducted and reported in *Le Sourne et al.* [53] and *Kim et al.* [108].

For this purpose, the Floodstand cruise ship B [177] has been selected and its bottom structure has been simplified to avoid some geometric uncertainties due to the complex real scantling - see Figure 7.6. The simplified structure is composed of a bottom, a double bottom, floors and girders. The main particulars of the structure are given in Table 7.1 and the ship bow is represented by an inclined bottom plating making an angle of 35° from the horizontal.

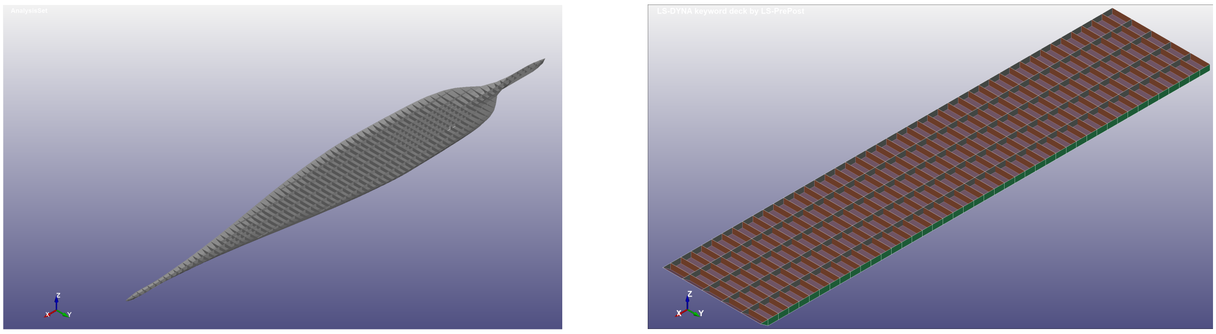

Figure 7.6: Floodstand ship B bottom - left (real) - right (simplification)

Two impact locations were considered, the first at the centre line, i.e., $y = 0$ (Centred impact) and the second at $y = B/4 = 7.125\,m$ from the centre line (Off-centred impact). The ship was given an horizontal velocity of 5 knots $\approx 2.572\,m/s$ and a friction coefficient $\mu = 0.3$ was chosen. Regarding the rock, the first peak of the real sharp rock presented in Chapter 5 was considered, with coefficients $C = 3.7$ and $E = 6$. The impact height was $2m$ in order to trigger the rupture on both the bottom and double bottom.

---

[1] Marine Safety Research Centre

Description	Dimensions
Length (m)	200
Breadth (m)	28.5
Double bottom height (m)	1.6
Transverse frame spacing (m)	3
Longitudinal girder spacing (m)	5.7
Outer bottom thickness (mm)	15
Inner bottom thickness (mm)	10
Transverse floor thickness (mm)	15
Longitudinal girder thickness (mm)	20

Table 7.1: Bottom structure main characteristics - Bottom grounding benchmark

Aalto and MSRC performed numerical analyses using *Ls-Dyna/MCOL* finite element software. A rigid perfectly plastic material associated to a 80mm element-size mesh was considered by Aalto while MSRC used a modified true stress-strain curve as proposed by *Paik & Thayamballi* [178], associated to a 250mm element size mesh. More details regarding the benchmark may be found in *Le Sourne et al.* [53] and in *Kim et al.* [108].

The evolution of the dissipated energy as a function of the breach length obtained by Aalto and MSRC are compared in Figure 7.7 with the results post-processed from *FLAGS/MCOL* simulations. This figure clearly underlines a very good performance of the simplified approach to estimate the breach length. The damage extent and dissipated energy obtained from Aalto and MSRC numerical simulations are compared to FLAGS results in Table 7.2.

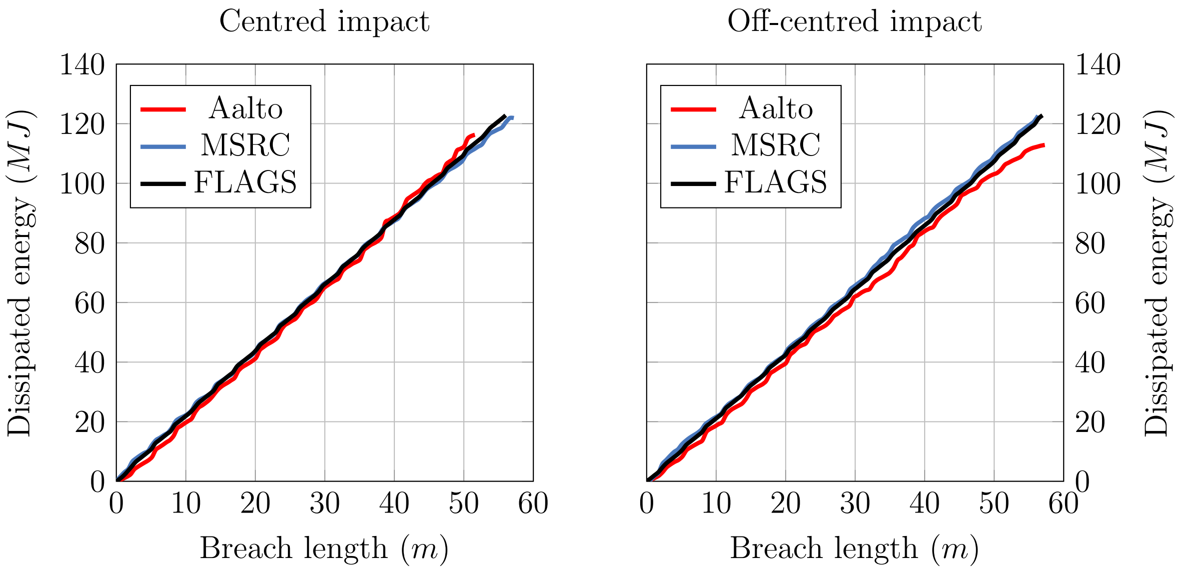

Figure 7.7: Dissipated energy versus breach length

Scenario	Partners	Damage length (m)	Dissipated energy (MJ)	Deviation damage length	Deviation dissipated energy
Centred	FLAGS	56.0	122.8	—	—
	Aalto	51.6	116.3	-7.9%	-5.3%
	MSRC	57.2	121.9	2.1%	-0.8%
Off-centred	FLAGS	57.0	122.8	—	—
	Aalto	57.3	112.9	0.6%	-8.1%
	MSRC	56.3	122.7	-1.1%	-0.1%

Table 7.2: Bottom grounding benchmark synthesis

The major advantage of the analytical solver is its rapidity: only 4 minutes are necessary to complete the simulation with *FLAGS/MCOL* while 4 days are needed with *Ls-Dyna/MCOL* using parallel computing (12 CPU and 20 GB of ram). The simplified approach is then around 1 500 times faster, with a discrepancy on the damage extent that does not exceed 8%. Further validations with different rocks and different ships are obviously needed to consolidate the reliability of the developed tool but these first results obtained on a full scaled structure are very encouraging regarding both the precision and the computation time.

Taking advantage of the rapidity of the tool, hundreds of scenarios have been simulated in the optic of investigating the effect of different parameters on the ship response. The next subsection presents this sensitivity analysis.

7.3.2 Parametric grounding analysis

7.3.2.1 Methodology

The objective here is to analyse the effect of different structural modifications on the damage extent. The methodology employed is based on the "indirect" or "comparative" approach presented in Chapter 1, which may be summarised as follows:

1. First, a series of grounding simulations are performed on the original ship configuration and, for each grounding scenario considered, the damaged extent L_0 is post-processed.
2. Simulations are then rerun varying only one parameter, for example the thickness of the bottom plating and the damage extent L_N related to the new design is post-processed.
3. L_N is finally compared to the initial damage L_0 and the influence of the structural modification is quantified by defining a breach reduction factor $k_b = \frac{L_N - L_0}{L_0}$.

Therefore, the effective breach reduction factor $\overline{k_b}$ may be obtained as the average reduction factor and calculated as :

$$\overline{k_b} = \frac{1}{N} \sum_{i=1}^{N} k_{bi} \tag{7.10}$$

Where N is the number of grounding scenarios that are investigated. As recently demonstrated by *Conti et al.* [3] for ship collision analysis, a large number of scenarios must be considered to obtain reliable conclusions. Here, for each structural modification, 540 bottom grounding scenarios are simulated, considering all the combinations of the parametric values listed in Table 7.3.

	Parameters	Values
Rock	C (m^{-1})	0.3 - 0.5 - 1.0 - 1.5 - 3 - 6
Parameters	E (m^{-1})	0.3 - 0.5 - 1.0 - 1.5 - 3 - 6
Impact	Y (m)	0 - 2.85 - 7.125
Position	Z (m)	0.3 - 0.5 - 1 - 2 - 3
Initial surge velocity	V_x (m/s)	2.572

Table 7.3: Scenario parameters - Bottom grounding analysis

Such values have been defined considering the following situations. First, according to *Youssef & Paik* [4], the lateral position (Y) of the impact follows a uniform distribution law. Three positions were therefore selected in such a way that the impact is located between 2 girders ($y = 0$), affects partially one girder ($y = 7.125$) and is located just below a girder ($y = 2.85$). Second, vertical positions (Z) of the rock apex with respect to the ship bottom were chosen to simulate both sliding and raking situations: small penetrations enable sliding grounding while large penetrations will foster raking grounding and, for the highest values, inner hull crushing. Finally, following the work of *Conti* [179], the rock parameters were selected to consider a large variety of rock shapes, from shallow ($E = 0.3$) to sharp ($E = 6$) rocks.

Now that the methodology has been introduced, the sensitivity analysis will focus on the following structural parameters:

- Outer bottom thickness (t_{hO})
- Inner bottom thickness (t_{hI})
- Floor thickness (t_{hF})
- Girder thickness (t_{hG})
- Material grade (σ_0)

Each parameter is changed by ±25% from its initial value. Combining 3 values for each parameters with the aforementioned 540 scenarios leads to 5 940 grounding simulations. It should be stressed that the structural modifications are supposed not to alter the hydrodynamic properties of the ship (i.e. the change in mass is negligible compared to the total ship mass).

A typical example of results obtained from the analysis of the influence of the outer shell thickness is depicted on Figure 7.8.

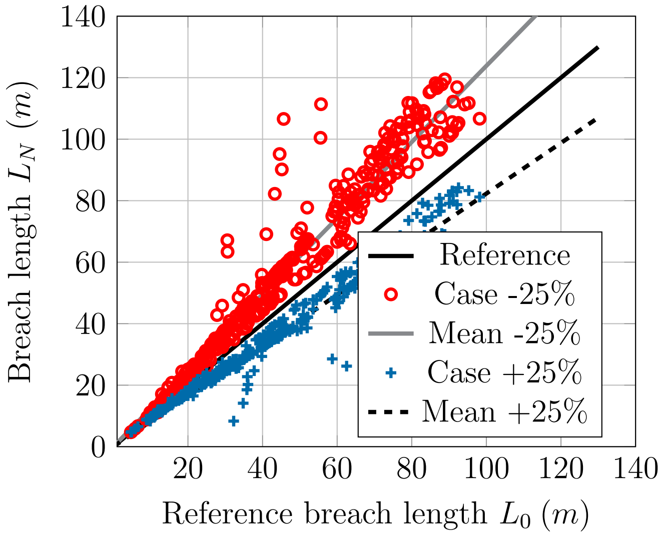

Figure 7.8: Evolution of the breach length when the outer shell thickness is varied

Table 7.4 presents the effective reduction factors $\overline{k_b}$ post-processed from the 5 940 simulations. It should be emphasised that, in order to compare like with like, the scenarios for which the damage extent equals the ship length ($130m$) have been removed from the analysis.

	Case -25%		Case +25%	
Parameter	Value	$\overline{k_b}$	Value	$\overline{k_b}$
t_{hO} (mm)	11.25	+28.6%	18.75	-21.9%
t_{hI} (mm)	7.5	+8.35%	12.5	-6.8%
t_{hF} (mm)	11.25	+0.6%	18.75	-0.6%
t_{hG} (mm)	15	+21.7%	25	-14.3%
σ_0 (MPa)	240	+29.0%	400	-18.0%

Table 7.4: Effective breach reduction factors - Bottom grounding

Let us denote by F_L the average longitudinal resisting force related to the reference ship and suppose that the modified scantling resits with a force equal to τF_L. Assuming that all the ship initial kinetic energy (E_0) has been entirely dissipated during the grounding event, the theoretical breach reduction factor λ may be estimated as:

$$\lambda = \frac{E_0/(\tau F_L) - E_0/F_L}{E_0/F_L} = \frac{1}{\tau} - 1 \tag{7.11}$$

According to Eq. 2.22, increasing the flow stress σ_0 by 25% leads to the increase of the resistance force F_L by 25%, i.e. $\tau = 1.25$. Therefore, using Eq. 7.11 with $\tau = 1.25$ yields $\lambda = -20\%$ and inversely, $\tau = 0.75$ yields $\lambda = 33\%$. These values are in accordance with the results summarised in Table 7.4.

More generally, several conclusions can be drawn from the analysis of Table 7.4:

- In the great majority of scenarios, the ship moves along a straight path meaning that the effect of hydrodynamic properties other than the ship surge added mass is very limited. Therefore, in the considered bottom grounding scenarios, the calculations stop either because the initial kinetic energy has been entirely dissipated or because the ship has been damaged along its full length ($130m$).

- As expected, since the contribution of transverse floors is limited, varying the floor thickness by ±25% has a marginal influence on the damage extent.
- The effect of the inner bottom thickness on the damage extent is rather limited. This is because the inner bottom is crushed in only 40% of the scenarios. Moreover, when the inner bottom is impacted by the rock, it contributes only by around 25% to the dissipated energy.
- Variations on the outer shell thickness t_{hO}, the girder thickness t_{hG} and the material flow stress σ_0 have almost the same effect on the breach length.
- The damage extent does not vary linearly with the scale factor τ but rather in $1/\tau$.

7.3.2.2 Effect of friction

The friction coefficient between the rock and the vessel is often arbitrarily defined as $\mu = 0.3$ - see for instance [12, 19, 34, 153]. To quantify its effect on the damage extent, 1080 additional grounding simulations with a friction coefficient set either to $\mu = 0.1$ or to $\mu = 0.6$ have been carried out and the results are plotted in Figure 7.9.

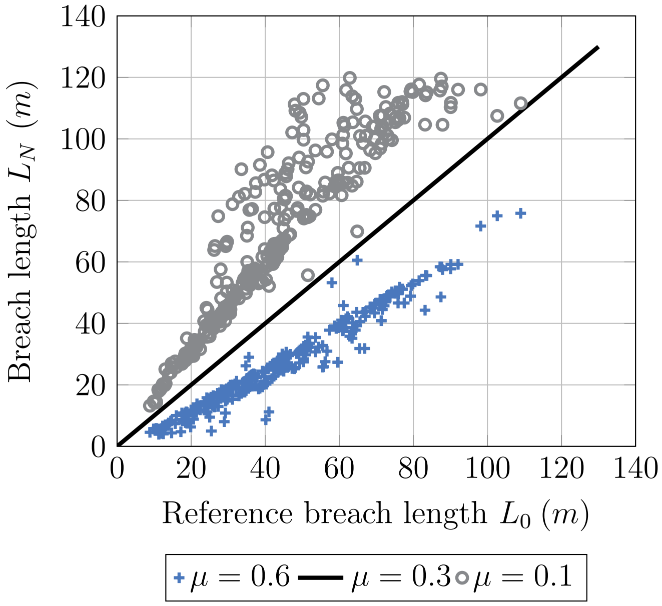

Figure 7.9: Influence of μ on the damage length - Bottom grounding

As expected, damage length and friction coefficient vary inversely. However, the remarkable thing is that by only decreasing μ from 0.3 to 0.1, the damage extent is increased by almost 50%. This highlights once again the large amount of energy that is dissipated through friction in a bottom grounding event but also the importance of systematically investigating the influence of this parameter.

7.3.3 Conclusion regarding bottom grounding

In this section, *FLAGS/MCOL* tool has been first confronted to numerical simulations and both its rapidity and reliability have been demonstrated. Then, thousands of grounding scenarios have been simulated to investigate the effect of structural modifications on the breach size.

It transpired from this analysis that the three most influencing parameters are the outer bottom thickness, the girder thickness and the steel grade, suggesting that a reinforcement strategy could be to increase outer shell or girder thickness or select a higher steel grade. However, increasing the thicknesses would also increase the ship mass, as well as the production cost. In fact, as the Floodstand ship B is concerned, increasing the outer shell thickness by 25% allows to reduce the damage extent by almost 20%, for an additional mass of around 110 tonnes, which corresponds to less than 0.5% of the total ship mass.

The damage extent does not vary linearly with the parameter scale factor τ but rather in $1/\tau$. Of course, other parameters such as transverse bulkheads or girder spacing as well as contribution of longitudinals could also be investigated. Recently, using *FLAGS/MCOL*, *Conti* [179] found that doubling the number of girders has the same effect as increasing by 25 % the material grade i.e., $\overline{k_b} \approx 20\%$.

The strong effect of friction on the damage extent has also been demonstrated. This means that in a grounding analysis aiming to predict the outer or inner shell opening, as the coefficient of friction between the rock and the ship hull cannot be known in advance, a sensitivity analysis of the results to this parameter is indispensable.

7.4 Application to side grounding

7.4.1 Introduction

The great majority of research in ship grounding focuses on "bottom grounding" events, i.e. the rock is supposed to be located below the ship. Nevertheless, recent accidents of the *Sea Diamond* and *Costa Concordia* have shown that side grounding events involving an impact on the lower part of the side shell is a reality and should also be considered in ship damage stability analyses. This section thus focuses on the response of a ship in "side grounding" condition.

The analytical formulations derived in Chapters 4 and 5 for the case of bottom grounding accident may be easily adapted to side grounding problems. Table 7.5 gives the correspondence between bottom and side grounding Super-Elements. The solver *FLAGS* has thus been adapted to allow for side grounding simulations. The axis of the rock is now horizontal, the impact is assumed to be located above the ship double bottom and the methodology of detection of the impacted elements is the same as in bottom grounding.

Side grounding S.E	Bottom grounding S.E
Side shell	Bottom plating
Deck	Longitudinal girder
Transverse bulkhead	Transverse floor
Intersection deck / transverse bulkhead	Intersection girder / floor

Table 7.5: Correspondence between bottom and side grounding S.E.

7.4.2 Validation of the program

Similarly to bottom grounding, the first step consists in validating the program by comparison with *Ls-Dyna/MCOL* simulations. For this purpose, the simplified side section extracted from the Floodstand ship B cruise ship and depicted in Figure 7.10 is considered. This model includes a side shell, an inner side, decks and transverse bulkheads.

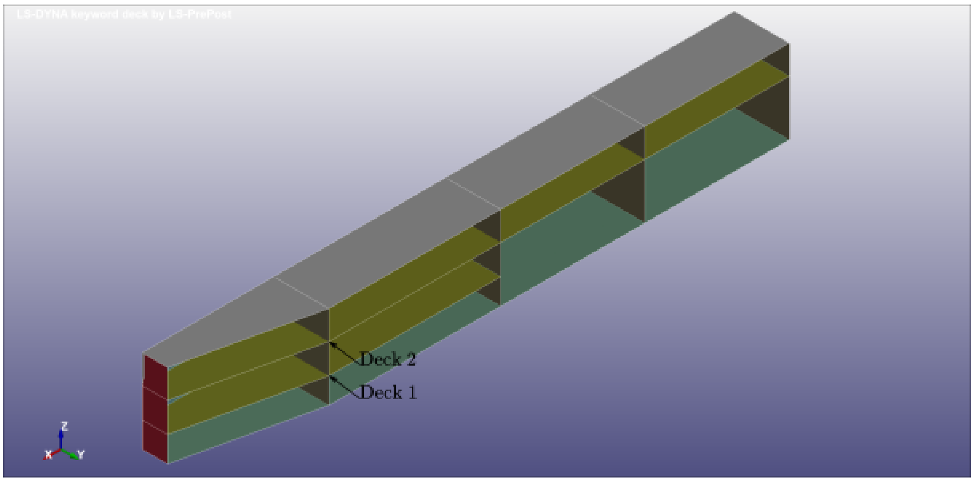

Figure 7.10: Side grounding benchmark - View of the ship model (without the side shell)

The model is $58m$ long and $16m$ wide. The fore part of the side shell makes an angle $\alpha = 12.7°$ with respect to the ship longitudinal axis and represents the fore part of the ship. The spacing between the transverse bulkheads and between the decks is $15m$ and $2.8m$ respectively. Table 7.6 gives the thickness of the different sub-structures. Regarding the finite element modelling, Belytschko-Tsay under-integrated shell elements with a size of $30mm$ and five integration point through thickness are used. The failure strain is calculated according to Eq. 2.10 and the material characteristics are listed in Table 3.1. Finally, a static friction coefficient $\mu = 0.3$ is imposed for the whole structure.

Item	Thickness (mm)
Side shell	15
Inner Side	10
Transverse bulkheads	10
Deck	8

Table 7.6: Side grounding model : component thickness

Three different scenarios are considered and related parameters are resumed in Table 7.7. The first scenario corresponds to an impact by a sharp rock between two adjacent decks (decks 1 and 2 in Figure 7.10). In the second one, a medium rock impacts the side shell directly on deck 1 and the last scenario simulates a large rock impacting the side shell just above deck 1.

Scenario id	Y (m)	Z (m)	C (m^{-1})	E (m^{-1})	V_x (m/s)
1	14	3.95	3.7	6	1.285
2	14.5	2.5	1	1	2.572
3	14.5	2.95	0.3	0.3	2.572

Table 7.7: Validation of side grounding solver - Scenario parameters

Figures 7.11, 7.12 and 7.13 compare the resisting forces F_L and F_T as well as the dissipated energy for the three scenarios. Finally, Table 7.8 resumes the damage extent and the total dissipated energy retrieved from numerical and analytical calculations.

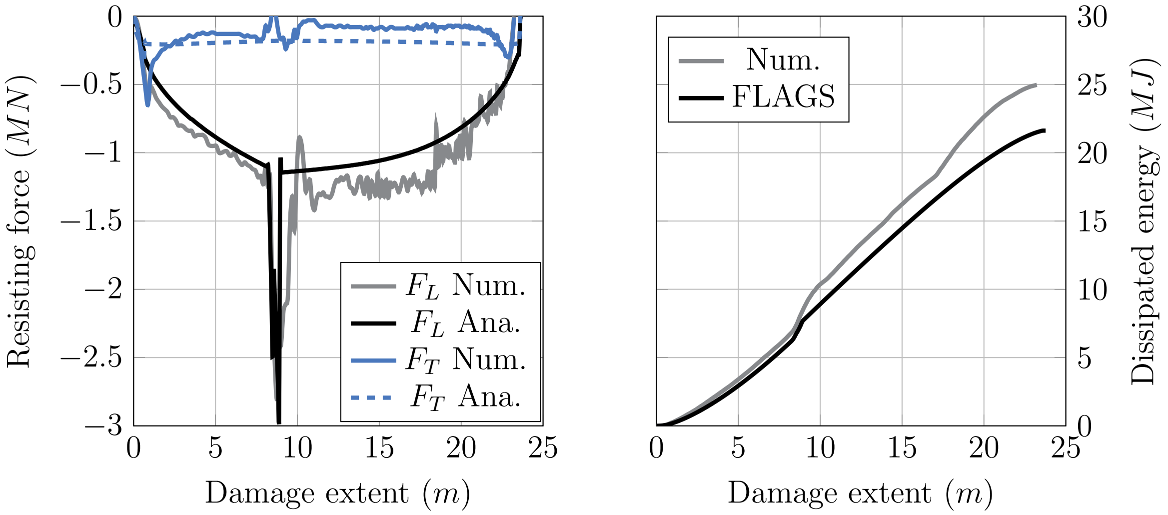

Figure 7.11: Side grounding benchmark - scenario 1

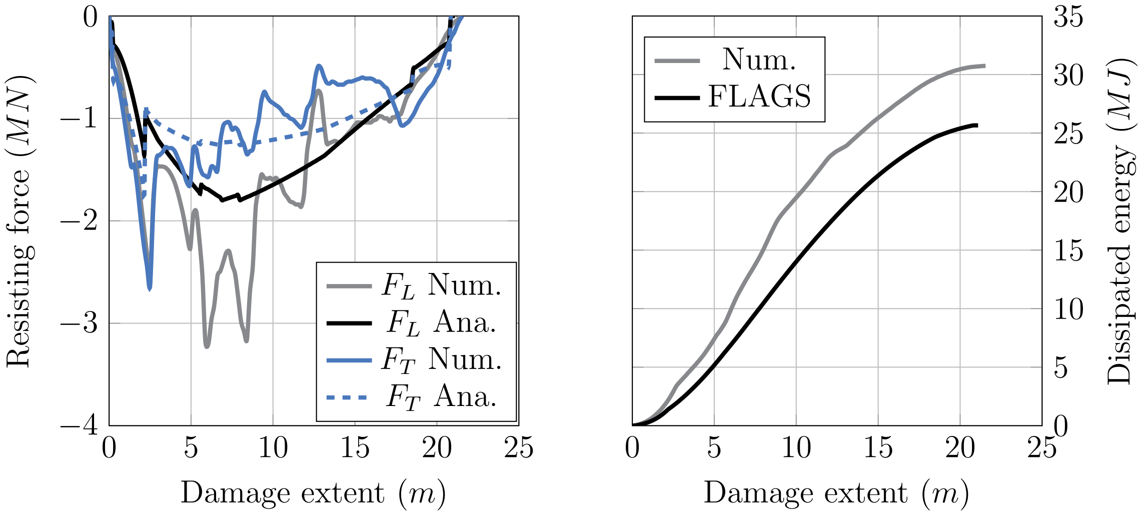

Figure 7.12: Side grounding benchmark - scenario 2

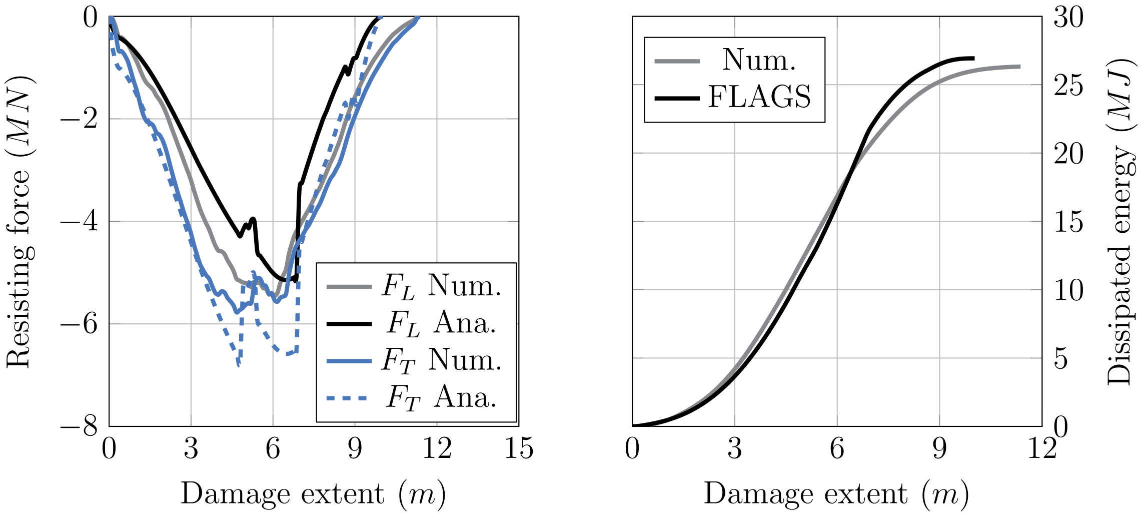

Figure 7.13: Side grounding benchmark - scenario 3

These figures show a relatively good accordance between numerical and analytical results, even if the longitudinal resisting force is slightly underestimated by *FLAGS/MCOL* tool. The highest discrepancy regarding the dissipated energy (16.5%) is observed in scenario n^o 2, in which the rock impacts the side shell at the deck level. In the numerical model, side shell failure occurs just above the junction with the deck (and only on the upper side). This leads to an opening above the deck as shown by Figure 7.14. Resulting vertical force F_V pushes downward the ship. As a consequence, the impacted deck is subjected to shearing rather than the wave pattern described in Chapter 4. The side shell below the deck also deforms, dissipating additional energy. Such deformations modes were not considered when deriving analytical solutions and may explain the discrepancy observed on both the resisting forces and dissipated energy.

All in all, Table 7.8 shows that the damage extent given by numerical and analytical solutions are in pretty good accordance, the discrepancy not exceeding 13%.

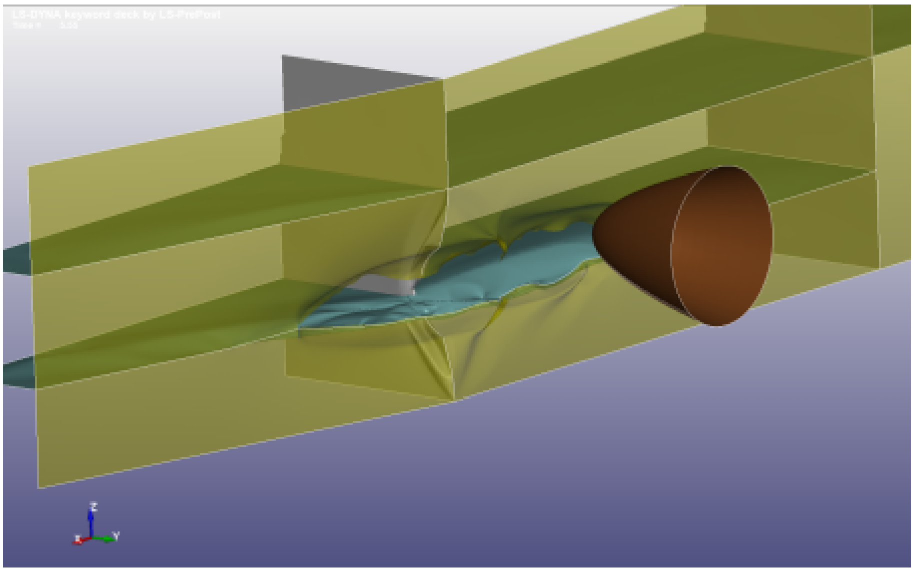

Figure 7.14: Numerical simulation of side grounding scenario 2

Scenario id	Energy Num. (MJ)	Energy Ana. (MJ)	Damage extent Num. (m)	Damage extent Ana. (m)	Dev. Energy	Dev. Damage
1	24.97	21.62	23.23	23.54	13.42%	-1.33%
2	30.74	25.66	21.55	21.1	16.5%	2.1%
3	26.32	26.93	11.37	9.93	-2.3%	12.6%

Table 7.8: Side grounding benchmark - Total dissipated energy and damage extent

For each scenario, the final surge velocity is non-zero, meaning that the calculation stops when the stop criterion “Out of ship” is activated.

The transverse force exerted by the rock has the effect of pushing the ship away from the rock. The vessel thus undergoes sway and yaw movements, which progressively decrease the penetration of the rock into the side shell until the contact is entirely removed - see Figure 7.15. The transverse force F_T exerted by the rock appears therefore to be of crucial importance since it significantly limits the damage along the ship.

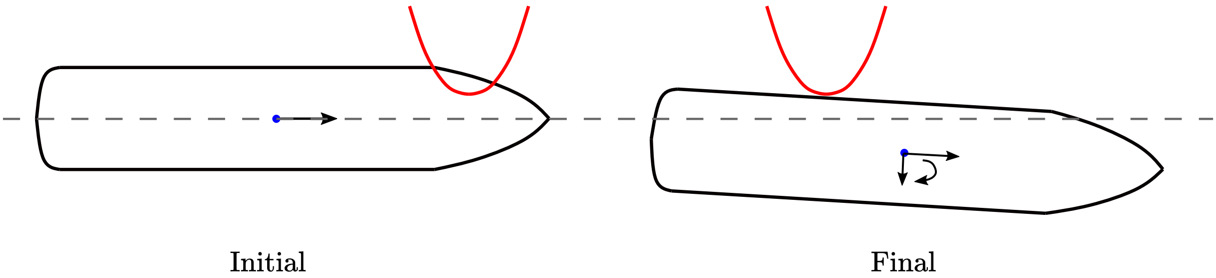

Figure 7.15: Ship side grounding initial and final position

Now regarding case n° 3, the initial penetration of the rock into the hull was $16 - 14.5 = 1.5m$. At the end of the calculation, the displacement of the centre of gravity along the sway direction is $1.22m$, the yaw angle closed to $0°$ and the roll angle $\approx 5°$. Neglecting the roll motion would have resulted in a longer damage extent. Therefore, one may conclude that the motion of the ship is clearly not restrained to surge, sway and yaw motions but the 6-DOF rigid body movement must be considered.

Several conclusions can be drawn from this benchmark study:

- First, unlike bottom grounding in which the damage extent is mostly governed by the longitudinal resisting F_L, both forces F_L and F_T play an important role in side grounding. Similarly to bottom grounding, F_L has for effect to decrease the ship surge velocity and dissipate a large amount of energy, while F_T has for effect to trigger sway, yaw and roll rigid body motions. The ship is thus pushed away from the rock, reducing drastically the damage extent.
- Second, the ship is not limited to surge, sway and yaw motions and it has been shown that out-of-plane rigid body movements must also be considered in such analysis.
- Finally, it is worth mentioning that the average computation time for one scenario is about 110 hours (4 days and 14 hours) using *Ls-Dyna/MCOL*, while the simplified tool allows to complete one simulation in around 40 seconds. In average, *FLAGS/MCOL* thus appears to be around 10 000 times faster with an average discrepancy on dissipated energy and damage extent of 10.6% and 5.3% respectively.

7.4.3 Parametric side grounding analysis

7.4.3.1 Effect of structural modifications

As for bottom grounding, now that the program has been validated by confrontation to numerical simulations, it can be advantageously used to study the sensitivity of the side damage extent to a variation of the following parameters:

- The side shell thickness (t_{hS})
- The inner deck thickness (t_{hI})
- The transverse bulkhead thickness (t_{hB})
- The material grade (σ_0)

The $140m$ long and $16.1m$ wide ship model used for the parametric analysis is depicted on Figure 7.16 (without side shell). Indeed, this is the overall Floodstand B cruise ship side that has been geometrically simplified. Its main characteristics are given in Table 7.9.

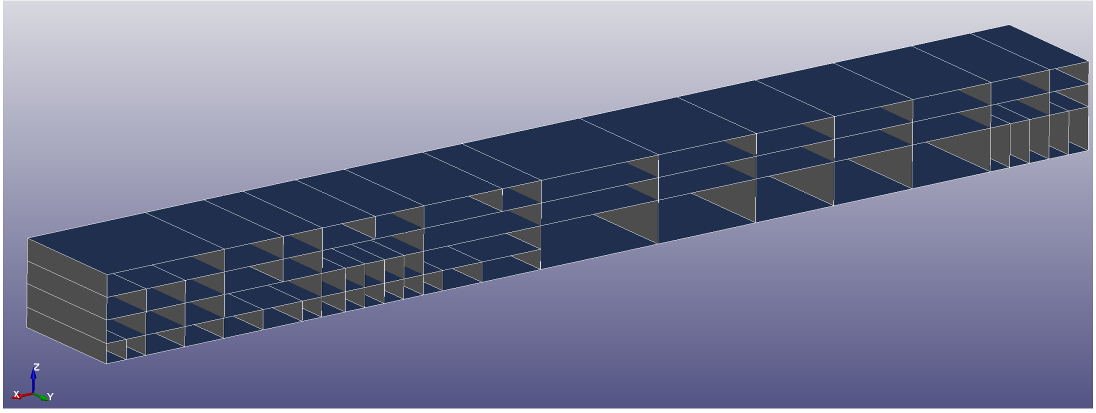

Figure 7.16: S.E. model used in side grounding parametric analysis (without side shell)

Element	Thickness (mm)
Side Shell	15
Mid decks ($z = 4.1m$ and $z = 7m$)	10
Upper decks ($z = 9.8m$ and $z = 12.6m$)	8
Transverse bulkheads, below $z = 7m$	11
Transverse bulkheads, above $z = 7m$	8

Table 7.9: Sub-structures thickness - Side grounding parametric analysis

For each alternative design, 540 simulations are carried out taking into account all the combinations of the values listed in Table 7.10.

Parameters	Values
C (m^{-1})	0.3 - 0.5 - 1.0 - 1.5 - 3 - 6
E (m^{-1})	0.3 - 0.5 - 1.0 - 1.5 - 3 - 6
H (m)	0.3 - 0.5 - 1 - 2 - 3
Z (m)	5.55 - 7 - 9
V_{surge} (m/s)	2.572

Table 7.10: Scenario parameters - Side grounding parametric analysis

In total, 4860 scenarios are simulated varying t_{hS}, t_{hI}, t_{hB} and σ_0 by ±25% from their initial value. Resulting effective breach reduction factors $\overline{k_b}$ are given in Table 7.11.

	Case -25%		Case +25%	
Parameters	Value	$\overline{k_b}$	Value	$\overline{k_b}$
t_{hS} *(mm)*	11.25	+14.0%	18.75	-11.0%
t_{hI} *(mm)*	7.5	+10.0%	12.5	-11.0%
t_{hB} *(mm)*	7.5	+0.01%	12.5	-0.01%
σ_0 *(MPa)*	240	+15.0%	400	-12.0%

Table 7.11: Synthesis of the side parametric analysis

One may observe from this table that:

- Varying the thickness of transverse bulkheads does not affect the damage extent.
- Varying side shell thickness, deck thickness and material grade has almost the same effect on the damage extent.
- The effect of a structural modification is much less pronounced compared to bottom grounding. For instance, in bottom grounding, when the material grade is changed by ±25%, the damage length is also modified by ±25%. However for side grounding, the damage extent varies by only ±13.5% in average, i.e. around two times less.

In order to explain this last point, let us assume that the ship motions are limited to sway and surge (yaw is neglected for simplification). The second Newton's law writes:

$$\begin{cases} \ddot{x}(t) = -\tau \frac{F_L}{M_L} \\ \\ \ddot{y}(t) = \tau \frac{F_T}{M_T} \end{cases} \tag{7.12}$$

Where M_L and M_T are the ship mass plus the added mass along surge and sway direction respectively, F_L and F_T are the resisting forces acting and τ traduces the increase or decrease of the resisting force related to the modified structure. Solving Eq. 7.12 by considering the ship initial surge velocity v_{x0} gives:

$$\begin{cases} x(t) = -\frac{\tau}{2} \frac{F_L}{M_L} t^2 + v_{x0} t \\ \\ y(t) = \frac{\tau}{2} \frac{F_T}{M_T} t^2 \end{cases} \tag{7.13}$$

Now, let us further assumed that the breach is limited by the sway motion of the ship. In this case, the calculation stops once the ship has undergone a sway displacement equal to the initial rock penetration H, which is achieved within a time t_f:

$$t_f = \sqrt{\frac{2HM_T}{\tau F_T}} \tag{7.14}$$

Injecting in Eq. 7.14 into Eq. 7.13 allows to estimate the damage extent:

$$L(\tau) = -\frac{F_L M_T}{F_T M_L} H + v_{x0} \sqrt{\frac{2HM_T}{\tau F_T}} \tag{7.15}$$

Resulting theoretical reduction factor λ thus writes:

$$\lambda = \frac{L(\tau) - L(1)}{L(1)} \tag{7.16}$$

Unfortunately Eq. 7.16 does not lead to a simple form as in section 7.3. However, with the expected resisting forces and ship inertia, one can show (see Appendix D.1) that λ is bounded by:

$$1.2\left(\frac{1}{\sqrt{\tau}} - 1\right) \leq \lambda \leq \frac{1}{\sqrt{\tau}} - 1 \tag{7.17}$$

According to Eq. 2.22, when σ_0 is increased by 25%, F_L and F_T are also increased by 25%. Applying Eq. 7.17 with $\tau = 1.25$ leads to $-12.7\% \leq \lambda \leq -10.6\%$, which is in accordance with $\overline{k_b} = -12\%$ given in Table 7.11. The slight variation may be due to the fact that yaw and roll motions have been neglected in above reasoning.

Finally, using Eq. 7.11 and Eq. 7.17, the theoretical breach reduction factor for side and bottom grounding is plotted as a function of τ in Figure 7.17.

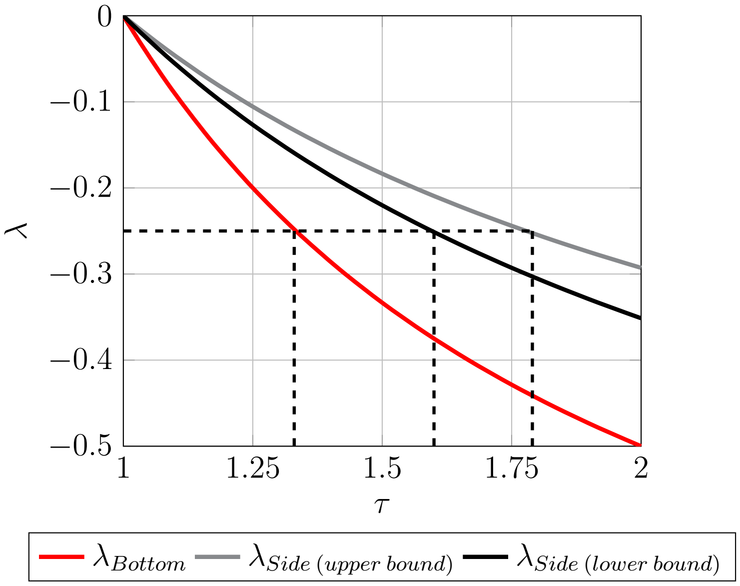

Figure 7.17: Effective reinforcement Bottom - Side grounding

Figure 7.17 shows that the effect of a structural reinforcement on the damage extent will be always lower in side grounding than in bottom grounding. For instance, if one wishes to decrease the damage extent by 25% in both bottom and side grounding, then the average resisting force should be increased by 33% in bottom grounding and 70% in side grounding. For more details please refer to Appendix D.2.

7.4.3.2 Effect of friction

As for bottom grounding, the effect of friction on the damage length is now investigated. For this purpose, simulations are once again carried out considering three friction coefficients: 0.1, 0.6 and 0.3, this later being the reference.

Figure 7.18 illustrates the effect of this coefficient on the breach length. As shown by the figure, the friction coefficient does not have a significant influence on the damage length (less than 2%) since the ship rapidly moves away from the rock. Thus one can conclude that unlike bottom grounding this parameter is not a determining factor in side grounding.

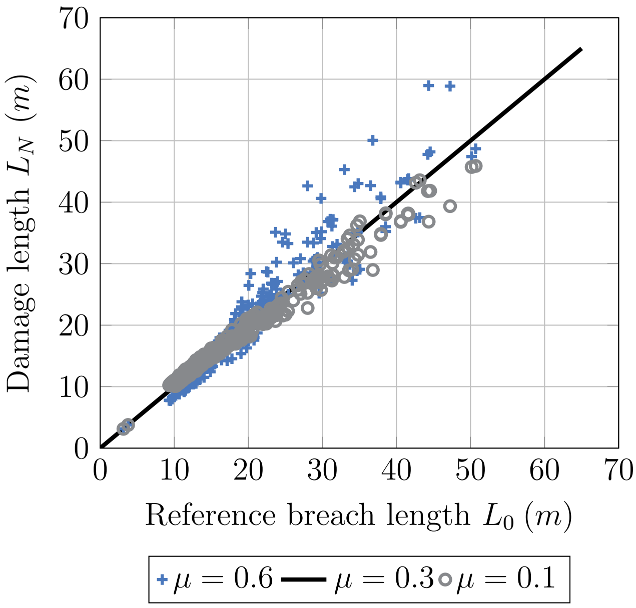

Figure 7.18: Influence of μ - Side grounding

7.4.3.3 Effect of initial kinetic energy

In bottom grounding, the damage extent is directly related to the ship initial kinetic energy (i.e. the velocity squared) but the question arises in side grounding. Side grounding scenarios are thus rerun on the reference design varying the initial velocity of the ship and the results in term of dimensionless damage extent are depicted in Figure 7.19.

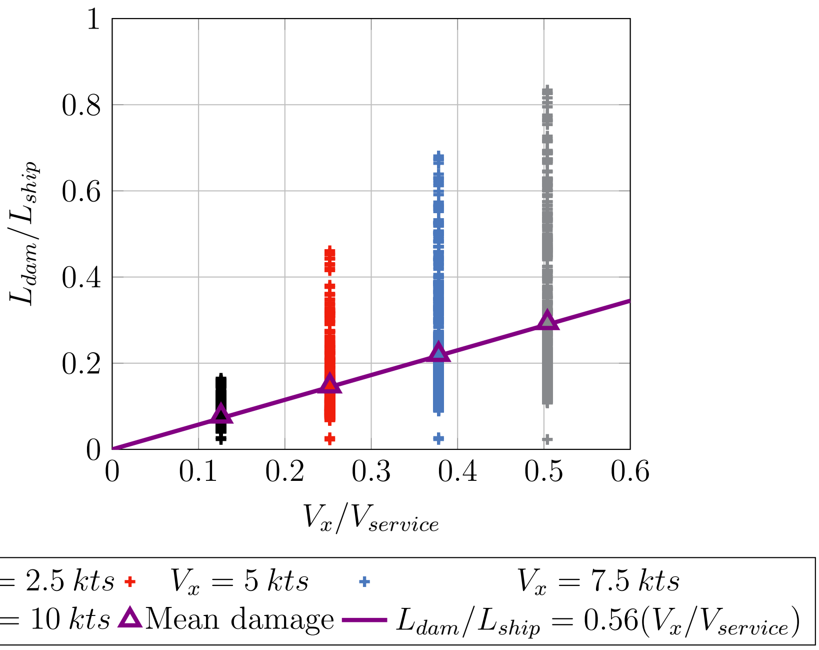

Figure 7.19: Damage length dependency on ship initial speed - Side grounding

As expected, the damage length increases with the initial surge velocity. Nevertheless, Figure 7.19 clearly indicates a linear dependency between damage extent and surge velocity, while the relation is rather quadratic in bottom grounding. This is directly related to the tendency of the ship to “escape” from the rock in side grounding. Besides, such result is in accordance with Eq. 7.15.

7.4.4 Conclusion regarding side grounding

In this section, side grounding accidents have been investigated. In a first step, *FLAGS/MCOL* tool has been confronted to *Ls-Dyna/MCOL* finite element solver considering three different scenarios and a pretty good correlation has been observed as the deviation does not exceed 20%. In a second step, the tool developed in the frame of this PhD thesis has been used to conduct a structural sensitivity analysis based on thousands of simulations. From all theses analyses, the following conclusions may be drawn:

- Due to the transverse force exerted by the rock, the ship tends to “escape” from the later, which strongly limits the damage extent.
- The most influencing parameters in damage reduction are the material grade as well as the side shell and deck thicknesses.
- The damage extent varies linearly with the initial ship velocity, unlike bottom grounding for which the relation is rather quadratic. This implies that damage extent will always be less in side grounding than in bottom grounding, even if the ship side is less stiffened that the bottom. Another consequence is that a reinforcement will always be more efficient in bottom grounding than in side grounding
- Effect of friction is negligible since it has only an influence of about 2% on the damage extent

7.5 Application to combined grounding

In sections 7.3 and 7.4, validations of *FLAGS/MCOL* tool have been performed assuming an initial surge velocity for the ship. The work presented in this section aimed to verify the reliability of the tool for *combined grounding* scenarios, in which the ship is given both surge and heave initial velocities.

7.5.1 Validation of the solver

Starting again by a confrontation to *Ls-Dyna/MCOL* simulations, five bottom grounding scenarios detailed in Table 7.12 have been simulated. The bottom structure under consideration is depicted in Figure 7.20 and its main characteristics are listed in Table 7.13.

Scenario id	$C\ (m^{-1})$	$E\ (m^{-1})$	$V_x\ (m/s)$	$V_z\ (m/s)$	$X\ (m)$	$Y\ (m)$
1	0.3	0.3	6	-1.5	49.2	0
2	0.3	0.3	3	-1.0	49.2	0
3	2.0	2.0	3	-0.75	49.2	0
4	1.0	1.0	3	-1.0	49.2	0
5	1.0	1.0	3	-1.0	49.2	5.7

Table 7.12: Validation of combined grounding solver - Scenario parameters

Description	Dimensions
Length (m)	54.6
Breadth (m)	28.5
Double bottom height (m)	1.6
Transverse frame spacing (m)	4.2
Longitudinal girder spacing (m)	5.7
Outer bottom thickness (mm)	15
Inner bottom thickness (mm)	10
Transverse floor thickness (mm)	15
Longitudinal girder thickness (mm)	20

Table 7.13: Bottom structure main characteristics - Combined grounding analysis

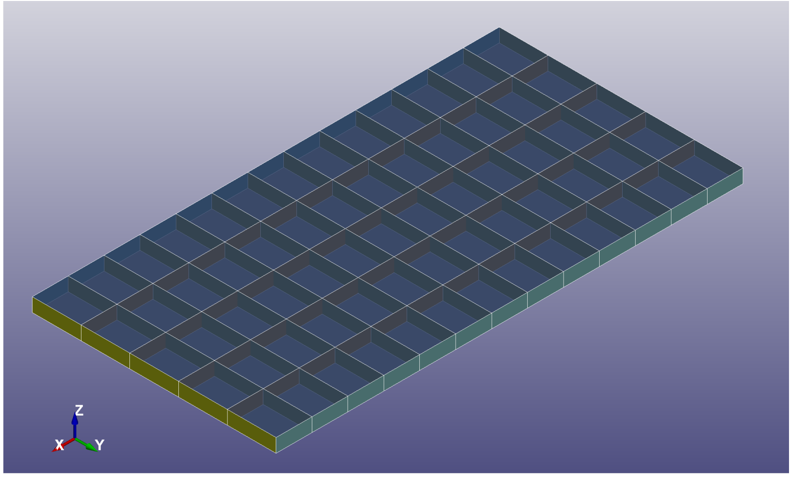

Figure 7.20: Ship bottom model - Combined grounding analysis

Figures 7.21 to 7.25 compare the resisting forces and the dissipated energy post-processed from *Ls-Dyna/MCOL* and *FLAGS/MCOL* simulations. In addition, Table 7.14 summarises the dissipated energies and damage length at the end of the calculations.

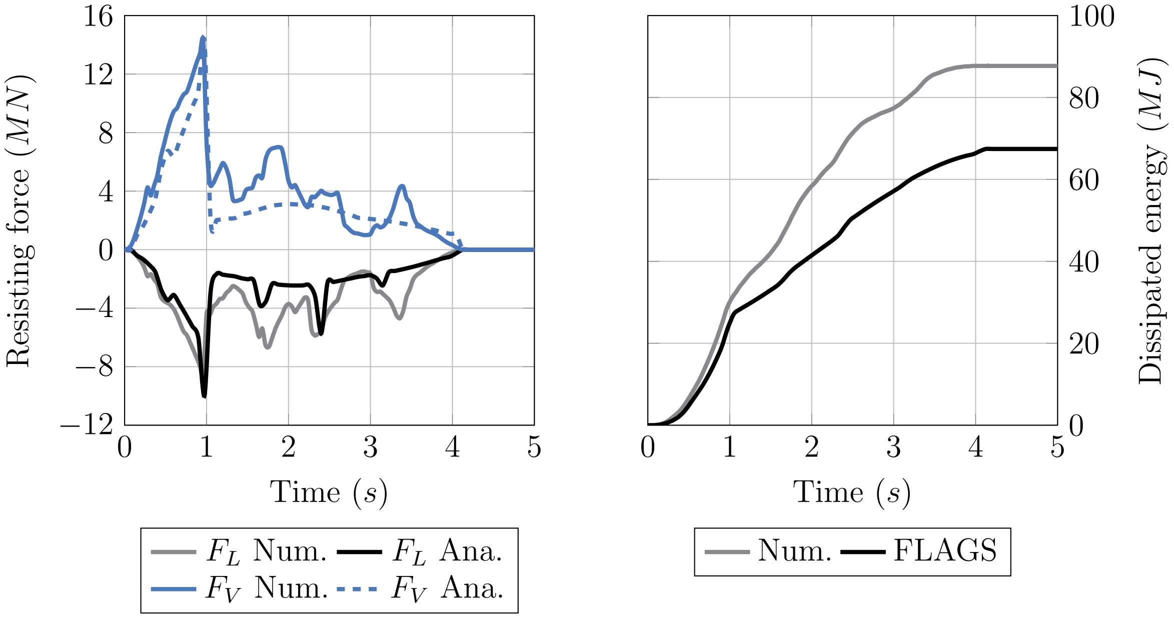

Figure 7.21: Combined grounding benchmark - Scenario 1

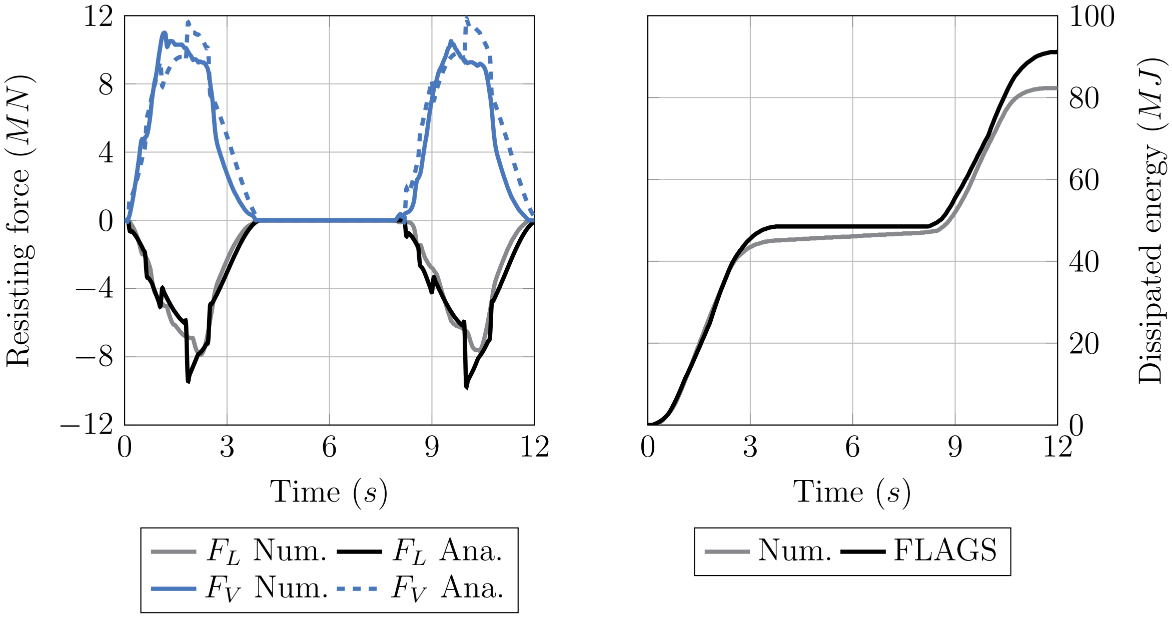

Figure 7.22: Combined grounding benchmark - Scenario 2

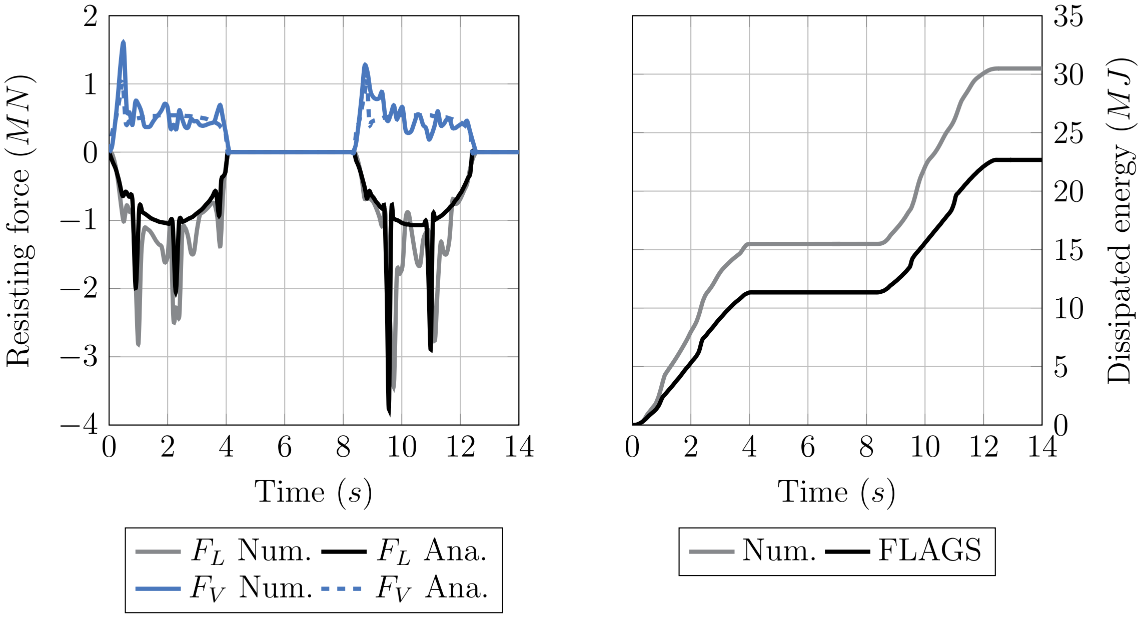

Figure 7.23: Combined grounding benchmark - Scenario 3

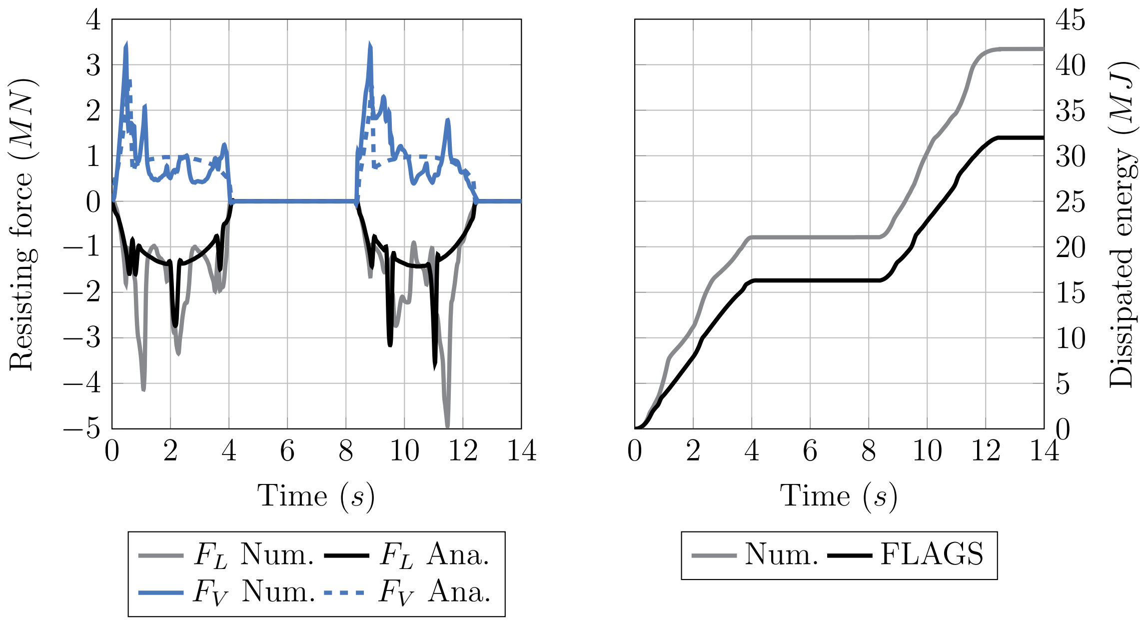

Figure 7.24: Combined grounding benchmark - Scenario 4

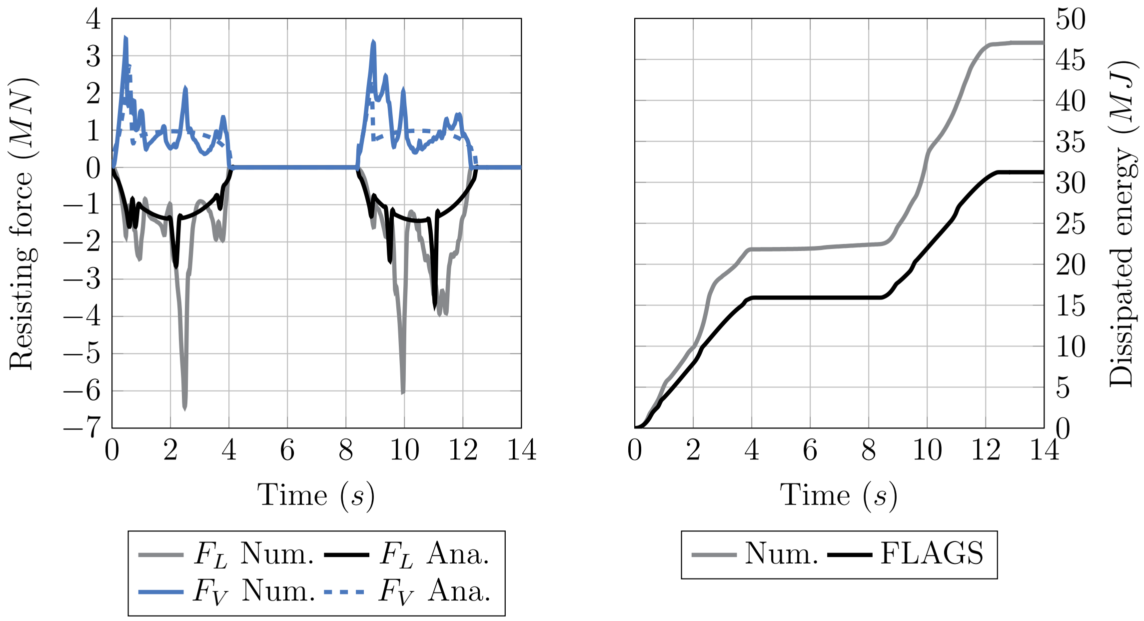

Figure 7.25: Combined grounding benchmark - Scenario 5

Case id	Energy Num. (MJ)	Energy Ana. (MJ)	Damage length Num. (m)	Damage length Ana. (m)	Dev. Energy	Dev. Damage
1	87.9	67.4	23.2	23.8	-23.3%	2.6%
2	82.3	91.1	19.2	19.9	10.7%	3.6%
3	30.5	22.7	22.9	23.0	-25.6%	0.6%
4	41.7	32.0	22.9	23.1	-23.2%	0.9%
5	47.0	31.3	22.3	22.7	-33.3%	1.8%

Table 7.14: Dissipated energy & damage length - Combined grounding

From Table 7.14 and Figures 7.21 to 7.25, the following observations can be done:

- As far as the outer shell deforms without rupturing, the response of the different components are very well captured, underlining the good performance of the solutions developed in Chapter 6 for intact plating.
- The rupture is correctly triggered in *FLAGS* compared to *Ls-Dyna*.
- Once the outer shell has fractured, the analytical solution always underestimates the resisting forces. This is mainly due to the bottom plating model in which the straining as well as the petalling of the plate are not considered.
- Once transverse floors have collapsed, the resisting force is abruptly set to zero in the proposed model. In reality, the resistant force slowly decreases until vanishing. A significant part of the energy absorbed by the floors is thus missed.
- In scenario n° 5, the deformation mode of the outer shell switches from local tearing to concertina tearing at time 10.5 seconds, explaining why the deviation is the most important in this case.
- Although the analytical model globally underestimates the resisting forces, the global trends for F_L and F_V are well transcribed. The average deviation regarding the dissipated energy and damage length are respectively 23.2% and 1.9%.

For illustration purpose, the damaged areas post-processed from *Ls-Dyna* and *FLAGS* simulations (scenario n°3) are superposed on Figure 7.26. Note that in *FLAGS* post-processor, a Super-Element turns orange when teared. It is observed that the breaches are pretty well captured, even if the deviation in term of dissipated energy reaches around 25%. It should be stressed that the real dimensions of damage extent (length and width) are calculated according to the rock shape and vertical penetration of this latter in the outer / inner hull, at each time step and saved in the "Results.csv" file. Finally, Figure 7.27 illustrates the displacement of the ship for scenario n° 4 (side view). Additional figures describing the heave and surge velocities are given Appendix F.

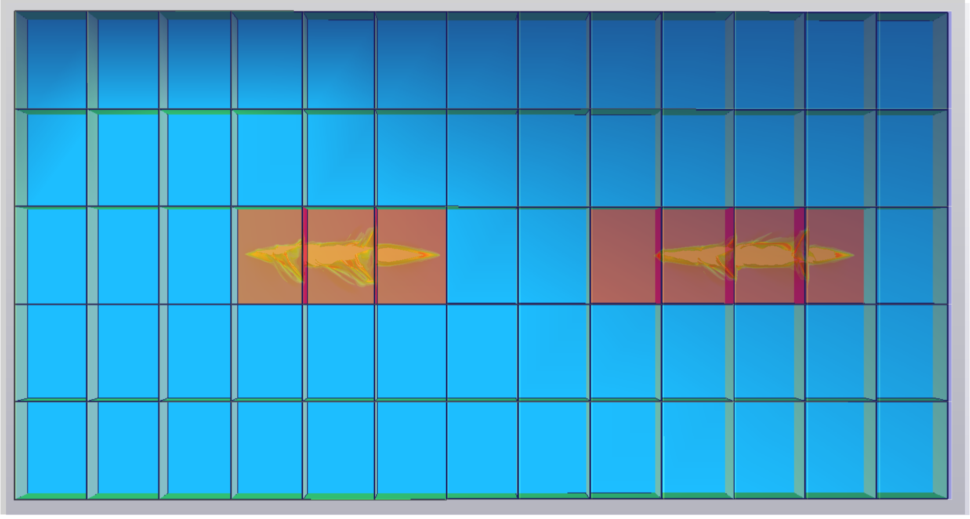

Figure 7.26: Comparison of F.E. and S.E. breaches - Scenario 3

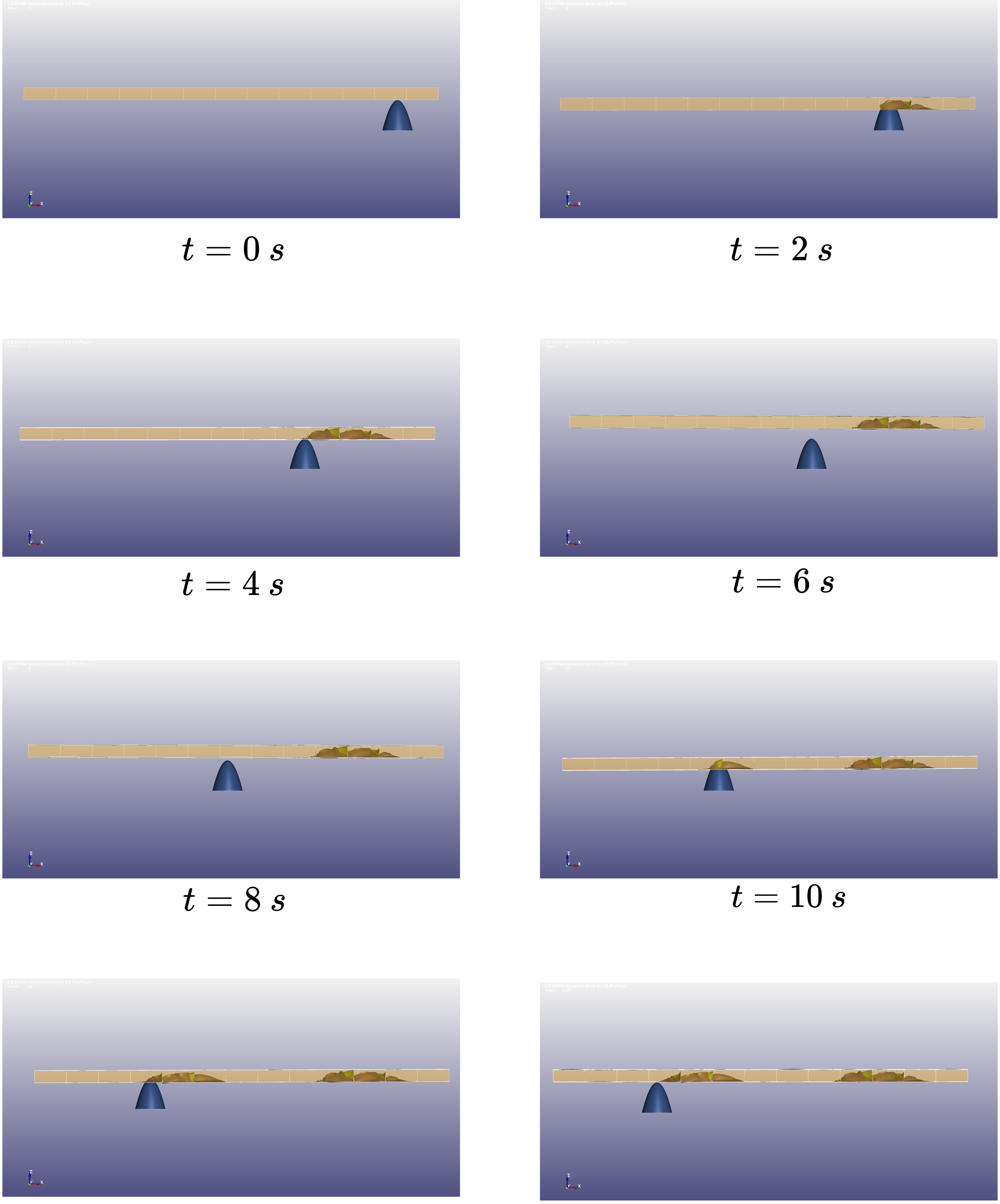

$t = 0\ s$

$t = 2\ s$

$t = 4\ s$

$t = 6\ s$

$t = 8\ s$

$t = 10\ s$

$t = 12\ s$

$t = 12.7\ s$

Figure 7.27: Combined grounding - Side view of the ship motion - scenario 4

7.5.2 Influence of the initial heave velocity

From *Ls-Dyna/MCOL* simulations, *Le Sourne et al.* [35] recently showed that heave oscillations may greatly affect the ship grounding damage. Depending on the amplitude of the oscillations, multiple breaches of the outer/inner shell may occur and the overall damaged length was shown to be up to 4 times the one obtained when the vessel runs aground the rock without heave motion. From a practical point of view, this means that a larger number of compartments are liable to get flooded and the stability of the ship after accident is likely to be more critical. Therefore, the influence of the heave velocity V_z is now investigated. In pure sliding/raking accidents, the initial kinetic energy of the ship is given by:

$$E_{k0} = \frac{1}{2}(m_{ship} + m_x)V_{xp}^2 \tag{7.18}$$

Where m_{ship} is the mass of the vessel, m_x the added mass in the surge direction and V_{xp} the initial surge velocity.

For sake of comparison, initial kinetic energies in pure and combined grounding are supposed to be the identical. Resulting initial surge velocity (V_{xc}) in combined grounding may thus be calculated as:

$$V_{xc} = \sqrt{\frac{m_{ship} + m_x}{m_{ship} + m_x + (m_{ship} + m_z)tan^2(\varphi)}}V_{xp} \tag{7.19}$$

Where m_z denotes the added mass along the heave motion and $tan(\varphi) = V_{zc}/V_{xc}$.

Applying Eq. 7.19 for $\varphi = 0°; 7°; 14°$ and $20°$, the velocity pairs $(V_x; V_z)$ may be calculated and are given in Table 7.15 in m/s.

φ	0°	7°	14°	20°
$(V_x; V_z)$	(1.0;0)	(0.98; 0.12)	(0.92; 0.23)	(0.84; 0.31)
	(1.5;0)	(1.47; 0.18)	(1.37; 0.34)	(1.26; 0.46)
	(2.0;0)	(1.96; 0.24)	(1.83; 0.46)	(1.69; 0.61)
	(2.5;0)	(2.44; 0.30)	(2.29; 0.57)	(2.11; 0.77)
	(3.0;0)	(2.93; 0.36)	(2.75; 0.69)	(2.53; 0.92)
	(4.0;0)	(3.90; 0.48)	(3.66; 0.91)	(3.37; 1.25)

Table 7.15: Combined grounding initial velocity

In Table 7.15, each column corresponds to a given collision angle φ while each row corresponds to a given initial kinetic energy.

In combined grounding, the penetration of the rock into the structure varies with the time. To compare with pure sliding/raking cases, 5 penetration heights are considered $z = 0.5/0.75/1.0/1.5/2.0\,m$. Combining the 36 rocks with the 5 penetration depths leads to the study of 1 080 scenarios for the pure sliding/raking cases and 648 scenarios for combined grounding.

A typical damage extent obtained in combined grounding accident is illustrated in Figure 7.28. Due to the heave motion, the total breach length L_{dam} is not continuous and is therefore calculated as the sum of all the breaches created in the outer shell. In Figure 7.28 for instance, the total breach length $L_{dam} = L_1 + L_2$, while the total distance travelled (damage extent) by the ship between the first and the last breach is L_{tot}.

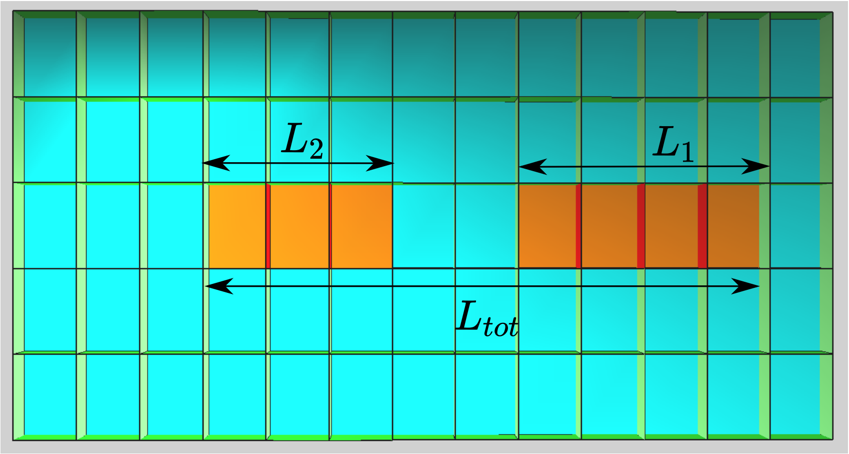

Figure 7.28: Breach length calculation - Combined grounding

After analysing the 1 728 scenarios, for a given initial kinetic energy the average damage extent L_p for pure sliding/raking accidents were extracted in addition to the average breach length L_{dam} and damage extent L_{tot} for combined scenarios. Then for each angle φ (7°, 14°, 20°), the ratios $R_1 = L_{tot}/L_p$ and $R_2 = L_{dam}/L_p$ are calculated. Results are plotted on Figure 7.29 as a function of the initial kinetic energy.

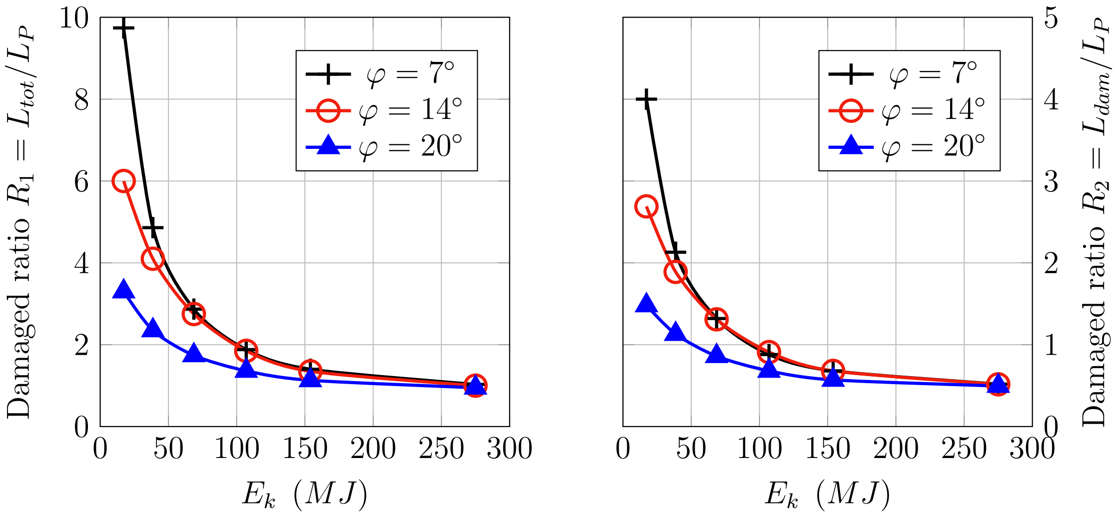

Figure 7.29: Damage ratios - Combined grounding

Looking at these graphs, it can be concluded that:

- Both ratios R_1 and R_2 are observed to decrease when the ship initial kinetic energy increases.
- When the ship initial kinetic energy is low ($E_k \leq 100MJ$), the ship in pure sliding/raking is almost instantly stopped so L_p is small. On contrary, the ship in combined grounding oscillates vertically and the energy is dissipated only when the rock is in contact with the ship. As a consequence, L_{dam} and L_{tot} are relatively

more important. It is noteworthy that the overall damage extent L_{tot} in combined grounding may be up to 10 times the damage extent observed in ship pure sliding/raking. The distribution of the flooded compartments may thus be drastically different.

- When the ship initial kinetic energy is high ($E_k \geq 150MJ$), ratios R_1 and R_2 converge to 1 and 0.5 respectively, no matter the impact angle. This means that pure sliding/raking scenarios become the most critical because the overall damage extent is almost the same ($R_1 = 1$) while the opening size (breach length) in combined grounding is half the one in pure sliding/raking ($R_2 = 0.5$).
- The higher the impact angle φ, the higher the rock penetration H. In addition, the energy dissipated is proportional to H^2. Consequently, the higher the impact angle φ, the lower L_{tot} and L_{dam} so the lower R_1 and R_2.
- Finally, the ratio L_{dam}/L_{tot} for combined accident lies in the range $[0.45, 0.5]$, meaning that in combined grounding, the total breach length is around half the overall damage extent.

Naturally, all the previous conclusions hold for the Floodstand ship B that has been considered in this study. To confirm these conclusions, further analyses should be carried out for other ships with different masses, hydrodynamic properties and structural arrangements.

7.5.3 Conclusion regarding combined grounding

In this section, *FLAGS/MCOL* simplified tool has been confronted to numerical simulations for ship combined grounding. Five scenarios were considered with different rock dimensions, initial surge and heave velocities and lateral impact positions. The following conclusions may be drawn from this validation phase:

- As far as the outer shell slides on the rock without rupturing, the response of the ship bottom is very well captured by the developed model.
- The outer shell rupture is correctly triggered in *FLAGS*, which confirms the reliability of the failure criterion proposed in Chapter 6.
- Once the outer shell has fractured, the analytical model always underestimates the resisting forces. The reason is that it does not consider the outer shell membrane straining (only shear is considered) and the petalling of plate due to the vertical indentation.
- In the analytical model, once a floor has fractured, its resisting force is set to zero. In reality, the resistant force slowly decreases down to zero so a significant part of the energy dissipated by the floors is missed by the analytical model.
- Although the analytical model predicts lower resisting forces, the global trends for F_L, F_V and the position of the possible flooded compartment are well transcribed. In addition, the average deviation from *Ls-Dyna* simulations is less than 25% while the computation time is divided by 23 000.

In a second step, the simplified tool has been used to investigate the effect of heave oscillations on both the overall damage extent and breach length compared to pure sliding/raking scenarios. In total 1 728 Floodstand ship B grounding simulations have been carried out with *FLAGS/MCOL*. Main interesting findings are as follows:

- When the ship initial kinetic energy is low, the overall damage extent in combined grounding may be up to around 10 times the one observed in pure sliding/raking. This means that a larger number of compartments are liable to get flooded and consequently the stability of ship after accident will probably be more critical.
- When the initial kinetic energy is high, pure sliding/grounding becomes the most critical scenario as resulting breach is continuous and its length is around twice the one obtained in combined grounding

7.6 Conclusion

This chapter was dedicated to the presentation of the Super-Element program *FLAGS* developed for fast and reliable analyses of ship grounding events. In a first part, the input and output files, the overall algorithm, the S.E. detection procedure and the graphic interface have been presented. The core of the computational solver has been developed from the simplified expressions derived in Chapters 4, 5 and 6. In a second step, *FLAGS* solver has been coupled with the external dynamics program *MCOL*, which allows to model the action of the surrounding water. In a third step, *FLAGS/MCOL* tool has been confronted to a series of finite element simulations, considering bottom and side grounding events as well as scenarios where the surge movement of the ship is combined with heave oscillations.

In general, a good correlation between S.E. and F.E. results has been observed, knowing that the super-element approach is much faster than finite element analysis. Indeed, the rapidity of *FLAGS/MCOL* solver is illustrated in Table 7.16, where *Ls-Dyna* and *FLAGS* average computation times are compared. The mean deviation between numerical and analytical results is also given. It appears that the Super-Element program is nearly 14 000 times faster than F.E. solutions, while the mean discrepancies with numerical results remain acceptable regarding the simplifications made.

Grounding type	*Ls-Dyna* Computation time (*hours*)[2]	*FLAGS* Computation time (*minutes*)	Ratio *NLFEM/FLAGS*	Average deviation
Bottom	720	≈ 4	11 000	-4.0%
Side	110	<1	10 000	-10.6 %
Combined	380	<1	23 000	-23.0 %

Table 7.16: Summary of computation time and average deviation between *Ls-Dyna* and *FLAGS* calculations

It was also observed from F.E. and S.E. simulations that while the damage extent is mainly governed by the ship initial kinetic energy in bottom grounding, the transverse force exerted by the rock in side grounding significantly affects the resulting breach size. Indeed, the ship tends to "escape" from the rock and resulting sway, yaw and even roll ship motions limit the damage extend compared to bottom grounding.

In a fourth step, the influence of different structural properties on the damage extent has been investigated by running thousands of *FLAGS/MCOL* simulations in bottom and side grounding. A statistical analysis of the results has shown that the most interesting reinforcement strategy consists in increasing the material grade and the outer hull thickness. In addition, it has been found that the effect of a reinforcement is always less efficient in side grounding than in bottom grounding. Finally, pure sliding/raking scenarios have been compared to scenarios in which the ship is also given an initial heave velocity, which leads to vertical oscillations and creation of multiple breaches. It was shown that the most critical scenarios mainly depend on the ship initial kinetic energy.

Of course, there is still room for improvement of *FLAGS* solver, especially regarding the simplified expressions derived for combined grounding simulations, but one may conclude

---

[2] Computation time obtained using 8 SMP thread on Intel Xeon CPU E5-2680 V4 at 2.88 GHz

this chapter by saying that the current version of the tool can already be used with confidence for ship damage stability analyses involving many grounding scenarios. The target set as the beginning of *FLARE* research project has thus been met.

Part IV

General conclusion

Chapter 8

Conclusion, personal contributions and perspectives

8.1 Summary of the research

As discussed in **Chapter 1**, ship grounding still remains one of the principal accident causalities. Currently, to minimise the damage extent and hence the probability of capsize during and after a ship collision, the maritime sector refers to the SOLAS 2009 and 2020 regulatory instruments. However, these regulatory instruments are totally independent on the ship scantlings (presence of a double hull for instance) and the energy absorption capacity (material, thickness...). In this context the European **FLARE** aims to develops a risk-based methodology for the assessment and control of "real" flooding risks.

Formal risk assessment requires to quantify the consequences of such accidents considering numerous scenarios. The classical nonlinear finite element analysis (NLFEA) is the most accurate and multipurpose approach for simulating a ship grounding accident. Nonetheless, it is not always possible to efficiently use such method since both the model set-up and numerical solution may be very time consuming. Therefore, the purpose of the present thesis was to contribute to the understanding of the mechanisms involved in ship grounding as well as the development of analytical expressions to rapidly assess the damage extent in such accident.

In the optic of evaluating the crashworthiness of a grounded ship, the approach consists in dividing the problem into *external dynamics* and *internal mechanics*. *External dynamics* target the global rigid movements of the ship. It is governed not only by the impact force but also by hydrodynamic forces acting on the immersed part of the hull. In the present thesis, the external dynamics of the ship are accounted for by using an existing code named *MCOL*. *Internal mechanics*, on the other hand, focuse on the modes of deformation and failure of the crushed components, and are modelled using the Super-Element method. The ship is divided into a set of large and independent structures called Super-Elements (S.E). Each S.E may represent either the outer/inner bottom plating, or transverse floors or longitudinal girders and is characterised by geometrical/mechanical properties. The individual resistance of each impacted S.E is evaluated through the Upper-bound theorem of plasticity. Finally, all the analytical (or semi-analytical) expressions derived in the frame of this PhD thesis are implemented in a structural solver named *FLAGS* and, once the later has been coupled with *MCOL*, the resulting tool is validated by confrontation to numerical simulations for different grounding situations.

Chapter 1 was dedicated to the presentation of the general context of the **FLARE** project, the different methods for conducting a ship damage stability analysis as well as the scope and objectives of the present thesis.

In **Chapter 2**, a synthetic bibliography review was presented. The review includes methods dedicated to the study of the internal mechanics in ship collision and grounding and methods that allow to account for the influence of the hydrodynamic forces on the ship external dynamics. Internal mechanics and external dynamics can be decoupled, semi-coupled and fully-coupled. Semi-coupled approaches appear to offer an interesting compromise between computation time and accuracy, and an example of such coupling is given through the description of the rigid body solver *MCOL*. Among the methods used to analyse the internal mechanics, non-linear finite element (NLFEM) and Super-Element (SEM) methods are highlighted. While NLFEM often leads to prohibitive calculation times, SEM appears to be very efficient as the ship is divided into a reduced number of large elements. The response of these later is calculated through closed-form expressions derived from plastic limit analysis. The literature review also pointed out the current limitations regarding ship grounding analysis:

- The rock shape directly governs the response of the grounded vessel but simplified shapes reported in the literature like cones or truncated pyramids cannot be easily used in a full ship damage stability analysis. On contrary, the paraboloid shape proposed by *Nguyen et al.* [15] allows to readily represent a large variety of rocks, from sharp and shallow rocks. It appears however that no simplified model has been reported in the literature for such rock shape.
- The effect of the surrounding water is often disregarded in grounding analysis. When it is not, it is limited to the use of a water added mass as well as surge, heave, and yaw motions for the ship.

From this literature review, it emerged that the research work performed in the frame of this PhD thesis had to focus on (i) the development of a set of super-elements to model the response of a ship grounding on a paraboloid shaped rock (ii) the coupling of the resulting semi-analytical solver with the existing 6-DoFs external dynamic program *MCOL*.

Chapter 3 aimed to calibrate the parameters that govern finite element simulations by confronting *Ls-Dyna* results to ship-ship collision and ship grounding experimental results extracted from the literature. The best fit was obtained using a shell element size of $30mm$ and five integration points through thickness. An elastic-plastic bi-linear behaviour law was adopted as well as the failure strain criterion based on the formula proposed by *Lehmann & Peschmann* [87].

The structural behaviour of a ship bottom in sliding condition was investigated in **Chapter 4**. Both horizontal and inclined bilge-like bottoms were considered as well as impacts between and onto girders. Closed-form expressions were derived using the upper-bound theorem of plasticity and systematically confronted to numerical simulations. In general, a pretty good agreement was obtained. The highest discrepancies were mainly observed when the rock is very sharp. In such case, the dissipated energy given by the analytical model is systematically underestimated.
The sliding simulations showed that the most energy-absorbing parts are respectively the bottom plating and the girders, while the floors absorb less than 10% of the energy. Fric-

tion between the rock and the structure also greatly affects both the longitudinal resisting force and the dissipated energy distribution, while the vertical component of the force is found to be independent of friction. The inclination of the bottom with respect to the horizontal plane was also shown to significantly affect the results. Finally, the simplified solutions were compared to finite element calculations considering the shape of a real rock proposed by *Sormunen et al.* [155] and a surprising good performance of the proposed model was observed.

Chapter 5 was dedicated to the response of a ship bottom raking on a paraboloid shaped rock. Closed-form expressions were first derived for the problem of outer/inner shell tearing. The proposed model revealed that plate cutting is highly sensitive to the plate-rock friction coefficient, while the vertical resistant force is almost insensitive to both the friction and vertical penetration depth. In a second step, the response of transverse floors was shown to be coupled with the bottom plating response but including such coupling in an analytical approach still remains a challenge. A simplified model was nonetheless proposed and the deviation between analytical and numerical results was found to be around 15%. At the same time, it was observed that floors only contribute by less than 20% to the overall energy dissipation. In a third step, the response of girders was analysed. The deformations undergone by these longitudinal stiffeners highly depends on the rock shape. When a large rock is involved in the raking process, the deformation mechanism of the girder is similar to the one exhibited in sliding situation. However, when the rock becomes sharper, it no longer stays under the girder but rather slides on its edge, dissipating energy by shearing. Finally, the applicability of the model to real sharp rocks was discussed. Although the proposed analytical solution is able to give a rather good prediction of the energy absorbed by an unstiffened plate, significant deviation with numerical results appeared when a full double structure was considered. In fact, the dissymmetry of the real rock leads to some inconsistency in the prediction of vertical and transverse resistant forces by the model that is based on symmetry assumption.

The work presented in **Chapter 6** aimed to extend the analytical approach to the problem of a ship bottom running aground a paraboloid shaped rock through a combined surge and heave movement. The response of an unstiffened bottom plating was first investigated and a simplified model based on solutions derived in Chapters 4 and 5 as well as additional developments to account for the heave motion were derived. The contribution of this later was shown to be significant, especially when the rock is large. The response of transverse floors was then investigated and the derived model was shown to correctly capture the deformation mechanisms as far as the outer shell deforms without rupture. It then underestimates the resistant force because additional energy dissipated by membrane straining after rupture is not accounted for. The behaviour of longitudinal girders was also studied and the correlation between analytical and numerical results was shown to be acceptable. The main discrepancies were shown to come from the premature rupture of the outer shell when the girder is directly impacted by the rock. In this case, clear conclusions are difficult to draw because the reliability of the F.E. model (considered as the reference) is questionable. Indeed, the failure criterion proposed by *Lehmann & Peschmann* [87] is probably no longer suitable in areas where large out-of-plane shear strains dominate. Finally, from the observation of numerical simulations, a simple failure criterion combing membrane straining and bending of the bottom plating was established to switch from the sliding to the raking mode.

All super-elements derived in previous chapters were implemented into a solver named *FLAGS* and this later was coupled with the 6-DoFs external dynamics solver *MCOL* to simulate the action of the surrounding water. In **Chapter 7**, the operating principle as well as the modules of *FLAGS/MCOL* solver were presented. S.E and F.E. results were then confronted considering both ship bottom and ship side grounding events. The accuracy and reliability of the tool was shown to be satisfying, the discrepancy not exceeding 20%. The major advantage of *FLAGS/MCOL* solver is obviously its rapidity: a S.E. simulation is around 10 000 times faster than a F.E simulation.
The comparison between the F.E. and S.E. simulations also highlighted two points: In bottom grounding, the damage extent is mostly governed by the ship initial kinetic energy. On contrary, the ship tends to “escape” from the rock when subjected to side grounding and this clearly reduces the damage.
Taking advantage of the rapidity of the tool, sensitivity analyses were then carried out, running thousands of grounding accidents. It was demonstrated that (i) increasing the outer shell (resp. side shell) thickness is the best strategy to increase the ship crashworthiness in bottom (resp. side) grounding and, (ii) a reinforcement will be always more efficient in bottom grounding than in side grounding. Finally, the breach size was shown to be linearly dependent on the initial kinetic energy in side grounding, while the dependency is rather quadratic in bottom grounding.

The present thesis is summarised in **Chapter 8**, personal scientific contributions are listed and perspectives regarding further research work are suggested.

8.2 Personal contributions

The purpose of this PhD thesis was to provide a reliable and fast tool to assess the resistance of ships in hard grounding accidents. The main personal contributions are then related to the development of analytical formulations to assess the resistance of the main ship components as well as their implementation in a Super-Element solver. They are detailed below.

- The local deformations exhibited by the bottom plating in sliding and raking grounding were modelled considering a paraboloid shaped rock. This shape was explicitly considered in the derivations, which was not the case in previous research works - see **[III,IV]**.

- Simplified models reported in the literature assume that the hull plating grounds over the rock horizontally. However, when the ship impacts the rock far from its centreline, a significant roll motion may occur. That is why analytical solutions have been derived for an inclined hull sliding on a paraboloid shaped rock, which allows to model bilges as well - see **[II]**.

- A simplified model for the response of transverse floors in sliding and raking scenarios was derived accounting for the rock shape, while the developments found in the literature are rather based on the assumption of a punctual impact - see **[I,II]**.

- The response of longitudinal girders was divided into two distinct phases, a steady state phase corresponding to the response of the girder between two adjacent transverse floors and a phase where a transverse floor is also involved in the deformation (intersection). This two step approach was shown to be in good agreement with numerical results. Note also that the girder/floor intersections were observed to dissipate twice the energy absorbed by the girder alone - see **[II]**.

- The friction coefficient was found to significantly contribute to the energy dissipation during the grounding event. However, the presence of floors and girders has the effect of changing the pressure distribution on the rock and consequently the ratios g_f and k_v. A set of simple equations was then derived to account for the presence of floors/girders elements. Obtained results were shown to be in very good accordance with numerical simulations. It should be stressed that in the literature, the effect of friction is assumed not to depend on the presence of the main stiffeners.

- Recent study by *Le Sourne et al.* [35] showed that giving the ship an initial heave velocity may have a significant influence on the deformation modes and consequently on the grounding damage extent. Indeed, the ship is subjected to vertical heave oscillations that sometimes lead to several breaches in the outer shell. Analytical expressions were then derived considering oblique impacts between the rock and the ship bottom. It should be emphasised that such a study may also be seen as an innovative work as in the literature, the ship is always assumed to follow an horizontal path - see **[V]**.

- The analytical developments carried out for sliding and raking grounding situations were also tested considering real rocks retrieved from sonar scan measurements. Comparison with rock shapes usually considered in the literature (cones or truncated pyramids) showed that a paraboloid shape is a wise choice as it allows to approximate a wider range of real rock geometries.

- A simple failure criterion was established on the basis of numerical simulations. By taking explicitly into account the rock shape, this criterion allows to capture quite precisely the transition between sliding to raking modes. It should be stressed that in classical plastic analyses reported in the literature, the failure criterion is generally independent on the indenter shape.
- A solver based on analytical formulations was developed and coupled to *MCOL* external dynamics solver. Resulting tool was then validated by confrontation to numerical simulations for ship bottom, side, and combined grounding scenarios. It was observed that the developed tool is 10 000 times faster than F.E. simulations, while keeping a deviation with F.E. results less than 25%.
- *FLAGS/MCOL* coupled solvers were finally advantageously used to perform sensitivity analyses involving thousands of scenarios, not only in ship bottom grounding but also in side grounding. Such analyses showed that external dynamics are very different in side grounding since the ship tends to move away from the rock. In addition, it was demonstrated that reinforcing the structure will always be less efficient in side grounding than in bottom grounding - see [**VI-VII**].

Published papers:

- [I] Pineau J.P, Le Sourne H., and Soulhi Z. - Rapid assessment of ship raking grounding on elliptic paraboloid shaped rock. Ships and Offshore Structures, 2021 https://doi.org/10.1080/17445302.2021.1927357
- [II] Pineau J.P and Le Sourne H. - A simplified approach to assess the resistance of a ship sliding on elliptic paraboloid rock. Marine Structures, 83 (2022) 103151 https://doi.org/10.1016/j.marstruc.2021.103151
- [III] Pineau J.P, Le Sourne H., and Soulhi Z. - An upper bound solution for the problem of ship bottom plating teared by an elliptic paraboloid shaped rock. In 5^{th} International Conference on Ships and Offshore Structures, Glasgow, 2020
- [IV] Pineau J.P and Le Sourne H. - Rapid assessment of ship bottom sliding on paraboloid shaped rock. In 8^{th} International Conference on Marine Structures MARSTRUCT, 2021
- [V] Pineau J.P and Le Sourne H. - Rapid Assessment of Ship Bottom Grounding Damage Considering Combined Surge and Heave Initial Velocities. In 41^{th} Conference on Ocean, Offshore and Arctic Engineering OMAE, 2022
- [VI] Pineau J.P, Le Sourne H., Lerondel E., De Champs P., Looten T., Conti F. - Ship side grounding parametric analysis based on a Super-Element approach. In 15^{th} Int. Symp. Practicle Design of Ships and Other Floating Structures - PRADS, Dubrovnik, 2022. (Submitted)
- [VII] Pineau J.P, Conti F., Le Sourne H., Looten T. - A fast simulation tool for ship grounding damage analysis. Ocean Engineering. (Submitted)

8.3 Recommendations for future work

Although the simplified models developed in the frame of this thesis are generally in pretty good agreement with F.E. simulations, the following suggestions may be of interest for improving the reliability and accuracy of *FLAGS* S.E. solver:

- Analytical developments were performed under the assumption that as far as an element is not directly impacted by the rock, it does not deform. However, sliding numerical simulations showed that transverse floors tend to buckle before being touched by the rock. Doing so, additional energy is dissipated and the boundary of the current outer shell S.E. is not rigid anymore. Taking into account this particular situation would undoubtedly allow to improve the outer shell sliding response.

- The sliding response of longitudinal girders was developed under the steady-state hypothesis, i.e. the wave deformation develops as soon as the rock is located between two floors. Numerical simulation shows that the proximity of the next floor stops the wave propagation while in the current version of the model, the wave propagation is supposed to continue as far as the next floor is not touched by the rock.

- Floor/girder intersections were assumed to deform under a vertical force exerted by the rock. No doubt that a specific solution that would consider a combined longitudinal and vertical moving load would provide better results.

- When a ship bottom grounds over a large shallow rock without rupture, the overall bottom panels bounded by two transverse bulkheads are sometimes subjected to global bending, as observed by *Nguyen et al.* [180]. A simplified model that would consider such global deformation could be easily developed and integrated to the solver, following for instance the approach proposed by *Buldgen* [94].

- Although the analytical solution derived for plate tearing gives pretty good results, the model appears to often underestimate the dissipated energy. From numerical and experimental analyses, it was observed that after passing the rock, the flaps do not stay perfectly flat, indicating the presence of stretching in addition to shearing. One possible improvement would thus consist in adding flap stretching, such as proposed by *Zeng et al.* [12]. Doing so would increase the resisting forces by nearly 5%.

- Simplified formulas for ship raking have been developed for an horizontal hull. As done for sliding, the extension of these formulations to an inclined hull plating would also improve the accuracy and reliability of the solver, especially when the ship is subjected to large roll movement or when a bilge is perforated.

- Response of transverse structures like floors when the bottom plating has been torn up were complex to model. The deformation mechanisms were observed to change depending on the rock shape and the vertical penetration of the rock into the structure. Further investigations should be performed in this direction to better understand the crushing/tearing mechanisms of the floors. Moreover, once floors start to tear, the resisting force is abruptly set to zero in the proposed model. In reality, it slowly decreases until vanishing. A significant part of the energy absorbed by the floors is thus missed by the model. Adding a post collapse solution like the one proposed by *Ozdogan* [181] for ship side openings would certainly improve the accuracy of the solver.

- Capturing properly the plating rupture in FE models is still a challenge today. The effective plastic strain failure criterion used in the current work is mostly valid for elements that are mainly subjected to membrane tension. However, when the rock impacts the ship bottom just under a girder, out-of-plane shearing predominates so the suitability of such criterion becomes questionable. Multi-axial stress state criteria such as RCTL proposed by *Tørnqvist* [88] would probably remove some uncertainties but further confrontations to reduced or full scaled experiments are still necessary.

- Small longitudinals attached to outer / inner bottom or side shell are currently treated through the smeared thickness approach. Nevertheless, derivation of specific solutions for such components - see *Simonsen* [11] or *Yu et al.* [123] for example - would probably improve the model.

- Sensitivity analyses may be performed on combined grounding to quantify the effect of hydrodynamic properties, rock shape or structural reinforcements on the damage extent.

- In the current version of *FLAGS*, the possible reinforcements are limited to thickness, material grade and main scantling of the ship. With the aim of proposing alternative and innovative reinforcement strategies, new S.E formulations could be developed for energy-absorbing structures such as metal foams or other cellular structures that could efficiently dissipate energy.

In addition to recommendations regarding the internal mechanics, the following potential developments may be investigated or added in future research:

- *FLAGS/MCOL* program could advantageously be coupled with a multi-objective optimisation algorithm in order to investigate alternative ship designs combining the best crashworthiness with an optimised mass. Such work has already been performed for the optimisation of ships against collision [182] or in sagging and hogging conditions [183]. A particle swarm optimisation (PSO) solver was coupled with finite element simulations to evaluate the performance of alternative designs. Using the S.E. approach is obviously of major interest in such optimisation process as the reduced calculation cost allows to investigate a wider range of design parameters and grounding scenarios.

- When both the outer and inner hulls have been perforated, the water may ingress rapidly into the breached compartments and, doing so, modify not only the mass of the ship but also its hydrodynamic properties (water added mass, hydro-static restoring, wave radiation and drag damping). The influence of such modifications on the ship dynamics and consequently on the breach size is also worth to be investigated.

- Side grounding analyses were performed under the assumption of an only surge velocity. However, during an avoidance manoeuvre, both the sway and gyration velocities of the ship are non-zero and may counterbalance the transverse force exerted by the rock. Their influence on the ship damage during and after a side grounding event would also be interesting to investigate.

Part V

Appendices

Appendix A

Main characteristics of experimental models

A.1 ASIS model experiment

The ASIS model for deck crushing is composed of five different parts namely side shell, deck, web girder, deck's stiffeners and web's stiffeners. Principal dimensions of the structure are resumed in Table A.1.

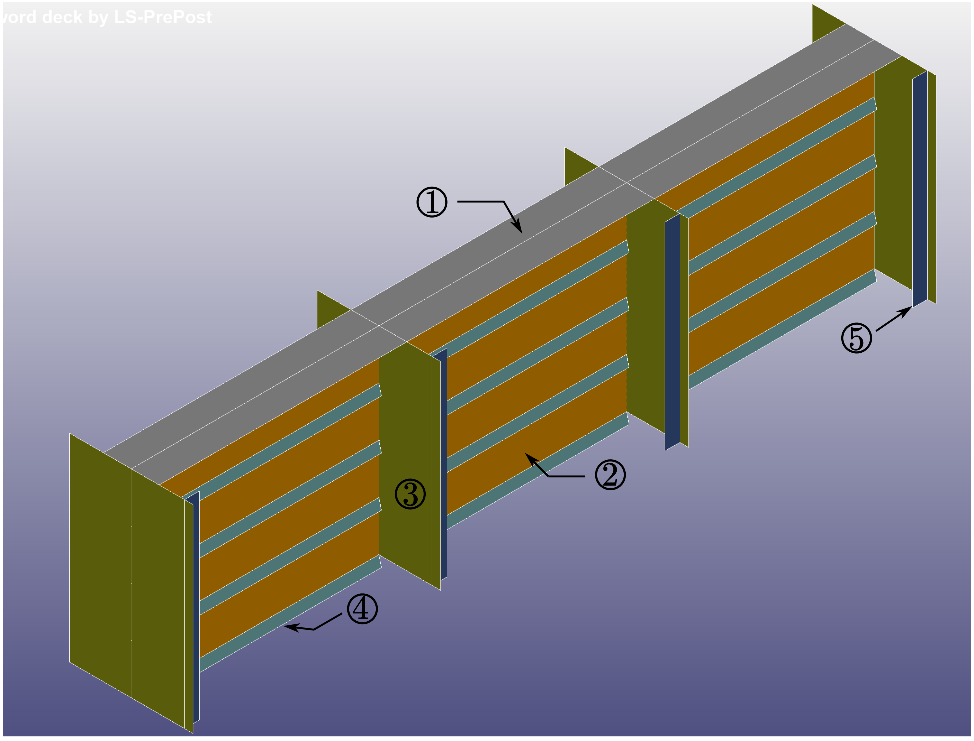

Figure A.1: ASIS model main parts

Item	Value (mm)
Height of the structure	1600
Length of the structure	6000
Web spacing	2000
Width of side shell	450
Deck stiffener height	100
Deck stiffener spacing	400
Web stiffener height	120
Web stiffener spacing	930

Table A.1: ASIS main dimensions

A.2 NSWC model experiment

Principals characteristics of NSWC model are listed in Table A.2 and Table A.3.

Item	Value (mm)
Double bottom height	370
Floor spacing	460
Transverse bulkhead spacing	3680
Longitudinal girder spacing	1270
Outer shell thickness	3
Inner shell thickness	3
Transverse bulkhead thickness	3
Floor thickness	4.76
Girder thickness	2.3

Table A.2: NSWC ship principal dimensions

Stiffener location	Type	Spacing (mm)	Web (mm)	Flange (mm)	Thickness (mm)
Outer bottom	L	127	70	32	2.3
Inner bottom	L	127	35	35	3.4
Transverse bulkheads	L	127	89	51	3
Transverse bulkheads (below inner shell)	FB	127	38	-	3
Transverse floor	FB	-	38	-	4.8

Table A.3: NSWC stiffener characteristics

Appendix B

Ship sliding appendix

B.1 Out of plane displacement field

This appendix is concerned with the expression of displacement fields and the associated strain for an inclined bottom plating in sliding mode.

$$w_1 = \frac{\left(-B_1 + \sqrt{\Delta_1}\right)^2}{4A_1} cos(\gamma) \tag{B.1}$$

$$y_s = \frac{-B_1 + \sqrt{\Delta_1}}{2A_1} \tag{B.2}$$

With :

$$\begin{cases} A_1 = \frac{\delta_1}{y_1^2} \\ B_1 = tan(\gamma) + \frac{1}{tan(\gamma)} \\ \Delta_1 = B_1^2 - 4A_1Q_1 \\ Q_1 = -\frac{y_p}{sin(\gamma)} \end{cases} \tag{B.3}$$

Strain for w_1 is given by :

$$\varepsilon_{y1} = \frac{1}{2}\frac{1}{tan(\gamma)^2}\frac{\left(B_1 - \sqrt{\Delta_1}\right)^2}{\Delta_1} \tag{B.4}$$

For $w = w_2$

$$w_2 = \left(H_R - E(\frac{-B_2 + \sqrt{\Delta_2}}{2A_2} - b_R)^2 - tan(\gamma)\frac{-B_2 + \sqrt{\Delta_2}}{2A_2}\right) cos(\gamma) \tag{B.5}$$

$$y_s = \frac{-B_2 + \sqrt{\Delta_2}}{2A_2} \tag{B.6}$$

With :

$$\begin{cases} A_2 = -E \\ B_2 = \frac{1}{tan(\gamma)} + 2b_RE \\ \Delta_2 = B_2^2 - 4A_2Q_2 \\ Q_2 = H_R - Eb_R^2 - \frac{y_p}{sin(\gamma)} \end{cases} \tag{B.7}$$

Strain for w_2 is given by :

$$\varepsilon_{y2} = \frac{1}{2}\frac{1}{tan(\gamma)^2}\frac{\left(B_1 - \sqrt{\Delta_2}\right)^2}{\Delta_2} \tag{B.8}$$

For $w = w_3$

$$w_3 = A_3\left(\frac{-B_3 + \sqrt{\Delta_3}}{2A_3} - bcos(\gamma)\right)^2 cos(\gamma) \tag{B.9}$$

$$y_s = \frac{-B_3 + \sqrt{\Delta_3}}{2A_3} \tag{B.10}$$

With :

$$\begin{cases} A_3 = \frac{\delta_2}{(y_2 - bcos(\gamma))^2} \\ B_3 = tan(\gamma) + \frac{1}{tan(\gamma)} - 2bA_3 \\ \Delta_3 = B_3^2 - 4A_3Q_3 \\ Q_3 = A_3b^2cos(\gamma)^2 - \frac{y_p}{sin(\gamma)} \end{cases} \tag{B.11}$$

Strain for w_3 is given by :

$$\varepsilon_{y3} = \frac{1}{2}\frac{1}{tan(\gamma)^2}\frac{\left(B_1 - \sqrt{\Delta_3}\right)^2}{\Delta_3} \tag{B.12}$$

B.2 Calculation of straining

This appendix is concerned with the calculations of straining v_{01} and v_{02} for the case of an inclined bottom plating. Two cases are to be distinguish :

```
if $b_1 < y_{1p}$ then
    $v_{01} = \int_0^{b_1} \varepsilon_{y1} \, dy_p = \frac{J(x_1)-J(x_0)}{4A_1}$
    $v_{02} = \int_{b_1}^{y_{1p}} \varepsilon_{y1} \, dy_p + \int_{y_{1p}}^{y_{2p}} \varepsilon_{y2} \, dy_p + \int_{y_{2p}}^{b} \varepsilon_{y3} dy_p = \frac{J(x_2)-J(x_1)}{4A_1} + \frac{J(x_3)-J(x_2)}{4A_2} + \frac{J(x_4)-J(x_3)}{4A_3}$
else
    $v_{01} = \int_0^{y_{1p}} \varepsilon_{y1} \, dy_p + \int_{y_{1p}}^{b_1} \varepsilon_{y2} \, dy_p = \frac{J(x_2)-J(x_0)}{4A_1} + \frac{J(x_5)-J(x_2)}{4A_2}$
    $v_{02} = \int_{b_1}^{y_{2p}} \varepsilon_{y2} \, dy_p + \int_{y_{2p}}^{b} \varepsilon_{y3} dy_p = \frac{J(x_3)-J(x_2)}{4A_2} + \frac{J(x_4)-J(x_3)}{4A_3}$
end if
```

With :

$$y_{p1} = \sqrt{g_1(y_1)^2 + y_1^2} cos \left(atan \left(\frac{g_1(y_1)}{y_1} \right) - \gamma \right) \tag{B.1}$$

$$y_{p2} = \sqrt{g_2(y_2)^2 + y_2^2} cos \left(atan \left(\frac{g_2(y_2)}{y_2} \right) - \gamma \right) \tag{B.2}$$

$$J(x) = \frac{sin(\gamma)}{2tan^2(\gamma)} \left(B_1^2 log(x) - 4B_1\sqrt{x} + x \right) \tag{B.3}$$

$$x_0 = \Delta_1(0) = B_1^2 \tag{B.4}$$

$$x_1 = \Delta_1(b_1) = B_1^2 + 4A_1 \frac{b_1}{sin(\gamma)} \tag{B.5}$$

$$x_2 = \Delta_1(y_{1p}) = \Delta_2(y_{1p}) \tag{B.6}$$

$$x_3 = \Delta_2(y_{2p}) = \Delta_3(y_{2p}) \tag{B.7}$$

$$x_4 = \Delta_3(b) \tag{B.8}$$

$$x_5 = \Delta_2(b_1) \tag{B.9}$$

Appendix C

Ship raking appendix

C.1 Floor

In this appendix, we summarize some additional mathematical results for the development of analytical formulation of the floor's resistance. The resisting force provided by the fibres oriented along the ζ axis is given by:

$$F_\zeta = \sum_{n=1}^{2} F_{\zeta,n} \tag{C.1}$$

Where $F_{\zeta,1}$ and $F_{\zeta,2}$ are:

$$F_{\zeta,1} = \frac{4}{9}\sigma_0 t_f A \frac{\partial A}{\partial \delta} y_0^3 Z_m \tag{C.2}$$

$$F_{\zeta,2} = 0 \tag{C.3}$$

With the definition of A and $\frac{\partial A}{\partial \delta}$ and $\frac{\partial y_0}{\partial \delta}$ as:

$$A = \frac{\delta - R_x + \frac{R_x}{R_y}\sqrt{R_y^2 - (y_0 - a_1)^2}}{y_0^2} \tag{C.4}$$

$$\frac{\partial A}{\partial \delta} = \frac{1}{y_0^2}\left(1 + (a_1 - y_0)\frac{\partial y_0}{\partial \delta}\frac{R_x}{R_y\sqrt{R_y^2 - (y_0 - a_1)^2}}\right) - \frac{2A}{y_0}\frac{\partial y_0}{\partial \delta} \tag{C.5}$$

$$\frac{\partial y_0}{\partial \delta} = -2\frac{R_y}{R_x}\frac{\left(R_y^2 - (a_1 - y_0)^2\right)^{\frac{3}{2}}}{a_1 R_y^2 - (a_1 - y_0)^3} \tag{C.6}$$

The resisting force provided by the fibres oriented along the η axis is given by:

$$F_\eta = \sum_{n=1}^{2} F_{\eta,n} \tag{C.7}$$

Where $F_{\eta,1}$ and $F_{\eta,2}$ are:

$$F_{\eta,1} = \frac{1}{5}\sigma_0 t_f A \frac{\partial A}{\partial \delta}\frac{y_0^5}{Z_m} \tag{C.8}$$

$$F_{\eta,2} = \frac{\sigma_0 t_f}{Z_m} \left[(\delta - R_x)(a_1 - y_0) - \frac{R_x}{2R_y} \left((y_0 - a_1) \sqrt{R_y^2 - (y_0 - a_1)^2} + R_y^2 \operatorname{atan} \left(\frac{y_0 - a_1}{\sqrt{R_y^2 - (y_0 - a_1)^2}} \right) \right) \right] \tag{C.9}$$

Appendix D

Ship side grounding appendix

D.1 Theoretical reduction factor

This appendix is dedicated to the derivation of the Upper and Lower bound of the breach reduction factor λ in side grounding.

The simplified damage length in side grounding is given by :

$$L(\tau) = -\frac{F_L M_T}{F_T M_L} H + v_{x0} \sqrt{\frac{2HM_T}{\tau F_T}} \tag{D.1}$$

Resulting theoretical reduction factor λ thus writes:

$$\lambda = \frac{L(\tau) - L(1)}{L(1)} \tag{D.2}$$

Or in its extended forms :

$$\lambda = v_{L0} \sqrt{\frac{2HM_T}{F_T}} \frac{\frac{1}{\sqrt{\tau}} - 1}{-\frac{F_L M_T}{F_T M_L} H + v_{L0} \sqrt{\frac{2HM_T}{F_T}}} \tag{D.3}$$

Let β and α defined as :

$$\beta = v_{L0} \sqrt{\frac{2HM_T}{F_T}} \tag{D.4}$$

$$\alpha = \frac{F_L M_T}{F_T M_L} H \tag{D.5}$$

In the case of reinforcement $\frac{1}{\sqrt{\tau}} - 1 < 0$ and since $-\alpha < 0$, one can show :

$$\lambda = \frac{\beta}{\beta - \alpha} \left(\frac{1}{\sqrt{\tau}} - 1 \right) \leq \frac{\beta}{\beta} \left(\frac{1}{\sqrt{\tau}} - 1 \right) = \frac{1}{\sqrt{\tau}} - 1 \tag{D.6}$$

Therefore $\frac{1}{\sqrt{\tau}} - 1$ constitute an Upper-bound for λ.

Dealing with the Lower-bound is a bit more complex. However by noticing that β corresponds to the distance travelled by the ship without any deceleration, and $\beta - \alpha$ correspond to the distance travelled by the ship considering the effect of the deceleration. Therefore, $\beta/(\beta - \alpha)$ may be rewritten as :

$$R = \frac{\beta}{\beta - \alpha} = \frac{v_{L0} t_0}{-F_L / M_L t_0^2 / 2 + v_{L0} t_0} \tag{D.7}$$

For the floodstand ship B, the ship inertia M_L is 34 325 $tons$, the average resisting force F_L is 2.5 MN, therefore the expected ratio R remains lower than 1.2 - see Figure D.1. The lower bound is then :

$$1.2\left(\frac{1}{\sqrt{\tau}}-1\right)\leq\lambda \tag{D.8}$$

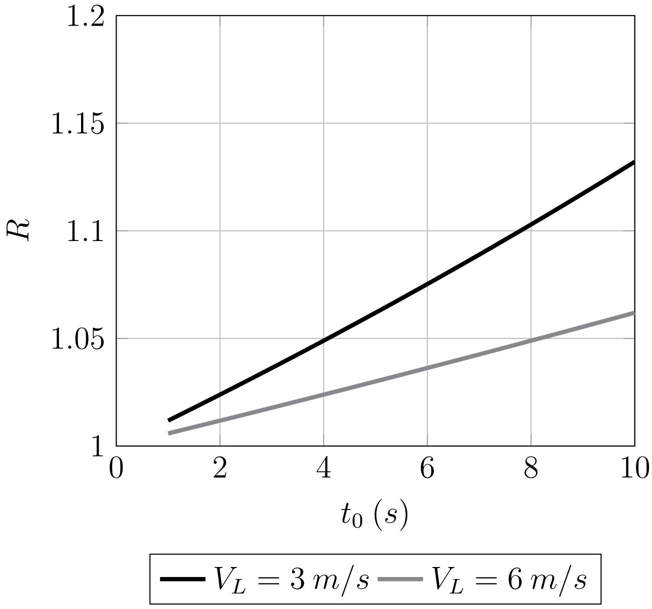

Figure D.1: Lower bound for λ factor - Side grounding

Using Eq. D.6 and Eq. D.8 we finally obtain :

$$1.2\left(\frac{1}{\sqrt{\tau}}-1\right)\leq\lambda\leq\frac{1}{\sqrt{\tau}}-1 \tag{D.9}$$

D.2 Effect of a reinforcement

Assuming one wishes decreases the damage length in both bottom and side grounding by $X\%$, then using Eq. 7.11 and Eq. D.9 one can have :

$$\frac{1}{\tau_{Bottom}} - 1 = k\left(\frac{1}{\sqrt{\tau_{Side}}} - 1\right) \tag{D.10}$$

Where k lies between 1 and 1.2, then τ_{Side} may be expressed as :

$$\tau_{Side} = k^2 \frac{\tau_{Bottom}^2}{1 + \tau_{Bottom}(k-1)} \tag{D.11}$$

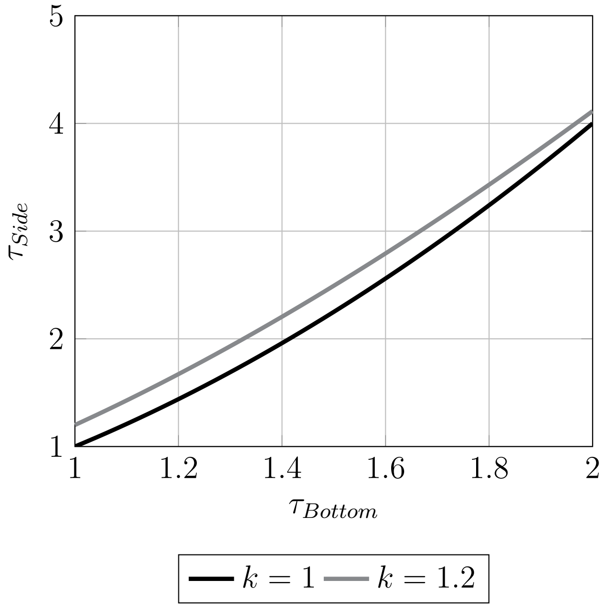

Figure D.2: τ_{Side} as a function of τ_{Bottom}

Using Eq. D.11 or Figure D.2, it can be concluded that in order to reduce by $X\%$ the damage length in both bottom and side grounding the reinforcement to be applied in side grounding must $\tau_{Side}/\tau_{Bottom} \approx \tau_{Bottom}$ more important than the one to be applied in bottom grounding.

Appendix E

FLAGS input files

This appendix contains the principal hydrodynamic properties used in the F.E and S.E simulations for the floodstand ship B. The *Ship.mco* file contains three principal matrices:

1. Rigid body mass matrix, which corresponds to structural mass and inertia of the ship
2. Added mass matrix, which includes all the added mass effect due to the surrounding water
3. Hydrostatic restoring matrix, which traduces the buoyancy forces

The following matrices corresponds to floodstand ship B, and were obtained using *Hydrostar* program from *Bureau Veritas* and are expressed in international system of units.

1-Rigid body mass matrix *(Mrb)*

3.3923E+07	0.0000E+00	0.0000E+00	0.0000E+00	0.0000E+00	0.0000E+00
0.0000E+00	3.3923E+07	0.0000E+00	0.0000E+00	0.0000E+00	0.0000E+00
0.0000E+00	0.0000E+00	3.3923E+07	0.0000E+00	0.0000E+00	0.0000E+00
0.0000E+00	0.0000E+00	0.0000E+00	4.1047E+09	0.0000E+00	0.0000E+00
0.0000E+00	0.0000E+00	0.0000E+00	0.0000E+00	1.2212E+11	0.0000E+00
0.0000E+00	0.0000E+00	0.0000E+00	0.0000E+00	0.0000E+00	1.2623E+11

2-Added mass matrix *(Ma)*

3.9990E+05	0.0000E+00	7.4090E+05	0.0000E+00	2.1639E+08	0.0000E+00
0.0000E+00	8.2640E+06	0.0000E+00	3.5063E+06	0.0000E+00	1.0640E+08
7.2753E+05	0.0000E+00	7.1953E+07	0.0000E+00	4.6024E+08	0.0000E+00
0.0000E+00	3.2945E+06	0.0000E+00	1.1321E+09	0.0000E+00	1.2099E+09
2.1526E+08	0.0000E+00	4.6298E+08	0.0000E+00	1.5023E+11	0.0000E+00
0.0000E+00	1.0629E+08	0.0000E+00	1.2180E+09	0.0000E+00	3.2693E+10

3-Hydrostatic restoring matrix *(Ks)*

0.0000E+00	0.0000E+00	0.0000E+00	0.0000E+00	0.0000E+00	0.0000E+00
0.0000E+00	0.0000E+00	0.0000E+00	0.0000E+00	0.0000E+00	0.0000E+00
0.0000E+00	0.0000E+00	5.9943E+07	0.0000E+00	1.5302E+08	0.0000E+00
0.0000E+00	0.0000E+00	0.0000E+00	4.5697E+09	0.0000E+00	0.0000E+00
0.0000E+00	0.0000E+00	1.5302E+08	0.0000E+00	1.8268E+11	0.0000E+00
0.0000E+00	0.0000E+00	0.0000E+00	0.0000E+00	0.0000E+00	0.0000E+00

E.1 Ship.xml file

```xml
<?xml version="1.0" encoding="UTF-8"?>
<STRUCK_SHIP_COMPUTATION_MODEL> <!-- Description of the Super-Element mesh-->
    <SUPER_ELEMENT_MESH>
        <NODES>      <!-- Postion X/Y/Z of nodes in the earth fixed frame-->
             <Node Label="1">
                <X>36.0</X>
                <Y>-2.85</Y>
                <Z>0.0</Z>
            </Node>
            <Node Label="2">
                <X>39.0</X>
                <Y>-2.85</Y>
                <Z>0.0</Z>
            </Node>
            <Node Label="3">
                <X>36.0</X>
                <Y>2.85</Y>
                <Z>0.0</Z>
            </Node>
            <Node Label="4">
                <X>39.0</X>
                <Y>2.85</Y>
                <Z>0.0</Z>
            </Node>
        </NODES>
        <SUPER_ELEMENTS> <!-- Super-Element type and associated nodes -->
            <Super_Element Label="1">
                <Name>bottom_</Name>
                <Tag>0.0</Tag>
                <Connectivities>
                    <Node>3</Node>
                    <Node>4</Node>
                    <Node>2</Node>
                    <Node>1</Node>
                </Connectivities>
                <Material>Steel</Material> <!-- Super-Element characteristics -->
                <Thickness>0.015</Thickness>  <!-- Material and thickness  -->
            </Super_Element>
         </SUPER_ELEMENTS>
    </SUPER_ELEMENT_MESH>
        <PROPERTIES> <!-- Ship properties -->
        <CGX>65.0</CGX> <!-- Positions of CoG in earth fixed frame -->
        <CGY>0.0</CGY>
        <CGZ>15.15</CGZ>
    </PROPERTIES>
</STRUCK_SHIP_COMPUTATION_MODEL>
```

Figure E.1: Super-Element mesh input file

Appendix F

Ship combined grounding appendix

This appendix contains additional results from *Ls-Dyna/MCOL* and *FLAGS/MCOL* calculations regarding combined benchmark of Section 7.5.

Figures F.1 to F.5 illustrate the evolution of V_x, V_z as well as the heave motion of the CoG obtained from *Ls-dyna* numerical simulation and *FLAGS* calculation for combined benchmark scenario from (Section 7.5).

Regarding the evolution of velocities and displacement both numerical and simplified program give almost the same results even if the resisting forces are underestimated in *FLAGS*. The major discrepancies are observed for the roll angle on Figure F.5. Therefore, one can conclude that even if the resisting forces are slightly different between *Ls-Dyna* and *FLAGS*, the rigid-body dynamic is still well captured by the simplified program.

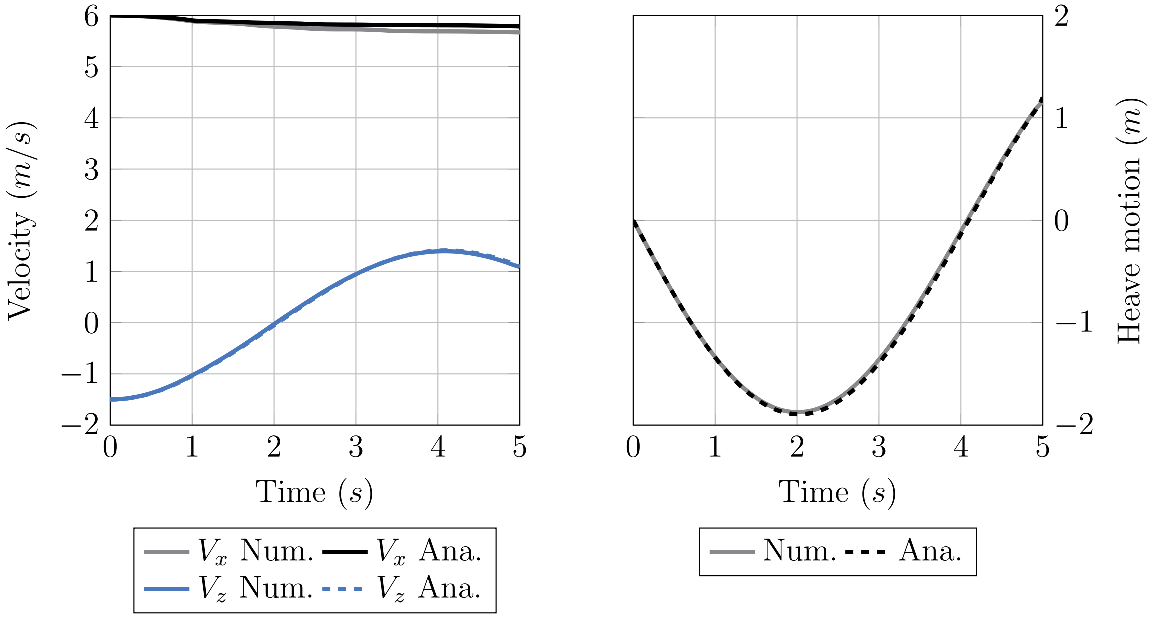

Figure F.1: Ship dynamic - Combined Scenario 1

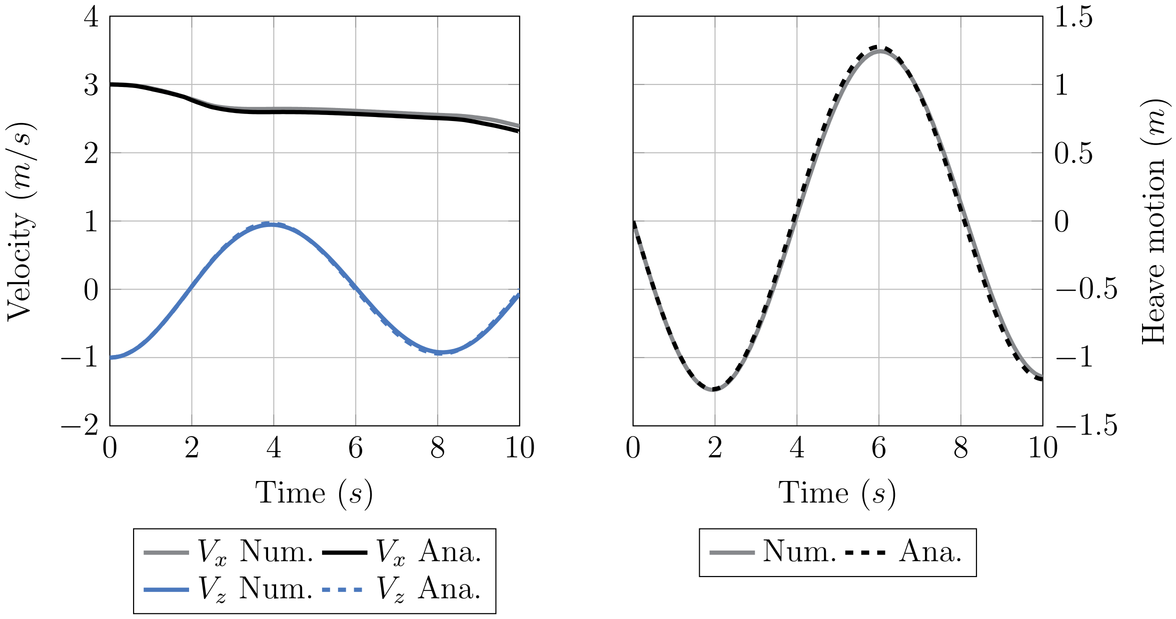

Figure F.2: Ship dynamic - Combined Scenario 2

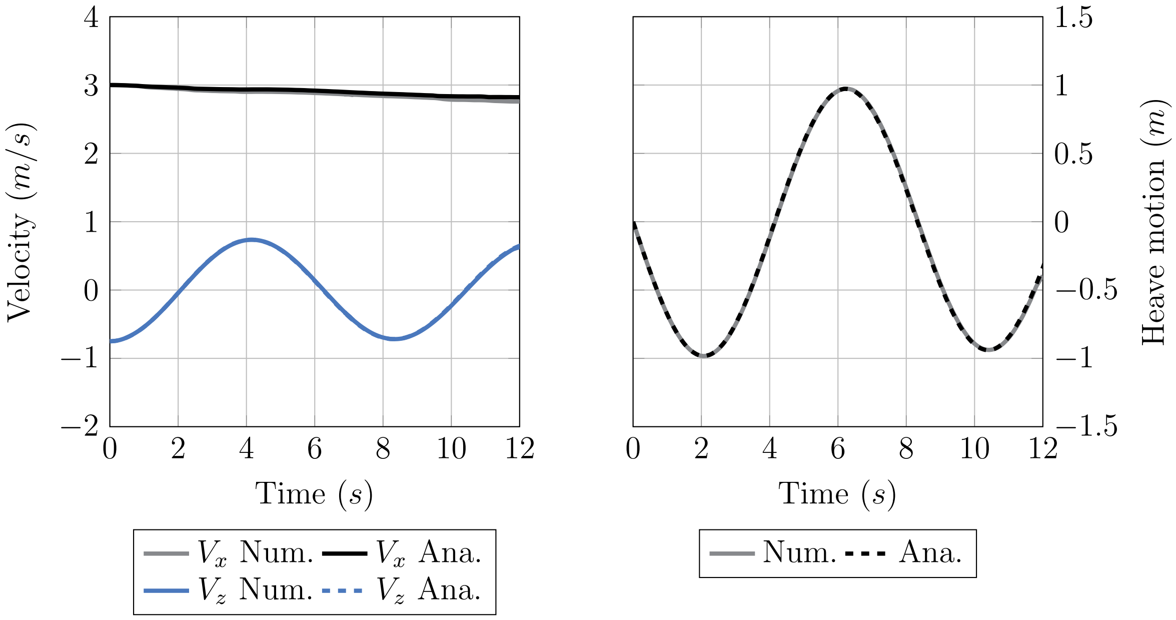

Figure F.3: Ship dynamic - Combined Scenario 3

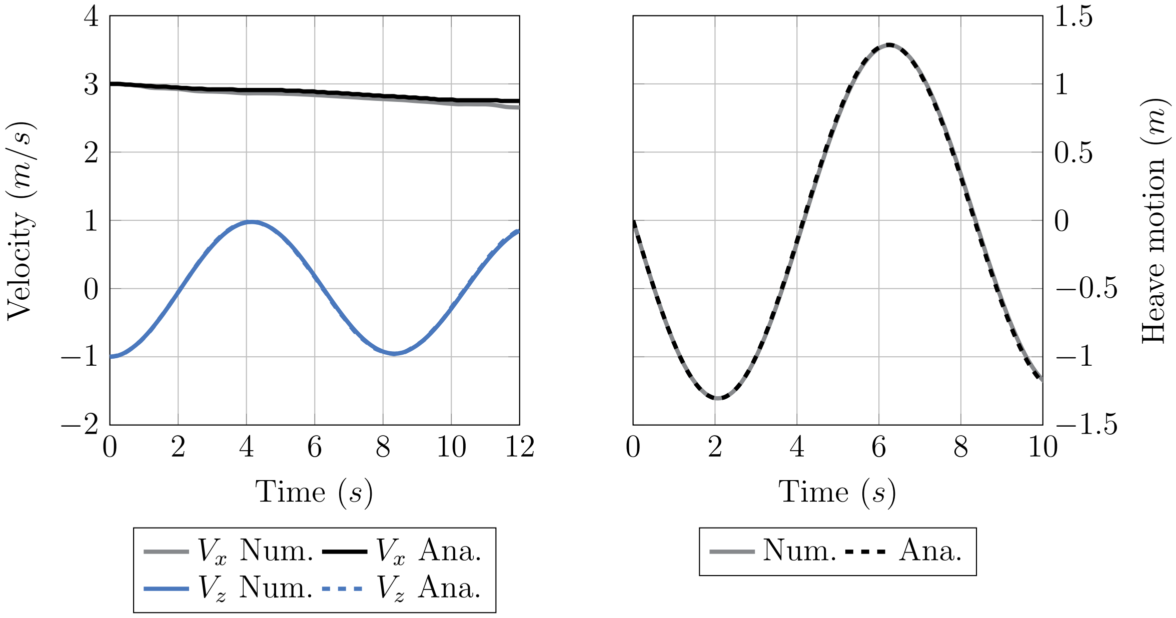

Figure F.4: Ship dynamic - Combined Scenario 4

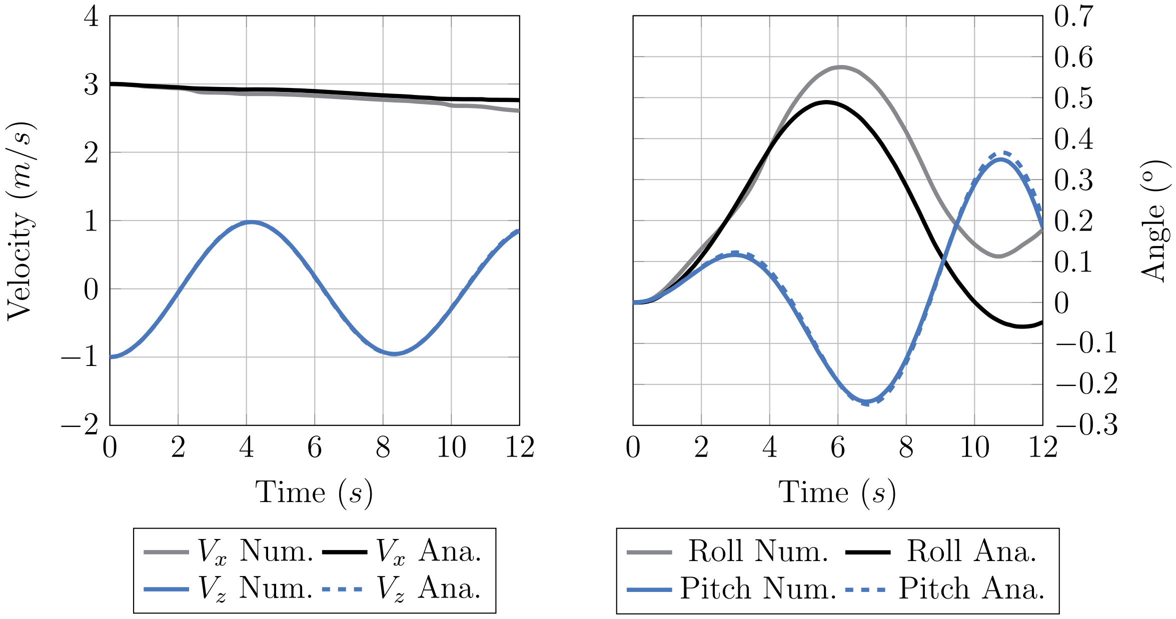

Figure F.5: Ship dynamic - Combined Scenario 5

For illustration purpose scenario n° 2 is carried out on a ship long of $130m$. Temporal evolution of the heave velocity is depicted on Figure F.6. As the simulation progresses, the magnitude of the heave velocity decreases due to the energy transferred to the surrounding water. In addition, the heave speed is found to be bounded by two exponential functions.

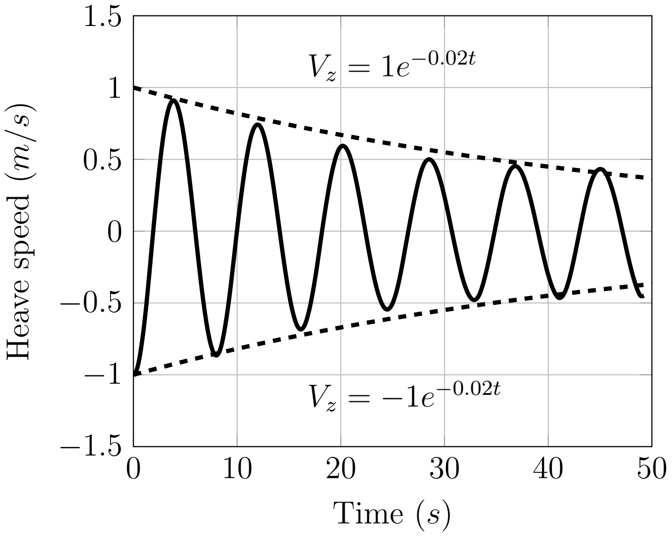

Figure F.6: Evolution of heave speed in long combined grounding

Bibliography

1. *EMSA. Annual Overview of Marine Casualties and Incidents* tech. rep. 15-12-2021 (EMSA2021, 2021), 1–23.
2. *Zhang,* M., *Conti,* F., *Le Sourne,* H., *Vassalos,* D., *Kujala,* P., *Lindroth,* D. & *Hirdaris,* S. A method for the direct assessment of ship collision damage and flooding risk in real conditions. *Ocean Engineering* **237.** doi:`10.1016/j.oceaneng.2021.109605` (2021).
3. *Conti,* F., *Le Sourne,* H., *Vassalos,* D., *Kujala,* P., *Lindroth,* D., *Kim,* S. J. & *Hirdaris,* S. A comparative method for scaling SOLAS collision damage distributions based on ship crashworthiness–application to probabilistic damage stability analysis of a passenger ship. *Ships and Offshore Structures* **0,** 1–17. doi:`10.1080/17445302.2021.1932023` (2021).
4. *Youssef,* S. A. M. & *Paik,* J. K. Hazard identification and scenario selection of ship grounding accidents. *Ocean Engineering* **153,** 242–255. doi:`10.1016/j.oceaneng.2018.01.110` (2018).
5. *Zhang,* S., *Villavicencio,* R., *Zhu,* L. & *Pedersen,* P. T. Ship collision damage assessment and validation with experiments and numerical simulations. *Marine Structures* **63,** 239–256. doi:`10.1016/j.marstruc.2018.09.005` (2019).
6. *Le Sourne,* H., *Besnard,* N., *Cheylan,* C. & *Buannic,* N. A Ship Collision Analysis Program Based on Upper Bound Solutions and Coupled with a Large Rotational Ship Movement Analysis Tool. *Journal of Applied Mathematics* **2012,** 1–27. doi:`10.1155/2012/375686` (2012).
7. *Friis-Hansen,* P. & *Simonsen,* B. GRACAT: Software for grounding and collision risk analysis. *Marine Structures* **15,** 383–401. doi:`10.1016/S0951-8339(02)00009-6` (2002).
8. *Alsos,* H. S. & *Amdahl,* J. On the resistance of tanker bottom structures during stranding. *Marine Structures* **20,** 218–237. doi:`10.1016/j.marstruc.2007.06.001` (2007).
9. *Wang,* G. & *Ohtsubo,* H. Deformation of ship plate subjected to very large load. *Journal of offshore Mechanics and Artic Engineering* **119,** 173–180 (1997).
10. *Simonsen,* B. C. & *Wierzbicki,* T. Plasticity, fracture and friction in steady state plate cutting. **19,** 667–691 (1997).
11. *Simonsen,* B. C. *Mechanics of Ship Grounding* PhD thesis (1997).
12. *Zeng,* J., *Hu,* Z. & *Chen,* G. A steady-state plate tearing model for ship grounding over a cone-shaped rock. *Ships and Offshore Structures* **11,** 245–257. doi:`10.1080/17445302.2014.985429` (2016).
13. *Sun,* B., *Hu,* Z. & *Wang,* J. Bottom structural response prediction for ship-powered grounding over rock-type seabed obstructions. *Marine Structures* **54,** 127–143. doi:`10.1016/j.marstruc.2017.04.002` (2017).

14. *Hong,* L. & *Amdahl,* J. Crushing resistance of web girders in ship collision and grounding. *Marine Structures* **21,** 374–401. doi:`10.1016/j.marstruc.2008.02.001` (2008).
15. *Nguyen,* T.-H., *Amdahl,* J., *Garrè,* L. & *Leira,* B. A study on dynamic grounding of ships. *Advances in Marine Structures,* 373–380. doi:`10.1201/b10771-46` (2011).
16. *Heinvee,* M., *Tabri,* K. & *Kõrgesaar,* M. *A simplified approach to predict the bottom damage in tanker grounding* doi:`10.1201/b14915-20` (June 2013).
17. *Wang,* G., *Ohtsubo,* H. & *Liu,* D. A simple method for predicting the grounding strength of ships. *Journal of Ship Research* **41,** 241–247 (Sept. 1997).
18. *Turgeon,* J. *Analysis of hull damage without fracture in single-bottom transversally framed ships subjected to grounding* tech. rep. (Joint MIT-Industry Program on Tanker Safety, 1995).
19. *Hong,* L. & *Amdahl,* J. Rapid assessment of ship grounding over large contact surfaces. *Ships and Offshore Structures* **7,** 5–19. doi:`10.1080/17445302.2011.579003` (Mar. 2012).
20. *Heinvee,* M. *The Rapid Prediction of Grounding Behavior of Double Bottom Tankers. Doctoral thesis* PhD thesis (2016).
21. *Schuler,* M. *GCaptain.com* `https://gcaptain.com/maib-ship-grounded-after-late-turn-from-nervous-new-master/`.
22. *Lezza,* L. *Costa Concordia* `https://www.gettyimages.fi/detail/uutiskuva/close-up-view-of-the-damage-caused-to-the-hull-of-the-cruise-uutiskuva/137237850?adppopup=true`.
23. *OMB. OMB* `https://omb.report/icr/201507-1014-003/doc/57511901`.
24. *Cho,* S. K., *Hong,* S. Y., *Kim,* Y. H. & *Lee,* K. J. Investigation of dynamic characteristics of the flooding water of the damaged compartment of an ITTC RO-RO passenger ship. *Marine Systems & Ocean Technology* **2,** 73–80. doi:`10.1007/bf03449186` (2006).
25. *Ruponen,* P. *Progressive flooding of a damaged passenger ship* PhD thesis (2007).
26. *Ruponen,* P., *Kurvinen,* P., *Saisto,* I. & *Harras,* J. Experimental and numerical study on progressive flooding in full-scale. *Transactions of the Royal Institution of Naval Architects Part A: International Journal of Maritime Engineering* **152.** doi:`10.3940/rina.2010.a4.195` (2010).
27. *Acanfora,* M. & *Cirillo,* A. A simulation model for ship response in flooding scenario. *Proceedings of the Institution of Mechanical Engineers Part M: Journal of Engineering for the Maritime Environment* **231,** 153–164. doi:`10.1177/1475090215627839` (2017).
28. *Lee,* G. J. Dynamic orifice flow model and compartment models for flooding simulation of a damaged ship. *Ocean Engineering* **109,** 635–653. doi:`10.1016/j.oceaneng.2015.09.051` (2015).
29. *DNV GL. Evaluation of risk from raking damages due to grounding, Final report.* tech. rep. (2015).
30. *Pedersen,* P. T. Ship grounding and hull-girder strength. *Marine Structures* **7,** 1–29. doi:`10.1016/0951-8339(94)90008-6` (1994).

31. *Quéméner,* Y., *Huang,* C.-h. & *Chen,* K.-c. Critical Scenario Prediction of a Bulk Carrier Subjected to Soft Grounding, 1–8 (2012).

32. *Le Sourne,* H., *Donner* R.and Besnier, F. & *Ferry,* M. External Dynamics of Ship-Submarine Collision. *2nd International Conference on Collision and Grounding of Ships (ICGS),* 137–144 (2001).

33. *Prabowo,* A. R., *Cao,* B., *Bae,* D. M., *Bae,* S. Y., *Zakki,* A. F. & *Sohn,* J. M. Structural analysis of the double bottom structure during ship grounding by finite element approach. *Latin American Journal of Solids and Structures* **14,** 1106–1123. doi:`10.1590/1679-78253648` (2017).

34. *Liu,* B. Analysis of structural crashworthiness of double-hull ships based on collision and grounding. *Marine Structures* **3.** doi:`10.1016/j.marstruc.2020.102898` (2020).

35. *Le Sourne,* H., *Pineau,* J., *Umunnakwe,* C., *Wesoly,* T. & *Dorival,* O. *On the influence of buoyancy forces, failure strain and friction coefficient on the damage extent of a grounded ship* in *Marine Structures - MARSTRUCT* (Trondheim, 2021).

36. *Minorsky,* V. U. *An analysis of ship collisions with reference to protection of nuclear power plants* (Jan. 1958).

37. *Zhang,* S. *The Mechanics of Ship Collisions* PhD thesis (Technical University of Danemark, 1999), 260.

38. *Motora,* S., *Fujino,* M., *Sugiura,* M. & *Sugita,* M. Equivalent added mass of ships in collisions. *Selected Papers, J of Soc of Naval Arch of Japan* **7** (1971).

39. *Brown,* A. J. Collision scenarios and probabilistic collision damage. *Marine Structures* **15,** 335–364 (2002).

40. *Tabri,* K., *Määttänen,* J. & *Ranta,* J. Model-scale experiments of symmetric ship collisions. *Journal of Marine Science and Technology* **13,** 71–84. doi:`10.1007/s00773-007-0251-z` (2008).

41. *Yu,* Z. & *Amdahl,* J. Influence of 6DOF ship motions in the damage prediction of ship collision and grounding accidents. *Proceedings of the ICCGS* **15** (2016).

42. *Kim,* S. J., *Kõrgersaar,* M., *Ahmadi,* N., *Taimuri,* G., *Kujala,* P. & *Hirdaris,* S. The influence of fluid structure interaction modelling on the dynamic response of ships subject to collision and grounding. *Marine Structures* **75,** 102875 (2021).

43. *Echeverry,* S., *Márquez,* L., *Rigo,* P. & *Le Sourne,* H. *Numerical crashworthiness analysis of a spar floating offshore wind turbine impacted by a ship* in *Dev. Collis. Grounding Ships Offshore Struct. - ICCGS 2019* **004** (2020), 85–95. doi:`10.1201/9781003002420-11`.

44. *Petersen,* M. J. & *Pedersen,* P. T. Collisions between ships and offshore platforms. *Proceedings of the Annual Offshore Technology Conference* **1981-May,** 163–169. doi:`10.4043/4134-ms` (1981).

45. *Petersen,* M. J. Dynamics of ship collisions. *Ocean Engineering* **9,** 295–329 (1982).

46. *Tabri,* K. *Dynamics of Ship Collisions* PhD thesis (Aalto University, 2010).

47. *Liu,* Z. & *Amdahl,* J. A new formulation of the impact mechanics of ship collisions and its application to a ship-iceberg collision. *Marine Structures* **23,** 360–384. doi:`10.1016/j.marstruc.2010.05.003` (2010).

48. *Brown,* A. J. Collision scenarios and probabilistic collision damage. *Marine Structures* **15,** 335–364. doi:`10.1016/S0951-8339(02)00007-2` (2002).
49. *Ferry,* M., *Le Sourne,* H. & *Besnier,* F. MCOL-theoretical manual. *Principia Marine, Nantes* (2002).
50. *Ferry,* M., *Le Sourne,* H. & *Besnier,* F. MCOL user's manual. *Principia Marine* (2002).
51. *Kim,* S. J., *Kõrgersaar,* M., *Ahmadi,* N., *Taimuri,* G., *Kujala,* P. & *Hirdaris,* S. The influence of fluid structure interaction modelling on the dynamic response of ships subject to collision and grounding. *Mar. Struct.* **75.** doi:`10.1016/j.marstruc.2020.102875` (2021).
52. *Paboeuf,* S., *Uzögüten,* H. Ö., *Le Sourne,* H. & *Nzengu,* W. Crashworthiness of an alternative construction within the scope of A.D.N. regulations using super-elements method. *Iccgs-2016,* 247–254. doi:`10.1038/onc.2011.317onc2011317[pii]` (2016).
53. *Le Sourne,* H., *Pineau,* J., *Looten,* T., *Conti,* F., *Kaydihan,* L., *Bae,* E., *Vassalos,* D., *Kujala,* P. & *Hirdaris,* S. *A comparison of crashworthiness methods for the assessment of ship damage extents* in *1st International Conference on the Stability and Safety of Ships and Ocean Vehicles* (Glasgow, 2021).
54. *Tabri,* K. Influence of coupling in the prediction of ship collision damage. *Ships and Offshore Structures* **7,** 47–54. doi:`10.1080/17445302.2011.553812` (2012).
55. *Liu,* B., *Villavicencio,* R., *Zhang,* S. & *Guedes Soares,* C. Assessment of external dynamics and internal mechanics in ship collisions. *Ocean Engineering* **141,** 326–336. doi:`10.1016/j.oceaneng.2017.06.053` (2017).
56. *Song,* M., *Ma,* J. & *Huang,* Y. Fluid-structure interaction analysis of ship-ship collisions. *Mar. Struct.* **55,** 121–136. doi:`10.1016/j.marstruc.2017.05.006` (2017).
57. *Rudan,* S., *Ćatipović,* I., *Berg,* R., *Völkner,* S. & *Prebeg,* P. Numerical study on the consequences of different ship collision modelling techniques. *Ships and Offshore Structures* **14,** 387–400. doi:`10.1080/17445302.2019.1615703` (2019).
58. *Sormunen.* Ship Grounding Damage Estimation Using Statistical Models (2014).
59. *Pedersen,* T., *Zhang,* S. & *Pedersen,* P. T. Absorbed energy in ship collisions and grounding-revising Minorsky's empirical method. *Journal of Ship Research* **44,** 140–154 (2000).
60. *Zhang,* S. & *Pedersen,* P. T. A method for ship collision damage and energy absorption analysis and its validation. **5302.** doi:`10.1080/17445302.2016.1254584` (2017).
61. *Calle,* M. A., *Oshiro,* R. E. & *Alves,* M. Ship collision and grounding: Scaled experiments and numerical analysis. *International Journal of Impact Engineering* **103,** 195–210. doi:`10.1016/j.ijimpeng.2017.01.021` (2017).
62. *Calle,* M. A., *Salmi,* M., *Mazzariol,* L. M. & *Kujala,* P. Miniature reproduction of raking tests on marine structure: Similarity technique and experiment. *Engineering Structures* **212,** 110527. doi:`10.1016/j.engstruct.2020.110527` (2020).
63. *Zhou,* Z., *Zhu,* L. & *Guo,* K. Plate tearing experiments over a cone-shaped rock considering friction in ship grounding. *Proceedings of the International Offshore and Polar Engineering Conference* **2020-Octob,** 3916–3920 (2020).

64. *Chen,* B. Q., *Liu,* B. & *Guedes Soares,* C. Experimental and numerical investigation on the influence of stiffeners on the crushing resistance of web girders in ship grounding. *Marine Structures* **63,** 351–363. doi:`10.1016/j.marstruc.2018.10.003` (2019).

65. *Amdahl,* J. Energy absorption in ship-platform impacts, 237 (1983).

66. *Pedersen,* P., *Valsgård,* S., *Olsen,* D. & *Spangenberg,* S. Ship impacts: Bow collisions. *International Journal of Impact Engineering* **13,** 163–187. doi:`10.1016/0734-743X(93)90091-K` (1993).

67. *Jones,* N. A literature survey in the collision and grounding protection of ships. *International Journal of Impact Engineering* **13,** 163–187 (1993).

68. *Ellinas,* C. P. & *Valsgard,* S. Collisions and Damage of Offshore Structures: A State-of-the-Art. *Journal of Energy Resources Technology* **107,** 297. doi:`10.1115/1.3231193` (2009).

69. *Muscat-Fenech,* C. *The tearing of ships plating upon grounding* tech. rep. (Technical report 2, Departement of Engineering,University of Reading, 1996).

70. *Rodd,* J. L. & *Sikora,* J. P. Double Hull Grounding Experiments. *Proceedings of the Fifth (1995) International Offshore and Polar Engineering Conference* **IV,** 446–456 (1995).

71. *Lu,* G. & *Calladine,* C. R. On the cutting of a plate by a wedge. *International Journal of Mechanical Sciences* **32,** 293–313. doi:`10.1016/0020-7403(90)90095-Z` (1990).

72. *Kuroiwa,* T. *Numerical simulation of actual collision and grounding experiments* in *International Conference on Design and Methodologies for Collision and Grounding Protection of Ships* (1996).

73. *Kitamura,* O., *Kuroiwa,* T., *Kawamoto,* Y. & *Kaneko,* E. *A study on the improved tanker structure against collision and grounding* in *International Conference on Design and Methodologies for Collision and Grounding Protection of Ships* (The Hague, 1998).

74. *Gu,* Y.-N., *Hu,* Z. & *Gao,* Z. *Numerical simulation of ship collision and grounding accident* 1176–1180 (Aug. 2003).

75. *Hong,* L. & *Amdahl,* J. Plastic design of laterally patch loaded plates for ships. *Marine Structures* **20,** 124–142. doi:`10.1016/j.marstruc.2007.05.003` (2007).

76. *Zheng,* Y., *Aksu,* S., *Vassalos,* D. & *Tuzcu,* C. Study on side structure resistance to ship-ship collisions. *Ships and Offshore Structures* **2,** 273–293. doi:`10.1080/17445300701594336` (Nov. 2007).

77. *Aga,* H. L. *Assessment of structural requirements related to LNG fuel tanks Halvor Larsson Aga* PhD thesis (Norwegian University of Science and Technology, 2013).

78. *Heinvee,* M. & *Tabri,* K. A simplified method to predict grounding damage of double bottom tankers. *Marine Structures* **43,** 22–43. doi:`10.1016/j.marstruc.2015.04.002` (2015).

79. *Brubak,* L., *Hu,* Z., *Kõrgesaar,* M., *Schipperen,* I. & *Tabri,* K. *Numerical Simulations of Grounding Scenarios–Benchmark Study on Key Parameters in FEM Modelling* in *Practical Design of Ships and Other Floating Structure* (Singapore, 2020), 257–269. doi:`10.1007/978-981-15-4672-3_16`.

80. *Zhu,* L. *Failure Criteria for Ship Collision and Grounding* in *7th, Practical design of ships and mobile units* **11** (DEVELOPMENTS IN MARINE TECHNOLOGY, The Hague, 1998), 141–148.

81. *Ehlers,* S. & *Varsta,* P. Strain and stress relation for non-linear finite element simulations. *Thin-Walled Structures* **47,** 1203–1217. doi:`10.1016/j.tws.2009.04.005` (2009).

82. *Calle,* M. A., *Oshiro,* R. E., *Kõrgesaar,* M., *Alves,* M. & *Kujala,* P. Combined strain rate, mesh size and calibration test influence on structural failure: Miniature ship grounding test. *Ocean Engineering,* 215–226. doi:`10.1016/j.oceaneng.2019.01.002`.

83. *Yu,* X. *Structural analysis with large deformations until fracture and with dynamic failure* PhD thesis (Hambourg University, 1996).

84. *Lehmann,* E. & *Yu,* X. *On ductile rupture criteria for structural tear in the case of ship collision and grounding* in *nternational Conference on Practical Design of Ships and Mobile Units (PRADS)* (The Hague, 1998).

85. *Simonsen,* B. C. & *Lauridsen,* L. P. Energy absorption and ductile failure in metal sheets under lateral indentation by a sphere. *International Journal of Impact Engineering* **24,** 1017–1039. doi:`10.1016/S0734-743X(00)00024-5` (2000).

86. *Simonsen,* B. C. & *Törnqvist,* R. Experimental and numerical modelling of ductile crack propagation in large-scale shell structures. *Marine Structures* **17,** 1–27. doi:`10.1016/j.marstruc.2004.03.004` (2004).

87. *Lehmann,* E. & *Peschmann,* J. Energy absorption by the steel structure of ships in the event of collisions. *Marine Structures* **15,** 429–441. doi:`10.1016/S0951-8339(02)00011-4` (2002).

88. *Tørnqvist,* R. *Design of crashworthy ship structures* PhD thesis (2003). doi:`10.1007/s00726-011-1022-z`.

89. *Rice,* J. R. & *Tracey,* D. M. On the ductile enlargement of voids in triaxial stress fields*. *Journal of the Mechanics and Physics of Solids* **17,** 201–217. doi:`10.1016/0022-5096(69)90033-7` (1969).

90. *Cockroft,* M. & *Latham,* D. Ductility and the workability of metals. *Journal of the Institute of Metals* **96,** 33–39 (1968).

91. *Ehlers,* S., *Broekhuijsen,* J., *Alsos,* H. S., *Biehl,* F. & *Tabri,* K. Simulating the collision response of ship side structures: A failure criteria benchmark study. *International Shipbuilding Progress* **55,** 127–144. doi:`10.3233/ISP-2008-0042` (2008).

92. *Jones,* N. *Structural Impact* doi:`DOI:10.1017/CBO9780511624285` (Cambridge University Press, Cambridge, 1990).

93. *Wierzbicki,* T. Concertina tearing of metal plates. *International Journal of Solids and Structures* **32.** doi:`10.1016/0020-7683(94)00237-Q` (1995).

94. *Buldgen,* L. Simplified analytical methods for the crashworthiness and the seismic design of lock gates. *Ship Technology Research* **62,** 108–108. doi:`10.1179/0937725515z.00000000012` (2014).

95. *Pire,* T. Crashworthiness of offshore wind turbine jackets based on the continuous element method. PhD Thesis (2018).

96. *Wierzbicki,* T. & *Thomas,* P. Closed-form solution for wedge cutting force through thin metal sheets. *International Journal of Mechanical Sciences* **35,** 209–229. doi:`10.1016/0020-7403(93)90077-8` (1993).
97. *Hong,* L. Simplified analysis and design of ships subjected to collision and grounding, 1–95 (2008).
98. *Pedersen,* P. T. & *Li,* Y. On the global ship hull bending energy in ship collisions. *Marine Structures* **22,** 2–11. doi:`10.1016/j.marstruc.2008.06.005` (2009).
99. *Çerik,* B. & *Choung,* J. *On the modelling of strain-rate effects in nonlinear FE analysis of ship collisions* in *International Conference on Ships and Offshore Structures - ICSOS* (Glasgow, UK, 2020).
100. *Calder,* C. A. & *Goldsmith,* W. Plastic deformation and perforation of thin plates resulting from projectile impact. *International Journal of Solids and Structures* **7.** doi:`10.1016/0020-7683(71)90096-5` (1971).
101. *Wang,* Z., *Liu,* K., *Chen,* G. & *Hu,* Z. An analytical method to assess the structural responses of ship side structures by raked bow under oblique collision scenarios. *Proceedings of the Institution of Mechanical Engineers Part M: Journal of Engineering for the Maritime Environment.* doi:`10.1177/1475090220980277` (2020).
102. *Wierzbicki,* T., *Bhat,* S., *Abramowicz,* W. & *Brodkin,* D. Alexander revisited—A two folding elements model of progressive crushing of tubes. *International Journal of Solids and Structures* **29,** 3269–3288 (1992).
103. *Ueda,* Y., *Rashed,* S. M. & *Paik,* J. K. Buckling and ultimate strength interaction in plates and stiffened panels under combined inplane biaxial and shearing forces. *Marine Structures* **8,** 1–36. doi:`10.1016/0951-8339(95)90663-F` (1995).
104. *Fujikubo,* M. & *Kaeding,* P. with New Lateral Shape Functions (2nd Report) (2000).
105. *Pei,* Z., *Iijima,* K., *Fujikubo,* M., *Tanaka,* S., *Okazawa,* S. & *Yao,* T. Simulation on progressive collapse behaviour of whole ship model under extreme waves using idealized structural unit method. *Mar. Struct.* **40,** 104–133. doi:`10.1016/j.marstruc.2014.11.002` (2015).
106. *Lützen,* M. *Ship Collision Damage* PhD thesis (Technical university of Denmark, 2001). doi:`10.1111/j.1365-2958.2006.05502.x`.
107. *Buldgen,* L., *Le Sourne,* H., *Besnard,* N. & *Rigo,* P. Extension of the super-elements method to the analysis of oblique collision between two ships. *Marine Structures* **29,** 22–57. doi:`10.1016/j.marstruc.2012.08.002` (2012).
108. *Kim,* S.-j. *et al.* Comparison of numerical approaches for structural response analysis of passenger ships in collisions and groundings. *Mar. Struct.* **81,** 1–32. doi:`10.1016/j.marstruc.2021.103125` (2021).
109. *Taimuri,* G., *Kim,* S. J., *Mikkola,* T. & *Hirdaris,* S. A two-way coupled FSI model for the rapid evaluation of accidental loads following ship hard grounding. *Journal of Fluids and Structures* **112,** 103589. doi:`10.1016/j.jfluidstructs.2022.103589`. `https://doi.org/10.1016/j.jfluidstructs.2022.103589` (2022).
110. *Bracco,* M. A Study on the Wedge Cutting Force through Longitudinally Stiffened Plates An Application to Grounding Resistance of Single and Double Hull Ships (1994).

111. *Zheng,* Z. *Theoretical analyses of wedge cutting through metal plates* PhD thesis (Massachusetts Institute of Technology, 1994).
112. *Hong,* L. & *Amdahl,* J. Plastic mechanism analysis of the resistance of ship longitudinal girders in grounding and collision. *Ships and Offshore Structures* **3,** 159–171. doi:`10.1080/17445300802263849` (2008).
113. *Yu,* Z., *Hu,* Z., *Wang,* G. & *Liu,* K. *An Analysis of Structural Performances for Bottom Longitudinal Girder and Attached Stiffeners During Shoal Grounding Accident* 2013.
114. *Song,* Z. & *Hu,* Z. An Integrated Analytical Tool on Predicting Structural Responses of Ships Under Collision and Grounding Scenarios, V03AT02A001. doi:`10.1115/omae2017-61220` (2017).
115. *Kim,* S. J., *Kõrgersaar,* M., *Ahmadi,* N., *Taimuri,* G., *Kujala,* P. & *Hirdaris,* S. The influence of fluid structure interaction modelling on the dynamic response of ships subject to collision and grounding. *Marine Structures* **75.** doi:`10.1016/j.marstruc.2020.102875` (2021).
116. *Little,* P. *A study of the wedge cutting force through transversely stiffened plates: an application to ship grounding resistance* tech. rep. (1994).
117. *Pippenger,* D. T. *Coupled vertical and horizontal resistance of hull girder in grounding accidents* tech. rep. (1995).
118. *Wierzbicki,* T., *Peer,* D. & *Rady,* E. The anatomy of tanker grounding. *Marine Technology and SNAME News* **30,** 71–78 (1993).
119. *Puente,* I. J. *Correlation of NSWC grounding tests* tech. rep. (Cambridge, 1995).
120. *Rood,* J. L. *Large Scale Tanker Grounding Experiments* Los Angeles, California, USA, 1996.
121. *Muscat-Fenech,* C. & *Atkins,* A. Denting and fracture of sheet steel by blunt and sharp obstacles in glancing collisions. *International Journal of Impact Engineering* **21,** 499–519. doi:`10.1016/s0734-743x(98)00009-8` (2002).
122. *Samuelides,* M., *Voudouris,* G., *Toulios,* M., *Amdahl,* J. & *Dow,* R. Simulation of the behaviour of double bottoms subjected to grounding actions. *4th International Conference on Collision and Grounding of Ships,* 93–102 (2007).
123. *Yu,* Z., *Hu,* Z. & *Wang,* G. Plastic mechanism analysis of structural performances for stiffeners on bottom plate during shoal grounding accident. *Analysis and Design of Marine Structures,* 219–229. doi:`10.1201/b15120-30` (2013).
124. *Yu,* Z., *Hu,* Z. & *Wang,* G. Plastic mechanism analysis of structural performances for stiffeners on bottom longitudinal web girders during a shoal grounding accident. *Marine Structures* **40,** 134–158. doi:`10.1016/j.marstruc.2014.11.001` (2015).
125. *Abubakar,* A. & *Dow,* R. S. Simulation of ship grounding damage using the finite element method. *International Journal of Solids and Structures* **50,** 623–636. doi:`10.1016/j.ijsolstr.2012.10.016` (2013).
126. *Hu,* Z., *Wang,* G., *Yao,* Q. & *Yu,* Z. Rapid prediction of structural responses of double-bottom structures in shoal grounding scenario. *Journal of Marine Science and Application* **15,** 73–85. doi:`10.1007/s11804-016-1344-z` (2016).

127. *Lee,* S. G., *Lee,* J. S., *Lee,* H. S., *Park,* J. H. & *Jung,* T. Y. Full-scale Ship Collision, Grounding and Sinking Simulation Using Highly Advanced M&S System of FSI Analysis Technique. *Procedia Engineering* **173,** 1507–1514. doi:`10.1016/j.proeng.2016.12.232` (2017).

128. *Evans,* J. H. Basic design concepts. *J. Am. Soc. Nav. Eng.* **71,** 671–678 (1957).

129. *Paik,* J. Cutting of a longitudinally stiffened plate by a wedge. *Journal of Ship Research* **38,** 340–348 (1994).

130. *Ohtsubo,* H. & *Wang,* G. *An upper-bound solution to the problem of plate tearing* **1,** 46–51. doi:`10.1007/BF01240012` (Feb. 1995).

131. *Hu,* Z. & *Amdahl,* J. A Study on the Effect of Plate Stiffeners of Double Bottom. *Omae,* 1–8 (2011).

132. *Simonsen,* B. C. Ship grounding on rock - I. Theory. *Marine Structures* **10,** 519–562. doi:`10.1016/S0951-8339(98)00002-1` (1998).

133. *Ohtsubo,* H., *Kawamoto,* Y. & *Kuroiwa,* T. Experimental and numerical research on ship collision and. *Nucl. Eng. Des.* **150,** 385–396 (1994).

134. *Paik,* J. K. Practical techniques for finite element modeling to simulate structural crashworthiness in ship collisions and grounding (Part I: Theory). *Ships and Offshore Structures* **2,** 69–80. doi:`10.1533/saos.2006.0148` (Jan. 2007).

135. *Paik,* J. *et al. Collision and Grounding* tech. rep. (2003), 203–221. doi:`10.1016/b978-008044076-7/50042-8`.

136. *Wierzbicki,* T. & *Abramowicz,* W. On the Crushing Mechanics of Thin-Walled Structures. *Journal of Applied Mechanics* **50/727,** 2–4 (1983).

137. *Hallquist,* J. *LS-DYNA Theory Manual* tech. rep. (2006).

138. *Smith,* C. S. & *Dow,* R. S. Residual strength of damaged steel ships and offshore structures. *Journal of Constructional Steel Research* **1,** 2–15. doi:`10.1016/0143-974X(81)90019-5` (1981).

139. *Bin,* S., *Zhiqiang,* H., *Jin,* W. & *Zhaolong,* Y. An analytical method to assess the damage and predict the residual strength of a ship in a shoal grounding accident scenario. *Journal of Ocean Engineering and Science* **1,** 167–179. doi:`10.1016/j.joes.2016.03.007` (2016).

140. *Liu,* Y., *Hu,* Z. & *Amdahl,* J. *Investigation on smeared thickness method for plating stiffeners on prediction of grounding character of double bottom tanker over obstacles with large contact surface* in *Proceedings of the International Conference on Offshore Mechanics and Arctic Engineering - OMAE* **2** (2012), 115–122. doi:`10.1115/OMAE2012-83238`.

141. *Simonsen,* B. C. Plate tearing by a cone. *International Journal of Mechanical Sciences* **40,** 1145–1158. doi:`10.1016/S0020-7403(98)00015-0` (1998).

142. *Alexander,* J. M. An approximate analysis of the collapse of thin cylindrical shells under axial loading. *Quarterly Journal of Mechanics and Applied Mathematics* **13,** 10–15. doi:`10.1093/qjmam/13.1.10` (1960).

143. *Simonsen,* B. C. & *Ocakli,* H. Experiments and theory on deck and girder crushing. *Thin-Walled Structures* **34,** 195–216. doi:`10.1016/S0263-8231(99)00015-4` (1999).

144. *Gao,* Z., *Yang,* S. & *Hu,* Z. The Resistance of Ship Web Girders in Collision and Grounding. *Mathematical Problems in Engineering* **2014,** 1–13. doi:`10.1155/2014/720542` (2014).

145. *Sormunen,* O., *Castrén,* A., *Romanoff,* J. & *Kujala,* P. Estimating sea bottom shapes for grounding damage calculations. *Marine Structures* **45,** 86–109. doi:`10.1016/j.marstruc.2015.10.004` (2016).

146. *Akita,* Y., *Ando,* N., *Fujita,* Y. & *Kitamura,* K. *Studies on collision-protective structures in nuclear powered ships* 365–401. doi:`10.1016/0029-5493(72)90137-9` (May 1972).

147. *Vaughan,* H. Bending and tearing of plate with application to ship bottom damage. *The Naval Architect* **3,** 97–99 (1978).

148. *Vaughan,* H. *The tearing strength of mild steel plate* 96–100 (June 1980).

149. *Woisin,* G. Comments on Vaughan: "The Tearing Strength of Mild Steel Plate". *Journal of Ship Research* **26,** 50–52. doi:`10.5957/jsr.1982.26.1.50` (1982).

150. *Jones,* N. & *Jouri,* W. S. A study of plate tearing for ship collision and grounding damage. *Journal of Ship Research* **31** (1987).

151. *Zheng,* Z. *A theoretical study of steady-state wedge cutting through metal plates* PhD thesis (Mar. 1996), 45–66. doi:`10.1007/BF00018500`.

152. *Rodd,* J. *Observations on conventional and advanced double hull grounding experiements* in *International Conference on Design and Methodologies for Collision and Grounding Protection of Ships* (San Francisco, 1996), 13.1–13.13.

153. *Heinvee,* M., *Tabri,* K., *Kõrgesaar,* M. & *Urbel,* A. Influence of longitudinal and transverse bulkheads on ship grounding resistance and damage size. *Proceedings of International Conference on Collision and Grounding of Ships and Offshore Structures,* 99–109 (2016).

154. *Atkins,* A. G. Modelling metal cutting using modern ductile fracture mechanics: Quantitative explanations for some longstanding problems. *International Journal of Mechanical Sciences* **45,** 373–396. doi:`10.1016/S0020-7403(03)00040-7` (2003).

155. *Sormunen,* O., *Kõrgesaar,* M., *Tabri,* K., *Heinvee,* M., *Urbel,* A. & *Kujala,* P. Comparing rock shape models in grounding damage modelling. *Marine Structures* **50,** 205–223. doi:`10.1016/j.marstruc.2016.07.004` (2016).

156. *Zhang,* S. Plate tearing and bottom damage in ship grounding. *Marine Structures* **15,** 101–117. doi:`10.1016/S0951-8339(01)00021-1` (2002).

157. *Wierzbicki,* T. & *Simonsen,* B. C. Rupture Analysis of Oil Tankers in a Side Collision Global Structural Model of Bow Indentation into Ship Side (1996).

158. *Buldgen,* L., *Le Sourne,* H. & *Rigo,* P. A new super-element for estimating the collision resistance of an inclined ship side. *Analysis and Design of Marine Structures,* 137–145. doi:`10.1201/b15120-22` (2013).

159. *Lützen,* M., *Simonsen,* B. & *Pedersen,* P. *Rapid Prediction of Damage to Struck and Striking Vessels in a Collision Event* 2000.

160. *Buldgen,* L., *Le Sourne,* H. & *Rigo,* P. A simplified analytical method for estimating the crushing resistance of an inclined ship side. *Marine Structures* **33,** 265–296. doi:`10.1016/j.marstruc.2013.06.005` (2013).

161. *EMSA. Annual Overview of Marine Casualties and Incidents 2019* tech. rep. (EMSA, 2019), 1–135.

162. *Yu,* Z., *Hu,* Z., *Amdahl,* J. & *Liu,* Y. Investigation on structural performance predictions of double-bottom tankers during shoal grounding accidents. *Marine Structures* **33,** 188–213. doi:`10.1016/j.marstruc.2013.06.003` (2013).

163. *Prabowo,* A. R., *Cao,* B., *Sohn,* J. M. & *Bae,* D. M. Crashworthiness assessment of thin-walled double bottom tanker: Influences of seabed to structural damage and damage-energy formulae for grounding damage calculations. *Journal of Ocean Engineering and Science.* doi:`10.1016/j.joes.2020.03.002` (2020).

164. *Manolakos,* D. E. & *Mamalis,* A. G. On ship collisions: The plastic collapse of longitudinally framed shell plating subjected to oblique loading. *International Journal of Impact Engineering* **3,** 41–55. doi:`10.1016/0734-743X(85)90024-7` (1985).

165. *Yamada,* Y. *et al. Effects of Highly Ductile Steel on the Crashworthiness of Hull Structure in Oblique Collision* in *Proceedings of the International Conference on Offshore Mechanics and Arctic Engineering - OMAE* **3** (2016). doi:`10.1115/OMAE201541074`.

166. *Prabowo,* A. R., *Bae,* D. M. & *Sohn,* J. M. Comparing structural casualties of the Ro-Ro vessel using straight and oblique collision incidents on the car deck. *Journal of Marine Science and Engineering* **7.** doi:`10.3390/jmse7060183` (2019).

167. *Sun,* B., *Hu,* Z. & *Wang,* G. An analytical method for predicting the ship side structure response in raked bow collisions. *Marine Structures* **41,** 288–311. doi:`10.1016/j.marstruc.2015.02.007` (2015).

168. *Hill,* R. On discontinuous plastic states, with special reference to localized necking in thin sheets. *Journal of the Mechanics and Physics of Solids* **1,** 19–30. doi:`10.1016/0022-5096(52)90003-3` (1952).

169. *Landkof,* B. & *Goldsmith,* W. Petalling of thin, metallic plates during penetration by cylindro-conical projectiles. *International Journal of Solids and Structures* **21,** 245–266. doi:`10.1016/0020-7683(85)90021-6` (1985).

170. *Wierzbicki,* T. Petalling of plates under explosive and impact loading. *International Journal of Impact Engineering* **22,** 935–954. doi:`10.1016/S0734-743X(99)00028-7` (1999).

171. *Wang,* G., *Arita,* K. & *Liu,* D. Behavior of a double hull in a variety of stranding or collision scenarios. *Marine Structures* **13,** 147–187. doi:`10.1016/S0951-8339(00)00036-8` (2000).

172. *Wang,* G. Some Recent Studies on Plastic Behavior of Plates Subjected to Large Impact Loads. *Journal of Offshore Mechanics and Arctic Engineering* **124,** 125. doi:`10.1115/1.1490933` (2002).

173. *Wu,* Q. & *Wen,* H. Petalling of a thin metal plate struck by a conical-nosed projectile. *Acta Mechanica Solida Sinica* **28,** 568–577. doi:`10.1016/S0894-9166(15)30050-1` (2015).

174. *Zhang,* M., *Sun,* Q., *Liu,* J., *Hu,* Z. & *Zhang,* S. A study of the rupture behavior of a ship side plate laterally punched by a full-shape bulbous bow indenter. *Ocean Engineering* **182,** 48–60. doi:`10.1016/j.oceaneng.2019.04.081` (2019).

175. *Le Sourne,* H. *A ship Collision Analysis Program Based on Super-element Method Coupled with Large Rotational Ship Movement Analysis* in *4th International Conference on Collision and Grounding of Ships* (Hamburg, 2007), 131–138.

176. *Marine Principia. MCOL-User's Manual* tech. rep. (2002).

177. *Luhmann,* H. *Integrated flooding and standard for stability and crises management* tech. rep. October (2009), 202.

178. *Paik,* J. K. & *Thayamballi,* A. K. *Ultimate limit state design of steel plated structures* English. Chichster, England; Hoboken, NJ, 2003.

179. *Conti,* F. *FLARE D3.4 - Annex C : Comparative method for derivation of bottom grounding damage distributions taking into account ship crashworthiness* tech. rep. (2021).

180. *Nguyen,* T. H., *Garrè,* L., *Amdahl,* J. & *Leira,* B. J. Benchmark study on the assessment of ship damage conditions during stranding. *Ships and Offshore Structures* **7,** 197–213. doi:`10.1080/17445302.2010.537087` (2012).

181. *Ozdogan,* B. *Improvement and Validation of an Analytical Code for Ship Collisions Based on Super-Element Method Bayram Ozdogan* tech. rep. January 2018 (Icam, 2015).

182. *Ehlers,* S. A procedure to optimize ship side structures for crashworthiness. *Proceedings of the Institution of Mechanical Engineers Part M: Journal of Engineering for the Maritime Environment* **224,** 1–11. doi:`10.1243/14750902JEME179` (2010).

183. *Raikunen,* J., *Avi,* E., *Remes,* H., *Romanoff,* J., *Lillemäe-Avi,* I. & *Niemelä,* A. Optimisation of passenger ship structures in concept design stage. *Ships Offshore Struct.* **14,** 320–334. doi:`10.1080/17445302.2019.1590947` (2019).

Resumé subtantiel des travaux

Présentation du contexte

Cette thèse, partie intégrante du projet de recherche Européen **FLARE** (**FL**ooding **A**ccident **RE**sponse), concerne la réponse structurelle des navires lors d'un échouement.

Les récents accidents du MV Wakashio (2020) et du Costa Concordia (2012) ont montré que malgré l'investissement continuel de l'industrie navale pour accroître la sécurité des navires, des efforts sont encore nécessaires afin de limiter le nombre d'accidents maritimes et leurs conséquences.
Le secteur maritime se réfère aux guides SOLAS 2009 et SOLAS 2022 pour minimiser l'endommagement et la probabilité pour un navire de sombrer suite à une collision ou à un échouement. La réglementation SOLAS 2022 est fondée sur une approche probabiliste issue d'analyses statistiques d'accidents impliquant essentiellement des navires de charge. Elle ne prend pas explicitement en compte la structure du navire (présence ou non d'une double coque, espacement des raidisseurs...) et la capacité d'absorption d'énergie (matériaux, épaisseurs...). Les distributions statistiques d'endommagement sont pilotées uniquement par la longueur, la largeur et le tirant d'eau du navire. Par conséquent, il est très difficile, voire impossible de quantifier une possible réduction de l'endommagement associée à un design alternatif de navire.

Dans ce contexte, le projet européen **FLARE**[1] initié en juin 2019 avait entre autres pour objectif de développer une méthode fiable et rapide pour l'analyse de stabilité des navires à passagers après endommagement (collision et échouement). Ce projet collaboratif est actuellement conduit en partenariat avec des armateurs de navires à passagers, des chantiers navals, des sociétés de classification, des centres de recherche et des universités européens.

L'analyse de stabilité des navires après endommagement nécessite de quantifier les conséquences d'un accident en considérant des centaines voire des milliers de scénarios. Le calcul non-linéaire par éléments finis est aujourd'hui reconnu comme l'approche la plus précise et la plus polyvalente pour simuler les collisions et échouements de navires. Néanmoins, les temps de calculs associés sont très importants (parfois prohibitifs) et rendent la méthode inadaptée aux phases d'avant-projet ou lorsque de nombreux scénarios doivent être étudiés.
Les travaux de thèse visent donc à développer un solveur basé sur des formulations simplifiées, permettant d'estimer rapidement l'endommagement subi par un navire à passagers lors d'un échouement. Les objectifs suivants ont donc été définis au démarrage de la thèse :

---

[1] `https://www.flare-project.eu/`

- Développer des formulations analytiques basées sur l'analyse limite plastique permettant une estimation rapide de l'endommagement d'un navire échoué sur un rocher idéalisé par une forme paraboloïde.
- Implémenter les développements dans un solveur fiable et rapide puis coupler ce solveur à un code "fluide" existant permettant de prendre en compte l'action des forces hydrodynamiques. L'outil ainsi créé sera utilisé en bureaux d'étude au stade de la préconception ou pour l'évaluation de la stabilité des navires suite à un échouement sur fond rocheux.
- Valider, par comparaison à des simulations numériques, les fonctionnalités suivantes : échouement sans déchirure de coque, échouement avec perforation de coque et cas particulier où les oscillations verticales du navire conduisent à la création de plusieurs brèches.

Représentation du fond marin

La réponse d'un navire lors d'un échouement est fortement influencée par la forme du rocher. La première étape de l'analyse consiste à définir une forme simple représentative des fonds marins. Dans la littérature, quatres principales formes mathématiques décrivent les fonds marins. Les représentations en forme de "coin" ou bien coniques déclenchent quasi instantanément la rupture de la coque. Les rochers larges modélisés comme des pyramides tronquées n'amènent jamais à la rupture de la coque.
Les fonds marins peuvent aussi être modélisés à l'aide de fonctions elliptiques paraboloïdes. Cette dernière description permet d'envisager un large panel de scénarios et de générer des rochers aussi bien saillants que larges et bombés, en faisant varier uniquement deux coefficients dimensionnels. Par conséquent, dans cette thèse, le fond marin est systématiquement décrit par une fonction elliptique paraboloïde.

Chapitre 2

Le second chapitre est consacré à l'explication des différents mécanismes impliqués dans un échouement de navire. La mécanique des collisions/échouements dans le domaine naval est habituellement scindée en deux parties :

- La dynamique externe
- La mécanique interne

La dynamique externe traite des mouvements rigides globaux d'un navire impliqué dans une collision ou un échouement. Elle est régie non seulement par la force d'impact mais aussi par les forces hydrodynamiques agissant sur la partie immergée de la coque du navire. La mécanique interne, quant à elle, traite des modes de déformation et de déchirure des différents constituants du navire tels que le bordé, les ponts, les cloisons et les raidisseurs secondaires... Ces déformations et ruptures (flexion, déformation membranaire, déchirure, écrasement, flambement, etc.) se produisent essentiellement à proximité de la zone d'impact.

Une revue bibliographique présentant les différentes méthodes permettant de modéliser la dynamique externe et la mécanique interne ainsi que leurs avantages et inconvénients sont présentées dans ce chapitre. Compte tenu de cette synthèse bibliographique et dans l'objectif de développer un code de calcul précis et rapide, il résulte que :

- La dynamique externe sera prise en compte à l'aide d'un solveur "fluide" existant nommé *MCOL*.
- La mécanique interne sera traitée par la méthode des Super-Éléments.

La méthode des Super-Éléments consiste à diviser le navire en macro-éléments appelés Super-Éléments (S.E). Ils représentent les principaux composants d'un fond de navire : les panneaux de coques externe et interne, les varangues et les carlingues.
Pour chaque S.E, les principaux mécanismes de déformations sont identifiés. Des expressions analytiques pour le calcul de la force résistante et de l'énergie dissipée sont alors construites à partir du théorème de la borne supérieure en plasticité, puis validées individuellement par comparaison aux résultats numériques.

Chapitre 3

Le troisième chapitre est dédié à la calibration des différents paramètres nécessaires aux simulations par éléments finis car celles-ci seront utilisées comme référence dans la suite de la thèse. La calibration des modèles éléments finis se fait par comparaison à des essais à échelle réduite d'échouements et collisions de navires extraits de la litérature. Après une étude de convergence de maillage, il s'avère que pour bien capturer l'ensemble des mécanismes de déformations, la taille des éléments finis doit suffisament petite. Les futures simulations numériques seront donc réalisées avec une taille de maille de 30mm associée à des éléments de coque type Belytschko-Tsay comprenant cinq points d'intégration dans l'épaisseur des tôles. Le matériau est représenté par un modèle elastoplastique bi-linaire et les effets de vitesse de déformation sont négligés compte tenu des vitesses attendues au moment de l'impact ($\leq 10m/s$).

Chapitre 4

Dans ce chapitre, les réponses des principaux constituants d'un fond de navire sont analysées en supposant que la coque se déforme sur le rocher sans rupture (pas de perforation). Des fonds de navires horizontaux mais aussi inclinés (bouchains) sont étudiés. Les développements analytiques réalisés pour un fond horizontal constituent en fait un cas particulier du fond incliné. Les formulations simplifiées sont développées en se basant sur le théorème de la borne supérieure en plasticité puis systématiquement confrontées à des simulations numériques. En règle générale, une bonne corrélation des résultats est obtenue. Les écarts les plus importants sont observés principalement lorsque le rocher est très saillant. Dans ce cas, l'énergie dissipée est systématiquement sous-estimée par le modèle analytique (jusqu'à environ 20%).
De ces développements et analyses, il résulte que les constituants dissipant le plus d'énergie sont : la coque extérieure et les carlingues, alors que les varangues absorbent moins de 10% de l'énergie cinétique initiale du navire. Le frottement quant à lui a une influence significative sur les résultats. Augmenter le coefficient de friction de 0.1 à 0.3 entraîne le doublement de l'énergie dissipée par frottement. A contrario, la force de réaction verticale

est indépendante du coefficient de friction. D'autre part, l'inclinaison du fond par rapport au plan horizontal a une influence significative sur les résultats. Une inclinaison de 10° suffit à réduire de 2/3 la force longitudinale et de 1/2 la force verticale.

Chapitre 5

Le chapitre 5 est consacré aux réponses des différents Super-Éléments lors d'un échouement avec perforation. Dans un premier temps, le problème de la déchirure de plaque est étudié. Les principaux mécanismes de dissipation d'énergie sont le frottement, la déformation en membrane (cisaillement), la flexion plastique et la propagation de la fissure. Les expressions analytiques font intervenir un paramètre libre, l'angle θ, qui est censé s'ajuster pour donner la force résistante la plus faible. Le modèle analytique révèle que l'énergie dissipée par ce mode de déformation est très sensible au coefficient de friction coque/rocher. Dans le même temps, la force verticale apparaît une nouvelle fois quasi indépendante du coefficient de frottement et de la profondeur de pénétration verticale du rocher dans la coque.

Dans un deuxième temps, le comportement des varangues est traité. La réponse des varangues est fortement couplée à celle du fond du navire et modéliser avec précision leur contribution reste un défi. Une formulation simplifiée est néanmoins proposée et les écarts observés par rapport aux calculs numériques n'exèdent pas 15%. Il convient aussi de souligner que la contribution en termes d'énergie dissipée de ces grands raidisseurs transversaux reste relativement faible ($\leq 20\%$).

Enfin, l'étude de la réponse des carlingues montre que celle-ci est dépendante de la forme du rocher. Pour des rochers larges, lorsque la coque est déchirée, cette réponse est semblable à celle observée dans le cas d'une coque impactée sans déchirure (Chapitre 4). En revanche, plus le rocher est saillant, plus la carlingue a tendance à "glisser" sur le côté du rocher, ne laissant place qu'à du cisaillement (la flexion étant très faible).

L'ensemble des formulations développées permettent d'estimer l'énergie dissipée avec un écart maximum de 20% par rapport au calcul numérique.

Chapitre 6

Ce chapitre présente les développements analytiques réalisés lorsque le rocher impacte la coque avec un angle oblique. Cette situation correspond à celle d'un navire soumis à un mouvement de cavalement (horizontal) combiné à un mouvement de pilonnement (vertical).

Dans ce type de scénario, le navire est supposé être animé d'une vitesse horizontale et verticale au moment de l'impact. Il vient tout d'abord toucher le rocher puis, sous l'action combinée de ce dernier et de la poussée d'Archimède, il repart vers le haut. Dans le même temps, le navire est soumis à un mouvement de cavalement en raison de sa vitesse longitudinale. Sous l'effet de la gravité, le navire redescend ensuite et vient de nouveau impacter le rocher un peu plus loin sur sa structure. Il est donc soumis à un mouvement combiné de cavalement et de pilonnement, les oscillations verticales étant gouvernées par la force de contact et par le rappel hydrostatique. Ces mouvements mettent en exergue de nouveaux modes de déformation et d'absorption d'énergie. Des modèles simplifiés sont ainsi développés pour les prendre en compte.

Dans cette situation, la coque exterieure absorbe par déformation plastique jusqu'à 35% de l'énergie totale dissipée (déformation + frottement). Il apparaît également qu'aussi longtemps que la coque reste non perforée, le modèle proposé représente correctement les forces résistantes. En revanche, lorsque que la déchirure est déclenchée, les expressions analytiques développées tendent à sous-estimer l'énergie dissipée (jusqu'à 20%) car certains modes de déformations ne sont pas pris en compte, notamment les modes de créations de pétales.

Chapitre 7

L'ensemble des formulations précédemment développées est implémentées dans un solveur Super-Eléments nommé FLAGS et ce dernier est couplé au solveur MCOL, ce qui permet de prendre en compte l'action de l'eau environnante.

Dans ce septième chapitre, le fonctionnement global de l'outil FLAGS/MCOL ainsi que les différents modules du programme sont présentés. Cet outil est ensuite confronté à des simulations par éléments finis Ls-Dyna/MCOL pour des échouements sur le fond du navire, sur le côté du navire mais également des échouements au début desquels le navire dispose à la fois d'une vitesse horizontale et verticale. Comparativement aux simulations par éléments finis, l'écart moyen sur l'énergie dissipée est d'environ 20%. Le temps de calcul est quant à lui divisé par 10 000, ce qui rend l'outil FLAGS/MCOL très efficace par rapport à la simulation numérique.

Les calculs numériques (Ls-Dyna) et analytiques (FLAGS) mettent en évidence les deux points suivants :

- Dans le cas d'un échouement sur le fond du navire, l'étendue de l'endommagement est principalement pilotée par l'énergie cinétique initiale du navire.
- Dans le cas d'un échouement latéral (sur le côté) le navire a tendance à "s'échapper" du rocher. La zone endommagée dépend alors en grande partie non seulement de l'énergie disspée par déformation et frottement mais aussi de la facilité avec laquelle le navire "s'échappe" du rocher, ce phénomène étant favorisé à la fois par la relativement faible inertie du navire en embardée, lacet et roulis et par l'absence de rappel hydrostatique.

L'outil FLAGS/MCOL, une fois validé, est utilisé pour étudier l'influence de différents paramètres structuraux sur l'étendue de la zone endommagée. Des milliers de configurations d'accidents sont traités. Après analyse, il apparait que les paramètres influents sont les suivants :

- L'épaisseur de la coque extérieure
- Le grade du matériau caractérisé par sa contrainte d'écoulement plastique
- Le coefficient de frottement

On montre également que l'effet d'un renforcement structurel sera toujours moins efficace (d'environ 50%) en cas d'échouement sur le côté du navire qu'en cas d'échouement par le fond, en raison de la tendance du navire à "s'échapper" du rocher dans le premier cas.

Chapitre 8

Les travaux de thèse sont enfin résumés au chapitre 8. Les contributions scientifiques personnelles sont énumérées et des perspectives de poursuite de ces travaux de recherche sont suggérées.

Titre : Développement d’un solveur rapide et fiable basé sur des formules simplifiées pour l’étude de l’échouement de navire

Mots clés : Echouement de navire, NLFEA, Analyse limite plastique, Méthodes simplifiées

Résumé : Le calcul non-linéaire par éléments finis est aujourd’hui l’approche la plus précise pour l’étude des échouements de navires. Néanmoins, les temps de calculs importants rendent cette méthode inadaptée lorsque de nombreux scenarios doivent être étudies. Dans le cadre du projet de recherche Européen **FLARE** (**FL**ooding **A**ccident **RE**sponse), ces travaux de thèse visent à développer un solveur basé sur des formulations simplifiées permettant d’estimer rapidement l’endommagement subi par un navire à passagers lors d’un échouement. Le fond marin est représenté par un paraboloïde elliptique, permettant de générer des rochers à la fois tranchants ou larges, en faisant varier deux coefficients. Le navire quant à lui est divise en macro-éléments appelés Super-Eléments (S.E), qui représentent les principaux composants d’un fond de navire. Pour chaque S.E, des simulations par E.F. sont réalisées avec le code Ls-Dyna. A l’issue de ces simulations, des expressions analytiques de la force résistante sont construites, puis validées individuellement par comparaison aux résultats numériques. Dans la seconde partie de la thèse, les expressions simplifiées sont implémentées dans un solveur nomme FLAGS qui est couple au solveur existant « fluide » MCOL afin de prendre en compte les effets hydrodynamiques. L’outil FLAGS/MCOL est confronté avec succès aux calculs par éléments finis Ls-Dyna/MCOL pour différents échouements de navire a échelle 1. Pour finir, l’outil est utilisé pour simuler des milliers de scenarios dans le but de quantifier l’influence de divers renforcements structurels sur la taille de brèche.

Title : Development of a fast and reliable solver based on simplified formulae for ship grounding Analyses

Keywords : Ship grounding, NLFEA, Plastic analysis, Simplified methods

Abstract : Although non-linear finite element method is the most accurate approach for ship grounding damage analyses, its high computing cost makes it unsuitable when numerous scenarios have to be simulated. As part of the European research project **FLARE** (**Fl**ooding **A**ccident **RE**sponse), this PhD thesis aims to develop a solver based on simplified formulae to rapidly assess cruise ship grounding damage. The seabed is represented by an elliptic paraboloid allowing to generate both sharp and shallow rocks varying two parameters. The ship is divided into large elements, called Super-Elements (S.E), representing the main bottom components. For each S.E, Ls-Dyna simulations are carried out. Based on these simulations, closed-form expressions are derived for the resistant force according to the Upper-Bound theorem of plasticity. Finally, the analytical expressions are validated by comparison with numerical results. In the second part of the thesis, the developments are implemented in a structural solver named FLAGS, which is coupled with the external dynamics solver MCOL to account for the action of the surrounding water. FLAGS/MCOL solver is validated by confrontation to Ls-Dyna/MCOL F.E. solutions for various full scale grounding accidents. Finally, the simplified tool is used to simulate thousands of grounding events with the aim of quantifying the influence of different reinforcements on the ship damage extent.